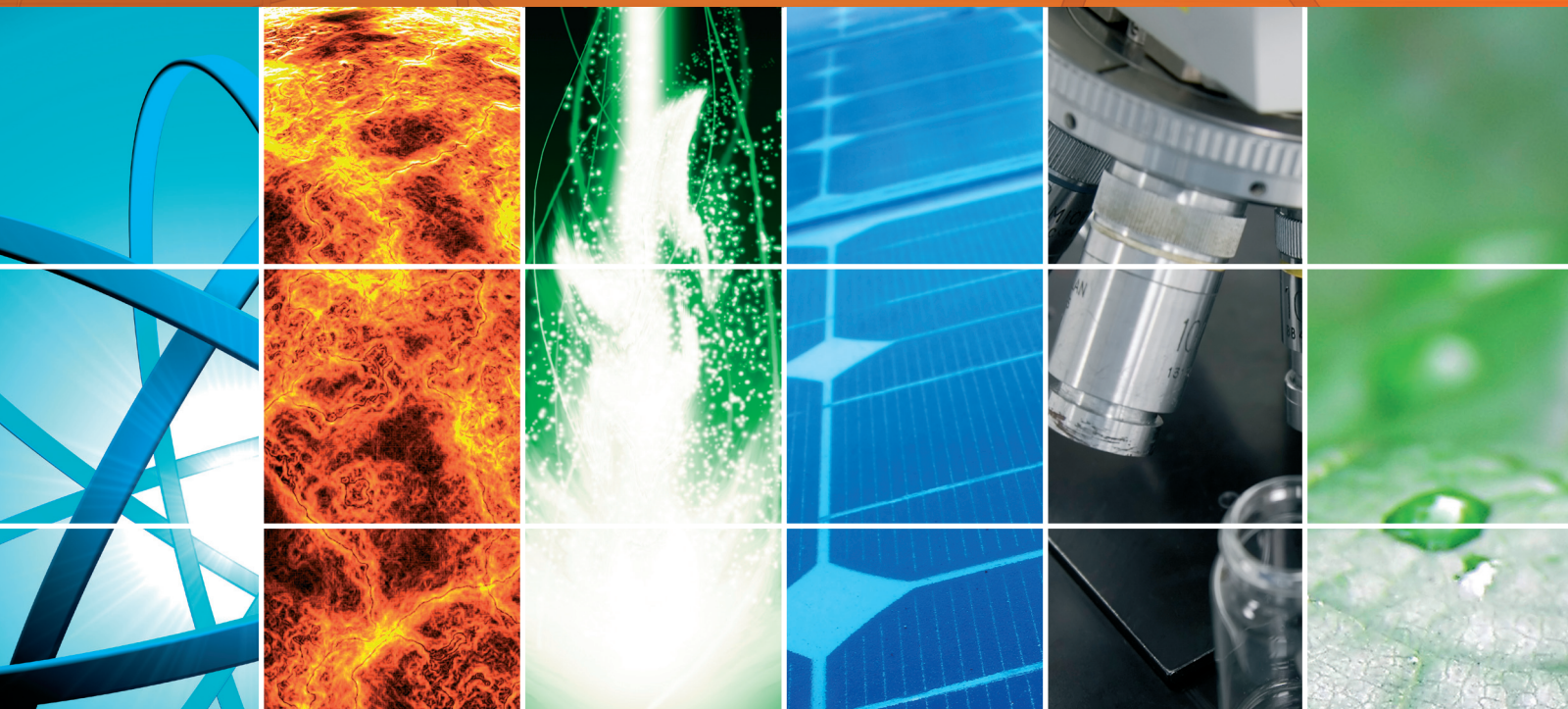# Environmental Photocatalysis

Guest Editors: Jiaguo Yu, Pengyi Zhang, Huogen Yu, and Christos Trapalis

Environmental Photocatalysis

Environmental Photocatalysis

Guest Editors: Jiaguo Yu, Pengyi Zhang, Huogen Yu, and Christos Trapalis

Editorial Board

Contents

Editorial

Environmental Photocatalysis

Jiaguo Yu,[1] Pengyi Zhang,[2] Huogen Yu,[3] and Christos Trapalis[4]

[1] *State Key Laboratory of Advanced Technology for Material Synthesis and Processing, Wuhan University of Technology, Luoshi Road 122, Wuhan 430070, China*

[2] *State Key Joint Laboratory of Environment Simulation and Pollution Control, School of Environment, Tsinghua University, Beijing 100084, China*

[3] *Department of Chemistry, School of Science, Wuhan University of Technology, Wuhan 430070, China*

[4] *Institute of Materials Science, National Centre for Scientific Research "Demokritos," Agia Paraskevi, Attica 15310 Athens, Greece*

Correspondence should be addressed to Jiaguo Yu, jiaguoyu@yahoo.com

In recent years, semiconductor photocatalytic technology has been demonstrated to be one of the "green" and effective strategies for solving environmental pollution problems. Therefore, environmental photocatalysis, including water disinfection, hazardous waste remediation, air and water purification, deodorization, antibacterial, and self-cleaning, has caused more and more attention in recent years (see the work of J. G. Yu et al. "*TiO$_2$ photocatalytic materials*" [1–9]). However, owing to low photocatalytic efficiency and activity of photocatalytic materials, the environmental applications of various photocatalytic technologies and materials are still very limited. Thus, more investigations are highly required from the viewpoint of practical use and commerce.

This special issue contains eighteen papers, which mainly deal with environmental photocatalysis. Among them eight papers are related to preparation, characterization, and photocatalytic performance of photocatalytic materials including CeO$_2$-SiO$_2$, BiVO$_4$, mesoporous TiO$_2$, Bi$_2$WO$_6$, Bi$_2$O$_3$-Bi$_2$CrO$_6$, H$_3$PW$_{12}$O$_{40}$/SiO$_2$, Mn-C-codoped TiO$_2$, ZnO, and N-doped TiO$_2$, three papers, are devoted to decolorization and treatment of industrial wastewater, three papers present photocatalytic degradation of dyes, one paper reports on indoor air purification, two papers are related to photo-Fenton and photoelectron-Fenton reactions, and the remaining one deals with photocatalytic degradation of nitrobenzene. Furthermore, in this special issue, 16 papers are research articles and two papers are review articles. We wish to express our thanks to all the authors who have made this special issue possible. A brief summary of all eighteen papers is presented below.

The article entitled "*Comparison between solar and artificial photocatalytic decolorization of textile industrial wastewater*" mainly reported the photocatalytic decolorization of industrial wastewater by using TiO$_2$ and ZnO photocatalysts. Heterogeneous photocatalysis applied under natural weathering conditions, in the presence of solar radiation, shows a promising degradation capability. The complete removal of color was achieved in a relatively short time of about 20 minutes when ZnO was used, and about 100 minutes when TiO$_2$ was used under solar irradiation. The results indicated that the photocatalytic decolorization of textile industrial wastewater was obviously influenced by different factors including mass and type of catalyst, reactor, dye concentration, and temperature.

In the article entitled "*Synthesis and characterization of CeO$_2$-SiO$_2$ nanoparticles by microwave-assisted irradiation method for photocatalytic oxidation of methylene blue dye*," CeO$_2$-SiO$_2$ nanoparticles were prepared for the first time by a facile microwave-assisted irradiation process. The photocatalytic activities were evaluated by the decomposition of methylene blue dye under UV light irradiations. The results showed that all solid samples exhibited mesoporous textures with high specific surface areas, relatively small pore size diameters, and large pore volume. The sample prepared by 30 min microwave irradiation time exhibited the best

photocatalytic activity. The photocatalytic activity of CeO_2-SiO_2 nanoparticles prepared by 30 min irradiation times was found to have better performance than commercial reference P25.

In the paper entitled "*Electrochemical techniques in textile processes and wastewater treatment*," the authors review the electrochemical techniques applied to textile industry. In particular, they are an efficient method to remove color of textile effluents. The reuse of the discolored effluent is possible, which implies an important saving of salt and water (i.e., by means of the "UVEC Cell"). Electrochemical reduction reactions are mostly used in sulfur and vat dyeing, but, in some cases, they are applied to effluents discoloration. However, the main applications of electrochemical treatments in the textile sector are based on oxidation reactions. Most of electrochemical oxidation processes involve indirect reactions which imply the generation of hypochlorite or hydroxyl radical in situ. These electrogenerated species are able to bleach indigo-dyed denim fabrics and to degrade dyes in wastewater in order to achieve the effluent color removal.

In the paper entitled "*Impact of preparative pH on the morphology and photocatalytic activity of BiVO$_4$*," single-crystalline $BiVO_4$ was prepared using aqueous-phase precipitation method by adjusting pH. The effects of pH on structure, surface morphology, visible-light photocatalytic activity, and light absorption performance of $BiVO_4$ were explored and discussed. The highest photocatalytic performance on the degradation of a methylene blue solution was observed under pH = 7.0 for $BiVO_4$ in monoclinic scheelite, which is attributed to its small grain size and marked surface oxygen evolution ability.

In the paper entitled "*Mesoporous TiO$_2$ micro-nanometer composite structure: synthesis, optoelectric properties, and photocatalytic selectivity*," mesoporous anatase TiO_2 micro-nanometer composite structure was prepared using solvothermal method at 180°C, followed by calcination at 400°C for 2 h. The photocatalytic activity was characterized by photodegradation of sole rhodamine B (RhB) and sole phenol aqueous solutions under simulated sunlight irradiation and compared with that of Degussa P-25 under the same conditions. The photodegradation preference of this mesoporous TiO_2 was also investigated for an RhB-phenol mixed solution. The results showed that the TiO_2 composite structure consisted of microspheres with a size of ~0.5–2 μm and irregular aggregates with rough surfaces. The photodegradation activities of this mesoporous TiO_2 on both RhB and phenol solutions were higher than those of P25. Moreover, the prepared TiO_2 exhibited photodegradation preference on RhB in the RhB-phenol mixture solution.

The article entitled "*Rapid decolorization of cobalamin*" examined the photocatalytic decolorization of cobalamin in aqueous solution with different types of catalysts including ZnO, TiO_2 (Degussa P25), TiO_2 (Hombikat UV100), TiO_2 (Millennium PC105), and TiO_2 (Koronose 2073) under UVA irradiation. The effects of experimental parameters on photocatalytic oxidation were investigated. The results indicated that the photocatalytic decolorization of cobalamin was well described by pseudo-first-order kinetics according to the Langmuir-Hinshelwood model. The activation energy was calculated according to Arrhenius plot and was found to be 28 ± 1 kJ·mol^{-1} for ZnO and 22 ± 1 kJ·mol^{-1} for TiO_2 (Degussa P25). The total organic carbon (TOC) analysis indicated that the decolorization rate of dye was faster than the total mineralization. The activity of different types of catalysts used in this study was of the following sequence: ZnO > TiO_2 (Degussa P25) > TiO_2 (Hombikat UV100) > TiO_2 (Millennium PC105) > TiO_2 (Koronose 2073).

The article entitled "*Feasibility of carbonaceous nano-material-assisted photocatalysts calcined at different temperatures for indoor air applications*" examined the characteristics and photocatalytic activity of multiwall carbon nanotube-assisted TiO_2 (MWNT-TiO_2) nanocomposites and their potential indoor air applications. The results indicated that the MWNT-TiO_2 composites calcined at low temperatures showed higher photocatalytic activity for decomposition of aromatic hydrocarbons at indoor concentrations than those calcined at high temperatures. The mean rates for the decomposing benzene, toluene, ethyl benzene, and o-xylene (BTEX) by the composite calcined at 300°C were 32%, 70%, 79%, and 79%, respectively, whereas they were 33%, 71%, 78%, and 78% for the composite calcined at 400°C, respectively. In contrast, the rates decreased to close to zero when the calcination temperature increased to 600°C. Moreover, the MWNT-TiO_2 exhibited superior photocatalytic performance for the decomposition of indoor air pollutants compared to pure TiO_2 under conventional UV-lamp irradiations.

The article entitled "*Heterogeneous photo-Fenton reaction catalyzed by nanosized iron oxides for water treatment*" reviewed the recent developments in the heterogeneous photo-Fenton reaction which utilized nanosized iron oxides as catalysts for maximizing the activity due to the enhanced physical and chemical properties caused by the unique structures. This paper also summarized the fundamentals of the Fenton reaction, which determined the inherent drawbacks and associated advances, to address the advantages of iron oxides and nanosized iron oxides.

In the paper entitled "*UV-irradiated photocatalytic degradation of nitrobenzene by titania binding on quartz tube*," a new method for UV-irradiated degradation of nitrobenzene by titania photocatalysts was presented. Titania nanoparticles were coated on a quartz tube by the addition of tetraethyl orthosilicate into the matrix. The dependence of nitrobenzene photodegradation on pH, temperature, concentration, and air feeding was discussed, and the physical properties such as the activation energy, entropy, enthalpy, adsorption constant, and rate constant were acquired by conducting the reactions in a variety of experimental conditions. The optimum efficiency of the photodegradation with the nitrobenzene residue as low as 8.8% was obtained and the photodegradation mechanism was also investigated by HPLC, GC/MS, ion chromatography (IC), and chemical oxygen demand (COD) analyses.

In the paper entitled "*Hydrothermal synthesis of iodine-doped Bi$_2$WO$_6$ nanoplates with enhanced visible and ultraviolet-induced photocatalytic activities*," the iodine-doped

Bi_2WO_6 (I-BWO) photocatalyst was prepared by a hyline-breakdrothermal method using KI as the source of iodine. The photocatalytic activity of I-BWO for the degr-adation of rhodamine B (RhB) was higher than that of pure BWO and I_2-loaded Bi_2WO_6 (I_2-BWO) sample regardless of visible light (>420 nm) or ultraviolet light (<400 nm) irradiation. The results of DRS analysis showed that the I-BWO and I_2-BWO catalysts had narrower band gaps. XPS analysis proved that the multivalent iodine species including I^0 and I^- were coadsorbed on the defect surface of Bi_2WO_6 in I-BWO. The enhanced photocatalytic activity of I-BWO for degradation of RhB was due to the synergetic effect of a small crystalline size, a narrow band gap, and plenty of oxygen vacancies.

The article entitled "*Synthesis and photocatalytic properties of one-dimensional composite Bi_2O_3-Bi_2CrO_6 nanowires*" reported preparation of one-dimensional composite Bi_2O_3-Bi_2CrO_6 nanowires by a simple microwave-assistant hydrothermal method. The diameter of the nanowires varied from 30 to 100 nm and the length was a few micrometers. Methylene blue (MB) solutions were used to evaluate the visible light photocatalytic activities of the prepared samples. Compared with Bi_2O_3, the Bi_2O_3-Bi_2CrO_6 composite nanowires showed enhanced performance in oxidization of MB under visible light.

In the paper entitled "*Pretreatment of color filter wastewater towards biodegradable by Fresnel-lens-assisted solar TiO$_2$ photocatalysis*," the experimental design of response surface methodology (RSM) was employed to assess the effect of critical process parameters (including initial pH, TiO_2 dosage, and reaction time) on pretreatment performance in terms of BOD5/COD, COD, and TOC removal efficiency. Appropriate reaction conditions were established as an initial pH of 7.5, a TiO_2 dosage of 1.5 g/L with a reaction time of 3 h for increasing the BOD5/COD ratio to 0.15, which implied that the treated wastewater would be possibly biodegradable. Meanwhile, the rates of COD and TOC removals reached 32.9% and 24.4%, respectively. With the enhancement of Fresnel lens, the required reaction time for improving the biodegradability of wastewater to 0.15 was 1 h only. Moreover, the rates of COD and TOC removals were promoted to 37.4% and 25.8%, respectively. This was mainly due to the concentrated effect of Fresnel lens for solar energy, including an increase of 2 times of solar irradiation and a increase of 15–20°C of wastewater temperature. Consequently, solar TiO_2 photocatalytic process with the use of a PMMA Fresnel lens could offer an economical and practical alternative for the pretreatment of industry wastewater containing diversified biorefractory pollutants with a high concentration of COD such as color filter wastewater.

In the paper entitled "*Photocatalytic degradation of rhodamine B with $H_3PW_{12}O_{40}$/SiO_2 sensitized by H_2O_2*," the Keggin-type $H_3PW_{12}O_{40}$ was loaded on the surface of SiO_2 by the sol-gel method and sensitized by H_2O solution. The photocatalytic degradation of rhodamine B (RhB) by $H_3PW_{12}O_{40}$/SiO_2 (x) under simulated natural light irradiation was investigated. The results indicated that at optimal condition (initial concentration of methyl orange is 10 mg/L, catalyst dosage is 0.8 g, and the pH is 2.5) the degradation rate of RhB was as high as 97.7% after 2 h

under simulated natural light irradiation. The photocatalytic reaction of RhB could be expressed as a first-order kinetic model.

In the paper entitled "*Synthesis and characterization of Mn-C-codoped TiO$_2$ nanoparticles and photocatalytic degradation of methyl orange dye under sunlight irradiation*," novel visible-light-driven Mn-C-TiO$_2$ nanoparticles were synthesized by sol-gel method using polyoxyethylenes orbitan monooleate (Tween 80) as template and carbon precursor and manganese acetate as manganese precursor. The photocatalytic activity of synthesized catalyst was evaluated by photocatalytic oxidation of methyl orange (MO) solution under the sunlight irradiation. The results showed that Mn-C-TiO$_2$ nanoparticles had higher activity than other samples under sunlight, which was due to their high specific surface area, smaller particle size, and lower band gap energy.

The article entitled "*Photocatalytic performance of ZnO : Al films under different light sources*" reported preparation of ZnO and Al doped ZnO films by spray pyrolysis. Their photocatalytic activity was evaluated by the decomposition of the methyl orange dye using different light sources: ultraviolet light, artificial white light, and direct sunlight. The Al doped ZnO films presented a very high degradation rate not only under UV and sunlight (100% degradation), but also under white light (90% degradation after the same irradiation time). An unexpected high degradation was also obtained in the dark, which indicated that a nonphotonic process took place parallel to the photocatalytic process. This was due to the extra electrons—provided by the aluminum atoms—that migrated to the surface and produced $O_2^{\bullet-}$ radicals favoring the decomposition process even in the dark. The high activity achieved by the ZnO : Al films under natural conditions could be potentially applied to water treatment processes.

The article entitled "*Supported nanosized α-FeOOH improves efficiency of photoelectro-Fenton process with reaction-controlled pH adjustment for sustainable water treatment*" demonstrated that the overall efficiency of photoelectro-Fenton process was improved by rapidly recycling the iron substance. Nanosized iron oxide was prepared and employed to ensure such rapid recycling. SEM and XRD results showed that the as-prepared iron oxide was α-FeOOH with 20 nm in size. The experimental results of dimethyl phthalate (DMP) degradation indicated that diatomite-supported α-FeOOH (N-α-FeOOH/diatomite) could reduce the DMP concentration and total organic carbon. Furthermore, compared with Fe^{3+}, the N-α-FeOOH/diatomite saved 160 min for iron settlement at 20 mg L^{-1} DMP concentration. Also, with increasing the initial DMP concentration, extra energy consumed by the individual step of PE-Fenton reaction using the N-α-FeOOH/diatomite became negligible compared with that using free iron ions with increasing the initial DMP concentration.

The article entitled "*Photocatalytic degradation of organic dyes under visible light on N-doped TiO$_2$ photocatalysts*" focused on the application of white and blue light emitting diodes (LEDs) as light sources for the photocatalytic degradation of organic dyes in liquid phase with visible light. The photocatalytic activity of N-doped TiO_2, synthesized

by direct hydrolysis of titanium tetraisopropoxide with ammonia, was evaluated by means of a batch photoreactor. The bandgap energy of TiO_2 was moved into the visible range from 3.3 eV to 2.5 eV. The results demonstrated that the right selection of operating conditions was allowed to effectively degrade different dyes with the N-doped TiO_2 photocatalysts irradiated with visible light emitted by LEDs.

In the paper entitled "*Photocatalytic treatment of rhodamine 6G in wastewater using photoactive ZnO*," the photocatalytic activity of zinc oxide, prepared by precipitation followed by calcinations, was tested using rhodamine 6G as an organic pollutant. The results were compared with those obtained on P-25 titania and one of the samples had similar performances in terms of dye degradation degree, but needed higher pH values to prevent the photocatalyst degradation.

The above synopsis of the articles collected in this special issue on environmental photocatalysis indicates that this area of research is continuously expanding. Our hope is this special issue will stimulate further developments in the field of environmental photocatalysis.

Jiaguo Yu
Pengyi Zhang
Huogen Yu
Christos Trapalis

References

[1] J. G. Yu, M. Jaroniec, H. G. Yu, and W. H. Fan, "Synthesis, characterization, properties, and applications of nanosized photocatalytic materials," *Journal of Nanomaterials*, vol. 2012, Article ID 783686, 3 pages, 2012.

[2] Q. J. Xiang, J. G. Yu, and M. Jaroniec, "Graphene-based semiconductor photocatalysts," *Chemical Society Reviews*, vol. 41, pp. 782–796, 2012.

[3] Q. J. Xiang, J. G. Yu, and M. Jaroniec, "Synergetic effect of MoS_2 and graphene as cocatalysts for enhanced photocatalytic H_2 production activity of TiO_2 nanoparticles," *Journal of the American Chemical Society*, vol. 134, pp. 6575–6578, 2012.

[4] X. M. Zhou, G. Liu, J. G. Yu, and W. H. Fan, "Surface plasmon resonance-mediated photocatalysis by noble metal-based composites under visible light," *Journal of Materials Chemistry*, vol. 22, pp. 21337–21354, 2012.

[5] S. W. Liu, J. G. Yu, and M. Jaroniec, "Anatase TiO_2 with dominant high-energy 001 facets: synthesis, properties, and applications," *Chemistry of Materials*, vol. 23, pp. 4085–4093, 2011.

[6] S. Liu, J. Yu, and M. Jaroniec, "Tunable photocatalytic selectivity of hollow TiO_2 microspheres composed of anatase polyhedra with exposed 001 facets," *Journal of the American Chemical Society*, vol. 132, no. 34, pp. 11914–11916, 2010.

[7] W. G. Wang, J. G. Yu, Q. J. Xiang, and B. Cheng, "Enhanced photocatalytic activity of hierarchical macro/mesoporous TiO_2-graphene composites for photodegradation of acetone in air," *Applied Catalysis B*, vol. 119-120, pp. 109–116, 2012.

[8] J. Yu and X. Yu, "Hydrothermal synthesis and photocatalytic activity of zinc oxide hollow spheres," *Environmental Science and Technology*, vol. 42, no. 13, pp. 4902–4907, 2008.

[9] J. Yu, Y. Su, and B. Cheng, "Template-free fabrication and enhanced photocatalytic activity of hierarchical macro-/mesoporous titania," *Advanced Functional Materials*, vol. 17, no. 12, pp. 1984–1990, 2007.

Research Article

Photocatalytic Treatment of Rhodamine 6G in Wastewater Using Photoactive ZnO

Doina Lutic,[1] **Cristina Coromelci-Pastravanu,**[1] **Igor Cretescu,**[2]
Ioannis Poulios,[3] **and Catalina-Daniela Stan**[4]

[1] *Department of Materials Chemistry, Alexandru Ioan Cuza University, 11 Carol I Boulevard, 700506 Iaşi, Romania*

[2] *Department of Environmental Engineering and Management, Faculty of Chemical Engineering and Environmental Protection, Gheorghe Asachi Technical University of Iasi, 73 Professor D. Mangeron Street, 700050 Iaşi, Romania*

[3] *Department of Chemistry, Aristotle University of Thessaloniki, 54124 Thessaloniki, Greece*

[4] *Department of Drug Industry and Pharmaceutical Biotechnology, Grigore T. Popa University of Medicine and Pharmacy, 16 Universitatii Street, 700115 Iaşi, Romania*

Correspondence should be addressed to Igor Cretescu, icre@tuiasi.ro

Received 27 July 2012; Accepted 22 October 2012

Academic Editor: Christos Trapalis

The photocatalytic activity of zinc oxide, prepared by precipitation followed by calcination, was tested using rhodamine 6G as a rebel organic compound. The experiments were planned in order to allow an optimization procedure, by investigating the effects of different parameters such as the preparative method of the solid, amount of photocatalyst, pH of the reaction medium, and initial concentration of the dye. The results were compared with those obtained on P-25 Titania, and one of the samples had similar performances in terms of dye degradation degree, but needed higher pH values to prevent the photocatalyst degradation.

1. Introduction

The interest for the photocatalytic degradation of different refractory organics present in wastewaters, such as dyes, drugs, and pesticides, comes from the relatively simple procedure and somehow easy-to-set practical setup. The photocatalytic reactions occur in conditions somehow similar to heterogeneous catalysis, involving the simultaneous adsorption of the organic reactant species and oxygen on solid, followed by the oxidation on the surface. The photoactive solid is a semiconductive oxide able to capture the energy for the reaction from photons. The photocatalyst must therefore adsorb simultaneously significant amounts of oxygen and reducing species (organic molecules). A performant photocatalyst is expected to offer adsorption sites for the organics, meaning that a high specific surface area and/or open pore structure are welcome. A very important feature of the photocatalysis is that the reaction can occur at temperature values close to ambient; therefore, the photoreactions are "greener," since the thermal energy is expensive and, most often, its production is pollutant [1–4].

The most intensively species used as photocatalyst is the titanium dioxide in the anatas form; due to its $3.2\,\text{eV}$ band gap, it is able to capture the energy even from solar light, widely available, green, and costless. Current research is however devoted to investigate the behavior of other oxidic species such as ZnO, WO_3, Fe_2O_3, SnO_2, and combinations thereof as photocatalysts [5–9].

Rhodamine 6G (R₋6G) is a chemically stable organic dye, used often as a tracer to allow finding the transport direction and flow rate of water courses. Other applications concern the biotechnology (such as fluorescence microscopy and fluorescence correlation spectroscopy), and the biochemistry laboratories (as a diagnostic tool in medicine and plant pathology for the enzyme-linked immunosorbent assay (ELISA), to detect the presence of a substance, usually an antigen, in a liquid sample or wet sample). Due to its high stability, it is interesting to find photocatalytic systems able to decompose R₋6G to smaller biodegradable species or eventually mineralize it. There are quite many papers in the literature dealing with the photocatalytic degradation of several rhodamines, especially rhodamine B [10–16].

The aim of the present work was to synthesize photo-catalytically active zinc oxide (band gap around 3.3 eV [17]) and test it in the R_6G photodegradation. We investigated the influence of several operation parameters on the dye removal performance: the initial dye concentration, the pH value, and the photocatalyst concentration in the reaction medium. This study aims to investigate the properties of ZnO prepared in a very simple way in the photocatalytic degradation of a rebel test molecule, without investigating the degradation mechanism. The results will be used for comparisons with other transition metal oxides in the future studies.

2. Experimental Setup

The zinc oxide was prepared by precipitation as zinc hydroxide, followed by calcination. Zinc nitrate was used as precursor, due to its easy thermal decomposition in the target compound, if traces of the initial salt remain in the precipitate. Two precipitation agents were used, NaOH and urea.

The precipitation with NaOH was performed at room temperature, by the simultaneous pouring of zinc nitrate and NaOH solutions under continuous magnetic stirring in a beaker, while monitored by a Hanna HI 991003 pH-meter, to help keeping the pH value at 9. The achievement of the complete precipitation degree occurred by heating the slurry at 353 K for 16 hours.

The precipitation in the presence of urea was performed using a 5/1 molar ratio urea/Zn, by mixing the zinc nitrate solution with urea solution, at a concentration of zinc of about 0.25 moles L^{-1} in the final solution mixture. This solution was stirred at 363 K for 14 h under reflux; the final pH settled at 7. In the case of urea, the settlement of a basic pH value necessary for the precipitation is slowly obtained, due to the thermal decomposition of urea in ammonia and carbon dioxide. This procedure allows obtaining solids with special textures and superficial properties [18, 19], due to the slow formation of the crystal nuclei in the precipitation medium. The method is widely used in the synthesis of layered oxide structures and offers the possibility to obtain particles with a lower agglomeration degree and a more ordered structure, as regarded to those obtained in alkali precipitation medium.

The solids were recovered in both cases by centrifugation at 4000 rpm, washed several times with ultrapure water, dried at 353 K, then calcined 4 h at 500°C with a heating rate of $1°$ min^{-1}, then cooled down spontaneously. The samples were labeled as with ZnO-NaOH and ZnO-Urea.

The characterization of the solids was performed by X-ray diffraction, IR spectroscopy, scanning electron microscopy (SEM), and BET nitrogen adsorption. The XRD patterns were obtained on a Shimadzu D6000 machine, in the range of 5–70°, using CuKα radiation ($\lambda = 1.5406$ Å), in steps of 0.05°. The IR spectra were collected on an ABB MB 3000 apparatus. The scanning electron microscopy (SEM) was used to show the morphology of the synthesized solids; a SEM Tescan VEGA II LSH was used in this respect.
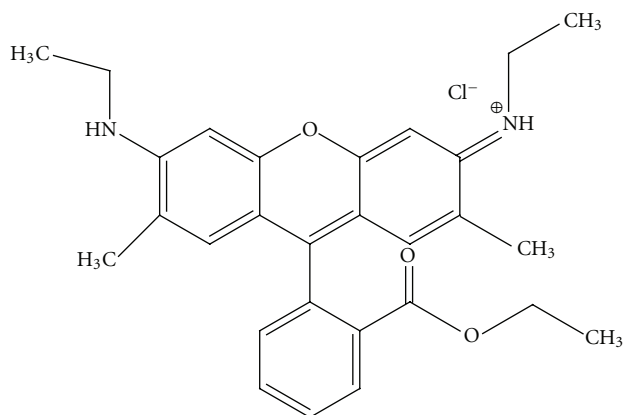
Figure 1: Chemical structure of R_6G.

(1) Glass reactor
(2) Pierced cap
(3) Quartz tube
(4) Magnetic range
(5) Magnetic agitator
(6) UV lamp
    Black cover
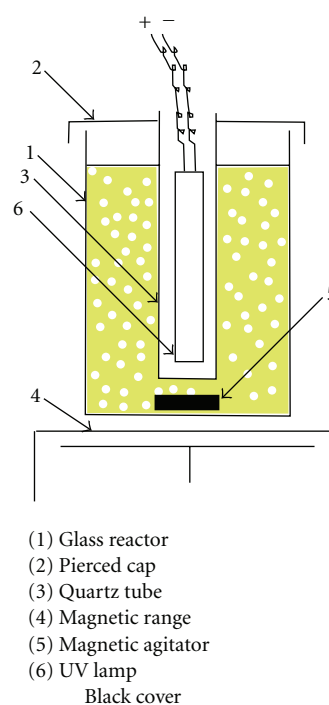
Figure 2: Experimental setup for the photocatalytic degradation.

The photocatalytic activities of both synthesized ZnO samples were studied for the photodegradation of R_6G dye ($C_{28}H_{31}N_2O_3Cl$); the formula is presented in Figure 1.

The photocatalytic degradation was performed using a cylindrical glass reactor (Figure 2), accommodating a central quartz tube in which an Osram UV-A lamp of 9 W (wavelength range 350–400 nm, maximum at 370 nm) is placed to irradiate the dye solution. At the bottom of the reactor, a magnetic range assures the homogenization. The experiments were performed on samples of 300 mL aqueous solutions of dye prepared with ultrapure water. The pH value was set using sulfuric acid 0.1 M or natrium hydroxide 0.1 M. The photocatalyst powder was dispersed in the dye solution, magnetically stirred for 30 minutes in dark, in order to enable establishing the adsorption/desorption equilibrium, then the lamp was turned on. Samples of 5 mL suspension were taken
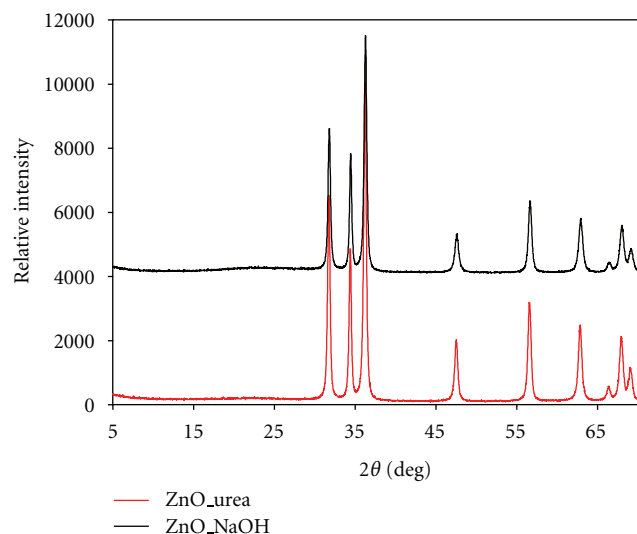
Figure 3: XRD pattern of ZnO samples.

(a)

(b)

Figure 4: SEM images of ZnO-urea (a) and ZnO-NaOH (b).

at specific time intervals, filtered immediately to separate completely the catalyst particles, and measured to determine the remaining dye concentration. Zero time reading was considered the moment when the lamp was turned on.

The dye concentration was measured by UV-vis spectroscopy, using a Shimadzu UV-1700 spectrophotometer; the UV-vis spectrum of R_6G displays a net maximum at 530 nm. An initial calibration was performed to check the extinction-concentration linearity and to ease the calculation of the concentration value by simple reading of the extinction for the dye solutions exposed to UV and/or contacted in dark with ZnO.

The photocatalytic tests were performed in ambient air. The pH values were monitored using a Microprocessor WTW pH 95 pH Meter. A scheme of the experimental setup is displayed in Figure 2.

The decolorization and photocatalytic degradation efficiency were calculated using the following:

$$\text{Dye\_removal } (\%) = \frac{C_0 - C_t}{C_0} \times 100, \qquad (1)$$

where C_0 and C_t are the initial and t is time concentrations of R_6G.

3. Results and Discussions

3.1. Characterization of the Photocatalyst. The XRD patterns of the samples ZnO-NaOH and ZnO-urea, presented in Figure 3, indicate well-crystallized solids, exhibiting the main peaks due to zinc oxide phase, as filed in JCPDS: 89–7102 [20] and no impurity phases. The peaks are somehow sharper and higher for the sample obtained with urea, indicating a more uniform and better-crystallized solid.

The XRD pattern also allowed calculating the medium crystallite size using Debye-Scherrer equation. The particle medium size, considering the factor $K = 0.94$, gave values of 21.5 nm for the sample ZnO-urea and 14.4 nm for

ZnO-NaOH. These particle sizes represent the dimensions of the primary particles, which associate in groups of several hundreds of nanometers, as shown on the SEM images (Figure 4). The grouping of the particles keeps a relatively uniform aspect of the bulk powder.

The agglomerations of ZnO-urea particles are almost spherical in shape and still keep a big free volume fraction in between, which is beneficial for the organic diffusion to the solid surface during the adsorption step. The ZnO-NaOH sample consists of grain associations with more planar shape and have the tendency to agglomerate very tightly, offering a smaller interparticle free space.

The IR transmission spectra of our samples were compared with those of a commercial zinc oxide, see Figure 5.

The spectra for the samples synthesized in our laboratory are quite similar and in line with the literature data [21]; only small differences in peaks intensities are noticed for
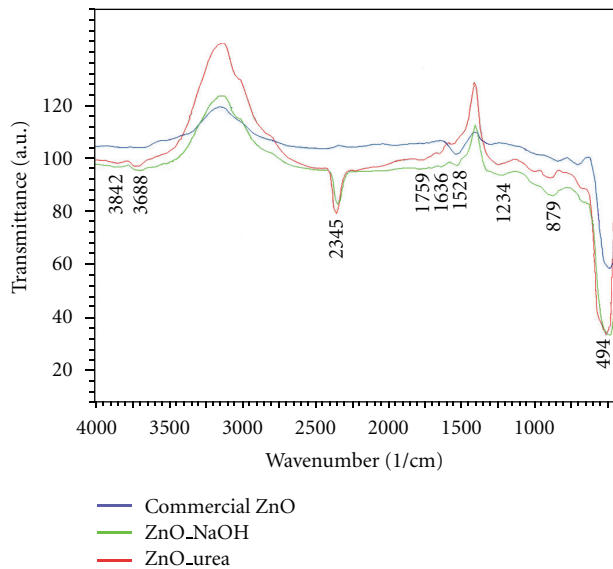
FIGURE 5: IR spectra of zinc oxide samples.
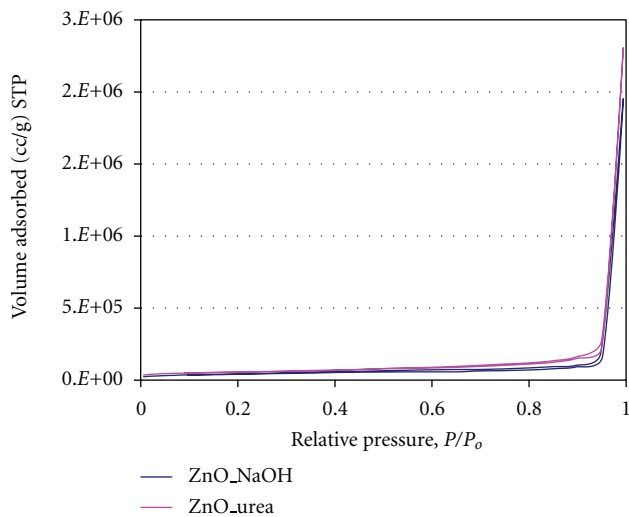
FIGURE 6: BET analysis results for ZnO.

our two samples. The peaks around $3600\,cm^{-1}$ indicate the presence of OH groups derived from water adsorption [22], while the one at $1636\,cm^{-1}$ is due to the characteristic H_2O scissoring mode. The peak from $2345\,cm^{-1}$ is due to the CO_2 adsorption on the basic sites of ZnO [23] and is missing in the commercial sample.

The BET analysis allowed the determination of the BET-specific surface areas, found to be $17.3\,m^2\,g^{-1}$ for ZnO-urea and, respectively, $13.04\,m^2\,g^{-1}$ for the ZnO-NaOH sample. The slow precipitation leads to higher specific surface areas, as expected. The isotherms of type 3 according to IUPAC, indicates low porosity solids, with a very narrow hysteresis loop. No significant internal porosity is found on these samples, see Figure 6.

3.2. Photocatalytic Experiments.
Three parameters were considered important for dye degradation process, namely, the
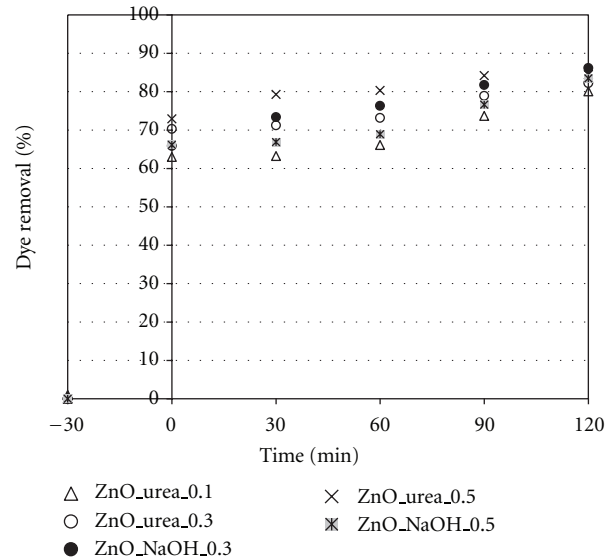
FIGURE 7: The influence of catalyst concentration on R_6G decolorization (pH = 10, 50 ppm initial dye concentration).

photocatalyst concentration, the pH value, and the initial dye concentration. In the parametric study, two of the above-mentioned factors were kept constant and the third was varied, in order to define their individual and simultaneous influence on the process. The comparison between our samples and titanium dioxide P-25 was made, in some cases, by performing selected experiments in similar conditions.

3.2.1. Influence of Catalyst Concentration. This series of experiments was performed at a constant pH = 10 value, working with an initial concentration of R_6G of 50 ppm. We used three concentrations of solid photocatalyst: 0.1, 0.3, and 0.5 g photocatalyst per liter of dye solution. A blank probe (irradiation with no catalyst) gave very low degrees of decolorizing, so we considered negligible the contribution of the radiation alone to decompose R_6G, in the time duration involved in the experiments; similar behavior for rhodamine B has been communicated by Fan et al., [24], Natarajan et al. [25], and Chen et al. [26]. The removal degree in time is displayed in Figure 7.

For all the tested photocatalyst samples, the same characteristic for the removal of R_6G is noticed. They strongly adsorb the dye in the equilibrium period of 30 minutes before the exposure to UV light; more than 60% of the dye is removed from the solution in all the tested mixtures. The photocatalytic reaction follows a slow increasing slope. The values of the total removal degree are similar for both samples, over 80% in 2 hours of irradiation. Since the removal degree of the dye on the photocatalyst in the medium containing 0.3 g catalyst per liter of dye solution is very close to the ones in the system with 0.5 g catalyst, we admit from this point forward the 0.3 g/L as the optimal concentration value.

3.2.2. The Influence of the Reaction pH. In order to investigate the influence of the pH role of the reaction medium on R_6G
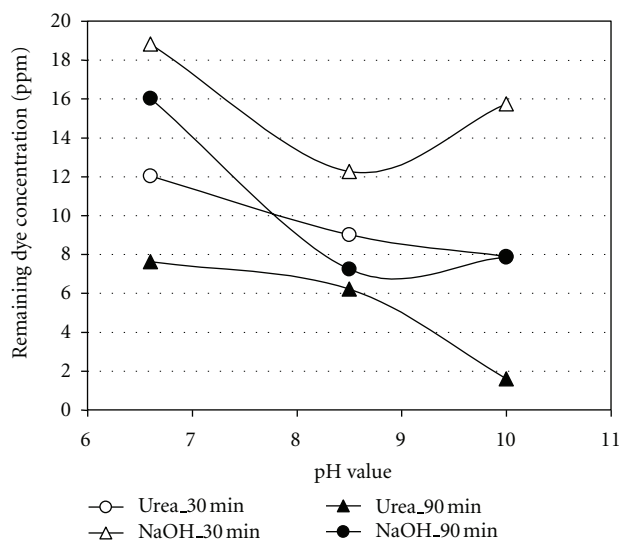
FIGURE 8: The pH influence on R‗6G decolorizing after 30 and 90 minutes of photoreaction (0.3 g/L catalyst, 30 ppm pf dye initially).

FIGURE 9: R‗6G concentration profile in time (0.3 g/L photocatalyst, 30 ppm/L dye) and TOC values for ZnO-urea sample, at pH = 10 and two photocatalyst concentrations.

decolorizing, this series of experiments was performed using 0.3 g/L catalyst, at pH values of 6.6, 8.5, and 10. The initial R‗6G concentration in these experiments was 30 ppm. The dye removal in these conditions is presented in Figure 8.

The differences in the degree of dye removal at the mentioned pH values are interesting to comment. The high values of the pH are favorable on dye degradation on ZnO-urea sample at both mentioned irradiation durations, 30 and 90 minutes. On the ZnO-NaOH sample, an optimum value of 8.5 for the reaction run can be defined at the considered time values. The dye removal degree reaches 98% on ZnO-Urea at pH = 10 in 90 minutes.

This somehow unexpected behavior determined us to investigate the dye removal by measuring the remaining concentrations at intermediate time values between up to 120 minutes of the photocatalytic reaction, Figure 9.

The evolution of the dye removal in time follows a special dynamic. A strong removal degree by adsorption is noticed during the equilibrium stage before the irradiation, followed by the increase of the dye concentration in the beginning of the photocatalysis step. In some cases this behavior repeats several times, see the curve for ZnO-NaOH at pH = 8.5. As will be shown in the next paragraph, the phenomenon is not observed if the initial R‗6G concentration is low (5 ppm). The explanation for this behavior could be the massive adsorption of the dye on ZnO. The R‗6G molecules are adsorbed on the functional groups of ZnO (most probably, OH groups, able to interact with the amino and ammonium groups from the structure of R‗6G) and they allow the subsequent adsorption of the incoming R‗6G molecules, most probably by forming "multilayers," since the value of the specific surface area of the solid after the adsorption step does not change significantly ($17 \, m^2 \, g^{-1}$ for the ZnO-Urea sample after the adsorption, compared to $17.3 \, m^2 \, g^{-1}$ of the initial sample). When the photodegradation begins, the first layer of adsorbed molecules on the photocatalyst surface is destroyed by the photodegradation of several molecules. The other molecules stacked on them are mobilized to the solution and the concentration of the dye increases. They are subsequently readsorbed and finally photodegraded. This statement is further confirmed by the TOC values (inlet Figure 9), showing that the mineralization degree reaches only 20% in 2 hours of photocatalytic process. The chromophore groups were totally destroyed during this time; the behavior is similar to that observed by Chen et al. [27].
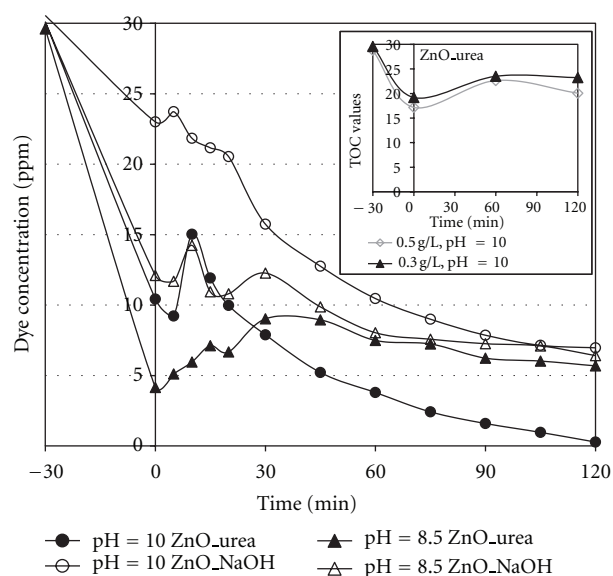
3.2.3. The Influence of Dye Concentration.
In order to study influence of the dye concentration on the degradation process, the pH value was kept at 8.5 and the catalyst concentration at 0.3 g/L, while the dye concentrations for the tests were 5, 30, and 50 ppm, see Figure 10.

An almost constant increase of the R-6G removal degree occurs at the low value of 5 ppm dye on the sample ZnO-Urea. In this case, after 2 hours of irradiation the removal of the organic is practically total. The other solid has a similar but less performant behavior. At the higher concentrations values, the removal occurs in 2 hours at degrees of around 80% for the initial value of 30 ppm and of 70–75% for the solution containing 50 ppm of R‗6G. This group of experiments proves a better net behavior of the ZnO-urea sample in comparison with ZnO-NaOH.

3.2.4. Comparison with TiO₂ Degussa P-25.
The use of other photocatalysts is interesting especially when the widely used and very versatile P-25 Titania cannot be used. Titania is stable and active in slightly acidic conditions, but occur important structural degradations at alkaline pH values, while ZnO is only stable in neutral to alkaline medium.

(a)

(b)

(c)
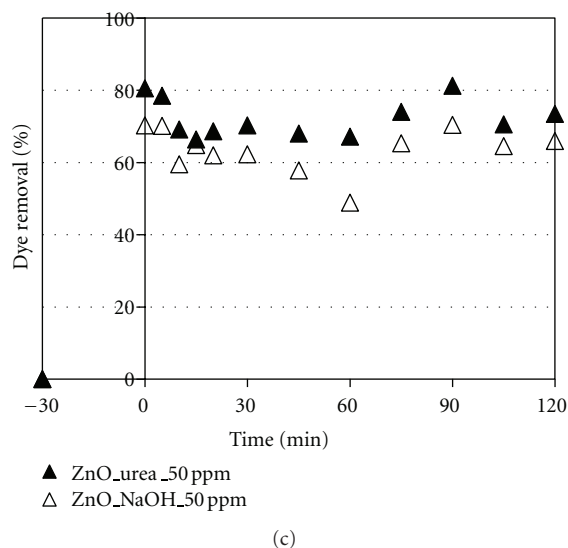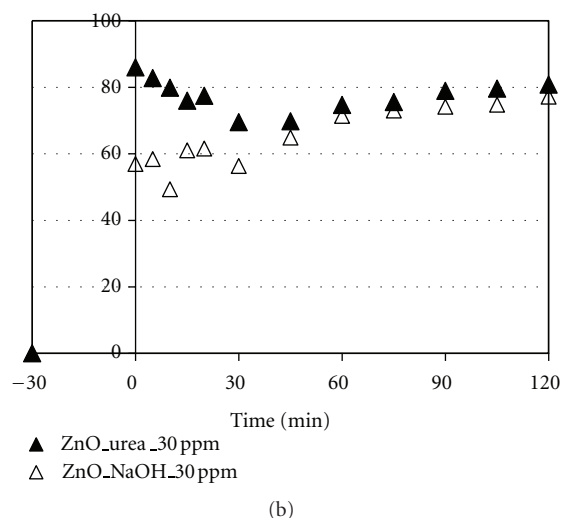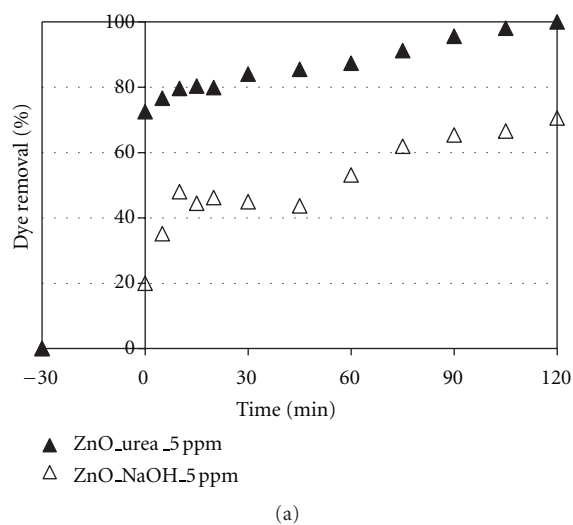
FIGURE 10: The dye removal in time at 5, 30, and 50 ppm of R_6G (0.3 g photocatalyst/L, pH = 8.5).
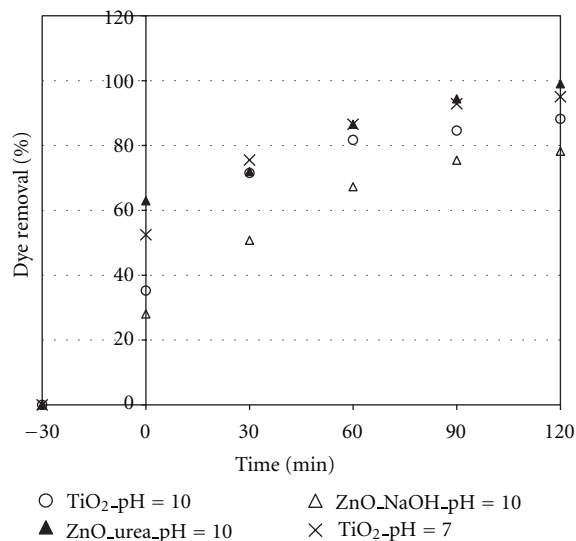
FIGURE 11: Comparison between R_6G removal on ZnO and TiO$_2$.

In order to compare the performance in the photoreaction of our ZnO samples with the results obtained on Titania, we performed two experiments on both ZnO samples at pH = 10 and on P-25 at pH values of 7 and 10, using an initial solution of 30 ppm R_6G at a photocatalyst concentration of 0.3 g/L, Figure 11.

The dye removal on TiO$_2$ indicates its different adsorptive behavior in function of the pH value. There is a clear higher adsorption degree at pH = 7 than at pH = 10, but the photocatalytic reaction brings quite similar removal degrees for both pH values, over 80% for both cases.

The performance of the ZnO-urea is closely similar to that on P-25. Since the stability at high pH values is better for ZnO than for TiO$_2$, our photocatalyst could be an alternative to the well-known P-25, for the photocatalytic reactions performed in basic solutions for rebel compounds decomposition.

In Table 1 are presented some selected results comparing the photocatalytic activity of ZnO samples and TiO$_2$, at pH values ensuring the stability of the samples.

The values show that the activity of ZnO-urea sample at alkaline pH is close to that of TiO$_2$ at pH values lower with about 3 units.

4. Conclusions

The zinc oxide prepared by zinc nitrate precipitation in urea medium, followed by calcination at 500°C, led to the obtaining of a zinc oxide sample with high capabilities of R_6G removal from slightly basic aqueous media. The study of parameters influencing the decolorizing process allowed us to find the operating conditions for achieving the highest dye removal rate: pH values over 8.5, up to 10; catalyst concentration 0.3 g/L; initial dye concentrations higher than 30 ppm. A strong initial adsorption is noticed on ZnO samples, followed by a slow photocatalytic reaction

Table 1: Selected results on photocatalytic activities of the ZnO and TiO$_2$ samples.

	ZnO_urea 90 min pH 8.5	ZnO_NaOH 90 min pH 8.5	ZnO_urea 90 min pH 10	ZnO_NaOH 90 min pH 10	TiO$_2$ 90 min pH 3.7	TiO$_2$ 90 min pH 5.5
R_6G 30 ppm	74.70	71.41	94.34	75.42	86.02	92.43
R_6G 50 ppm	67.10	48.86	85.19	—	—	84.68

on ZnO. The global performance in terms of dye removal is comparable with that obtained on P-25 Titania, known as the most typical and widely applied photocatalyst.

Acknowledgments

References

[1] S. Malato, J. Blanco, A. Vidal, and C. Richter, "Photocatalysis with solar energy at a pilot-plant scale: an overview," *Applied Catalysis B*, vol. 37, no. 1, pp. 1–15, 2002.

[2] M. N. Chong, B. Jin, C. W. K. Chow, and C. Saint, "Recent developments in photocatalytic water treatment technology: a review," *Water Research*, vol. 44, no. 10, pp. 2997–3027, 2010.

[3] A. Di Paola, E. García-López, G. Marcì, and L. Palmisano, "A survey of photocatalytic materials for environmental remediation," *Journal of Hazardous Materials*, vol. 211-212, pp. 3–29, 2012.

[4] I. Oller, S. Malato, and J. A. Sánchez-Pérez, "Combination of advanced oxidation processes and biological treatments for wastewater decontamination—a review," *Science of the Total Environment*, vol. 409, pp. 4141–4166, 2011.

[5] K. Nakata and A. Fujishima, "TiO$_2$ photocatalysis: design and applications—review article," *Journal of Photochemistry and Photobiology C*, vol. 13, no. 3, pp. 169–189, 2012.

[6] K. Hashimoto, H. Irie, and A. Fujishima, "TiO$_2$ photocatalysis: a historical overview and future prospects," *AAPPS Bulletin*, vol. 17, no. 6, 2007.

[7] A. Fujishima, T. N. Rao, and D. A. Tryk, "Titanium dioxide photocatalysis," *Journal of Photochemistry and Photobiology C*, vol. 1, no. 1, pp. 1–21, 2000.

[8] S. Anandan, Y. Ikuma, and V. Murugesan, "Highly active rare-earth-metal la-doped photocatalysts: fabrication, characterization, and their photocatalytic activity," *International Journal of Photoenergy*, vol. 2012, Article ID 921412, 10 pages, 2012.

[9] C. . Tian, Q. Zhang, A. Wu et al., "Cost-effective large-scale synthesis of ZnO photocatalyst with excellent performance for dye photodegradation," *Chemical Communications*, vol. 48, pp. 2858–2860, 2012.

[10] M. N. Ghazzala, H. Kebaili, M. Joseph et al., "Photocatalytic degradation of Rhodamine 6G on mesoporous titania films: combined effect of texture and dye aggregation forms," *Applied Catalysis B*, vol. 115-116, pp. 276–284, 2012.

[11] C. Guo, J. Xu, Y. He, Y. Zhang, and Y. Wang, "Photodegradation of rhodamine B and methyl orange over one-dimensional TiO$_2$ catalysts under simulated solar irradiation," *Applied Surface Science*, vol. 257, no. 8, pp. 3798–3803, 2011.

[12] X. Yang, L. Xu, X. Yu, and Y. Guo, "One-step preparation of silver and indium oxide co-doped TiO$_2$ photocatalyst for the degradation of rhodamine B," *Catalysis Communications*, vol. 9, no. 6, pp. 1224–1229, 2008.

[13] D. Arsene, C. P. Musteret, C. Catrinescu, P. Apopei, G. Barjoveanu, and C. Teodosiu, "Combined oxidation and ultrafiltration processes for the removal of priority organic pollutants from wastewaters," *Environmental Engineering and Management Journal*, vol. 10, no. 12, pp. 1967–1976, 2011.

[14] T. S. Natarajan, M. Thomas, K. Natarajan, H. C. Bajaj, and R. J. Tayade, "Study on UV-LED/TiO$_2$ process for degradation of Rhodamine B dye," *Chemical Engineering Journal*, vol. 169, no. 1–3, pp. 126–134, 2011.

[15] J. Zhang, S. Yan, L. Fu et al., "Photocatalytic degradation of rhodamine B on anatase, rutile, and brookite TiO$_2$," *Chinese Journal of Catalysis*, vol. 32, no. 6, pp. 983–991, 2011.

[16] J. Y. Li, W. H. Ma, P. X. Lei, and J. C. Zhao, "Detection of intermediates in the TiO$_2$-assisted photodegradation of Rhodamine B under visible light irradiation," *Journal of Environmental Sciences*, vol. 19, no. 7, pp. 892–896, 2007.

[17] S. M. . Soosen, B. Lekshmi, and K. C. George, "Optical properties of ZnO nanoparticles," *SB Academic Review*, vol. 16, no. 2, pp. 57–65, 2009.

[18] U. Costantino, F. Marmottini, M. Nocchetti, and R. Vivani, "New synthetic routes to hydrotalcite-like compounds—characterisation and properties of the obtained materials," *European Journal of Inorganic Chemistry*, no. 10, pp. 1439–1446, 1998.

[19] K. Okamoto, N. Iyi, and T. Sasaki, "The urea method for the direct synthesis of ZnAl layered double hydroxides with nitrate as the interlayer anion," *Applied Clay Science*, vol. 37, pp. 23–31, 2007.

[20] B. S. Barros, R. Barbosa, N. R. Dos Santos, T. S. Barros, and M. A. Souza, "Synthesis and x-ray diffraction characterization of nanocrystalline ZnO obtained by Pechini method," *Inorganic Materials*, vol. 42, no. 12, pp. 1348–1351, 2006.

[21] http://webbook.nist.gov/cgi/cbook.cgi?Spec=B6004648&Index=0&Type=IR&Large=on.

[22] H. Noei, H. Qiu, Y. Wang, E. Löffler, C. Wöll, and M. Muhler, "The identification of hydroxyl groups on ZnO nanoparticles by infrared spectroscopy," *Physical Chemistry Chemical Physics*, vol. 10, no. 47, pp. 7092–7097, 2008.

[23] G. Pragati, *Carbon dioxide adsorption on nanomaterials [Ph.D. dissertation]*, University of Iowa, 2010, http://ir.uiowa.edu/etd/670.

[24] Y. Fan, G. Chen, D. Li et al., "Highly selective deethylation of rhodamine B on TiO$_2$ prepared in supercritical fluids," *International Journal of Photoenergy*, vol. 2012, Article ID 173865, 7 pages, 2012.

[25] T. S. Natarajan, M. Thomas, K. Natarajan, H. C. Bajaj, and R. J. Tayade, "Study on UV-LED/TiO$_2$ process for degradation of

Rhodamine B dye," *Chemical Engineering Journal*, vol. 169, no. 1–3, pp. 126–134, 2011.

[26] X. Chen, Z. Xue, Y. Yao, W. Wang, F. Zhu, and C. Hong, "Oxidation degradation of rhodamine B in aqueous by UV/S2O8^{2-} treatment system," *International Journal of Photoenergy*, vol. 2012, Article ID 754691, 5 pages, 2012.

[27] F. Chen, J. Zhao, and H. Hidaka, "Highly selective deethylation of Rhodamine B: adsorption and photooxidation pathways of the dye on the TiO_2/SiO_2 composite photocatalyst," *International Journal of Photoenergy*, vol. 5, no. 4, pp. 209–217, 2003.

Research Article

Photocatalytic Degradation of Organic Dyes under Visible Light on N-Doped TiO$_2$ Photocatalysts

Olga Sacco,[1] Marco Stoller,[2] Vincenzo Vaiano,[1] Paolo Ciambelli,[1] Angelo Chianese,[2] and Diana Sannino[1]

[1] *Department of Industrial Engineering, University of Salerno, Via Ponte Don Melillo, Salerno, 84084 Fisciano, Italy*
[2] *Department of Chemical Engineering, University of Rome "La Sapienza", Via Eudossiana 18, 00184 Rome, Italy*

Correspondence should be addressed to Diana Sannino, dsannino@unisa.it

This study was focused on the application of white and blue light emitting diodes (LEDs) as sources for the photocatalytic degradation of organic dyes in liquid phase with visible light. The photocatalytic activity of N-doped titanium dioxide, synthesized by direct hydrolysis of titanium tetraisopropoxide with ammonia, was evaluated by means of a batch photoreactor. The bandgap energy of titanium dioxide was moved in the visible range from 3.3 eV to 2.5 eV. The visible light responsive photocatalysts showed remarkably effective activity in decolorization process and in the removal of total organic carbon. Methylene blue was also used as a model dye to study the influence of several parameters such as catalyst weight and initial concentration. The effect of dye on the photocatalytic performance was verified with methyl orange (MO). The results demonstrated that the right selection of operating conditions allows to effectively degrade different dyes with the N-doped TiO$_2$ photocatalysts irradiated with visible light emitted by LEDs.

1. Introduction

In recent years, an enormous interest has been devoted to heterogeneous photocatalysis using oxide semiconductors owing to its potential applications to both environmental applications and organic synthesis [1–17]. Titanium dioxide, TiO$_2$, is characterized by chemical stability, no toxicity and cheap production cost, so that it represents one of the most important oxides employed in several fields of photochemistry, for example, in environmental remediation, photoelectrolysis of water and dye-sensitized solar cells [18–22]. Since TiO$_2$ absorbs only a small fraction of the solar spectrum emission, due to the value of its bandgap energy (3.0–3.3 eV), the metal-doped TiO$_2$ has attracted considerable attention due to its reported activity in the visible light. Various metals such as Fe, Cr, Co, Mo, and V have been employed to tune the electronic structure and enhance the photocatalytic activity of titanium dioxide [23–25]. However, metal doping can result in thermal instability and increase of carriers trapping, which may decrease the photocatalytic efficiency. Furthermore, the typical preparation of transition metal-doped TiO$_2$ requires more expensive ion-implantation facilities [26, 27].

Recently, many efforts have been made to modify titanium dioxide with nonmetals, such as B, C, N, S, and F, to efficiently extend the photoresponse from the UV to the visible light region [28–40]. Furthermore, some theoretical calculations have also been performed to suggest that anion doping of TiO$_2$ has considerable effects on the band gap alteration. Since the first report by Kobayakawa et al. [41], considerable research has been done with respect to the preparation, characterization, photocatalytic activity, and mechanism of nitrogen-doped TiO$_2$ in visible light. The N-doped TiO$_2$ seems to be the most promising among the so-called second generation photocatalysts. N-doping can be obtained by various methods such as sputtering [42], treating of TiO$_2$ powders in ammonia atmosphere [43], or hydrolysis with urea in the presence of organic or inorganic titanium-based compounds [44]. N-doped titanium dioxide nanoparticles (N-TiO$_2$) demonstrated the

ability to degradate using tungsten bulb lamp [45] also industrial wastewaters as tannery wastewater, which instead requires a complex combination of conventional treatments to be satisfactory depolluted, as reported in [46].

Until now, there are very few reports on the use of LEDs emitting in visible region for the degradation of methylene blue, typically performed at very low dye concentration (≤ 1 ppm) [47].

For the above reasons the objective of this study was to explore the possibility of using this type of LEDs as source of visible light for the photocatalytic degradation of dyes with higher concentration in the presence of N-doped TiO_2 photocatalyst. The catalyst was obtained by direct nitration with NH_3 during the hydrolysis of titanium tetraisopropoxide. The influence of several parameters, such as catalyst weight, methylene blue concentration, and dye type were investigated.

2. Experimental

2.1. Photocatalysts Preparation and Characterization. N-doped TiO_2 photocatalysts were prepared by sol-gel method, according to the modified synthetic procedure developed by Sato [47]. Different amounts (25 mL, 50 mL, 75 mL, and 100 mL) of ammonia aqueous solution at 30 wt%, supplied by Carlo Erba, were added quickly to 25 mL of 97 wt% titanium tetraisopropoxide (TTIP by Sigma Aldrich) at $0°C$, while the solution was vigorously stirred, leading to the formation of a white precipitate. The precipitate was carefully washed with water and centrifuged to be separated. Finally, the obtained powder was dried and calcined at $450°C$ for 30 minutes to get TiO_2 in the anatase phase. X-ray diffraction (XRD) measurements of the obtained yellow samples were carried out with an X-ray microdiffractometer Rigaku D-max-RAPID, with Cu-Kα radiation. Laser Raman spectra were obtained at room temperature with a Dispersive Micro-Raman (Invia, Renishaw), equipped with 785 nm diode-laser, in the range 100–2500 cm^{-1} Raman shift. Aggregates sizes of photocatalyst particles in aqueous suspension were measured by a DLS instrument (Brookhaven Plus 91). UV-Vis DRS measurements were obtained by means of a Perkin Elmer spectrometer Lambda 35 using a RSA-PE-20 reflectance spectroscopy accessory (Labsphere Inc., North Sutton, NH). All spectra were obtained using an $8°$ sample positioning holder, giving total reflectance relative to a calibrated standard SRS-010-99 (Labsphere Inc., North Sutton, NH). The reflectance data were reported as the $F(R_\infty)$ value from Kubelka-Munk theory versus the wavelength. Band gap determinations were made by plotting $[F(R_\infty) * h\nu]^2$ versus $h\nu$ (eV) and calculating the x intercept of a line passing through $0.5 < F(R_\infty) < 0.8$.

2.2. Photocatalytic Activity Tests under Visible Light. In a typical activity test a defined amount of photocatalyst was suspended in 100 mL of MB solution. The suspension was left in dark condition for 2 hours to reach the adsorption equilibrium, and then photocatalytic reaction was initiated under visible light up to 3 h. The experiments were
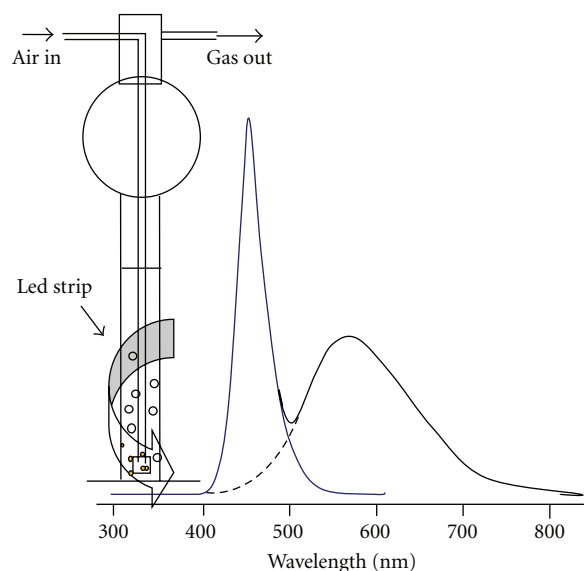
FIGURE 1: Emission spectrum of the light sources and schematic picture of the photoreactor.

performed with a pyrex cylindrical photoreactor (ID = 2.5 cm) equipped with an air distributor device (Q_{air} = 150 cm^3/min (STP)), a magnetic stirrer to maintain the photocatalyst suspended in the aqueous solution, and a temperature controller. The photoreactor was irradiated by a strip composed by 30 white light LEDs (nominal power: 6 W) with wavelength emission in the range 400–800 nm or by a similar number of blue light LEDs (nominal power: 6 W) with wavelength emission in the range 400–550 nm. The LEDs strip was positioned around the reactor so that the light source uniformly illuminated the reaction volume. The curve inside Figure 1 represents the emission spectrum of white LEDs, while the fraction of curve coloured in blue evidence the spectrum emission of blue LEDs. On the left side of the same figure a schematic picture of the photocatalytic reactor is presented. Slurry samples were collected at fixed time intervals, and centrifuged for 20 minutes at 4000 rpm for removing photocatalyst particles. The centrifuged samples were analysed to determine the change of dyes concentration, measured with a Perkin Elmer UV-Vis spectrophotometer at $\lambda = 663$ nm. A standard calibration curve was obtained for different MB concentration and allowed to convert absorbance to concentration (mg/L) units. Total organic carbon (TOC) of solution was evaluated from CO_2 obtained by catalytic combustion at $T = 680°C$. CO_2 produced in gas-phase was monitored by continuous analyzers, measuring CO, CO_2 (Uras 14, ABB), and O_2 (Magnos 106, ABB) gaseous concentrations.

3. Results and Discussion

The list of catalysts and their bandgap energy is reported in Table 1.

The reflectance measurements of N-doped TiO_2 showed that the absorption onset shifted from 380 to 480 nm

TABLE 1: List of catalysts and their bandgap.

Catalysts	TTIP volume (mL)	NH$_3$ solution volume (mL)	N/Ti molar ratio	Crystallites size[2] (nm)	SSA[3] (m^2/g)	Aggregates size[4] (nm)	Bandgap energy[5] (eV)
TiO$_2$[1]	25	0	—	7	171	267	3.3
N_1	25	25	4.6	16	75	163	2.6
N_2	25	50	9.3	15	80	364	2.6
N_3	25	75	13.9	16	75	167	2.5
N_4	25	100	18.6	15	80	367	2.5

[1]TiO$_2$ by sol-gel method.
[2]From XRD analysis.
[3]From the equation SSA = $6000 * (\rho * d)^{-1}$, where SSA is the calculated specific surface area, d is crystallites size (nm) and ρ is TiO$_2$ density (g/cm^3), based on the assumption of spherical and nonporous particles [48].
[4]From DLS instrument.
[5]From UV-Vis spectra.
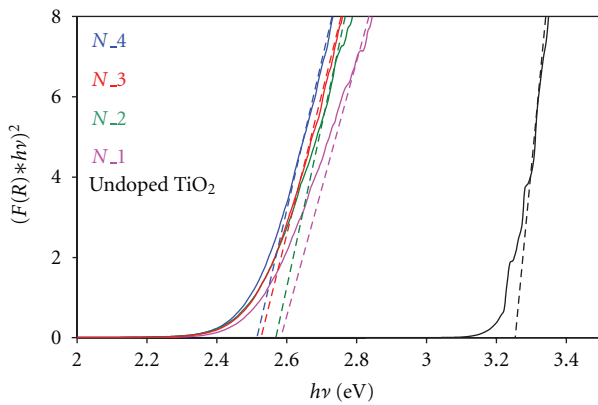
FIGURE 2: Bandgap estimation from UV-Vis DRS.

FIGURE 3: Raman spectra of undoped TiO$_2$, N_1; N_.2; N_3; N_4.

determining a decrease of bandgap values from 3.3 eV (the typical bandgap of undoped TiO$_2$) to 2.5 eV (Figure 2), which is an unexpected value for the only anatase phase. This change in bandgap is therefore attributed to the presence of nitrogen in the crystal structure phase. This result confirms the ability of photocatalysts to absorb visible light.

XRD analysis (not reported) revealed that for undoped TiO$_2$ and for N-TiO$_2$ samples the only crystalline phase is anatase and it did not change after the doping process. The average size of TiO$_2$ crystallites was calculated using the Scherrer equation [49] on diffraction plane (101) and the obtained values are reported in Table 1. The crystallite average size was 16 nm for N_1 and N_3 samples, while for N_2 and N_4 it was 15 nm. In contrast, DLS overestimated the size of TiO$_2$ particles due to agglomeration in the suspension. For N-TiO$_2$ samples, the degree of aggregation increased with decrease in crystallites size due to the high surface energy of smaller particles.

The results obtained from XRD are confirmed by Raman spectra (Figure 3), since the band positions are in complete accordance with those reported in previous studies for anatase powder [50–61]. In fact the Raman modes at 141, 194, 394, 515, and 636 cm^{-1} are assigned to the anatase phase.

The behaviour of MB decolourisation under visible light generated by white LEDs is represented in (Figure 4) for undoped TiO$_2$ and doped TiO$_2$ with different nitrogen content.

In dark conditions a decrease of MB concentration was observed during the first hour of the test and it was unchanged in the second hour, indicating that the adsorption equilibrium of dye on catalyst surface was reached. The curves show that N-TiO$_2$ catalysts have different amounts of MB adsorbed in dark. To explain this last result, the specific area was estimated (Table 1); for the sample N_1 and N_3 it was 75 m^2/g, while for N_2 and N_4 it was 80 m^2/g. As expected, the amount of organic dye adsorbed increases the higher is the specific surface area, fairly accordingly to the differences in the area values, as shown in Figure 4.
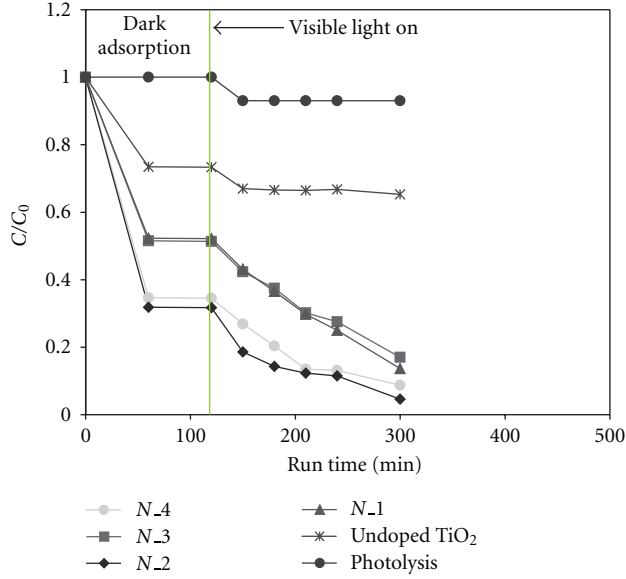
FIGURE 4: Decolorization of MB under visible light generated by white LEDs; catalyst weight: 0.3 g; initial MB concentration: 7.5 ppm.

After the dark period, the solution was irradiated with visible light and the reaction started to occur. Figure 4 shows that undoped TiO_2 is slightly effective for MB decolourization, the C/C_0 reduction being about 8%, a value similar to that of photolysis reaction (7%). On the contrary, all the N-doped TiO_2 photocatalysts exhibited higher photocatalytic activity under visible light irradiation. The order of decolorization activity of N-doped TiO_2 after 180 min was as following: N_2 > N_4 > N_3 ∼ N_1. The final value of MB conversion depends on dye concentration after the dark period.

The decolourization of MB does not necessary correspond to the oxidation and mineralization of the molecule; in fact the reduced form of MB (LMB, leuco) which is colourless can be produced in the presence of light [49]. The lack of coincidence among the best performing samples with respect to either decolorization or mineralization can be the result of different routes followed by MB during irradiation. Consider the following:

$$h^+ + OH^- \longrightarrow OH^\bullet \qquad (1)$$

$$MB + OH^\bullet \longrightarrow INTERMEDIATES \longrightarrow CO_2 \qquad (2)$$

$$MB + e^- \longrightarrow MB^{\bullet -} \qquad (3)$$

$$2MB^{\bullet -} \longrightarrow MB + LMB \qquad (4)$$

$$LMB + OH^\bullet \longrightarrow INTERMEDIATES \longrightarrow CO_2 \qquad (5)$$
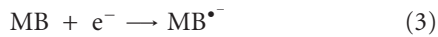
The MB molecule can be transformed into LMB through reduction by electrons in the conduction band (4) or oxidized by interactions with the valence band holes or native OH species, starting with a de-methylation step to be finally

mineralized (2). For long reaction times also LMB can be further degradated and mineralized.

The analysis of gases coming from the photoreactor showed the presence of CO_2 and SO_2 during the visible light irradiation, confirming the occurrence of MB mineralization (Figure 5). In fact, a significant TOC reduction was obtained. Its final value increased up to 97% by increasing the doping level (Figure 6). In this case, the order of activity was: N_4 > N_3 > N_2 ≫ N_1.

The photocatalyzed decolorization process can be described by a first-order kinetic equation (6) with respect to the concentration of MB [62, 63]. Consider

$$-\ln \frac{C}{C_0^*} = k_i \cdot t, \qquad (6)$$

where:

C = concentration of MB at any given time;
C_0^* = concentration of MB after dark adsorption:
t = irradiation time;
k_i = apparent kinetic constant.
The obtained results are plotted in Figure 7.

The order of kinetic constants of N-doped TiO_2 after 150 min of light irradiation is $k_2 > k_4 > k_3 \sim k_1$.

Many reports suggest that the amount of catalyst plays a major role in the degradation of organic compounds or dyes in photocatalytic systems. To avoid the use of a catalyst excess, it is necessary to identify the optimum loading for an efficient removal of dye or organic compound. So it is necessary to optimize the amount of catalyst with respect to the highest photocatalytic activity.

To study the effect of the amount of catalysts, different quantities of powder between 0.05 and 1.5 g were used. The initial concentration of MB dye (7.5 ppm) was kept the same in all these experiments. Figure 8 shows the effect of the amount of catalyst on the conversion of MB in the presence of white LEDs. The progress of the conversion is linear up to 0.3 g, while for further increase of catalyst amount, the conversion stabilizes. These data indicate that 0.3 g of powders are completely exposed to the radiation. This phenomenon may be explained considering that with an increase of catalyst loading in the aqueous medium, the light penetration through the solution becomes difficult. Therefore 0.3 g of photocatalyst loading is considered to be an optimal value.

Also the dye concentration plays a key role in the photocatalytic degradation. The effect of MB initial concentration on the photocatalytic activity was checked in the range between 4 and 95 ppm with N_4 catalyst and optimal catalyst loading (0.3 g in 100 mL of solution). The trend of the curves was similar and it is shown in Figure 9. After 120 minutes of dark adsorption, the photocatalytic test started. At fixed reaction times, the increase of MB initial concentration determined a decrease of the photocatalytic activity. This could be due to the increase of colour intensity of the solution that reduces the light penetration into the aqueous medium, meaning that the path length of photons inside the solution decreases. After 180 minutes of irradiation the final value of the decolorization was 100% in the case of 4 ppm and 15% in the case of 95 ppm MB initial concentration.
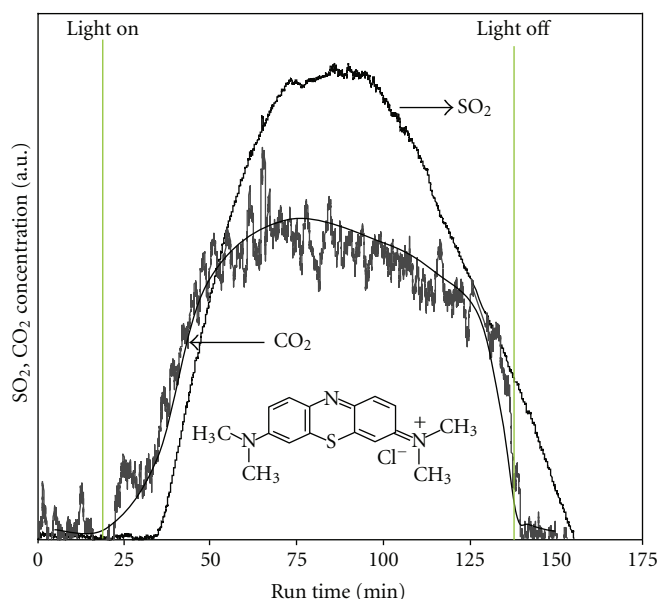
FIGURE 5: Gas analysis phase during visible irradiation of MB solution.
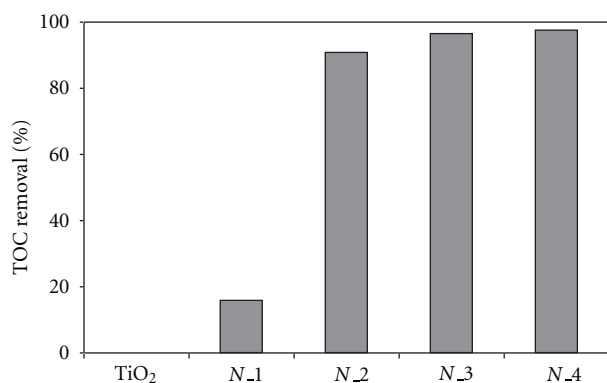
FIGURE 6: TOC removal after 180 min of irradiation time; catalyst weight: 0.3 g; initial MB concentration: 7.5 ppm.
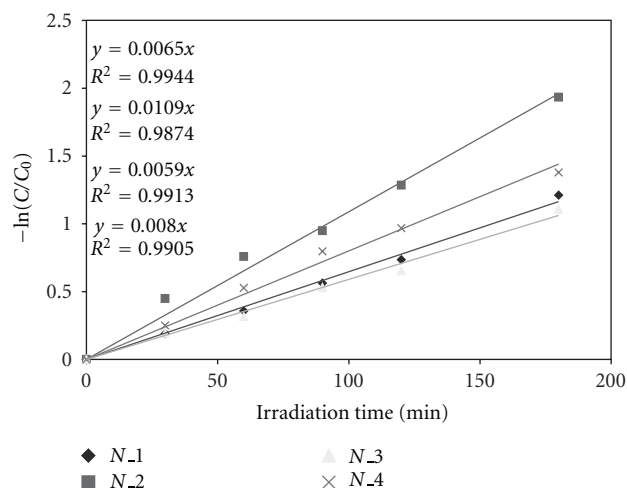
FIGURE 7: Evaluation of decolorization kinetic.

The same effect was observed by Matthews during the photocatalytic degradation of MB with TiO_2 catalysts [48].

Moreover, the efficiency of the system was also evaluated with blue LEDs as source of visible light and methyl orange (MO) as organic dye. Figure 10 shows the comparison between the obtained results in presence of white and blue LEDs. As expected from the evaluation of N_4 bandgap energy (2.5 eV), only a fraction of radiation is used in the decolorization process. In fact, the curves related to the MB concentration during the irradiation time showed a similar trend because the range of radiation used by the photocatalyst was that one having an emission wavelength lower than 440 nm. Similar results were obtained for methyl orange (MO).

The photocatalytic stability of N-doped TiO_2 was evaluated with recycling experiments (Figure 11). In the first cycle, the amount of MB adsorbed was lower than that one obtained with fresh catalyst because, using the same catalyst coming from the first test, a certain quantity of dye is already adsorbed. The rate of dye removal depends on the initial concentration in solution, so it is higher, the higher is residual MB after dark adsorption. However, it must be noted that the photocatalytic activity remained high and the level of final MB removal was the same at the end of the test, indicating that no deactivation occurred and the dye concentration decreased continuously under visible light irradiation.

4. Conclusions

In this study, the evaluation of the photodegradation of methylene blue (MB), as dye model system, in presence of
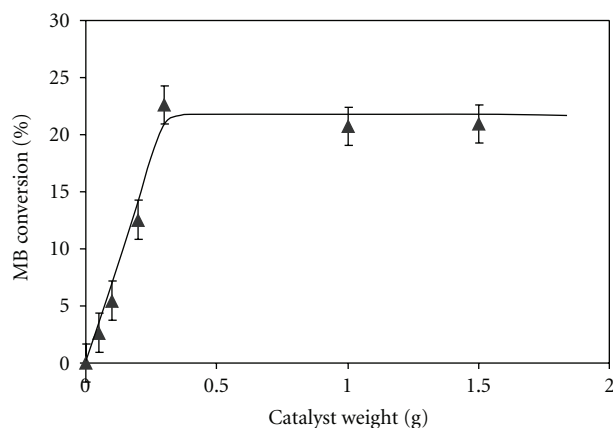
FIGURE 8: Evaluation of decolorization after 30 minute with different amount of N_4 catalyst.

FIGURE 10: Evaluation of decolorization with different dyes and different light source; initial MB and MO concentration: 9 ppm.

FIGURE 9: Evaluation of decolorization with different initial concentration of MB; catalyst: N_4.
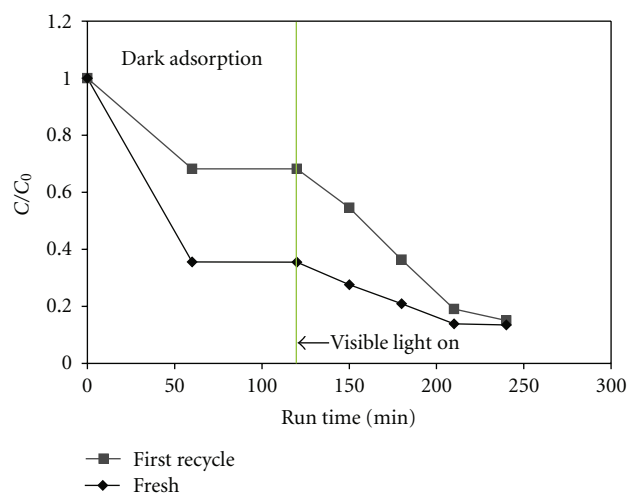
FIGURE 11: Evaluation of decolorization performances obtained on N_4 photocatalyst after one recycling experiment; initial MB concentration: 7.5 ppm.

white and blue light emitting diodes (LEDs) as source of visible light, was evaluated. The photoreactivity was assessed over N-doped TiO_2 photocatalysts in batch experiments, evaluating the abatement of methylene blue, and in addition of methyl orange. The best catalyst was N_4 that showed remarkable efficiencies in decolorization process and in the removal of total organic carbon. The influence of several parameters such as catalyst weight, dye concentration and type, light source was assessed.

References

[1] P. Ciambelli, D. Sannino, V. Palma, V. Vaiano, and R. S. Mazzei, "Intensification of gas-phase photoxidative dehydrogenation of ethanol to acetaldehyde by using phosphors as light carriers," *Photochemical and Photobiological Sciences*, vol. 10, no. 3, pp. 414–418, 2009.

[2] P. Ciambelli, D. Sannino, V. Palma, V. Vaiano, and R. S. Mazzei, "A step forwards in ethanol selective photo-oxidation," *Photochemical and Photobiological Sciences*, vol. 8, no. 5, pp. 699–704, 2009.

[3] P. Ciambelli, D. Sannino, V. Palma, and V. Vaiano, "Photocatalysed selective oxidation of cyclohexane to benzene on MoO_x/TiO_2," *Catalysis Today*, vol. 99, no. 1-2, pp. 143–149, 2005.

[4] P. Ciambelli, D. Sannino, V. Palma, and V. Vaiano, "Cyclohexane photocatalytic oxidative dehydrogenation to benzene on sulphated titania supported MoO_x," *Studies in Surface Science and Catalysis*, vol. 155, pp. 179–187, 2005.

[5] P. Ciambelli, D. Sannino, V. Palma, V. Vaiano, and R. I. Bickley, "Reaction mechanism of cyclohexane selective photo-oxidation to benzene on molybdena/titania catalysts," *Applied Catalysis*, vol. 349, no. 1-2, pp. 140–147, 2008.

[6] P. Ciambelli, V. Palma, D. Sannino, S. Vaccaro, and V. Vaiano, "Selective oxidation of cyclohexane to benzene on

molybdena-titania catalysts in fluidized bed photocatalytic reactor," *Studies in Surface Science and Catalysis*, vol. 172, p. 453, 2007.

[7] P. Ciambelli, D. Sannino, V. Palma et al., "Tuning the selectivity of MoO_x supported catalysts for cyclohexane photo oxidehydrogenation," *Catalysis Today*, vol. 128, no. 3-4, pp. 251–257, 2007.

[8] P. Ciambelli, D. Sannino, V. Palma et al., "Photocatalytic cyclohexane oxidehydrogenation on sulphated MoO_x/γ-Al_2O_3 catalysts," *Catalysis Today*, vol. 141, no. 3-4, pp. 367–373, 2009.

[9] J. J. Murcia, M. C. Hidalgo, J. A. Navío, V. Vaiano, P. Ciambelli, and D. Sannino, "Photocatalytic ethanol oxidative dehydrogenation over Pt/TiO_2: effect of the addition of blue phosphors," *International Journal of Photoenergy*, vol. 2012, Article ID 687262, 9 pages, 2012.

[10] D. Sannino, V. Vaiano, P. Ciambelli, and L. A. Isupova, "Structured catalysts for photo-fenton oxidation of acetic acid," *Catalysis Today*, vol. 161, pp. 255–259, 2011.

[11] D. Sannino, V. Vaiano, L. A. Isupova, and P. Ciambelli, "Heterogeneous photo-fenton oxidation of organic pollutants on structured catalysts," *Journal of Advanced Oxidation Technologies*, vol. 15, no. 2, pp. 294–300, 2012.

[12] D. Sannino, V. Vaiano, L. A. Isupova, and P. Ciambelli, "Photo-fenton oxidation of acetic acid on supported $LaFeO_3$ and $Pt/LaFeO_3$ perovskites," *Chemical Engineering Transactions*, vol. 25, pp. 1013–1018, 2011.

[13] D. Sannino, V. Vaiano, P. Ciambelli, M. C. Hidalgo, J. J. Murcia, and J. A. Navío, "Oxidative dehydrogenation of ethanol over Au/TiO_2 photocatalysts," *Journal of Advanced Oxidation Technologies*, vol. 15, no. 2, pp. 284–293, 2012.

[14] J. J. Murcia, M. C. Hidalgo, J. A. Navío, V. Vaiano, P. Ciambelli, and P. D. Sannino, "Ethanol partial photoxidation on Pt/TiO_2 catalysts as green route for acetaldehyde synthesis," *Catalysis Today*, In press.

[15] D. Sannino, V. Vaiano, and P. Ciambelli, "Innovative structured VO_x/TiO_2 photocatalysts supported on phosphors for the selective photocatalytic oxidation of ethanol to acetaldehyde," *Catalysis Today*, In press.

[16] D. Sannino, V. Vaiano, P. Ciambelli, P. Eloy, and E. M. Gaigneaux, "Avoiding the deactivation of sulphated MoO_x/TiO_2 catalysts in the photocatalytic cyclohexane oxidative dehydrogenation by a fluidized bed photoreactor," *Applied Catalysis A: General*, vol. 394, pp. 71–78, 2011.

[17] V. Palma, D. Sannino, V. Vaiano, and P. Ciambelli, "Fluidized-bed reactor for the intensification of gas-phase photocatalytic oxidative dehydrogenation of cyclohexane," *Industrial & Engineering Chemistry Research*, vol. 49, no. 21, pp. 10279–10286, 2010.

[18] M. Anpo, "Preparation, characterization, and reactivities of highly functional titanium oxide-based photocatalysts able to operate under UV-visible light irradiation: approaches in realizing high efficiency in the use of visible light," *Bulletin of the Chemical Society of Japan*, vol. 77, no. 8, pp. 1427–1442, 2004.

[19] G. Cappelletti, S. Ardizzone, C. L. Bianchi et al., "Photodegradation of pollutants in air: enhanced properties of nano-TiO_2 prepared by ultrasound," *Nanoscale Research Letters*, vol. 4, no. 2, pp. 97–105, 2009.

[20] M. Grätzel, "Photoelectrochemical cells," *Nature*, vol. 414, p. 338, 2001.

[21] X. Chen and S. S. Mao, "Titanium dioxide nanomaterials: synthesis, properties, modifications and applications," *Chemical Reviews*, vol. 107, no. 7, pp. 2891–2959, 2007.

[22] M. R. Hoffmann, S. T. Martin, W. Choi, and D. Bahnemann, "Environmental applications of semiconductor photocatalysis," *Chemical Reviews*, vol. 95, pp. 69–96, 1995.

[23] J. Peral, X. Domenech, and D. F. Ollis, "Heterogeneous photocatalysis for purification, decontamination and deodorization of air," *Journal of Chemical Technology and Biotechnology*, vol. 70, no. 2, pp. 117–140, 1997.

[24] J. Zhao and X. Yang, "Photocatalytic oxidation for indoor air purification: a literature review," *Building and Environment*, vol. 38, no. 5, pp. 645–654, 2003.

[25] X. Z. Fu, W. A. Zeltner, and M. A. Andreson, "The gas-phase photocatalytic mineralization of benzene on porous titania-based catalysts," *Applied Catalysis B*, vol. 6, no. 3, pp. 209–290, 1995.

[26] H. Choi, Y. J. Kim, R. S. Varma, and D. D. Dionysiou, "Thermally stable nanocrystalline TiO_2 photocatalysts synthesized via sol-gel methods modified with ionic liquid and surfactant molecules," *Chemistry of Materials*, vol. 18, no. 22, pp. 5377–5384, 2006.

[27] B. Li, X. Wang, M. Yan, and L. Li, "Preparation and characterization of nano-TiO_2 powder," *Materials Chemistry and Physics*, vol. 78, no. 1, pp. 184–188, 2003.

[28] A. Fujishima, T. N. Rao, and D. A. Tryk, "Titanium dioxide photocatalysis," *Journal of Photochemistry and Photobiology C*, vol. 1, no. 1, pp. 1–21, 2000.

[29] A. L. Linsebigler, G. Lu, and J. T. Yates, "Photocatalysis on TiO_2 surfaces: principles, mechanisms, and selected results," *Chemical Reviews*, vol. 95, no. 3, pp. 735–758, 1995.

[30] H. Tada, M. Yamamoto, and S. Ito, "Promoting effect of MgO_x submonolayer coverage of TiO_2 on the photoinduced oxidation of anionic surfactants," *Langmuir*, vol. 15, no. 11, pp. 3699–3702, 1999.

[31] G. Shang, H. Fu, S. Yang, and T. Xu, "Mechanistic study of visible-light-induced photodegradation of 4-chlorophenol by $TiO_{2-x}N_x$ with low nitrogen concentration," *International Journal of Photoenergy*, vol. 2012, Article ID 759306, 9 pages, 2012.

[32] S. Li, S. Lin, J. Liao, N. Pan, D. Li, and J. Li, "Nitrogen-doped TiO_2 nanotube arrays with enhanced photoelectrochemical property," *International Journal of Photoenergy*, vol. 2012, Article ID 794207, 7 pages, 2012.

[33] Q. Xiang, J. Yu, W. Wang, and M. Jaroniec, "Nitrogen self-doped nanosized TiO_2 sheets with exposed 001 facets for enhanced visible-light photocatalytic activity," *Chemical Communications*, vol. 47, no. 24, pp. 6906–6908, 2011.

[34] K. Li, H. Wang, C. Pan, J. Wei, R. Xiong, and J. Shi, "Enhanced photoactivity of Fe + N codoped anatase-rutile TiO_2 vanowire film under visible light irradiation," *International Journal of Photoenergy*, vol. 2012, Article ID 398508, 8 pages, 2012.

[35] J. Hu, H. Tang, X. Lin et al., "Doped titanium dioxide films prepared by pulsed laser deposition method," *International Journal of Photoenergy*, vol. 2012, Article ID 758539, 8 pages, 2012.

[36] J. Qian, G. Cui, M. Jing, Y. Wang, M. Zhang, and J. Yang, "Hydrothermal synthesis of nitrogen-doped titanium dioxide and evaluation of its visible light photocatalytic activity," *International Journal of Photoenergy*, vol. 2012, Article ID 198497, 6 pages, 2012.

[37] C.-C. Hu, T.-C. Hsu, and L.-H. Kao, "One-step cohydrothermal synthesis of nitrogen-doped titanium oxide nanotubes with enhanced visible light photocatalytic activity," *International Journal of Photoenergy*, vol. 2012, Article ID 391958, 9 pages, 2012.

[38] A. V. Emeline, V. N. Kuznetsov, V. K. Rybchuk, and N. Serpone, "Visible-light-active titania Photocatalysts: the case of n-doped TiO$_2$ s-properties and some fundamental issues," *International Journal of Photoenergy*, vol. 2008, Article ID 258394, 19 pages, 2008.

[39] J. A. Wang, R. Limas-Ballesteros, T. López et al., "Quantitative determination of titanium lattice defects and solid-state reaction mechanism in iron-doped TiO$_2$ photocatalysts," *Journal of Physical Chemistry*, vol. 105, no. 40, pp. 9692–9698, 2001.

[40] J. C. Yu, J. G. Yu, and J. C. Zhao, "Enhanced photocatalytic activity of mesoporous and ordinary TiO$_2$ thin films by sulfuric acid treatment," *Applied Catalysis*, vol. 36, no. 1, pp. 31–43, 2002.

[41] K. Kobayakawa, Y. Murakami, and Y. Sato, "Visible-light active N-doped TiO$_2$ prepared by heating of titanium hydroxide and urea," *Journal of Photochemistry and Photobiology*, vol. 170, no. 2, pp. 177–179, 2005.

[42] R. J. Tayade, P. K. Suroliya, R. G. Kulkarni, and R. V. Jasra, "Photocatalytic degradation of dyes and organic contaminants in water using nanocrystalline anatase and rutile TiO$_2$," *Science and Technology of Advanced Materials*, vol. 8, no. 6, pp. 455–462, 2007.

[43] R. Asahi, T. Morikawa, T. Ohwaki, K. Aoki, and Y. Taga, "Visible-light photocatalysis in nitrogen-doped titanium oxides," *Science*, vol. 293, no. 5528, pp. 269–271, 2001.

[44] H. Irie, Y. Watanabe, and K. Hashimoto, "Nitrogen-concentration dependence on photocatalytic activity of TiO$_{2-x}$N$_x$ powders," *The Journal of Physical Chemistry*, vol. 107, no. 23, pp. 5483–5486, 2003.

[45] O. Sacco, M. Stoller, V. Vaiano, A. Chianese, and D. Sannino, "On the comparison of different light sources in the photocatalytic degradation of tannery wastewater stream," in *Proceedings of the 7th European Meeting on Solar Chemistry and Photocatalysis: Environmental Applications (SPEA '7)*, Oporto, Portugal, June 2012.

[46] S. De Gisi, M. Galasso, and G. De Feo, "Treatment of tannery wastewater through the combination of a conventional activated sludge process and reverse osmosis with a plane membrane," *Desalination*, vol. 249, no. 1, pp. 337–342, 2009.

[47] S. Sato, "Photo catalytic activity of NO$_x$ doped TiO$_2$ in the visible region," *Chemical Physics Letters*, vol. 123, no. 1-2, pp. 126–128, 1986.

[48] R. W. Matthews, "Photocatalytic oxidation and adsorption of methylene blue on thin films of near-ultraviolet-illuminated TiO$_2$," *Journal of the Chemical Society*, vol. 85, no. 6, pp. 697–707, 1989.

[49] P. Scherrer, "Bestimmung der Grösse und der inneren Struktur von Kolloidteilchen mittels Röntgenstrahlen," *Nachr. Ges. Wiss. Göttingen*, vol. 26, pp. 98–100, 1918.

[50] T. Ohsaka, F. Izumi, and Y. Fujiki,, "Raman spectrum of anatase, TiO$_2$," *Journal of Raman Spectroscopy*, vol. 7, no. 6, pp. 321–324, 1978.

[51] S. P. S. Porto, P. A. Fleury, and T. C. Damen, "Raman spectra of TiO$_2$, MgF$_2$, ZnF$_2$, FeF$_2$, and MnF$_2$," *Physical Review*, vol. 154, no. 2, pp. 522–526, 1967.

[52] Y. Djaoued, S. Badilescu, P. V. Ashrit, D. Bersani, P. P. Lottici, and R. Brüning, "Low temperature sol-gel preparation of nanocrystalline TiO$_2$ thin films," *Journal of Sol-Gel Science and Technology*, vol. 24, no. 3, pp. 247–254, 2002.

[53] J. C. Parker and R. W Siegel, "Raman microprobe study of nanophase TiO$_2$ and oxidation-induced spectral changes," *Journal of Materials Research*, vol. 5, no. 6, pp. 1246–1252, 1990.

[54] G. J. Exarhous and N. J. Hess, "Spectroscopic measurements of stress relaxation during thermally induced crystallization of amorphous titania films," *Thin Solid Films*, vol. 220, no. 1-2, pp. 254–260, 1992.

[55] D. Bersani, P. P. Lottici, and X. Z. Ding, "Phonon confinement effects in the Raman scattering by TiO$_2$ nanocrystals," *Applied Physics Letters*, vol. 72, no. 1, pp. 73–75, 1998.

[56] M. Ivanda, S. Music, M. Gotic, A. Turkovic, A.M. Tonejc, and O. Gamulin, "The effects of crystal size on the Raman spectra of nanophase TiO$_2$," *Journal of Molecular Structure*, vol. 480-481, pp. 641–644, 1999.

[57] T. Mazza, E. Barborini, P. Piseri et al., "Raman spectroscopy characterization of TiO$_2$ rutile nanocrystals," *Physical Review*, vol. 75, no. 4, Article ID 045416, 2007.

[58] S. Balaji, Y. Djaoued, and J. Robichaud, "Phonon confinement studies in nanocrystalline anatase-TiO$_2$ thin films by micro Raman spectroscopy," *Journal of Raman Spectroscopy*, vol. 37, no. 12, pp. 1416–1422, 2006.

[59] K.R. Zhu, M.S. Zhang, Q. Chen, and Z. Yin, "Size and phonon-confinement effects on low-frequency Raman mode of anatase TiO$_2$ nanocrystal," *Physics Letters*, vol. 340, no. 1–4, pp. 220–227, 2005.

[60] I. A. Alhomoudi and G. Newaz, "Residual stresses and Raman shift relation in anatase TiO$_2$ thin film," *Thin Solid Films*, vol. 517, no. 15, pp. 4372–4378, 2009.

[61] C. R. Aita, "Raman scattering by thin film nanomosaic rutile TiO$_2$," *Applied Physics Letters*, vol. 90, no. 21, pp. 213112–213113, 2007.

[62] C. Yogi, K. Kojima, T. Takai, and N. Wada, "Photocatalytic degradation of methylene blue by Au-deposited TiO$_2$ film under UV irradiation," *Journal of Materials Science*, vol. 44, no. 3, pp. 821–827, 2009.

[63] M. A. Rauf, M. A. Meetani, A. Khaleel, and A. Ahmed, "Photocatalytic degradation of Methylene Blue using a mixed catalyst and product analysis by LC/MS," *Chemical Engineering Journal*, vol. 157, no. 2-3, pp. 373–378, 2010.

Research Article

Supported Nanosized *α*-FeOOH Improves Efficiency of Photoelectro-Fenton Process with Reaction-Controlled pH Adjustment for Sustainable Water Treatment

Chuan Wang,[1] Hong Liu,[1, 2] Zhimin Sun,[3] Jian Huang,[2] and Yang Liao[2]

[1] *Chongqing Institute of Green and Intelligent Technology, Chinese Academy of Sciences, Chongqing 401122, China*
[2] *School of Chemistry and Chemical Engineering, Sun Yat-sen University, Guangzhou 510275, China*
[3] *Guangzhou Municipal Engineering Design & Research Institute, Guangzhou 510060, China*

Correspondence should be addressed to Hong Liu, liuhong@cigit.ac.cn

The overall photoelectro-Fenton (PE-Fenton) process for water treatment with neutral initial pH includes three steps of pH reduction, PE-Fenton reaction, and pH elevation. Reaction-controlled pH adjustment (RCpA), which utilizes the intrinsic electrochemical reactions instead of chemical addition, has been employed to lower the pH, maintain the lowered pH for the Fenton reaction, and recover the pH for final effluent discharge. This study demonstrated that the overall efficiency of this sustainable PE-Fenton process was improved by rapidly recycling the iron substance. Nanosized iron oxide was prepared and employed to ensure such rapid recycling. SEM and XRD results showed that the as-prepared iron oxide was α-FeOOH with 20 nm in size. The experimental results of dimethyl phthalate (DMP) degradation showed that diatomite-supported α-FeOOH (N-α-FeOOH/diatomite) could efficiently reduce the DMP concentration and total organic carbon. Furthermore, compared with Fe^{3+}, the N-α-FeOOH/diatomite saved 160 min for iron settlement at 20 mg L^{-1} DMP concentration. Also, with the increment in the initial DMP concentration, extra energy consumed by the individual step of PE-Fenton reaction using the N-α-FeOOH/diatomite became negligible compared with that using free iron ions with the increment in the initial DMP concentration. This development is expected to be a major step of the PE-Fenton process with RCpA towards actual water treatment.

1. Introduction

The cathodic electro-Fenton reaction (E-Fenton) with electrogenerated H_2O_2 and added Fe^{2+} as an advanced oxidation process (AOP) has recently been developed on the basis of a well-established Fenton's reagent [1–4] for the degradation of recalcitrant organic pollutants in aqueous media. The cathodic and coupled anodic reactions of the E-Fenton reaction are expressed as follows [4–6]:

$$O_2 + 2H^+ + 2e \longrightarrow H_2O_2 \quad \text{(cathodic reaction)} \quad (1)$$

$$H_2O \longrightarrow \frac{1}{2}O_2 + 2H^+ + 2e \quad \text{(anodic reaction)} \quad (2)$$
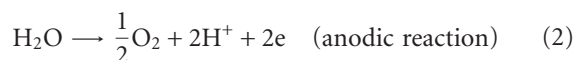
During this process, the electrogenerated H_2O_2 interacts with the added Fe^{2+} to form nonselective and highly active hydroxyl radicals that destroy the organic substrates. Many

reports have demonstrated that the E-Fenton process is a promising AOP for water purification [7–9].

Two hurdles must be surpassed for the development for a realistic application of the E-Fenton process. The first is the narrow pH required for the Fenton reaction [10–12]. The medium pH for the Fenton reaction must be maintained within the narrow range of 2.0–4.0 to preclude the iron precipitate. This pH limitation obviously requires chemical addition of an acid and a base to obtain the desired pH, essentially hampering the realistic application of the PE-Fenton reaction. The second is the running off of iron ions. Solid iron oxides can substitute iron ions and photo energy is simultaneously inputted to mediate the E-Fenton process, also known as the photoelectron-Fenton (PE-Fenton) process [3, 8, 13–15]. Without input of electricity, this system is called photo-Fenton system [16–18]. Furthermore, nanosized iron oxides have been observed to exhibit higher

reactivity. However, they present a difficulty for separation from the aqueous phase after use given their small size and fine dispersion in the solution. Therefore, the problems with pH conditioning and iron recovery need to be solved to develop a more efficient PE-Fenton process.

For the pH-conditioning obstacle, a reaction-controlled pH adjustment (RCpA) mechanism has been found, which can be explored to preclude the chemical addition and thereby bring sustainability to the associated water treatment process [19]. Briefly, spatial separation of the cathode and anode chambers ensures the use of the OH^- generated in the cathode (1) and H^+ in the anode (2). The former increases the pH, whereas the latter decreases the pH. A combination of the two chambers ensures the maintenance of a low pH. The strategy can obtain varied pH for all-pH conditioning without any chemical addition. Naturally, such mechanism works in the PE-Fenton process. Therefore, any measure that serves to separate the nanosized iron oxide rapidly for recovery is desirable in the PE-Fenton process with RCpA for sustainable water treatment.

The present study attempts to prepare nanosized iron oxide and support it on diatomite in the PE-Fenton process with RCpA to boost the overall efficiency significantly by shortening the duration of iron settlement. Diatomite, abundant in many areas of the world, has unique physical characteristics, such as high permeability and porosity, small particle size, and high surface area [20]. It is commonly used in the fields of catalysis and environmental purification as an environment friendly support material. Dimethyl phthalate (DMP), which is representative of dialkyl phthalate esters (DPEs), belongs to the family of endocrine-disrupting chemicals [21–24]. It was used as a model organic substrate in the study to assess the efficiency of the PE-Fenton process rapidly. The efficiency of the iron settlement was also evaluated through the settling time.

2. Experimental Section

2.1. Chemicals and Reagents. Except for acetonitrile (Dima Technology, Inc., Richmond Hill, Ontario, CA, USA), which is a high-performance liquid chromatography (HPLC) grade reagent, all other chemicals employed, such as DMP, $FeSO_4 \cdot 7H_2O$, and H_2O_2, were of analytical grade and used as obtained from Xilong Chemical, Inc. (Shantou, Guangdong, China). In all experiments, double-distilled water was used. The water used to prepare the Fe^{2+} solution was bubbled with high-purity N_2 gas (99.99%) for 30 min before solution preparation. Sulfuric acid and sodium hydroxide were used at 0.1 M concentration to obtain the initial pH (pH_0) of the solution.

2.2. Preparation and Characterization of Nanosized Iron Oxide Supported on Diatomite. The iron-oxide-supported diatomite was prepared. $FeCl_3$ solution at 0.5 mM concentration was immersed with diatomite for 2 h and filtered to separate the Fe^{3+}/diatomite from the supernatant. The latter was discarded, and the former was washed with water repeatedly until the Cl^- was completely removed, as confirmed by

a precipitation test using $AgNO_3$ solution. Finally, the Fe^{3+}/diatomite was heated to 400°C for 5 h at a temperature-increasing rate at 10°C min^{-1}. The theoretical iron content in the diatomite was calculated to be 5%. For comparison, unsupported iron oxide powder was also prepared in the absence of diatomite. The as-prepared samples were then observed by scanning electron microscopy (SEM) using a Philips Quanta 400 FE environmental scanning electromicroscope (FEI, Holland) coupled with an INCA energy dispersive X-Ray spectrometer (EDS, Oxford, UK) to obtain the atomic composition of the products. X-ray diffraction (XRD) was employed to investigate the chemical composition of the samples at 45 kV and 30 mA using a D/MAX 2200 VPC (RIGAKU, Japan) equipped with a graphite monochromator (Cu Kα, = 1.54056 Å).

2.3. Experimental Procedure. The design of the quartz electrochemical reactor with a graphite cathode (15 cm^2) and a Pt anode (1.0 × 1.0 cm^2) is presented in Figure 1. The reactor consisted of three chambers: a common chamber (undivided chamber) with both anode and cathode and two divided chambers (anodic chamber and cathodic chamber) connected by a bipolar membrane [25, 26]. Each chamber had an effective volume of 120 mL and a height of 15 cm. In the reactor, H_2O_2 was generated by purging air onto the cathode at a flow rate of 100 mL min^{-1} controlled by a needle valve. DMP degradation via the PE-Fenton reaction was performed. Sodium sulfate solution (0.05 M concentration) was used as the electrolyte. An 8 W near-UV lamp with a primary wavelength of 365 nm was employed to illuminate the cathode in the common and cathodic chambers. A PS-1 potentiostat/galvanostat (Zhongfu Corrosion and Protection Co., Ltd., Beijing, China) was employed to apply a cathodic current to the electrode system.

In the three-step PE-Fenton process, three-step pH conditioning by RCpA was also performed. In the first step, the pH was lowered below 4.0 through the anodic reaction. Keeping the low pH constant was the second step, and the third step was bringing the pH to neutral. Organic degradation occurred in the second step and continued into the third step. In this study, we focused on comparing the DMP degradation using free iron ions and supported nanosized iron oxide in the second step.

The as-prepared iron oxide was used in the PE-Fenton process (see Figure 1). For comparison, ferric ions were also used as the iron substance in the PE-Fenton process, during which iron sludge was formed due to the increased pH. In the third step of the PE-Fenton process, the iron substances in the form of iron sludge or solid iron oxide were relocated from the cathodic chamber to the anodic chamber for reuse. The settling time for the iron oxide and the iron sludge formed from Fe^{3+} was recorded. DMP solution was put into the cathode chamber for PE-Fenton degradation. During the PE-Fenton reaction, 1.0 mL sample was withdrawn for analysis, and 10 μL of methanol was injected into the sample to quench any potential radical reaction before the measurement the DMP concentration, while no chemical was injected to measure the total organic carbon (TOC).
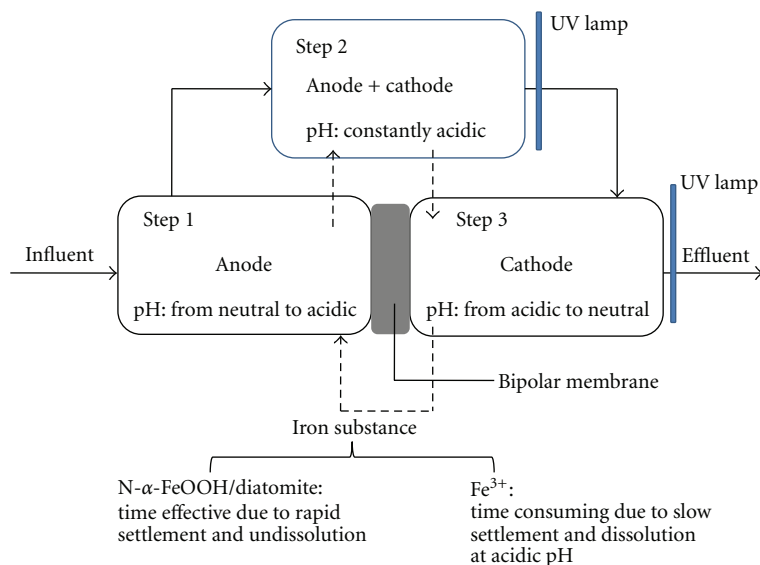
FIGURE 1: Schematic of the PE-Fenton process with reaction-controlled pH adjustment (RCpA).
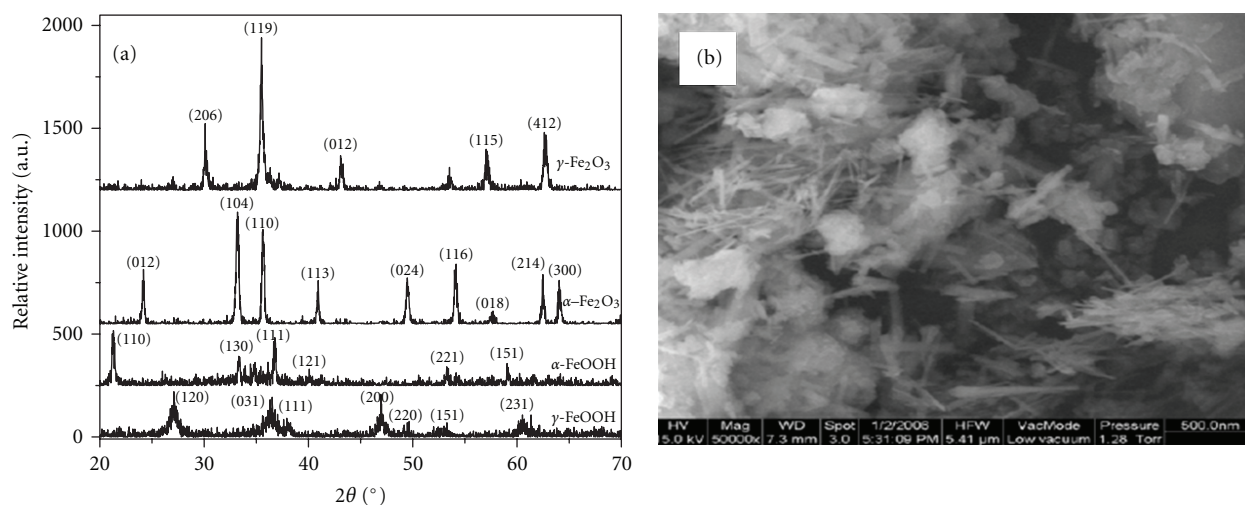
FIGURE 2: (a) XRD patterns of unsupported iron oxides and (b) SEM image of N-α-FeOOH.

2.4. Chemical Analysis.

2.4. Chemical Analysis. The DMP concentration was analyzed by HPLC (Techcomp, LC 2130, Shanghai, China) equipped with a reverse-phase column (Waters, XTerra MS C-18, 5 μm) and a UV detector. The mobile phase was composed of acetonitrile and water (50 : 50), and the measurement wavelength for the UV detector was set to 276 nm. The TOC concentration was measured using a TOC analyzer (Shimadzu 5000A) equipped with an autosampler. For the measurement of total iron, the Fe^{3+} in the solution was initially reduced to Fe^{2+} by hydroxylamine hydrochloride, then quantified via the light absorption intensity of the complex formed between the Fe^{2+} and 1,10-phenanthroline at 508 nm [27] using a UV-VIS spectrophotometer (TU1810, Universal Analysis, Beijing, China).

3. Results and Discussion

3.1. Characterization of the Iron Oxide Samples. Figure 2(a) shows the results of the XRD investigation of the as-prepared unsupported samples at different calcination temperatures. Iron oxide in the form of γ-FeOOH was obtained at the low calcination temperature of 65°C. By increasing the calcination temperature, the γ-FeOOH was transformed to α-FeOOH, then to α-Fe_2O_3, and finally to γ-Fe_2O_3.

3.2. Efficiency of the PE-Fenton Reaction in DMP Degradation Using Nanosized α-FeOOH. A set of DMP degradation experiments via the PE-Fenton reaction with RCpA was performed to evaluate the efficiency of the PE-Fenton reaction
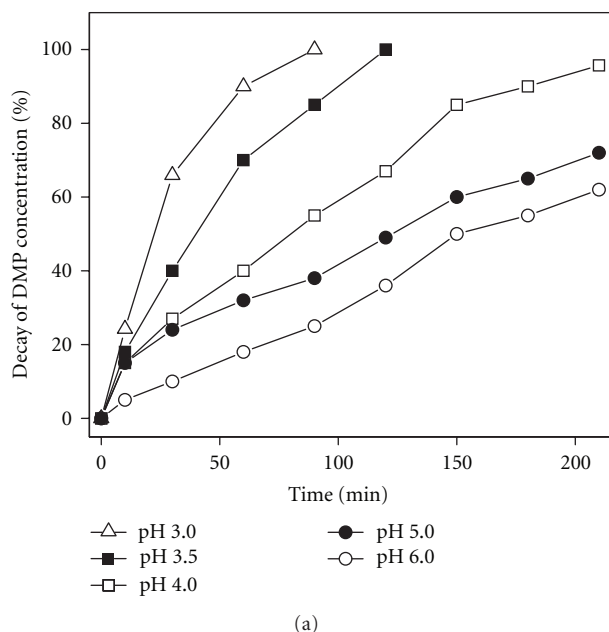
(a)
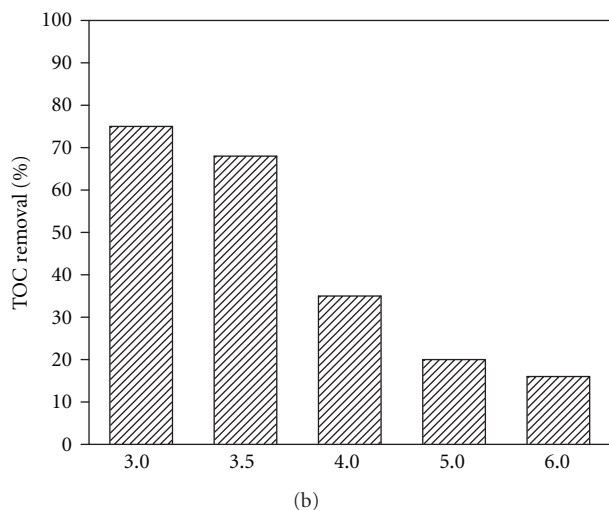
(b)

FIGURE 3: PE-Fenton degradation of DMP at $20 \, mg \, L^{-1}$ in the common chamber at different pH using N-α-FeOOH/diatomite. (a) Decay of DMP concentration (%) and (b) TOC removal after 210 min (%).

in the common chamber using the four types of iron oxides. N-α-FeOOH was the most active in DMP degradation (data not shown). The morphology of the N-α-FeOOH was then observed by SEM, and the results are shown in Figure 2(b). N-α-FeOOH was leaf-like with one dimension at nanoscale.

Another set of DMP degradation experiments via the PE-Fenton reaction with RCpA was subsequently performed to evaluate the efficiency of the PE-Fenton reaction in the common chamber using N-α-FeOOH at initial pH of 3.0, 3.5, 4.0, 5.0, and 6.0. In the common chamber, the OH^- in (1) and H^+ in (2) neutralized each other to maintain the solution pH. The results of the DMP degradation are shown in Figure 3(a). The decrease in DMP concentration in the Fenton reaction depended on the pH. Thus, a high pH was
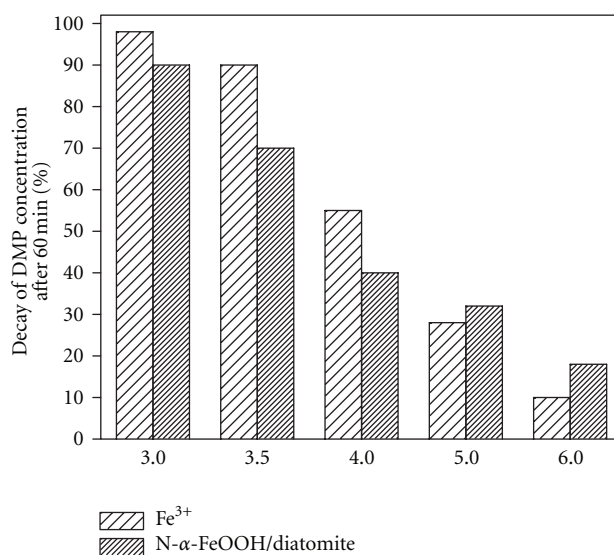
FIGURE 4: Decay of DMP at $20 \, mg \, L^{-1}$ initial concentration after 60 min of the PE-Fenton reaction using Fe^{3+} ions and N-α-FeOOH at different pHs.

detrimental for the PE-Fenton reaction from pH 3.5 to 6.0. A 100% decay of DMP concentration was obtained within 90 min at pH 3.0 and within 120 min at pH 3.5. At a pH above 4.0, the decrease in DMP concentration slowed down significantly, and only 62% of the DMP was reduced. TOC removal was detected after 210 min of the PE-Fenton reaction (Figure 3(b)). With increasing pH, TOC removal decreased significantly from 75% at pH 3.0 to 16% at pH 6.0.

For comparison, an optimal dose of free Fe^{3+} ions at 1.0 mM was used as the iron substance for the PE-Fenton reaction. After 10 min reaction at pH above 4.0, iron precipitate was formed. The DMP concentrations were detected after 60 min. The DMP concentrations at 60 min under different pHs were compared in Figure 4. At pH 3.0, 3.5, and 4.0, the DMP degradation efficiency in terms of Fe^{3+} concentration was higher than those for N-α-FeOOH. However, the opposite case was observed at pH 5.0 and 6.0. That was to say, at pH 5.0 and 6.0, the DMP removal efficiency using N-α-FeOOH after 60 min was higher than that using Fe^{3+}. This result implied that at higher pH, the Fe^{3+} precipitation impeded its competitiveness compared with the N-α-FeOOH. In addition, DMP degradation due to the coagulation of ferric hydroxide was negligible [19].

3.3. Supported and Unsupported N-α-FeOOH.

The activities of the supported and unsupported N-α-FeOOH in DMP degradation by the PE-Fenton reaction were further evaluated. Two sets of experiments were conducted with the two iron substances to degrade $20 \, mg \, L^{-1}$ DMP at pH 3.5. Each set included six experiments with different dosages of the iron materials. After 90 minutes of the reaction time, the DMP concentrations in the samples were measured (Figure 5). Supported N-α-FeOOH on diatomite exhibited markedly higher activity than unsupported N-α-FeOOH. Under
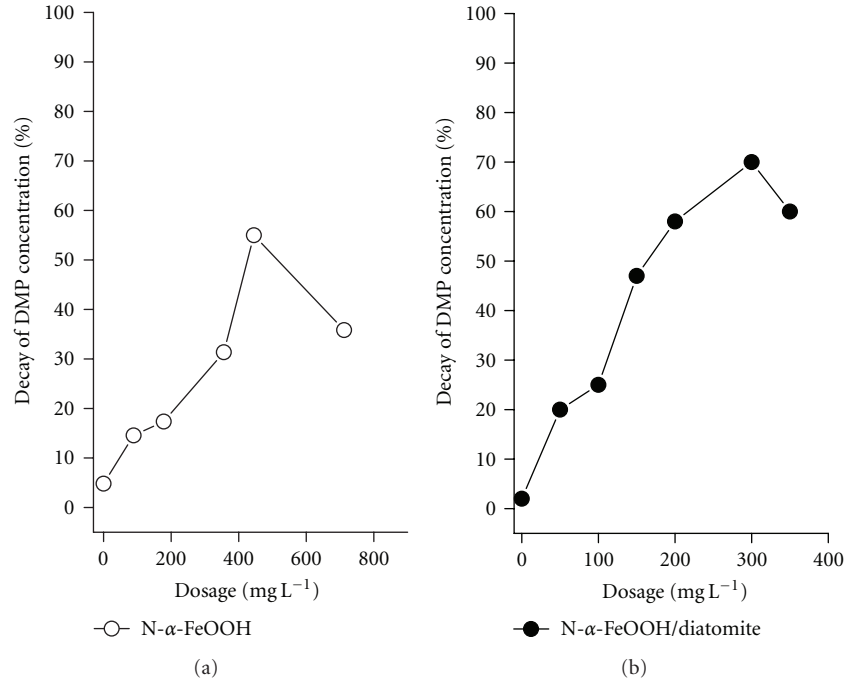
FIGURE 5: Decay of DMP at 20 mg L^{-1} initial concentration after 60 min of the PE-Fenton reaction using (a) unsupported N-α-FeOOH and (b) N-α-FeOOH/diatomite a pH 3.5.

an optimal dosage of unsupported N-α-FeOOH, the DMP concentration decreased by 55%; for the supported N-α-FeOOH on diatomite, the DMP concentration decreased by 70%. Since it was quite difficult for unsupported N-α-FeOOH to settle, this study focused on comparing the activities of N-α- FeOOH/diatomite and Fe^{3+} without paying any further attention to the unsupported N-α-FeOOH.

3.4. Duration of pH Elevation and Reduction and Iron Settlement. During the pH increase, the iron substances settled as ferric hydroxide or N-α-FeOOH/diatomite for separation and recovery from the aqueous solution. During the process of pH decrease, the ferric hydroxide dissolved. Besides the efficiency of the PE-Fenton reaction (Step 2) with RCpA, the overall efficiency of the PE-Fenton process also clearly relied on the duration of pH elevation and reduction steps.

Theoretically, the duration of pH increase equals that of pH decrease. The durations are listed in Table 1. It could be seen that during the step of pH reduction, the duration of iron settlement using Fe^{3+} was 45 min, slightly longer than that (40 min) using N-α-FeOOH/diatomite. As the pH decreased, the ferric hydroxide gradually dissolved. In contrast, such consumption of H$^+$ was precluded when N-α-FeOOH/diatomite was used. Thus, pH reduction using Fe^{3+} demanded more H$^+$ and slightly prolonged the operation time.

In the step of pH elevation, the duration of pH adjustment using Fe^{3+} reached 45 min, which was also slightly longer (40 min) than when using N-α-FeOOH/diatomite. The prolonged interval was attributed to the formation of ferric hydroxide that consumed OH$^-$ during the process of

TABLE 1: Duration of the steps in the PE-Fenton process with RCpA using different iron substances (current density, 6 mA cm^{-2}; N-α-FeOOH/diatomite, 500 mg L^{-1}; free iron, 25 mg L^{-1}).

Step	Duration of steps (min)	
	Fe^{3+}	N-α-FeOOH/diatomite
pH decrease	45	40
PE-Fenton reaction	75	100
pH increase	45	40
Iron settlement	180	15
Total time*	300	140

*pH decrease and pH increase proceeded simultaneously, and time was included for an individual step; the time for iron settlement was included in the pH increase as the time for pH increase was longer than the settlement, otherwise, the latter included the former.

pH increase. Furthermore, ferric hydroxide settled very slowly. As shown in Table 1, even if the pH increased to 7.0, the duration of ferric hydroxide settlement took as long as 180 min. OH$^-$ production via (1) occurred more slowly compared with via chemical addition. Thus, the ferric hydroxide particulates were finer and flocculation did not occur. In contrast, the duration of N-α-FeOOH/diatomite settlement was only 15 min. Besides, DMP degradation using Fe^{3+} and N-α-FeOOH/diatomite in the second step of the PE-Fenton reaction required 75 and 100 min, respectively. Therefore, the settlement time of the iron substances played a vital role in improving the efficiency of the PE-Fenton process with RCpA. Accordingly, the overall PE-Fenton process with RCpA using N-α-FeOOH/diatomite was more
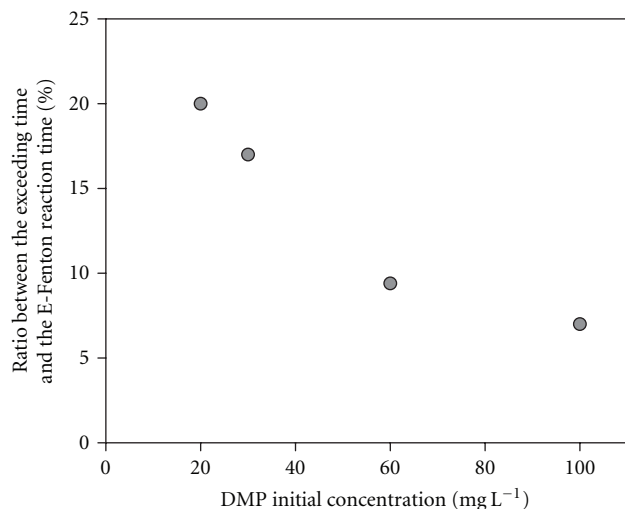
FIGURE 6: The proportion of the excess time to the duration of the PE-Fenton reaction using N-α-FeOOH/diatomite (current density, 6 mA cm^{-2}, and pH 3.5).

efficient than that using Fe^{3+}, because 160 min was saved in the present system.

3.5. Efficiency of the Reuse of Iron Substances. Following iron settlement, the iron substances can be recovered and reused. Thus, the application of this process is beneficial and environmentally safe from an engineering point of view. Interestingly, no significant decrease in the DMP degradation efficiency via the PE-Fenton process was observed either using the recycled N-α-FeOOH/diatomite or the recycled Fe^{3+} at pH 3.0 or 3.5. This finding is in agreement with previous reports [19].

3.6. Energy Efficiency of the PE-Fenton Reaction Steps. Table 1 also shows that although the durations of the iron settlement and the overall process were significantly shortened by using N-α-FeOOH/diatomite, the durations of the individual steps of the PE-Fenton reaction to degrade the DMP were prolonged. Since these steps consumed energy, assessing the energy efficiency using the two different iron substances was necessary.

The duration of the steps of the PE-Fenton reaction using N-α-FeOOH/diatomite was 100 min, whereas it was only 75 min using Fe^{3+}. The extra 25 min was spent for the consumption of electricity. Under the conditions we established, the current was 0.050 A, and the voltage was 2.0 V. The extra energy for the employment of N-α-FeOOH/diatomite was thus calculated to be 0.075 W h. Compared with the total energy consumption of 0.225 W h using Fe^{3+}, using N-α-FeOOH/diatomite for the PE-Fenton reaction consumed 33.3% additional energy at a DMP concentration of 20 mg L^{-1} degradation of different concentrations of DMP was performed, and the durations obtained for the complete decay of DMP via the PE-Fenton reaction. The average additional time ranged from 20 min to 25 min.

The proportion of the excess time to the duration of the PE-Fenton reaction using N-α-FeOOH/diatomite could be obtained, as shown in Figure 6. Interestingly, this ratio decreased from 20% at 20 mg L^{-1} initial DMP concentration to 7.0% at 100 mg L^{-1} initial DMP concentration. Thus, with increasing initial DMP concentration, compared with using Fe^{3+}, the energy efficiency of the PE-Fenton reaction using N-α-FeOOH/diatomite increased. Once the DMP concentration reached 100 mg L^{-1}, the added energy was less than 10%. Thus, although extra energy was consumed by using N-α-FeOOH/diatomite compared with using Fe^{3+}, the percentage of additional energy consumption became negligible as the substrate concentration increased.

4. Conclusion

In using RCpA in the PE-Fenton process for sustainable water treatment, increasing the overall efficiency of the process is important. In this study, supported nanosized iron oxide appeared to be a suitable alternative that maintains high activity and exhibits viable recyclability. The N-α-FeOOH/diatomite exhibited slightly lower activity than Fe^{3+} at lower pH, but as the pH increased to 5.0, the N-α-FeOOH/diatomite activity was higher. Since the second step of the PE-Fenton reaction occurred in acidic solution at pH 3.5, the time consumed for this step using N-α-FeOOH/diatomite was longer than that using Fe^{3+} and thus extra energy was consumed in using N-α-FeOOH. However, increasing the substrate concentration to 100 mg L^{-1} caused the extra energy to become negligible. More importantly, the overall duration of the PE-Fenton process using N-α-FeOOH/diatomite was significantly shorter than that using the Fe^{3+}. In our system, 160 min was conserved from the 300 min overall PE-Fenton process. The findings in this study imply that for any practical application of the PE-Fenton process in sustainable water treatment, the operation time and degradation efficiency, as well as the energy consumption, should be carefully balanced.

Acknowledgments

References

[1] E. Neyens and J. Baeyens, "A review of classic Fenton's peroxidation as an advanced oxidation technique," *Journal of Hazardous Materials*, vol. 98, no. 1–3, pp. 33–50, 2003.

[2] J. J. Pignatello, E. Oliveros, and A. MacKay, "Advanced oxidation processes for organic contaminant destruction based on the fenton reaction and related chemistry," *Critical Reviews in Environmental Science and Technology*, vol. 36, no. 1, pp. 1–84, 2006.

[3] E. Brillas, E. Mur, R. Sauleda et al., "Aniline mineralization by AOP's: anodic oxidation, photocatalysis, electro-Fenton and

photoelectro-Fenton processes," *Applied Catalysis B*, vol. 16, no. 1, pp. 31–42, 1998.

[4] M. A. Oturan, J. Peiroten, P. Chartrin, and A. J. Acher, "Complete destruction of p-Nitrophenol in aqueous medium by electro-fenton method," *Environmental Science and Technology*, vol. 34, no. 16, pp. 3474–3479, 2000.

[5] J. Casado, J. Fornaguera, and M. I. Galán, "Mineralization of aromatics in water by sunlight-assisted Electro-Fenton technology in a pilot reactor," *Environmental Science and Technology*, vol. 39, no. 6, pp. 1843–1847, 2005.

[6] E. Brillas, J. C. Calpe, and J. Casado, "Mineralization of 2,4-D by advanced electrochemical oxidation processes," *Water Research*, vol. 34, no. 8, pp. 2253–2262, 2000.

[7] S. S. Abu Amr and H. A. Aziz, "New treatment of stabilized leachate by ozone/Fenton in the advanced oxidation process," *Waste Management*, vol. 32, no. 9, pp. 1693–1698, 2012.

[8] A. El-Ghenymy, S. Garcia-Segura, R. M. Rodríguez et al., "Optimization of the electro-Fenton and solar photoelectro-Fenton treatments of sulfanilic acid solutions using a pre-pilot flow plant by response surface methodology," *Journal of Hazardous Materials*, vol. 221-222, pp. 288–297, 2012.

[9] V. J. P. Vilar, J. M. S. Moreira, A. Fonseca et al., "Application of Fenton and solar photo-Fenton processes to the treatment of a sanitary landfill leachate in a pilot plant with CPCs," *Journal of Advanced Oxidation Technologies*, vol. 15, no. 1, pp. 107–116, 2012.

[10] R. G. Zepp, B. C. Faust, and J. Holgné, "Hydroxyl radical formation in aqueous reactions (pH 3-8) of iron(II) with hydrogen peroxide: the photo-fenton reaction," *Environmental Science and Technology*, vol. 26, no. 2, pp. 313–319, 1992.

[11] E. Lipczynska-Kochany, G. Sprah, and S. Harms, "Influence of some groundwater and surface waters constituents on the degradation of 4-chlorophenol by the Fenton reaction," *Chemosphere*, vol. 30, no. 1, pp. 9–20, 1995.

[12] M. L. Kremer, "The fenton reaction. Dependence of the rate on pH," *Journal of Physical Chemistry A*, vol. 107, no. 11, pp. 1734–1741, 2003.

[13] S. Irmak, H. I. Yavuz, and O. Erbatur, "Degradation of 4-chloro-2-methylphenol in aqueous solution by electro-Fenton and photoelectro-Fenton processes," *Applied Catalysis B*, vol. 63, no. 3-4, pp. 243–248, 2006.

[14] B. Boye, M. M. Dieng, and E. Brillas, "Anodic oxidation, electro-Fenton and photoelectro-Fenton treatments of 2,4,5-trichlorophenoxyacetic acid," *Journal of Electroanalytical Chemistry*, vol. 557, pp. 135–146, 2003.

[15] E. Brillas, M. A. Baños, M. Skoumal, P. L. Cabot, J. A. Garrido, and R. M. Rodríguez, "Degradation of the herbicide 2,4-DP by anodic oxidation, electro-Fenton and photoelectro-Fenton using platinum and boron-doped diamond anodes," *Chemosphere*, vol. 68, no. 2, pp. 199–209, 2007.

[16] X. R. Zhao, L. H. Zhu, Y. Y. Zhang et al., "Removing organic contaminants with bifunctional iron modified rectorite as efficient adsorbent and visible light photo-Fenton catalyst," *Journal of Hazardous Materials*, vol. 215, pp. 57–64, 2012.

[17] X. M. Zhou, J. Y. Lan, G. Liu et al., "Facet-mediated photo-degradation of organic dye over hematite architectures by visible light," *Angewandte Chemie International Edition*, vol. 51, pp. 178–182, 2012.

[18] M. Hartmann, S. Kullmann, and H. Keller, "Wastewater treatment with heterogeneous Fenton-type catalysts based on porous materials," *Journal of Materials Chemistry*, vol. 20, no. 41, pp. 9002–9017, 2010.

[19] H. Liu, C. Wang, X. Li, X. Xuan, C. Jiang, and H. N. Cui, "A novel electro-Fenton process for water treatment: reaction-controlled pH adjustment and performance assessment," *Environmental Science and Technology*, vol. 41, no. 8, pp. 2937–2942, 2007.

[20] H. E. G. M. M. Makr, "Diatomite: its characterization, modification and applications," *Asian Journal Materias Science*, vol. 2, no. 3, pp. 121–136, 2010.

[21] C. A. Staples, D. R. Peterson, T. F. Parkerton, and W. J. Adams, "The environmental fate of phthalate esters: a literature review," *Chemosphere*, vol. 35, no. 4, pp. 667–749, 1997.

[22] A. Wang and J. Chi, "Phthalic acid esters in the rhizosphere sediments of emergent plants from two shallow lakes," *Journal of Soils and Sediments*, vol. 12, no. 7, pp. 1189–1196, 2012.

[23] C. Zhang and Y. Wang, "Removal of dissolved organic matter and phthalic acid esters from landfill leachate through a complexation-flocculation process," *Waste Management*, vol. 29, no. 1, pp. 110–116, 2009.

[24] H. Yan and G. Pan, "Increase in biodegradation of dimethyl phthalate by *Closterium lunula* using inorganic carbon," *Chemosphere*, vol. 55, no. 9, pp. 1281–1285, 2004.

[25] C. Huang and T. Xu, "Electrodialysis with bipolar membranes for sustainable development," *Environmental Science and Technology*, vol. 40, no. 17, pp. 5233–5243, 2006.

[26] T. Xu, "Ion exchange membranes: state of their development and perspective," *Journal of Membrane Science*, vol. 263, no. 1-2, pp. 1–29, 2005.

[27] American Public Health Association/American Water Works Association/Water Environment Federation, *Standard Methods For the Examination of Water and Wastewater*, American Public Health Association/American Water Works Association/Water Environment Federation, Washington, DC, USA, 19th edition, 1995.

Research Article

UV-Irradiated Photocatalytic Degradation of Nitrobenzene by Titania Binding on Quartz Tube

Thou-Jen Whang, Mu-Tao Hsieh, Tjaun-En Shi, and Chun-Hsiung Kuei

Department of Chemistry, National Cheng Kung University, No. 1 University Road, Tainan 70101, Taiwan

Correspondence should be addressed to Thou-Jen Whang, twhang@mail.ncku.edu.tw

A new method for UV-irradiated degradation of nitrobenzene by titania photocatalysts was proposed, titania nanoparticles were coated on a quartz tube through the introduction of tetraethyl orthosilicate into the matrix. The dependence of nitrobenzene photodegradation on pH, temperature, concentration, and air feeding was discussed, and the physical properties such as the activation energy, entropy, enthalpy, adsorption constant, and rate constant were acquired by conducting the reactions in a variety of experimental conditions. The optimum efficiency of the photodegradation with the nitrobenzene residue as low as 8.8% was achieved according to the experimental conditions indicated. The photodegradation pathways were also investigated through HPLC, GC/MS, ion chromatography (IC), and chemical oxygen demand (COD) analyses.

1. Introduction

Wastewater discharged from industrial effluents has been a serious problem of the environmental issues [1]. Due to the relatively stable chemical structures of aromatic dyes, most of the dyestuffs that the industries produced are unlikely to decompose and therefore causing severe contaminations to the drinking water and irrigation systems. Many of the dyestuffs have even been considered health hazards and thus serious concerns have been raised [2, 3]. Nitrobenzene (NB) is one of the frequently used chemicals for aniline manufacturing, rubber making, textile, pesticide, cosmetic, and pharmaceutical purposes [4]. It is a highly toxic pollutant. Through skin contact and inhalation, it is readily absorbed into human body and is likely causing symptoms such as headache, vertigo, vomit, and weakness. For this reason, it was selected to be the model pollutant in this study. General treatments of such polluted wastewater include adsorption [5, 6], ozonation [7], or biodegradation [8]. However, those methods are somewhat inefficient or relatively expensive because they require further treatments and are very prone to cause secondary pollution.

Semiconductor photocatalysts have been considered potential candidates for treating various water pollutants [9–11] and are acclaimed as being one of advanced oxidation processes for eliminating the harmful contaminants. The efficient oxidation reaction of photocatalysts under UV irradiation processes provides an alternative way of managing these pollutants properly. Due to the extensive research for many years, semiconductor photocatalysts which have been frequently investigated include oxide compounds of TiO_2, ZnO, WO_3, SnO_2, ZrO_2, and sulfide compounds of CdS and ZnS [12, 13]. Among these compounds, titania (TiO_2) has been thoroughly investigated for its photocatalytic activities [14–18]. Novel preparations of titania with high photocatalytic activities have been proposed [19, 20]. It has drawn great attention in research and industries in recent years owing to its powerful oxidation capability, non-toxicity, biological inertness, chemical stability, and costeffectiveness [21]. Recently, selective photocatalysis of titania has been developed and gained success, it can be applied to separation process or selective elimination of specific molecules from a mixture [22, 23]. Some research explored further the photocatalytic activities of mixed oxides [24], and some

studied the effect of morphologies of titania [25, 26]. In addition, titania photocatalysis has been applied to solar disinfection of water [27] and degrading chemicals that caused hormonal imbalance in wildlife and humans [28].

The initial step involves the generation of e^-/h^+ pairs after irradiated with light of which the wavelength is shorter than 388 nm (413 nm for rutile crystalline phase), due to the wide direct band gap of TiO_2 (3.2, 3.0 eV for anatase and rutile crystalline phase, resp.), the valence band electrons of TiO_2 will be promoted up to the conduction band, leaving holes in valence band as shown in (1). The holes produced could subsequently react with H_2O molecules or hydroxide ions (OH^-) in aqueous solution forming powerful oxidants such as hydroxyl radicals ($^\bullet OH$) in (2). The electrons on conduction band could transform the dissolved oxygen to superoxide radicals in (3) and further to hydrogen peroxide in (4)–(7) [29]. These strong oxidants could be used to mineralize organic pollutants from wastewater as follows:

$$TiO_2 + h\nu \longrightarrow TiO_2(e^- + h^+) \tag{1}$$

$$h^+ + H_2O \longrightarrow {}^\bullet OH + H^+ (h^+ + OH^- \longrightarrow {}^\bullet OH$$
$$\text{in alkaline condition}) \tag{2}$$

$$e^- + O_2 \longrightarrow O_2^{\bullet -} \tag{3}$$

$$O_2^{\bullet -} + H^+ \longrightarrow HO_2^\bullet \tag{4}$$

$$HO_2^\bullet + HO_2^\bullet \longrightarrow H_2O_2 + O_2 \tag{5}$$

$$O_2^{\bullet -} + HO_2^\bullet \longrightarrow HO_2^- + O_2 \tag{6}$$

$$HO_2^- + H^+ \longrightarrow H_2O_2. \tag{7}$$
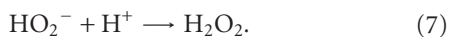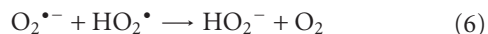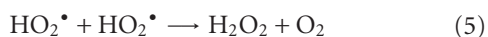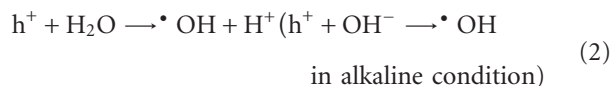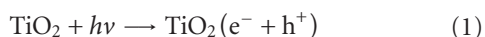
The photocatalytical degradation of NB may undergo either through direct oxidation reduction from electrons and holes or through indirect reaction with oxidants such as hydroxyl radicals, superoxide radicals, and hydrogen peroxide, which are generated by UV irradiation onto TiO_2.

The aim of this study is to investigate the optimized experimental conditions for the photodegradation of NB and to propose a new approach which can easily be applied repetitively without the necessity of separating the catalyst from solution after use. By employing HPLC, GC/MS, ion chromatography (IC), and chemical oxygen demand (COD) analyses, the authors attempted to probe into the 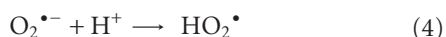photodegradation pathways. The structural and optical characterization of TiO_2 has been done by means of X-ray diffraction (XRD) and UV-vis spectroscopy (UV-vis). The photocatalytic activities of TiO_2 nanoparticles were evaluated through the degradations of NB solutions initiated by irradiation with an UV lamp.

2. Experimental

2.1. Materials. Degussa P25 titania (TiO_2, 80% in anatase phase, average particle size 30 nm, surface area 50 m^2 g^{-1}) was acquired from Degussa Co. Nitrobenzene was purchased from Panreac Co., *m-*, *o-*, *p-*nitrophenol, tetraethyl orthosilicate, perchloric acid, HPLC grade methanol, sodium nitrate, sodium nitrite, sodium carbonate, and sodium bicarbonate were acquired from Merck Co. Ethanol was purchased from Riedel-de Haen Co. Coumarin was purchased from Alfa Aesar Co. These chemicals were used without further purification. Ultrapure water (18 MΩ-cm) was used throughout the entire experiments.

2.2. Preparation of Tetraethyl Orthosilicate Polymer Solution. One mole of tetraethyl orthosilicate and 2.5 moL ethanol were mixed for 30 min at room temperature, hydrochloric acid solution was added to make the solution with a pH value of pH 1. Then a mixture of 2.5 moL ethanol and 4 moL H_2O was added into the solution above for 30 min to form a polymer solution which is in molar ratio of 1 : 4 : 5 for tetraethyl orthosilicate, H_2O, and ethanol. A quartz tube (2.2 cm in outer diameter and 28 cm in length) was first dipped into the solution composed of TiO_2 and polymer (1 : 20 w/w ratio) three times and was sintered in an oven at 400°C for 1 h.

2.3. NB Photodegradation Reactions. A 482 mL stainless steel tank was used as the container for TiO_2 photocatalytic degradation of NB solutions, inside the container the water bath was circulated by a peristaltic pump at a flow rate of 73 mL min^{-1} and thermostated by a HAAKE DC10 immersion circulator at 30°C. The quartz tube referred to above was put inside a glass tube, which is 5 cm in inner diameter and 30 cm in length and was used as the batch reactor. A 14 W Philips UV lamp with the wavelength of 254 nm was inserted into the quartz tube. Silicone tubing was introduced inside the reactor for feeding air into the solution. The degradation experiments were carried out by mixing each 400 mL of 0.407, 0.813, 1.220, 1.626, and 2.439 mM NB solution with 0.2 g TiO_2 photocatalyst supported on the quartz tube and covered with aluminum foil, the selected air feeding was 50, 100, and 150 mL min^{-1} (the dissolved oxygen is 5.8, 6.5, and 7.2 mg L^{-1}, resp.), the pH values of solutions were adjusted to pH 4, 7, and 11 using 0.1 N perchloric acid or 0.1 N NaOH solution. The solutions were sampled at 0, 15, 30, 45, 60, 90, 120, 150, and 180 min reaction time for HPLC, IC, and GC/MS analyses. The absorption maximum of the UV-vis absorbance spectroscopy appeared at 270 nm (λ_{max}) for NB solutions and was selected to be the analytical wavelength for NB measurements. For the identifications of intermediates, the photodegradation was manipulated in a slurry system with 1.0 g catalyst and 1.626 mM NB at pH 7 and 30°C with the air feeding of 150 mL min^{-1} for 10 h.

2.4. Characterization of TiO_2 Nanoparticles and Quantitative Analyses of Reaction Intermediates. A Shimadzu XD-D1 X-ray diffractometer was used to observe the XRD patterns of nanoparticles, and the 2θ range of 20° to 70° was scanned continuously with a step of 0.02° and at a speed of 1 degree min^{-1}. A Hitachi U-2000 UV-vis spectrophotometer was used to evaluate the degradation of NB solutions, the absorption maximum (λ_{max}) of the UV-vis absorbance spectroscopy of NB solutions was selected at 270 nm based on analytical sensitivity. A Hitachi L-7000 high-performance

liquid chromatography (HPLC; Hitachi L-7100 pump) using a C18 column (Waters 5 μm, 250 mm long) connected with a Hitachi L-7420 UV detector was used for the qualitative and quantitative determinations of the initial compound and reaction intermediates. A Dionex DX-120 ion chromatography (IC) system using IonPac AS9-HC analytical column (4 × 250 mm, 1700–1800 psi) and IonPac AG9-HC guard column (4 × 50 mm) with 9 mM Na_2CO_3 as the mobile phase was used for the qualitative and quantitative determinations of anions produced during the reaction. A Finnigan Trace MS connected with Trace GC 2000 GC/MS in electron impact (EI) mode were used to separate and analyze the intermediates of reaction. Samples were injected splitless into the gas chromatography equipped with a Rtx-5 ms column (30 m × 0.25 mm, 0.25 μm film thickness). The oven was programmed isotherm at 35°C for 2 min, then heating from 35°C to 250°C at the speed of 10°C min^{-1}, and keep isotherm at 250°C for 1 min. An AQUALYTIC AL31 chemical oxygen demand reactor was used to detect the amount of organic compound residue in solution.

2.5. Measurements of Hydroxyl Radicals Generated from Titania under UV Irradiation. The measurement of hydroxyl radicals was proposed using coumarin or terephthalic acid as probe molecules [30, 31]. Coumarin was selected as the probe molecule in this work. Each 0.1 g titania powder was dispersed in 20 mL 1.0 mM coumarin aqueous solution until it reached adsorption-desorption equilibrium before light irradiation. In a dish with 7.0 cm in diameter, the solution was located 10 cm below the light source and was irradiated using an UV lamp with the peak intensity of 366 nm. After UV illumination the solution was centrifuged and the PL spectrum of hydroxylated coumarin (7-hydroxycoumarin) was measured by a Hitachi F-4500 fluorescence spectrophotometer with the excitation wavelength of 332 nm, scanning speed 240 nm/min, PMT voltage 700 V, and slit width 2.5 nm. To investigate the effect of pH value on the production of hydroxyl radicals, the coumarin solution was adjusted to pH 4, 7, and 11 using 0.1 N perchloric acid or 0.1 N NaOH solution.

3. Results and Discussion

3.1. Background Experiments. To explore the background interferences, volatility of solvent, adsorption, and blank experiments were carried out to confirm the role of titania in the photocatalysis reactions. The results of volatility experiments showed no significant decrease of NB concentration was observed after 3 h. With respect to the adsorption of NB by the catalysts, the adsorption tests showed that saturated adsorption of NB was reached after about 150 min of adsorption. The results of blank experiments (direct photocatalysis of NB solution without the catalysts) showed more than 71.1% NB remained after 3 h irradiation under a variety of conditions. Therefore, the concentrations of NB were examined after 3 h of adsorption for all the degradation experiments.
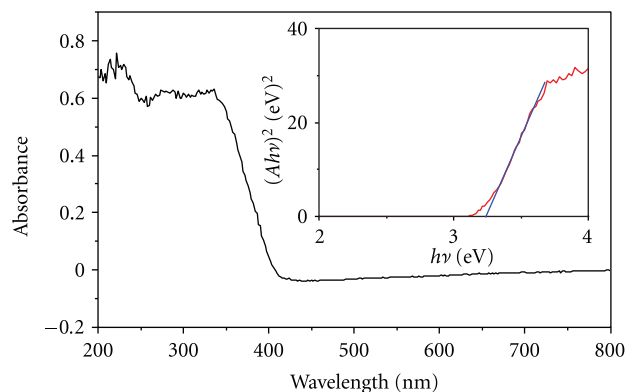
FIGURE 1: The UV-vis absorbance spectrum of TiO_2 photocatalyst. Inset shows the plot of $(Ah\nu)^2$ versus $h\nu$ for TiO_2, the straight line represents the extrapolation of the abscissa from the linear fit of the curve, through which the band gap was estimated at about 3.20 eV.

3.2. Characterization of TiO_2 Photocatalysts. From the UV-vis spectrum in Figure 1, very little light could be absorbed in the spectrum with wavelength greater than 420 nm by semiconductor TiO_2. The energy gap of TiO_2 nanoparticles can be obtained from the data treatment of optical absorbance by plotting $(Ah\nu)^2$ versus $h\nu$ according to the following relationship [32, 33]:

$$A = \frac{\left[k\left(h\nu - E_g\right)^{n/2}\right]}{h\nu}, \qquad (8)$$

where A is the absorbance, k is a constant, h is the Planck's constant, ν is the frequency of light, $n = 1$ for direct and $n = 4$ for indirect electron transfer, and E_g is the band gap of the object concerned. From the inset of Figure 1, P25 TiO_2 was estimated having the energy gap of 3.2 eV, which is in accordance with other research [34]. From the XRD patterns of TiO_2 photocatalysts (not shown), the characteristic signals of anatase crystalline phase TiO_2 were found at $2\theta = 25.4°$ (1 0 1), 37.9° (0 0 4), 48.2° (2 0 0), 55.1° (2 1 1), 62.8° (2 0 4), and the signals for rutile crystalline phase at 27.5° (1 1 0), 36.2° (1 0 1), 54.4° (2 1 1). Using the Scherrer equation with a shape factor of 0.89, $\lambda = 0.1541$ nm for the wavelength of the Cu Kα_1 X-ray source, and B the full peak width at half-maximum, the particle size (d; in nm) of nanoparticles can be estimated [35]. Applying XRD data of P25 TiO_2 nanoparticles to the equation above, the particle size was evaluated at 18.1 nm. Furthermore, the ratio of anatase phase in those nanoparticles can be evaluated according to the following equation [36]:

$$A(\%) = \frac{100}{(1 + 1.265I_R/I_A)}, \qquad (9)$$

where I_R is the intensity of the peak at $2\theta = 27.5°$ and I_A is the intensity of the peak at $2\theta = 25.3°$ (those are the most prominent signals of rutile and anatase form, resp.). By using this equation, the anatase phase ratio in P25 TiO_2 is estimated at 84%.
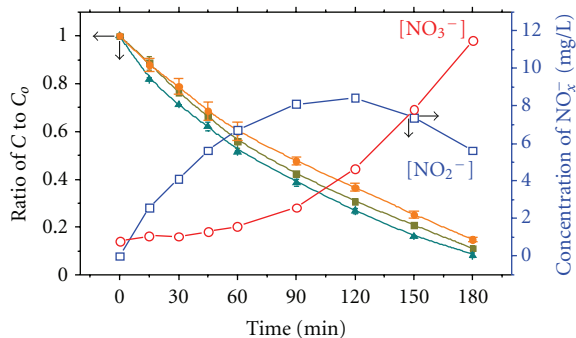
FIGURE 2: UV photocatalytic degradation of nitrobenzene at pH 4 (blue line with square symbols), 7 (green line with triangle symbols), and 11 (orange line with round symbols) with 0.2 g TiO$_2$ at 30°C and the air feeding of 150 mL min^{-1} for 3 h. Concentrations of reaction intermediates nitrate (red line with empty circles) and nitrite ions (blue line with empty squares) at pH 7 are corresponded to the right ordinate as time changes.

FIGURE 3: PL spectra of hydroxylated coumarin (7-hydroxycoumarin) solutions adjusted at pH 4, 7, and 11. Each 1.0 mM coumarin aqueous solution was mixed with 0.1 g TiO$_2$ and irradiated thereafter using an UV lamp with the peak intensity of 366 nm for 15 min.

3.3. Effects of pH on Photocatalytic Degradation of Nitrobenzene. The effects of pH on the photocatalytic degradation of nitrobenzene are shown in **Figure 2**. According to the degradation processes carried out in pH 4, 7, and 11, the most efficient degradation is in the case of pH 7 and the least one is in the case of pH 11. Because the surface of TiO$_2$ catalysts in aqueous solution is in the form of Ti-OH [37, 38], and the pH of zero point charge (pH$_{zpc}$) is about 6–6.4 for anatase phase and 5.8 for rutile phase [39]. In circumstance of pH value less than pH$_{zpc}$, the major species on the surface of catalysts in the form of Ti-OH$_2^+$ is likely to occur whereas with a pH greater than pH$_{zpc}$ the negative form of Ti-O$^-$ is prone to happen. To produce strong performance of the photocatalytic reaction, it is important to have fair interaction between the substance to be degraded and the catalysts [40]. Therefore, the pH value of the solution plays a significant role in the interactions between the surface of TiO$_2$ and the instinctive electron property of the degrading substance. In the case of NB molecule, it is very likely to be in the form of positive charge because of the low pK_a for NB [41].

Another aspect of the pH effects that comes into play is the formation of $^\bullet$OH radicals being more feasible in low pH condition [30], which is shown in **Figure 3** that hydroxyl radicals generated at pH 4 has more amount than those in pH 7 and 11. According to the results shown in **Figure 2**, combining the effects cited above indicate the interaction between the substance and surface has more influence on the catalytical effect than the generation of $^\bullet$OH radicals. The additional data included in **Figure 2** are the concentrations of intermediates NO$_3^-$, NO$_2^-$ which were generated during the degradation processes. The nitrite ions detected were assumed to be generated through the cleavage of nitro group on NB molecules. The nitrate ions were further produced through the oxidation of nitrite ions by the oxidants which were initiated by the UV irradiation of the catalysts and generated by a variety of reactions. These can be demonstrated from the observed trend in **Figure 2** how the concentration of nitrites reached the peak at 120 min and
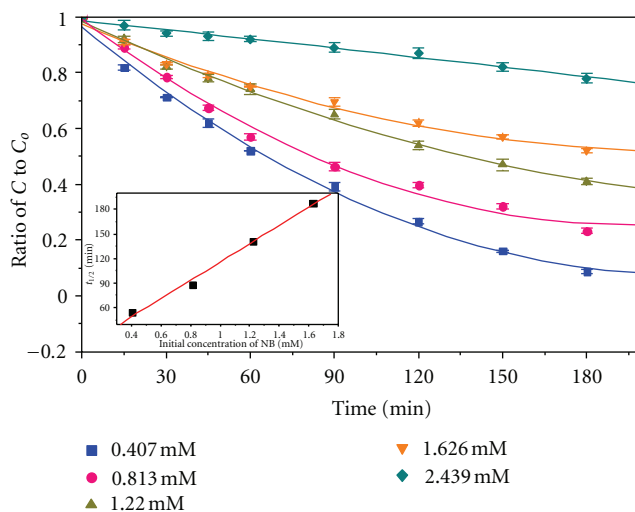
FIGURE 4: The initial concentration dependence of reaction rates for the photodegradation of nitrobenzene by TiO$_2$ as time changes. The processes were operated with 0.2 g TiO$_2$ and various concentrations of nitrobenzene at pH 7 and 30°C with the air feeding of 150 mL min^{-1} for 3 h. Inset shows the effect of the initial concentrations on the half-life of NB.

since then nitrates increased at the expense of nitrites. This observation will be discussed along with the investigation of mechanisms in later section.

3.4. Physical Properties of the Photodegradation Reaction. Figure 4 exhibits the initial concentration dependence of reaction rates for NB photodegradation. To examine whether this reaction follows the Langmuir-Hinshelwood dynamic model, a graph of $t_{1/2}$ versus C_o was plotted according to the following equation [42]:

$$t_{1/2} = \left(\frac{0.693}{k_{LH} K_{ads}} \right) + \left(\frac{0.5}{k_{LH}} \right) C_o, \qquad (10)$$
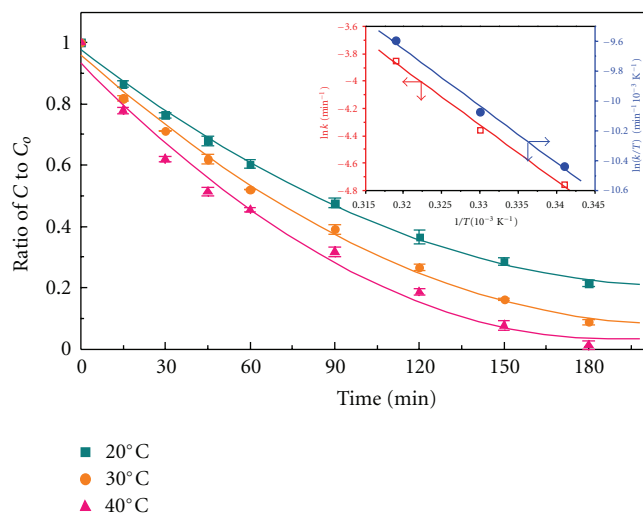
FIGURE 5: The temperature dependence of nitrobenzene photodegraded by TiO_2 as time changes. The processes were operated with 0.2 g TiO_2 and 0.407 mM nitrobenzene at pH 7 and 20°C, 30°C, 40°C with the air feeding of 150 mL min^{-1} for 3 h. Inset shows the linear fits of the data for ln$k$ and ln(k/T) versus the reciprocal of temperature.

FIGURE 6: The air feeding dependence of nitrobenzene photodegraded by TiO_2 as time changes. The processes were operated with 0.2 g TiO_2 and 0.407 mM nitrobenzene at pH 7 and 30°C for 3 h. Inset shows the relationships between the air feeding and rate constant, NB residue, respectively.

where $t_{1/2}$ is the half-life of the reactant, k_{LH} is the rate constant of photocatalytic reaction, K_{ads} is the adsorption constant of reactant, and C_o is the initial concentration of the reactant. While the reactions were conducted under the condition of 0.2 g P25 TiO_2, at pH 7 and 30°C with the air feeding of 150 mL min^{-1}, by deriving from the slope and intercept of the linear fitted line, the following constants were acquired: k_{LH} is 4.48×10^{-3} mM min^{-1}, and K_{ads} is 36.02 mM^{-1} for NB, as shown in the inset of Figure 4.

The temperature dependence of reaction rates is shown in Figure 5, the reactions were carried out under the conditions of 0.2 g TiO_2 at pH 7 with the air feeding of 150 mL min^{-1} for 3 h at temperatures of 20°C, 30°C, 40°C, respectively. According to the Arrhenius equation and the transition state theory [43], one can obtain the values of activation energy, entropy, and enthalpy of the reaction through the applications of these equations. From the left ordinate of the inset in Figure 5, the linear fit of the data is ln$k = -4143.8(1/T) + 9.3549$ with the activation energy of 34.45 kJ mol^{-1}. The enthalpy and entropy of reaction can be evaluated from the linear fit of the data with the right ordinate ln$(k/T) = -38.436 + 2.6511$: with $\Delta H = 0.31$ kJ mol^{-1} and $\Delta S = -0.041$ J mol^{-1} K^{-1}.

3.5. The Air Feeding Dependence of the Photodegradation Reaction.

The air feeding dependence of NB photodegradation by TiO_2 is shown in Figure 6. The processes were conducted with 0.2 g TiO_2 and 0.407 mM NB at pH 7 and 30°C for 3 h. The dissolved oxygen brought into the solution by air feeding could be used as the scavenger of the electrons on TiO_2 which were excited by UV irradiation. This can prevent the recombination of the photogenerated e$^-$/h$^+$ pairs since with such recombination, the efficiency of catalysts decreases dramatically. Furthermore, with large quantity
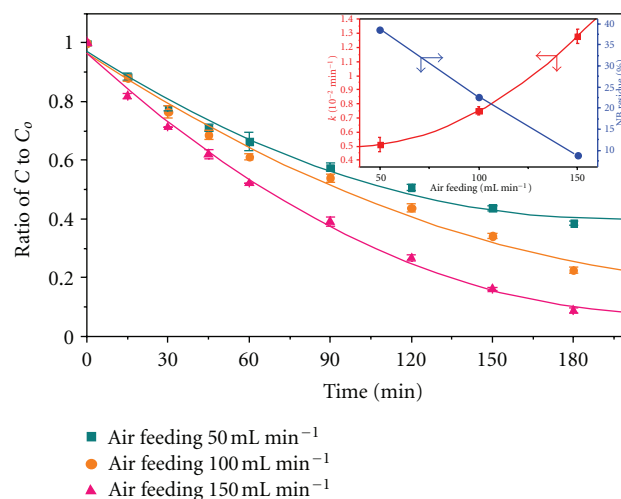
of dissolved oxygen in solution, more oxygen radicals will be produced and as they are adsorbed on the surface of TiO_2, these radicals will react further with H_2O molecules to generate $^{\bullet}OH$, which enhances the rate constants and therefore the efficiency of catalysts as shown in the inset of Figure 6. The results from the photodegradation in Figure 6 reveal that the larger amount of air feeding supplies the stronger performance it delivers, which is correspondent with the discussion above.

3.6. Investigation of the Mechanisms for NB Photodegradation Reaction.

It has been proposed that the photodegradation pathway of NB is related to partial oxidation of NB to hydroxyl derivatives [44], such as m-, o-, p-nitrophenol. To investigate the mechanisms of this photodegradation reaction, the solutions were prepared as indicated in experimental section and were sampled at every half hour interval and up to 10 h of the reacting time span for HPLC separation and identification. According to the characteristic retention times of HPLC authentic standards for the analytes, which is 6.4 min for m-nitrophenol, 8.7 min for o-nitrophenol, 5.7 min for p-nitrophenol, and 9.2 min for NB, the reaction intermediates can be identified with these data accordingly.

The concentration changes of the intermediates of NB photodegradation with corresponding time are shown in Figure 7, the total concentration of the intermediates is less than 7 μM, and it is conspicuous that m-nitrophenol was produced at the highest rate and p-nitrophenol the second highest for the initial 2 h of reaction and since then both decreased briskly while o-nitrophenol remained an approximate concentration level during this period. GC/MS analyses were also used to confirm the reaction intermediates. The pH decrease from the start of reaction of pH 5.84 to pH 3.82 after 3 h of reaction was observed as
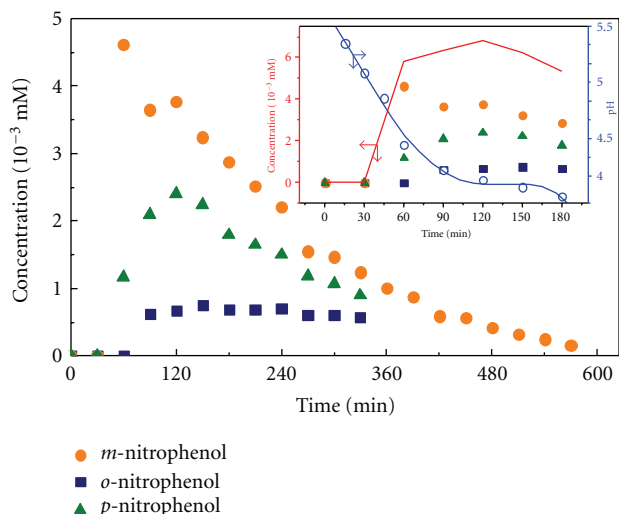
Figure 7: The concentration changes of intermediates m-, o-, p-nitrophenol as time changes. The photodegradation processes were operated with 1.626 mM nitrobenzene and 1.0 g TiO_2 at pH 7 and 30°C with the air feeding of 150 mL min^{-1} for 10 h. Inset shows the relationship between pH changes and the total concentration of intermediates (in red line) for the initial 3 h of reaction.

shown in the inset of Figure 7. The pH value of m-, o-, p-nitrophenol aqueous solution of the same concentration was measured as 6.16, 5.74, and 5.98, respectively. Combining these results with the generation of nitrites and nitrates from Figure 2, it can be assumed that the NB photodegradation reaction involves hydroxyl group grafting on NB molecules and undergoing the nitro group cleavage from the molecules.

After the photodegradation reaction, 8.8% NB residue was observed from a system of 0.2 g TiO_2 and 0.407 mM NB at pH 7 and 30°C with the air feeding of 150 mL min^{-1} for 4 h of photocatalysis whereas 4% residue from COD analysis was achieved with the same condition, it suggests that the mineralization of NB to CO_2 and H_2O may occur in parallel with the pathway cited above.

4. Conclusions

A new method of photocatalytic degradation of NB was proposed by coating the titania nanoparticles on a quartz tube through the introduction of tetraethyl orthosilicate into the matrix. Some parameters were discussed herein, such as the dependence of pH, temperature, air feeding on the photocatalysis, and some physical properties such as the activation energy, entropy, enthalpy, adsorption constant, and rate constant were also acquired. The photodegradation pathway was further investigated through HPLC, GC/MS, IC, and COD analyses.

The optimum efficiency of the photodegradation with NB residue as low as 8.8% was achieved with the experimental conditions mentioned. Although it is not the most efficient result compared to those from other studies, one of the advantages of practicing the NB photodegradation by adopting this approach is that the necessity of separating the

catalyst from solution after use is not required and therefore making it easy to be applied repetitively. With these considerations, treating the wastewater from the industries by UV photocatalytic mineralization of organic pollutants using TiO_2 photocatalyst coated on quartz tube with tetraethyl orthosilicate as the binder is one of the convenient and potential candidates for this issue.

Acknowledgments

References

[1] E. Bizani, K. Fytianos, I. Poulios, and V. Tsiridis, "Photocatalytic decolorization and degradation of dye solutions and wastewaters in the presence of titanium dioxide," *Journal of Hazardous Materials*, vol. 136, no. 1, pp. 85–94, 2006.

[2] T. Robinson, G. McMullan, R. Marchant, and P. Nigam, "Remediation of dyes in textile effluent: a critical review on current treatment technologies with a proposed alternative," *Bioresource Technology*, vol. 77, no. 3, pp. 247–255, 2001.

[3] L. B. Reutergådh and M. Iangphasuk, "Photocatalytic decolourization of reactive azo dye: a comparison between TiO_2 and CdS photocatalysis," *Chemosphere*, vol. 35, no. 3, pp. 585–596, 1997.

[4] P. Piccinini, C. Minero, M. Vincenti, and E. Pelizzetti, "Photocatalytic mineralization of nitrogen-containing benzene derivatives," *Catalysis Today*, vol. 39, no. 3, pp. 187–195, 1997.

[5] J. Pan and B. Guan, "Adsorption of nitrobenzene from aqueous solution on activated sludge modified by cetyltrimethylammonium bromide," *Journal of Hazardous Materials*, vol. 183, no. 1–3, pp. 341–346, 2010.

[6] A. El Sikaily, A. Khaled, A. El Nemr, and O. Abdelwahab, "Removal of Methylene Blue from aqueous solution by marine green alga *Ulva lactuca*," *Chemistry and Ecology*, vol. 22, no. 2, pp. 149–157, 2006.

[7] S. Contreras, M. Rodríguez, E. Chamarro, and S. Esplugas, "UV- and UV/Fe(III)-enhanced ozonation of nitrobenzene in aqueous solution," *Journal of Photochemistry and Photobiology A*, vol. 142, no. 1, pp. 79–83, 2001.

[8] L. S. Bell, J. F. Devlin, R. W. Gillham, and P. J. Binning, "A sequential zero valent iron and aerobic biodegradation treatment system for nitrobenzene," *Journal of Contaminant Hydrology*, vol. 66, no. 3-4, pp. 201–217, 2003.

[9] L. B. Khalil, W. E. Mourad, and M. W. Rophael, "Photocatalytic reduction of environmental pollutant Cr(VI) over some semiconductors under UV/visible light illumination," *Applied Catalysis B*, vol. 17, no. 3, pp. 267–273, 1998.

[10] J. Nishio, M. Tokumura, H. T. Znad, and Y. Kawase, "Photocatalytic decolorization of azo-dye with zinc oxide powder in an external UV light irradiation slurry photoreactor," *Journal of Hazardous Materials*, vol. 138, no. 1, pp. 106–115, 2006.

[11] J. Marugán, M. J. López-Muñoz, R. Van Grieken, and J. Aguado, "Photocatalytic decolorization and mineralization of dyes with nanocrystalline TiO_2/SiO_2 materials," *Industrial and Engineering Chemistry Research*, vol. 46, no. 23, pp. 7605–7610, 2007.

[12] J. M. Herrmann, "Heterogeneous photocatalysis: fundamentals and applications to the removal of various types of aqueous pollutants," *Catalysis Today*, vol. 53, no. 1, pp. 115–129, 1999.

[13] S. Sohrabnezhad, "Study of catalytic reduction and photodegradation of methylene blue by heterogeneous catalyst," *Spectrochimica Acta*, vol. 81, no. 1, pp. 228–235, 2011.

[14] D. S. Bhatkhande, V. G. Pangarkar, and A. A. C. M. Beenackers, "Photocatalytic degradation of nitrobenzene using titanium dioxide and concentrated solar radiation: chemical effects and scaleup," *Water Research*, vol. 37, no. 6, pp. 1223–1230, 2003.

[15] R. J. Tayade, R. G. Kulkarni, and R. V. Jasra, "Photocatalytic degradation of aqueous nitrobenzene by nanocrystalline TiO_2," *Industrial and Engineering Chemistry Research*, vol. 45, no. 3, pp. 922–927, 2006.

[16] R. J. Tayade and D. L. Key, "Synthesis and characterization of titanium dioxide nanotubes for photocatalytic degradation of aqueous nitrobenzene in the presence of sunlight," *Materials Science Forum*, vol. 657, pp. 62–74, 2010.

[17] T. J. Whang, H. Y. Huang, M. T. Hsieh, and J. J. Chen, "Laser-induced silver nanoparticles on titanium oxide for photocatalytic degradation of methylene blue," *International Journal of Molecular Sciences*, vol. 10, no. 11, pp. 4707–4718, 2009.

[18] D. I. Petkowicz, R. Brambilla, C. Radtke et al., "Photodegradation of methylene blue by in situ generated titania supported on a NaA zeolite," *Applied Catalysis A*, vol. 357, no. 2, pp. 125–134, 2009.

[19] J. G. Yu, H. G. Yu, B. Cheng, X. J. Zhao, J. C. Yu, and W. K. Ho, "The effect of calcination temperature on the surface microstructure and photocatalytic activity of TiO_2 thin films prepared by liquid phase deposition," *Journal of Physical Chemistry B*, vol. 107, no. 50, pp. 13871–13879, 2003.

[20] J. Yu, J. Xiong, B. Cheng, and S. Liu, "Fabrication and characterization of Ag-TiO_2 multiphase nanocomposite thin films with enhanced photocatalytic activity," *Applied Catalysis B*, vol. 60, no. 3-4, pp. 211–221, 2005.

[21] J. G. Yu, M. Jaroniec, and G. X. Lu, "TiO_2 photocatalytic materials," *International Journal of Photoenergy*, vol. 2012, Article ID 206183, 5 pages, 2012.

[22] S. Liu, J. Yu, and M. Jaroniec, "Tunable photocatalytic selectivity of hollow TiO_2 microspheres composed of anatase polyhedra with exposed 001 facets," *Journal of the American Chemical Society*, vol. 132, no. 34, pp. 11914–11916, 2010.

[23] Q. Xiang, J. Yu, and M. Jaroniec, "Tunable photocatalytic selectivity of TiO_2 films consisted of flower-like microspheres with exposed 001 facets," *Chemical Communications*, vol. 47, no. 15, pp. 4532–4534, 2011.

[24] H. Znad, M. H. Ang, and M. O. Tade, "Ta/TiO_2-and Nb/TiO_2-mixed oxides as efficient solar photocatalysts: preparation, characterization, and photocatalytic activity," *International Journal of Photoenergy*, vol. 2012, Article ID 548158, 9 pages, 2012.

[25] J. G. Yu, Y. R. Su, and B. Cheng, "Template-free fabrication and enhanced photocatalytic activity of hierarchical macro-/mesoporous titania," *Advanced Functional Materials*, vol. 17, no. 12, pp. 1984–1990, 2007.

[26] J. S. Wang, Q. Cai, H. G. Li, Y. T. Cui, and H. Wang, "A review on TiO_2 nanotube film photocatalysts prepared by liquid-phase deposition," *International Journal of Photoenergy*, vol. 2012, Article ID 702940, 11 pages, 2012.

[27] J. A. Byrne, P. A. Fernandez-Ibañez, P. S. M. Dunlop, D. M. A. Alrousan, and J. W. J. Hamilton, "Photocatalytic enhancement for solar disinfection of water: a review," *International Journal of Photoenergy*, vol. 2011, Article ID 798051, 2011.

[28] J. C. Sin, S. M. Lam, A. R. Mohamed, and K. T. Lee, "Degrading endocrine disrupting chemicals from wastewater by TiO_2 photocatalysis: a review," *International Journal of Photoenergy*, vol. 2012, Article ID 185159, 23 pages, 2012.

[29] K. I. Okamoto, Y. Yamamoto, H. Tanaka, M. Tanaka, and A. Itaya, "Heterogeneous photocatalytic decomposition of phenol over TiO_2 powder," *Bulletin of the Chemical Society of Japan*, vol. 58, no. 7, pp. 2015–2022, 1985.

[30] Q. Xiang, J. Yu, and P. K. Wong, "Quantitative characterization of hydroxyl radicals produced by various photocatalysts," *Journal of Colloid and Interface Science*, vol. 357, no. 1, pp. 163–167, 2011.

[31] J. Yu, W. Wang, B. Cheng, and B. L. Su, "Enhancement of photocatalytic activity of Mesoporous TiO_2 powders by hydrothermal surface fluorination treatment," *Journal of Physical Chemistry C*, vol. 113, no. 16, pp. 6743–6750, 2009.

[32] Z. Zainal, N. Saravanan, and H. L. Mien, "Electrodeposition of nickel selenide thin films in the presence of triethanolamine as a complexing agent," *Journal of Materials Science*, vol. 16, no. 2, pp. 111–117, 2005.

[33] T. J. Whang, M. T. Hsieh, J. M. Tsai, and S. J. Lee, "Lactic acid aided electrochemical deposition of c-axis preferred orientation of zinc oxide thin films: structural and morphological features," *Applied Surface Science*, vol. 257, no. 22, pp. 9539–9545, 2011.

[34] S. George, S. Pokhrel, Z. Ji et al., "Role of Fe doping in tuning the band gap of TiO_2 for the photo-oxidation-induced cytotoxicity paradigm," *Journal of the American Chemical Society*, vol. 133, no. 29, pp. 11270–11278, 2011.

[35] I. M. Arabatzis, T. Stergiopoulos, M. C. Bernard, D. Labou, S. G. Neophytides, and P. Falaras, "Silver-modified titanium dioxide thin films for efficient photodegradation of methyl orange," *Applied Catalysis B*, vol. 42, no. 2, pp. 187–201, 2003.

[36] R. A. Spurr, "Quantitative analysis of anatase-rutile mixtures with an X-ray diffractometer," *Analytical Chemistry*, vol. 29, no. 5, pp. 760–762, 1957.

[37] D. S. Bhatkhande, S. P. Kamble, S. B. Sawant, and V. G. Pangarkar, "Photocatalytic and photochemical degradation of nitrobenzene using artificial ultraviolet light," *Chemical Engineering Journal*, vol. 102, no. 3, pp. 283–290, 2004.

[38] J. Yao and C. Wang, "Decolorization of methylene blue with TiO_2 sol via UV irradiation photocatalytic degradation," *International Journal of Photoenergy*, vol. 2010, Article ID 643182, 2010.

[39] E. Pelizzetti and C. Minero, "Mechanism of the photo-oxidative degradation of organic pollutants over TiO_2 particles," *Electrochimica Acta*, vol. 38, no. 1, pp. 47–55, 1993.

[40] B. Cheng, Y. Le, W. Cai, and J. Yu, "Synthesis of hierarchical $Ni(OH)_2$ and NiO nanosheets and their adsorption kinetics and isotherms to Congo red in water," *Journal of Hazardous Materials*, vol. 185, no. 2-3, pp. 889–897, 2011.

[41] D. R. Lide, *CRC Handbook of Chemistry and Physics*, CRC Press, Boca Raton, Fla, USA, 2009.

[42] M. Bekbolet, A. S. Suphandag, and C. S. Uyguner, "An investigation of the photocatalytic efficiencies of TiO_2 powders on the decolourisation of humic acids," *Journal of Photochemistry and Photobiology A*, vol. 148, no. 1–3, pp. 121–128, 2002.

[43] N. San, A. Hatipoğlu, G. Koçtürk, and Z. Çınar, "Photocatalytic degradation of 4-nitrophenol in aqueous TiO_2 suspensions: theoretical prediction of the intermediates," *Journal of Photochemistry and Photobiology A*, vol. 146, no. 3, pp. 189–197, 2002.

[44] G. Palmisano, V. Loddo, V. Augugliaro, L. Palmisano, and S. Yurdakal, "Photocatalytic oxidation of nitrobenzene and phenylamine: pathways and kinetics," *AIChE Journal*, vol. 53, no. 4, pp. 961–968, 2007.

Research Article

Synthesis and Characterization of Mn–C–Codoped TiO$_2$ Nanoparticles and Photocatalytic Degradation of Methyl Orange Dye under Sunlight Irradiation

Wei Xin, Duanwei Zhu, Guanglong Liu, Yumei Hua, and Wenbing Zhou

Laboratory of Plant Nutrition and Ecological Environment Research,
Centre for Microelement Research of Huazhong Agricultural University, Wuhan 430070, China

Correspondence should be addressed to Guanglong Liu, liugl0924@hotmail.com

Novel visible-light-active Mn–C–TiO$_2$ nanoparticles were synthesized by modified sol-gel method based on the self-assembly technique using polyoxyethylenes orbitan monooleate (Tween 80) as template and carbon precursor and manganese acetate as manganese precursor. The samples were characterized by XRD, FTIR, UV-vis diffuse reflectance, XPS, and laser particle size analysis. The XRD results showed that Mn–C–TiO$_2$ sample exhibited anatase phase and no other crystal phase was identified. High specific surface area, small crystallite size, and small particle size distribution could be obtained by manganese and carbon codoped and Mn–C–TiO$_2$ exhibited greater red shift in absorption edge of samples in visible region than that of C–TiO$_2$ and pure TiO$_2$. The photocatalytic activity of synthesized catalyst was evaluated by photocatalytic oxidation of methyl orange (MO) solution under the sunlight irradiation. The results showed that Mn–C–TiO$_2$ nanoparticles have higher activity than other samples under sunlight, which could be attributed to the high specific surface area, smaller particle size, and lower band gap energy.

1. Introduction

Photocatalytic degradation of toxic organic compounds has received a great attention for the past several years. Due to its strong oxidizing powder, being cost effective, and long-term stability against photo- and chemical corrosion, TiO$_2$ has been widely used in water purification technology [1–4]. However, the practical applications of TiO$_2$ are limited by its large band gap (3.2 eV), which can be only active under the UV light irradiation [5–7]. Therefore, several strategies have been developed to shift the optical sensitivity of TiO$_2$ from UV to the visible-light region for the efficient use of solar energy, such as element doping, metal deposition, surface sensitization, and couping of composite semiconductors [8]. Recently, C, N, F, S anion-doped TiO$_2$ photocatalysts that show a relatively high level of activity under visible-light irradiation have been reported [9]. These nonmetal elements have been proved to be beneficial dopants in the TiO$_2$ via mixing their p orbital of nonmetal with O 2p orbital to reduce the band gap energy of TiO$_2$. The doping of various transitional metal ions into TiO$_2$ could shift its optical absorption edge from UV into visible-light range, but a prominent change in TiO$_2$ band gap has not been observed [10]. This red shift in metal doped TiO$_2$ was attributed to the charge-transfer transition between the d electrons of the dopant and the conduction band (CB) of TiO$_2$ [11]. However, transition metal-doped TiO$_2$ suffers from some serious drawbacks, such as thermal instability and low quantum efficiency. In order to further improve the photocatalytic activity, codoped titania with double nonmetal [12, 13], metal-nonmetal elements [14–16], and double metal ions [17, 18] have attracted more attention. Some studies demonstrated that the codoping with transition metal and nonmetal elements could effectively modify the electronic structures of TiO$_2$ and shift its absorption edge to a low energy [16]. However, to the best of our knowledge, the preparation of manganese and carbon codoped titania has never been reported.

In addition, the structural properties of TiO$_2$, such as crystalline phase, crystallite size, surface area, and pore distribution, are important for its photocatalytic properties.

Recently, the use of self-assembly surfactant-based sol-gel methods has been reported as an effective approach to tailor-design the structural properties of TiO$_2$ nanoparticles from molecular precursors [19–22]. High surface area, high porosity, small crystal size, and narrow pore size distribution of TiO$_2$ could be obtained by a sol-gel method with hydrocarbon surfactants added. Specifically, these hydrocarbon surfactants can serve as a nonmetal doping precursor to increase the photocatalytic activity of TiO$_2$ under visible-light irradiation [23].

Therefore, in this work, nonionic surfactant Tween 80 was used as a pore template and carbon doping reagent in the sol-gel method to synthesize visible-light-active Mn–C–TiO$_2$ nanoparticles and the Mn–C–TiO$_2$ nanoparticles were described for their application in degrading organic dyes. Methyl orange (MeO), a typical azo dye, was used as the target pollutant in aqueous media to assess the photocatalytic activities of the Mn–C–TiO$_2$ nanoparticles. The capacities in the photocatalytic activities of the Mn–C–TiO$_2$ nanoparticles under sunlight irradiation were studied; the influence of calcinations temperature on the photocatalytic activities of composites and degradation pathway of pollutant were also discussed.

2. Materials and Methods

2.1. Synthesis of Visible-Light-Activated Mn–C–TiO$_2$ Nanoparticles. Mn–C–TiO$_2$ was prepared by the self-assembly surfactant-based sol-gel method under mild conditions as follow. A nonionic surfactant Tween 80 (T80, polyoxyethylenes orbitan monooleate, Guoyao Chemical Co.) was employed as the pore directing agent and carbon precursor in the modified sol-gel solution. 5 mL T80 was dissolved in 20 mL isopropyl alcohol (i–PrOH, 99.8%, Guoyao Chemical Co.) and then 3 mL titanium tetraisopropoxide (TTIP, 97%, Sigma-Aldrich) was added under vigorous stirring. Finally, 3 mL acetic acid (AcOH, Guoyao Chemical Co.) was added into the solution for the formation of water in the mixture. The sol-gel was aged at 65°C for 24 hrs. To synthesize particles, the sol was dried at room temperature for 3 hrs and then calcined at 400°C for 3 hrs. For comparison, pure titania, C-doped TiO$_2$, and Mn-doped TiO$_2$ were prepared though the same method, without adding the corresponding dopants.

2.2. Characterization of Synthesized Mn–C–TiO$_2$ Nanoparticles. To study the crystal structure and crystallinity of the Mn–C–TiO$_2$ nanoparticles, X-ray diffraction (XRD) analysis was performed on X'Pert PRO (D8 Advance) XRD diffractometer using Cu Kα (λ = 1.5406 Å) radiation. The particle diameter distribution of the samples was measured by particle diameter analyzer (Ankersmid Ltd.). Fourier transform infrared (FT-IR) spectroscopy was carried out using Thermo Scientific Nicolet 6700 spectrometer to detect the presence of carbon group on the samples. Measurement range was 4000–400 cm^{-1}, with a 4 cm^{-1} resolution, 0.475 cm^{-1}/s scan speed, and 32 scans. The technique applied was attenuated total reflectance (ATR) with an Avatar multibounce HATR accessory with ZnSe crystal at 45°. To investigate the light absorption and optical band gap of the synthesized TiO$_2$ nanoparticles, the UV-vis absorption spectra were obtained with a UV-vis spectrophotometer (Shimadzu 2450 PC) mounted with an integrating sphere accessory (ISR1200) using BaSO$_4$ as reference standard. An X-ray photoelectron spectroscope (XPS, PerkinElmer Model 5300) was employed to establish the nature of boron in the prepared manganese oxides by determining the binding energy with respect to Mn and C. The conditions of the equipment include a takeoff angle of 45° and vacuum pressure of 10^{-8} to 10^{-9} Torr. The binding energies were referenced to the C 1s peak at 284.6 eV.

2.3. Photocatalytic Evaluation with Methyl Orange under Visible Light. After synthesis and characterization, the Mn–C–TiO$_2$ nanoparticles were tested under sunlight irradiation for the degradation of methyl orange in water. Firstly, a particles suspension (0.5 g/L) solution was prepared and dispersed using an ultrasonicator (2510R-DH, Bransonic) for 24 h. Secondly, 10 μL methyl orange solution (500 mg/L) was transferred to a 50 mL particles suspension placed in reactor to achieve an initial concentration of 500 μg/L. Finally, 50 μL HNO$_3$ (0.05 mol L^{-1}) was added into the solution. During irradiation with two fluorescent lamps (20 W, Cole-Parmer) imitating sunlight, the reactor was sealed with parafilm and continuously mixed to minimize mass transfer limitations and the schematic diagram of photochemical reactor is depicted in Figure 1. A 0.2 mL sample was withdrawn at time 0, 1, 2, 3, 4, and 5 h. The photocatalyst was immediately removed from the samples after centrifugation. The progress of photocatalytic degradation was monitored through measuring the characteristic absorbance of the solution samples by a UV-760CRT UV-Vis spectrophotometer (Shanghai Precision and Scientific Instrument Co., Ltd). The characteristic absorbance peaks were shown in Figure 2. Due to the acidic condition, the characteristic absorbance peaks shift from 460 to 517 nm. So, λ_{max} = 517 nm was chosen to measure the content of methyl orange left in the sample.

3. Results and Discussion

3.1. X-Ray Diffraction. The photocatalytic activity of catalyst was greatly affected by its crystal structure and crystal phase [24]. Generally, the anatase phase is reported with high photocatalytic activity. Therefore, the crystal structure and crystal phase characterization of pure TiO$_2$ is investigated by XRD. The XRD patterns of samples are shown in Figure 3. In TiO$_2$ sample, rutile phase was detected; however, only anatase TiO$_2$ crystal phase could be identified in C–TiO$_2$ and Mn–C–TiO$_2$ samples and no other dopant related crystal phases could be resolved. The intensity of anatase diffraction peaks for the Mn–C–TiO$_2$ and C–TiO$_2$ samples decreased slightly as the T80 adding. This is probably due to the fact that the T80 suppresses the hydrolysis of titanium alkoxide and the rapid crystallization of the TiO$_2$ particles by adsorbing on the TiO$_2$ particle surface [25]. The average crystalline size calculated by applying the Scherrer formula on
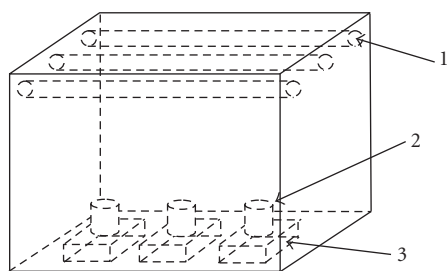
FIGURE 1: Schematic diagram of photocatalytic reactor. 1: fluorescent tube (20 W); 2: quartz petri dishes (diameter: 4.5 cm; height: 12 cm); 3: magnetic stirrers.
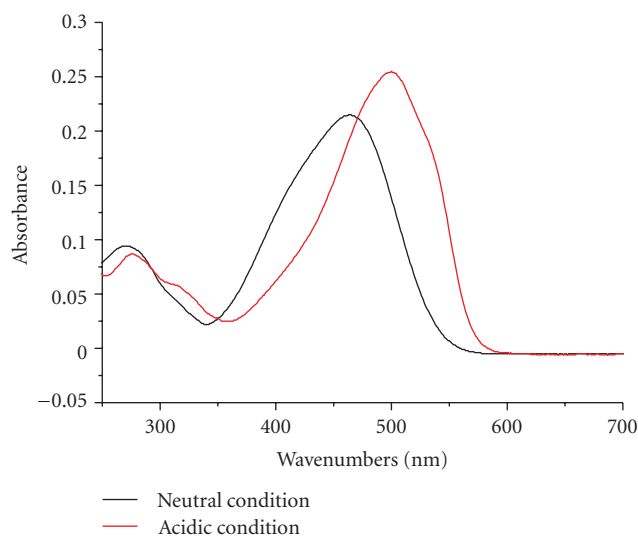
FIGURE 2: UV-vis spectra of methyl orange under neutral condition and acidic condition.

FIGURE 3: XRD patterns of as-prepared samples (A: anatase).

the anatase (101) diffraction peak was 37.23, 16.22, and 16.37 nm for the pure TiO_2, $C–TiO_2$, and $Mn–C–TiO_2$ samples, respectively, which is decreased as the surfactant used, since surfactant reduces the rate of titanium alkoxide hydrolysis and condensation of TiO_2 leading to smaller crystal size [26].

3.2. Particle Size Distribution. The particle diameter distribution of the pure TiO_2, $C–TiO_2$, and $Mn–C–TiO_2$ samples is shown in Figure 4. From the laser particle size analysis results, the mean particle diameter of the pure TiO_2, $C–TiO_2$, and $Mn–C–TiO_2$ samples is 80.46, 50.82, and 31.22 μm, respectively. The mean particle diameter also decreased with carbon and manganese doped, which may be associated with the role of the surfactant in the preparation process that decreases the polarity of titanium oxide (titania) and reduces the aggregation of the particles [26].

3.3. FT-IR Analysis. To give additional evidence and further to confirm the doping of manganese and carbon, FT-IR characterizations were performed. The infrared spectroscopy of pure TiO_2, $C–TiO_2$, and $Mn–C–TiO_2$ samples are presented

in Figure 5. The bands at 1640 cm^{-1} and the wide bands at 3100–3700 cm^{-1} is resultant from O–H stretching of adsorbed water molecules and the surface hydroxyl groups on TiO_2 have been recognized to play an important role in the photocatalytic process, as these groups can inhibit the recombination of photogeneration charges and interact with photogenerated holes to product reactive oxygen species [27]. The bands at 2330 cm^{-1} are assigned to the stretching vibrations of the C=O bonds. Compared with pure TiO_2 sample, we can infer that the C=O bonds in the $C–TiO_2$ and $Mn–C–TiO_2$ samples could be attributed to the T80 used in the sol. In the region below 1000 cm^{-1}, this peak was ascribed to absorption bands of Mn–O, which could be inferred that some manganese oxide may appear on the surface of TiO_2 nanoparticles [28].

3.4. UV-Vis Diffuse Reflectance Spectra. It is well know that the photocatalytic activity of a semiconductor is related to its band gap structure. Figure 6 shows the UV-vis absorption spectra of the pure TiO_2, $C–TiO_2$, and $Mn–C–TiO_2$ samples. The typical onset of absorption near 380 nm can be assigned to the intrinsic band gap absorption of TiO_2 [29]. It can be seen that there is a significant shift in the onset absorption toward the higher wavelength for the $Mn–C–TiO_2$ and $C–TiO_2$ sample. Specially, the codoped sample exhibits a greater red shift than $C–TiO_2$ sample which demonstrated that $Mn–C–TiO_2$ sample can greatly improve the absorption of visible light. The reason may be due to the new electronic state in the middle of the TiO_2 band gap, charge-transfer transition between the d electrons of the dopant and the CB of TiO_2, and the narrowed band gap resulted by C-doping, allowing visible light absorption [30]. It has been reported that nonmetal elements could reduce the band gap energy of TiO_2 by mixing their p orbital of nonmetal with O 2p orbital and the doping of various transitional metal ions into TiO_2 could shift its optical absorption edge from UV to visible-light range without a prominent change in TiO_2 band

(a)

(b)

(c)
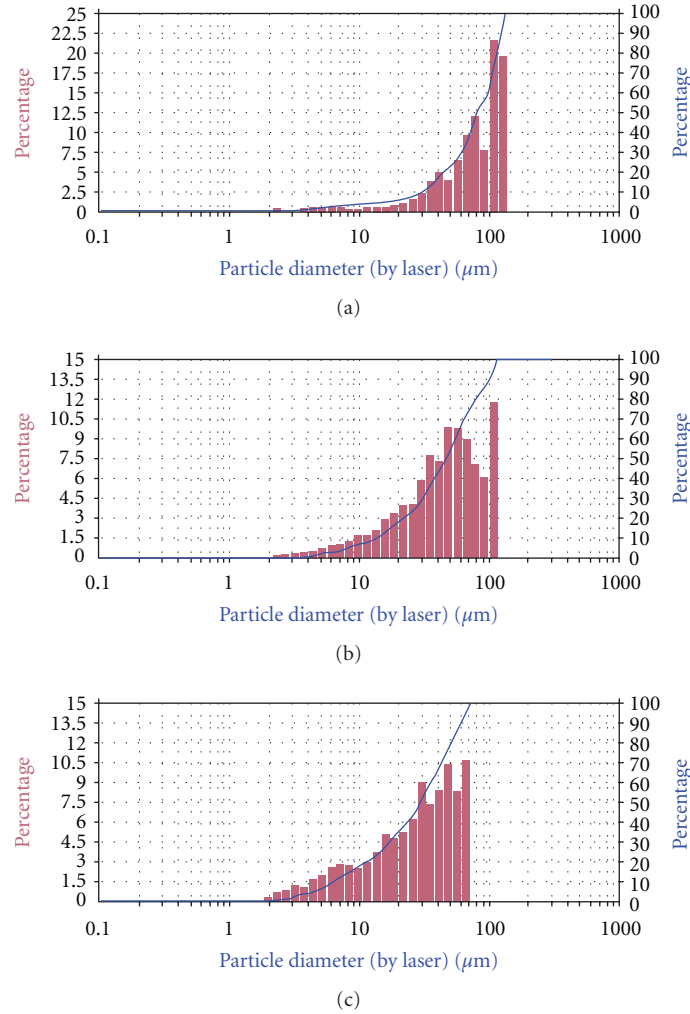
FIGURE 4: Particle size distribution of TiO$_2$, C–TiO$_2$, and Mn–C–TiO$_2$.
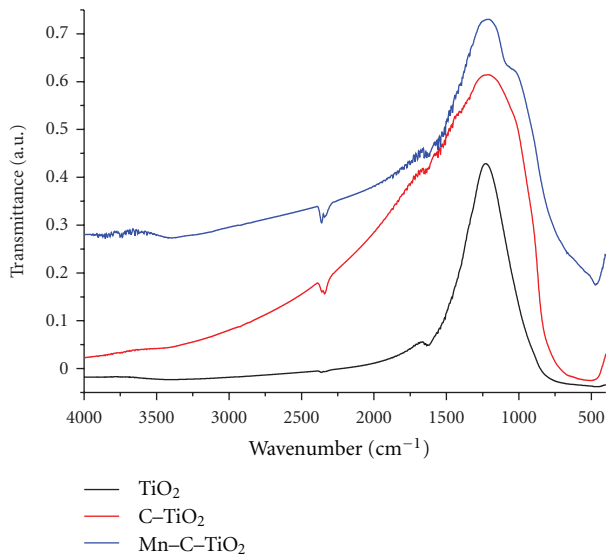
FIGURE 5: FT-IR spectra of TiO$_2$, C–TiO$_2$, and Mn–C–TiO$_2$.

gap [31]. However, the Mn–C doping TiO$_2$ samples showed smallest band gap energy in three kinds of samples shown in Figure 6(b). The direct band gap energy of Mn–C–TiO$_2$ sample was 2.6 eV, smaller than C–TiO$_2$ sample (3.0 eV) and pure TiO$_2$ sample (anatase, Ca. 3.2 eV). This result further approved the substitution of crystal lattice O or Ti to dopant species The enhanced ability to absorb visible light makes this Mn–C–TiO$_2$ an effective photocatalyst for solar-driven application.

3.5. XPS Spectra. XPS spectra showed further information on the structure of Mn–C–TiO$_2$. **Figure 7(a)** shows the high-resolution Mn 2p XPS spectra of Mn–C–TiO$_2$. The two Mn 2p peaks at the binding energy of 640.5 and 653.0 eV indicate the existence of MnO$_2$. The C 1s XPS spectra of Mn–C–TiO$_2$ were shown in **Figure 7(b)**. Three broad but well-separated peaks were observed in the C 1s binding region at 281.3, 284.6, and 288.2 eV for the as-synthesized carbon-doped titania, but only one peak at 284.6 eV for pure titania (data not shown), which arises from adventitious elemental
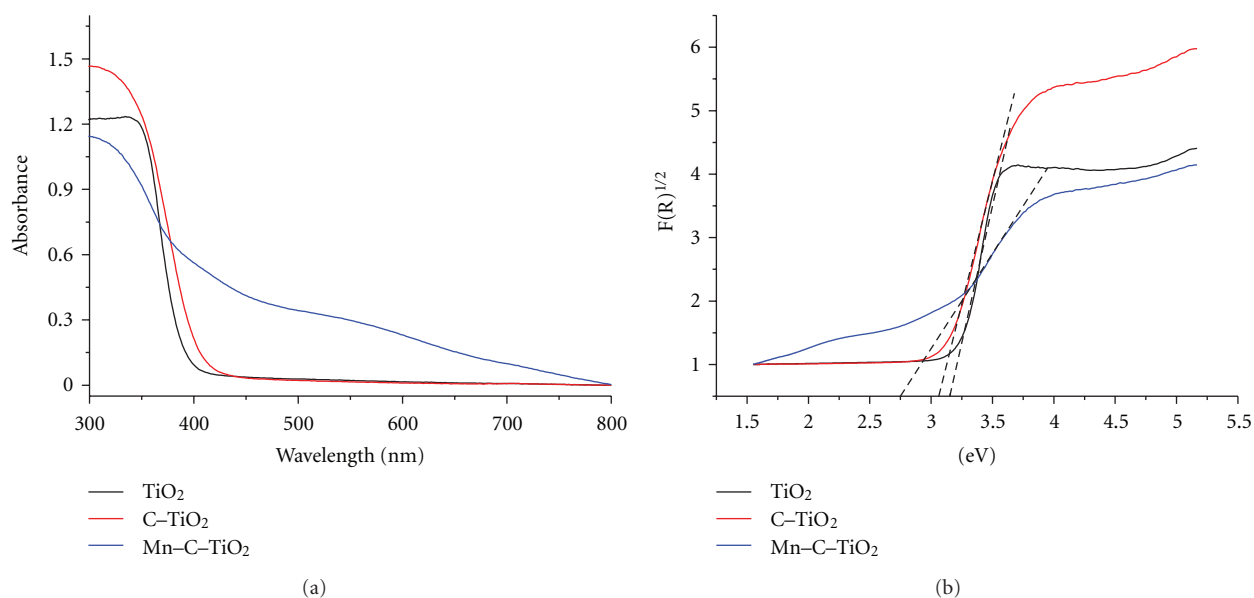
FIGURE 6: Optical properties of TiO_2, $C–TiO_2$, and $Mn–C–TiO_2$.
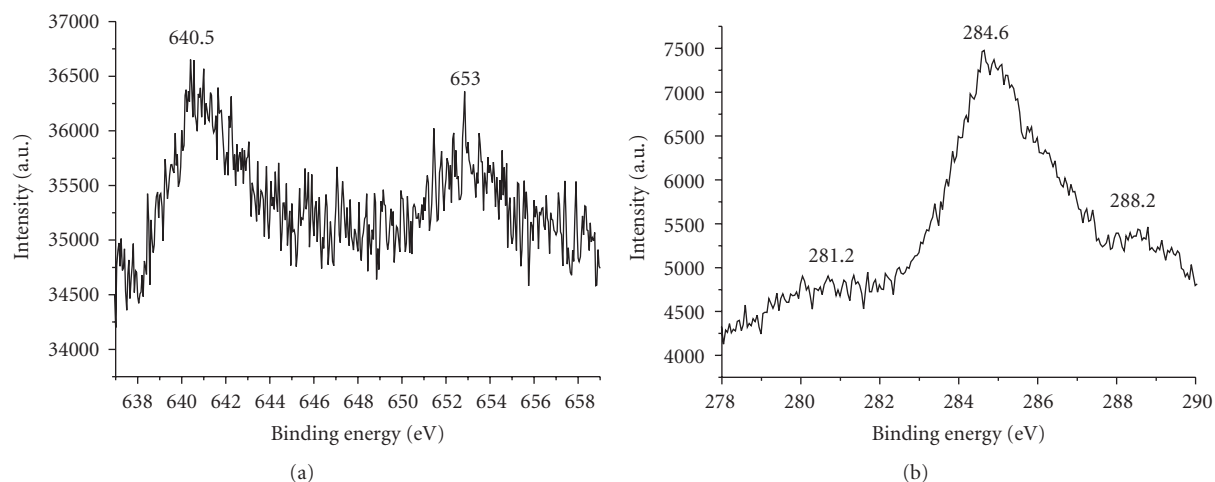
FIGURE 7: XPS spectra of codoped TiO_2 nanotube arrays. (a) A spectrum of Mn 2p; (b) a spectrum of C 1s.

carbon. The peak at the lower binding energy has been accordingly assigned to the formation of Ti–C bonds in $C–TiO_2$ in the previous reported [32]. The highest C 1s energy peak at 288.2 has been accordingly interpreted as the distinct feature of C–O bond formation in $C–TiO_2$ that in principle arises from interstitial and/or substitutional (for Ti) C atoms, while the underlying carbonate species have been considered as the source of the extended optical absorption tail of $C–TiO_2$ in the visible range [32]. In the present case, the coexistence of the 281.3 and 288.2 eV C 1s peaks corresponding to the binding energies of Ti–C and C–O bonds indicates both the presence of interstitial C atoms as well as carbon substitution for O and Ti atoms in the titania lattice [33].

3.6. *Photocatalytic Activity of Samples in Photodegradation of $Mn–C–TiO_2$*. To evaluate and compare the visible-light photocatalytic activity of the $Mn–C–TiO_2$ sample, the reactions of methyl orange degradation were preformed as photoreaction probes under the sunlight irradiation. In order to identify possible losses of methyl orange in the reactor system, control experiments without catalyst added were preformed. The course of methyl orange photocatalytic degradation used as catalyst pure TiO_2, $C–TiO_2$, and $Mn–C–TiO_2$ as well as control experiment is given in Figure 8. It was found that no obvious methyl orange loss was observed in control experiment which confirmed that the methyl orange was stable in our experiment. When adding the synthesized catalyst, it was seen from the figure that $Mn–C–TiO_2$ sample
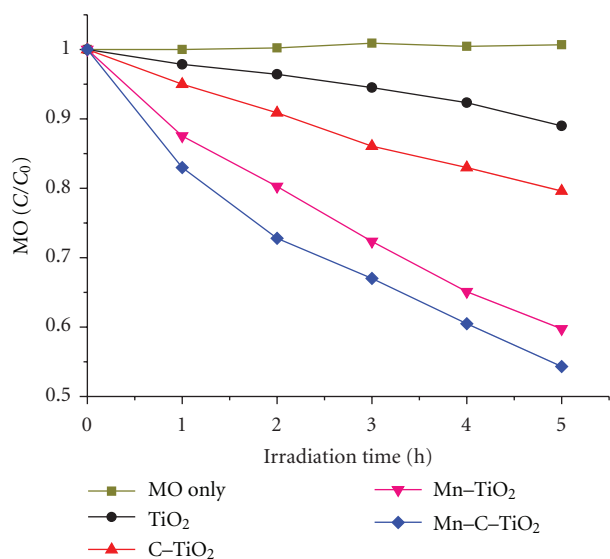
FIGURE 8: Photocatalytic degradation of MO with as-prepared samples.

exhibited higher photoactivity than that of pure TiO_2 and $C–TiO_2$ samples after 5 h irradiation under the sunlight. For pure TiO_2 sample, the degradation phenomenon could be attributed to the adsorption and photocatalytic degradation induced by trace UV light in the reaction system. In the Mn–$C–TiO_2$ system, the excellent photocatalytic activity could partially be due to its high specific surface area, smaller crystallite size, and lower band gap energy.

4. Conclusions

The manganese and carbon codoped TiO_2 nanoparticles as a novel catalyst were successfully prepared by surfactant-based sol-gel methods under mild conditions. For comparison, carbon doped TiO_2 and pure TiO_2 were also prepared by the same method without adding the corresponding dopants. Detailed characterization of the materials physicochemical properties by XRD and laser particle size analysis showed that the $C–TiO_2$ nanomaterials crystallize in the anatase phase with high specific surface area and small particle size distribution. Significant shift of the optical absorption edge toward the visible region was detected for the Mn–$C–TiO_2$ nanoparticles and much higher photocatalytic activity than that of $C–TiO_2$ and pure TiO_2 for methyl orange degradation in water was demonstrated under sunlight irradiation.

Acknowledgments

References

[1] A. Naldoni, M. Allieta, S. Santangelo et al., "Effect of nature and location of defects on bandgap narrowing in black TiO_2 nanoparticles," *Journal of the American Chemical Society*, vol. 134, no. 18, pp. 7600–7603, 2012.

[2] J. Yu, M. Jaroniec, and G. Lu, "TiO_2 photocatalytic materials," *International Journal of Photoenergy*, vol. 2012, Article ID 206183, 5 pages, 2012.

[3] S. K. Choi, S. Kim, S. K. Lim, and H. Park, "Photocatalytic comparison of TiO_2 nanoparticles and electrospun TiO_2 nanofibers: effects of mesoporosity and interparticle charge transfer," *Journal of Physical Chemistry C*, vol. 114, no. 39, pp. 16475–16480, 2010.

[4] L. Yang, X. Jiang, W. Ruan et al., "Charge-transfer-induced surface-enhanced raman scattering on Ag-TiO_2 nanocomposites," *Journal of Physical Chemistry C*, vol. 113, no. 36, pp. 16226–16231, 2009.

[5] J. Qian, G. Cui, M. Jing, Y. Wang, M. Zhang, and J. Yang, "Hydrothermal synthesis of nitrogen-doped titanium dioxide and evaluation of its visible light photocatalytic activity," *International Journal of Photoenergy*, vol. 2012, Article ID 198497, 6 pages, 2012.

[6] M. Zhou, J. Zhang, B. Cheng, and H. Yu, "Enhancement of visible-light photocatalytic activity of mesoporous Au-TiO_2 nanocomposites by surface plasmon resonance," *International Journal of Photoenergy*, vol. 2012, Article ID 532843, 10 pages, 2012.

[7] M. Zhou and J. Yu, "Preparation and enhanced daylight-induced photocatalytic activity of C,N,S-tridoped titanium dioxide powders," *Journal of Hazardous Materials*, vol. 152, no. 3, pp. 1229–1236, 2008.

[8] S. G. Kumar and L. G. Devi, "Review on modified TiO_2 photocatalysis under UV/visible light: selected results and related mechanisms on interfacial charge carrier transfer dynamics," *The Journal of Physical Chemistry A*, vol. 115, no. 46, pp. 13211–13241, 2011.

[9] X. Cheng, X. Yu, Z. Xing, and L. Yang, "Enhanced visible light photocatalytic activity of mesoporous anatase TiO_2 codoped with nitrogen and chlorine," *International Journal of Photoenergy*, vol. 2012, Article ID 593245, 6 pages, 2012.

[10] V. C. Papadimitriou, V. G. Stefanopoulos, M. N. Romanias et al., "Determination of photo-catalytic activity of un-doped and Mn-doped TiO_2 anatase powders on acetaldehyde under UV and visible light," *Thin Solid Films*, vol. 520, no. 4, pp. 1195–1201, 2011.

[11] J. C. S. Wu and C. H. Chen, "A visible-light response vanadium-doped titania nanocatalyst by sol-gel method," *Journal of Photochemistry and Photobiology A*, vol. 163, no. 3, pp. 509–515, 2004.

[12] X. Li, R. Xiong, and G. Wei, "S-N Co-doped TiO_2 photocatalysts with visible-light activity prepared by sol-gel method," *Catalysis Letters*, vol. 125, no. 1-2, pp. 104–109, 2008.

[13] L. Lin, R. Y. Zheng, J. L. Xie, Y. X. Zhu, and Y. C. Xie, "Synthesis and characterization of phosphor and nitrogen co-doped titania," *Applied Catalysis B*, vol. 76, no. 1-2, pp. 196–202, 2007.

[14] C. Liu, X. Tang, C. Mo, and Z. Qiang, "Characterization and activity of visible-light-driven TiO_2 photocatalyst codoped with nitrogen and cerium," *Journal of Solid State Chemistry*, vol. 181, no. 4, pp. 913–919, 2008.

[15] K. Obata, H. Irie, and K. Hashimoto, "Enhanced photocatalytic activities of Ta, N co-doped TiO_2 thin films under visible light," *Chemical Physics*, vol. 339, no. 1–3, pp. 124–132, 2007.

[16] X. Yang, C. Cao, K. Hohn et al., "Highly visible-light active C- and V-doped TiO_2 for degradation of acetaldehyde," *Journal of Catalysis*, vol. 252, no. 2, pp. 296–302, 2007.

[17] D. R. Zhang, Y. H. Kim, and Y. S. Kang, "Synthesis and characterization of nanoparticle of TiO_2 co-doped with Sc^{3+} and V^{5+} ions," *Current Applied Physics*, vol. 6, no. 4, pp. 801–804, 2006.

[18] R. Khan, S. W. Kim, T. J. Kim, and C. M. Nam, "Comparative study of the photocatalytic performance of boron-iron Co-doped and boron-doped TiO_2 nanoparticles," *Materials Chemistry and Physics*, vol. 112, no. 1, pp. 167–172, 2008.

[19] H. Choi, E. Stathatos, and D. D. Dionysiou, "Photocatalytic TiO_2 films and membranes for the development of efficient wastewater treatment and reuse systems," *Desalination*, vol. 202, no. 1–3, pp. 199–206, 2007.

[20] Y. Chen, E. Stathatos, and D. D. Dionysiou, "Microstructure characterization and photocatalytic activity of mesoporous TiO_2 films with ultrafine anatase nanocrystallites," *Surface and Coatings Technology*, vol. 202, no. 10, pp. 1944–1950, 2008.

[21] H. Choi, E. Stathatos, and D. D. Dionysiou, "Synthesis of nanocrystalline photocatalytic TiO_2 thin films and particles using sol-gel method modified with nonionic surfactants," *Thin Solid Films*, vol. 510, no. 1-2, pp. 107–114, 2006.

[22] H. Choi, A. C. Sofranko, and D. D. Dionysiou, "Nanocrystalline TiO_2 photocatalytic membranes with a hierarchical mesoporous multilayer structure: synthesis, characterization, and multifunction," *Advanced Functional Materials*, vol. 16, no. 8, pp. 1067–1074, 2006.

[23] H. Choi, M. G. Antoniou, M. Pelaez, A. A. De La Cruz, J. A. Shoemaker, and D. D. Dionysiou, "Mesoporous nitrogen-doped TiO_2 for the photocatalytic destruction of the cyanobacterial toxin microcystin-LR under visible light irradiation," *Environmental Science and Technology*, vol. 41, no. 21, pp. 7530–7535, 2007.

[24] M. Pelaez, A. A. de la Cruz, E. Stathatos, P. Falaras, and D. D. Dionysiou, "Visible light-activated N-F-codoped TiO_2 nanoparticles for the photocatalytic degradation of microcystin-LR in water," *Catalysis Today*, vol. 144, no. 1-2, pp. 19–25, 2009.

[25] P. D. Cozzoli, A. Kornowski, and H. Weller, "Low-temperature synthesis of soluble and processable organic-capped anatase TiO_2 nanorods," *Journal of the American Chemical Society*, vol. 125, no. 47, pp. 14539–14548, 2003.

[26] G. Liu, C. Han, M. Pelaez et al., "Synthesis, characterization and photocatalytic evaluation of visible light-activated C-doped TiO_2," *Nanotechnology*, vol. 23, 10 pages, 2012.

[27] Y. Huang, W. K. Ho, S. C. Lee, L. Z. Zhang, X. X. Fan, and Z. G. Zou, "Synthesis, characterization and photocatalytic evaluation of visible light-activated C-doped TiO_2," *Langmuir*, vol. 24, no. 7, pp. 3510–3516, 2008.

[28] G. Liu, S. Liao, D. Zhu, J. Cui, and W. Zhou, "Solid-phase photocatalytic degradation of polyethylene film with manganese oxide OMS-2," *Solid State Sciences*, vol. 13, no. 1, pp. 88–94, 2011.

[29] A. I. Kontos, A. G. Kontos, Y. S. Raptis, and P. Falaras, "Nitrogen modified nanostructured titania: electronic, structural and visible-light photocatalytic properties," *Physica Status Solidi*, vol. 2, no. 2, pp. 83–85, 2008.

[30] M. Hamadanian, A. Reisi-Vanani, M. Behpour, and A. S. Esmaeily, "Synthesis and characterization of Fe, S-codoped TiO_2 nanoparticles: application in degradation of organic water pollutants," *Desalination*, vol. 281, pp. 319–324, 2011.

[31] S. Liu, J. Yu, B. Cheng, and M. Jaroniec, "Fluorinated semiconductor photocatalysts: tunable synthesis and unique properties," *Advances in Colloid and Interface Science*, vol. 173, pp. 35–53, 2012.

[32] J. Yu, G. Dai, Q. Xiang, and M. Jaroniec, "Fabrication and enhanced visible-light photocatalytic activity of carbon self-doped TiO_2 sheets with exposed {001} facets," *Journal of Materials Chemistry*, vol. 21, no. 4, pp. 1049–1057, 2011.

[33] G. Liu, C. Han, M. Pelaez et al., "Synthesis, characterization and photocatalytic evaluation of visible light-activated C-doped TiO_2," *Nanotechnology*, vol. 23, no. 29, Article ID 294003, 10 pages, 2012.

Research Article

Photocatalytic Performance of ZnO: Al Films under Different Light Sources

Prashant Pradhan, Juan Carlos Alonso, and Monserrat Bizarro

Instituto de Investigaciones en Materiales, Universidad Nacional Autónoma de México, A.P. 70-360, Coyoacán 04510, DF, Mexico

Correspondence should be addressed to Monserrat Bizarro, monserrat@iim.unam.mx

ZnO and Al doped ZnO films were produced by spray pyrolysis. The films were characterized by X-ray diffraction (XRD), scanning electron microscopy (SEM), UV-vis spectroscopy, and photoluminescence. Their photocatalytic activity was evaluated by the decomposition of the methyl orange dye using different light sources: ultraviolet light, artificial white light, and direct sunlight. The films were also tested under darkness for comparison. The ZnO films were able to degrade the test pollutant under UV and sunlight in more than a 60% after 180 min of irradiation and a scarce degradation was obtained using white light. However, the Al doped ZnO films presented a very high degradation rate not only under UV and sunlight (100% degradation), but also under white light (90% degradation after the same irradiation time). An unexpected high degradation was also obtained in the dark, which indicates that a nonphotonic process is taking place parallel to the photocatalytic process. This can be due to the extra electrons—provided by the aluminum atoms—that migrate to the surface and produce $O_2^{\bullet-}$ radicals favoring the decomposition process even in the dark. The high activity achieved by the ZnO: Al films under natural conditions can be potentially applied to water treatment processes.

1. Introduction

Metal oxide photocatalysts are being considered as an effective alternative to decompose toxic organic pollutants in waste water [1]. TiO$_2$ and ZnO are two examples of efficient photocatalyst; nevertheless, both of them are activated only under UV light due to their large band gap of 3.2 eV [2, 3]. The big challenge of the last few years has been to extend the photocatalytic activity of these semiconductors to the visible region of the solar spectrum, since solar energy is the most desired light source for a clean and efficient photocatalytic system. If this goal is achieved, the use of photocatalysts for environmental remediation will be even more important and will contribute to the reduction of the excessive use of nonrenewable energy sources. The principal way to address the problem of extending the spectral range in which the photocatalyst can absorb light has been introducing electrically active dopants in these oxide semiconductors. For the case of photocatalysts in the form of fine powders or nanoparticles, good photocatalytic activity under visible light has been obtained by doping TiO$_2$ with metal or nonmetal atoms like nitrogen, carbon, iron, manganese, and cobalt among others [4–12]. In the case of zinc oxide, which is an alternative photocatalyst to TiO$_2$, with a similar band gap but with lower cost [13], it has been demonstrated that ZnO powders or nanoparticles doped with atoms such as Mn, N, Fe, W, La, and Ag possess also very good photocatalytic properties under visible light [14–20]. For water treatment application the powder and nanoparticles represent a drawback, as further separation steps are needed after the degradation process. This is the motivation to obtain supported ZnO in the form of thin films or membranes that can be removed easily after the water treatment. For instance, Liu and coworkers synthesized hierarchical CuO/ZnO membranes able to degrade different dyes [21]. In a previous work, we demonstrated that aluminum doped zinc oxide in the form of thin film highly increase the photocatalytic activity of pure ZnO under UV light [22]. As it

was pointed out in that work, one important advantage of using this material in the form of thin film, instead of fine powders or nanoparticles, is the elimination of filtration and separation steps after the dye removal. In that work, we observed that the activity enhancement under UV light can be due to factors such as the surface structure, the doping concentration, and the electronic distribution. However, it is important to study the mechanisms that allow the activation of the material with lower energy, in order to have an efficient ecological photocatalyst. In the present work we investigated the photocatalytic response, extended to the visible region, of ZnO: Al films using different illumination sources (sunlight and white light) compared to its activity under UV light. We also report an unexpected activity of the doped samples in the dark. A correlation of the photocatalytic activity with other physical properties, such as the band gap and photo-luminescence emission, is explored.

2. Experimental Setup

Pure and aluminum doped ZnO films were deposited by the pneumatic spray pyrolysis technique using a 0.2 M aqueous solution of zinc acetate dihydrate ($Zn(CH_3COO)_2 \cdot 2H_2O$, Sigma-Aldrich, 98%). Aluminum chloride hexahydrate ($AlCl_3 \cdot 6H_2O$, Sigma-Aldrich, 99%) was added as a source of aluminum, in an (Al)/(Zn) atomic ratio of 0.25 to the previous solution. The films were grown at a substrate temperature of 500°C on pyrex glass substrates of 1×0.5 inches; two of these substrates were placed in each film deposition and constitute one sample as they were introduced back inside the vial for the photocatalytic tests. The gas and solution flow rates were fixed at 8 L/min and 14.6 mL/min respectively, as previously determined [22]. Four identical, samples of pure and Al doped ZnO were deposited, in order to perform the photocatalytic experiments under different illumination conditions simultaneously. The films were characterized by X-ray diffraction (XRD) (Bruker D8) using the Cu Kα_1 wavelength (1.54056 Å), scanning electron microscopy (SEM) (Leica Cambridge 400) with an energy dispersed spectroscopy device (EDS) for chemical composition analysis, profilometry (Sloan DekTak IIA), and photo-luminescence (SPEX FluoroMax).

The photocatalytic efficiency of the films was evaluated by monitoring the discoloration of a methyl orange (MO) solution (Sigma-Aldrich, 85% purity) with a concentration of 10^{-5} M, at the maximum absorption wavelength using a UV-vis spectrophotometer (Perkin Elmer Lambda 35). Each pair of samples (doped and undoped ZnO films) was exposed to different illumination sources: (i) ultraviolet light (UV) lamp of 9 W and emission centered at 380 nm; (ii) direct exposure to sunlight (the experiments were performed in mostly sunny days but regardless the small changes in the weather conditions of Mexico City at the geographical coordinates: $\varphi = 19° \ 21'$ N, $\lambda = 99° \ 09'$ W); (iii) artificial white light (WL) of a 9 W lamp (cool light type) with a broad emission in the visible spectrum from 400 to 650 nm. The fourth pair of samples was kept in the dark as control (the samples were stored in a box and kept in a dark room). The
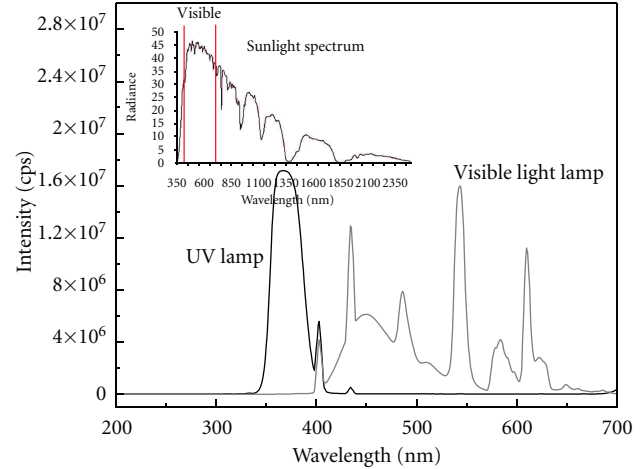
FIGURE 1: Emission spectra of the different illumination sources: (a) ultraviolet light (UV), (b) white light (WL), and (c) sunlight (inset).

emission spectra of the illumination sources were measured with a spectrofluorometer (SPEX FluoroMax) and are shown in Figure 1. The absorption spectra of the methyl orange solution were measured after each 30 minutes of illumination up to 3 hours. The degradation percentage of the dye was obtained with the absorbance maxima ratio of the methyl orange before (A_0) and after (A) an irradiation time, as follows:

$$\text{Degradation \%} = \left(1 - \frac{A}{A_0}\right) * 100. \tag{1}$$

3. Results

3.1. Microstructure and Composition. The characteristics of pure and Al doped films were analyzed in detail in a previous work [22]. It was observed that the deposition conditions have a great influence on the morphological characteristics of the films. Particularly, the surface topography is largely modified under certain temperature and flow rates conditions, and it also depends on the aluminum concentration in the precursor solution, as it can be appreciated in the SEM images inserted in Figure 2. It was also observed that the crystal structure was the wurtzite hexagonal phase of ZnO for all the samples (according to the International Centre for Diffraction Data, ICDD, database file 01-036-1451), with a preferential orientation along the (002) direction that increases with the aluminum concentration (Figure 2). No other phases or compounds were detected. However, the EDS analysis revealed the incorporation of the aluminum into the zinc oxide lattice, which is in a lower proportion than the aluminum added to the solution, as shown in Table 1. In addition, XPS analysis shows (Figure 3) that the incorporation of Al reduces the concentration of Zn in the ZnO: Al films, which is indicative that Al atoms substitute Zn atoms in the ZnO lattice.

The thickness and roughness of the films were measured and their average values are presented in Table 1. As it was said before, the incorporation of aluminum into the ZnO

TABLE 1: Composition of the films and their average thickness and roughness.

Sample name	Al/Zn in solution (at %)	Al/Zn in the film (at %)	Thickness (nm)	Roughness (nm)
ZnO	0	0	1114	65
ZnO : Al	25	0.12	2151	430
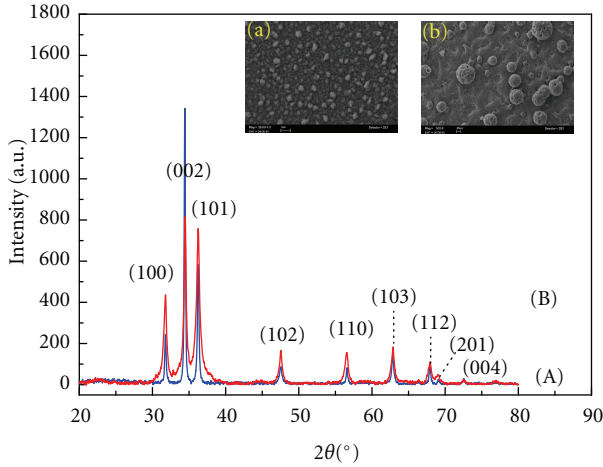
FIGURE 2: XRD patterns of pure (a) and Al doped (b) ZnO films. The insert shows the SEM images of their corresponding surfaces.
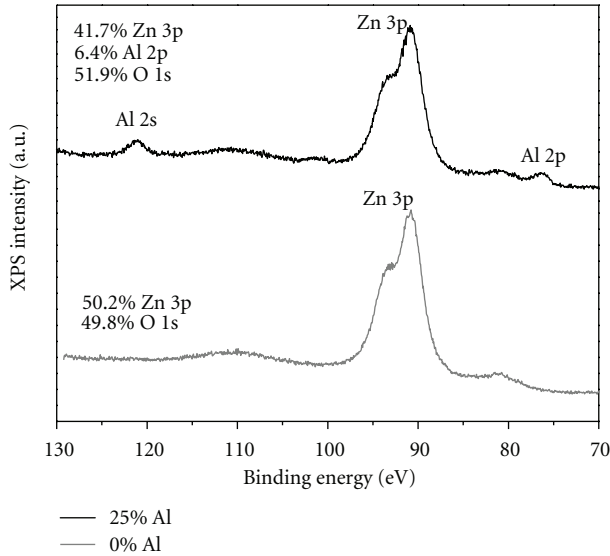
FIGURE 3: XPS spectra of the pure and Al doped ZnO films. The presence of aluminum decreased the concentration of Zn, indicating that Al is a substitutional impurity.

film produces morphological changes, but also the deposition rate is modified, so different thicknesses are obtained for similar flow rates.

3.2. Photocatalytic Activity.

The degradation of the methyl orange solution was measured using the pure and doped ZnO films under the three mentioned illumination sources. Figure 4(a) shows a picture taken of the different samples

exposed to sunlight after 2 hours. It is also shown a control sample without film that was irradiated and measured as well. No degradation of the methyl orange (MO) control sample was observed, but it is clearly seen that the complete discoloration of the dye is achieved faster for the sample doped with Al than for the pure ZnO film (Figure 4(b)).

To obtain the kinetics of the reactions, the natural logarithm of the maximum of absorption was obtained for each measurement and plotted as a function of time, as shown in Figure 4(c). The data follow a linear relation indicating a first-order reaction, as established by the Langmuir-Hinshelwood model [23]. The samples with aluminum showed the highest photocatalytic response. Surprisingly, this response was not only under illumination but also in the dark. Any effect was observed for the pure ZnO films under artificial white light or darkness; they could degrade the dye only under UV and sunlight. This is evidence that the aluminum impurities modify the original compound. The rates of reaction of every sample were calculated by the slope of the fitted lines in Figure 4(c) and are shown in Figure 4(d), where it is clearly seen that the activity of the doped films is more than 3 times greater than for the pure ZnO films under UV and sunlight illumination. In addition, a very high activity is observed for the ZnO: Al film in the dark. This indicates the existence of an alternative process that degrades the dye without light. This material offers a great alternative to purify water even at latitudes where low sunlight radiation is received.

In order to study the reproducibility and the reusability of the films, a complete set of new samples was fabricated and tested in photocatalysis. The repeated films provided similar results under the same conditions. In addition, the samples that were reused in the photocatalytic tests showed a small diminution of the activity (around 10%) that was more evident in the pure ZnO samples.

3.3. Optical Properties.

Although the films are relatively thick and their optical transparency is thus, low, their optical transmission spectra were recorded to obtain the absorption coefficient (α) and analyze the optical band gap of the films. To calculate the direct optical band gap of ZnO and ZnO: Al films the Tauc model was used as follows:

$$\alpha h\nu = A \left(h\nu - E_g \right)^n, \qquad (2)$$

where A is a constant, h is Planck's constant, ν is the photon frequency, E_g is the optical ban gap, and $n = 1/2$ for direct band gap semiconductors. A plot of $(\alpha h\nu)^2$ against the photon energy $h\nu$ is shown in Figure 5. The extrapolation of the linear part of the curve to zero gives the value of the optical band gap. The results show that the band gap is slightly higher for the doped films ($E_g = 3.25$ eV) than for the pure

(a)

(b)

(c)

(d)
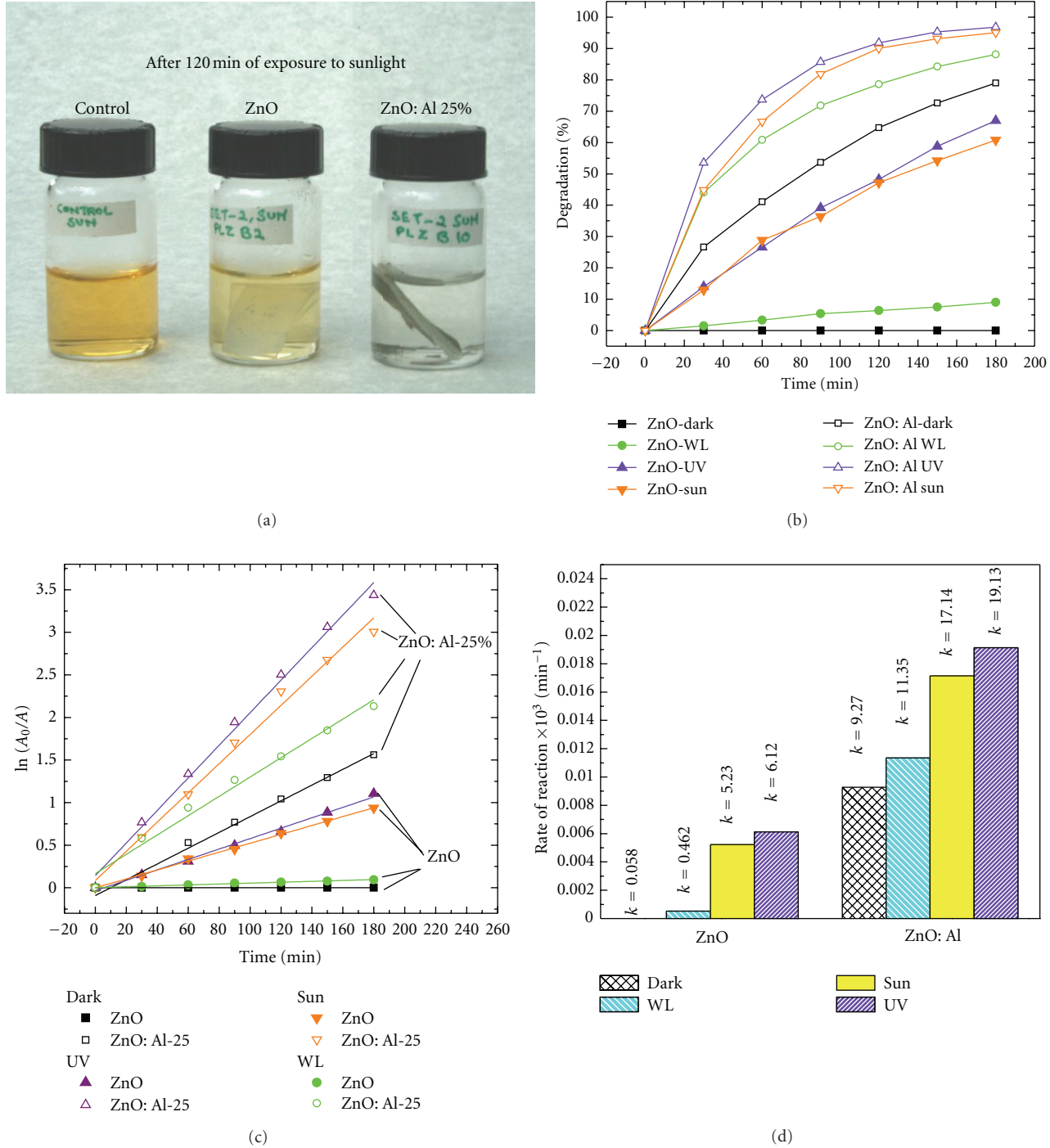
FIGURE 4: (a) Picture of the samples after 2 hours of exposure to sunlight. The control sample is the MO dye without film. The other two recipients contain the semiconductor film inside. (b) Degradation percentage and (c) kinetics of reaction of ZnO (filled symbols) and ZnO: Al (open symbols) under different illuminations: dark (black), artificial white light (green), ultraviolet light (purple), and sunlight (orange). (d) Rate of reaction of the ZnO and ZnO: Al films under different illumination sources and darkness for comparison.

ZnO films (3.22 eV). This increase in the ZnO band gap when aluminum is introduced is consistent with other works [24, 25] and may be due to the occupation of the lowest levels in the conduction band by the electrons of the impurity atoms and produce a direct transition with higher energy [26, 27].

The optical band gap values coincide with those obtained by room temperature photoluminescence spectra, shown in Figure 6. The spectra have a narrow peak centered at 383 and 381 nm (UV emission) for ZnO and ZnO: Al, respectively, which correspond to the band to band transitions (of 3.24 and 3.25 eV in each case), and a broad band centered
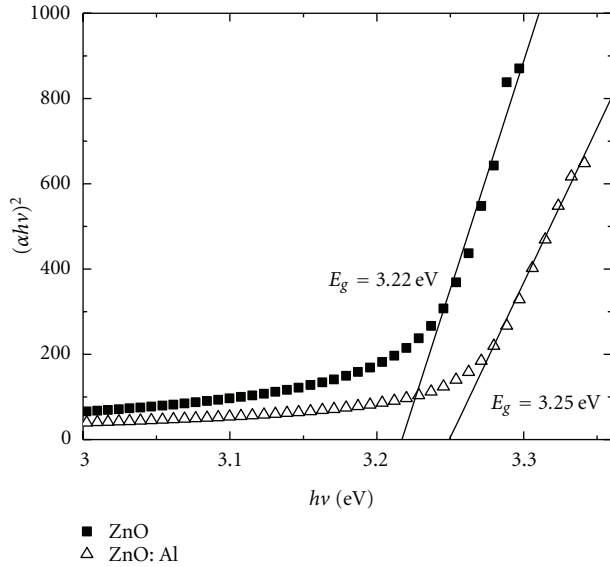
FIGURE 5: Determination of the band gap of ZnO and ZnO: Al films.
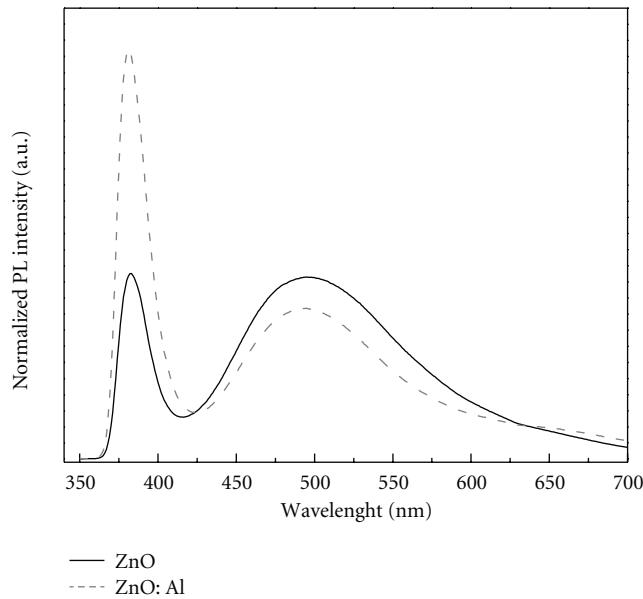
FIGURE 6: Normalized photoluminescence of ZnO and ZnO: Al films.

FIGURE 7: Schematic representation of defects in ZnO and ZnO: Al films. The red arrows indicate the diffusion of excess oxygen to the ZnO grain due to the presence of Al atoms.

around 500 nm called green emission. The green emission is attributed to structural defects in the crystalline lattice, although the type of defects responsible of this visible emission is not fully understood [28]. For the pure ZnO film, both peaks have the same intensity, indicating a similar probability of occurrence. However, for the doped film the intensity of the high energy peak increases and the green emission peak decreases. This indicates a higher band to band recombination rate and a diminution of the radiative transitions due to defects. Sharma et al. found that Al in ZnO matrix promotes the oxygen diffusion through the ZnO lattice, leading to the suppression of oxygen vacancies (V_O)

and the creation of oxygen interstitial (O_i) defects [29]. The work of Y. Liu et al. also coincides with this idea and they proposed a distribution model of the oxygen vacancies, the excess oxygen and the aluminum atoms in the ZnO grains that can explain the green and orange luminescence of ZnO: Al films [28]. Following these ideas, we can say that the incorporation of Al favors the oxygen diffusion and neutralizes some of the intrinsic oxygen vacancies of ZnO, as represented in Figure 7. This results in the diminution of the visible emission band of the doped samples. Furthermore, Mahmood et al. reported that O_i has a low energy of formation under oxidizing conditions [30], so it is easy to find this type of defect in our films, as they were grown under ambient conditions. However, we consider that the excess oxygen is not in a very large concentration because we do not observe a red shift of the green emission peak. This excess oxygen may be neutralizing some of the V_O inside the grains, but the V_O concentration in our samples may be high, giving only a slight diminution of the intensity of this peak.

The PL study of ZnO and ZnO: Al films can help us to understand the photocatalytic activity of the films. First, we can see that the undoped film has already a large amount of structural defects that introduce electronic levels within the band gap. These levels facilitate the electron transport from the valence band to the conduction band and can explain the weak activity under white light illumination. On the other hand, the Al doped ZnO films, in addition to the intrinsic defects—such as V_O—also have Al atoms that provide an extra electron, which contributes to the reduction of the O_2 dissolved in the aqueous medium and form the superoxide radical $O_2^{\bullet-}$, which in turn contribute to the formation of hydrogen peroxide on the semiconductor surface [20]. All these radicals produce the decomposition of the dye. This is the reason for the significant increase of the photocatalytic activity. However, the degradation of the dye without any light in presence of the ZnO: Al films could be attributed to high mobility of the extra electrons provided by the Al atoms, that migrate to the surface of the semiconductor and start the formation of $O_2^{\bullet-}$ radicals (it should be pointed out that

ZnO: Al has been used as transparent conductive oxide due to its high free carrier concentration and mobility [31, 32]). Considering the change in morphology of the doped films, that present higher roughness and more contact area, the number of reactions that can take place also increases, producing a high discoloration of the dye even without light.

4. Conclusions

The present work compared the photocatalytic activity of pure and aluminum doped ZnO films under white light, sunlight, and UV illumination. ZnO films showed good degradation efficiency under UV and sunlight and barely degraded using white light. However, the Al doped ZnO films not only increased three times the photocatalytic activity of ZnO under UV and sunlight, but also degraded the dye under white light and even in the dark. The degradation of the dye using white light is explained due to the intrinsic defects (such as V_O) in ZnO matrix that facilitates the charge transport between bands. This charge transport is enhanced by the aluminum atoms that provide an extra electron, which is able to migrate to the semiconductor surface even without needing a photon. The electron migration can start the formation of radicals that decompose the dye molecules, explaining the unexpected activity without illumination. The photocatalytic ability of the ZnO: Al films allows the development of a low cost, high efficiency, and environmentally friendly material for water treatment applications using sunlight.

Acknowledgments

References

[1] D. Bahnemann, "Photocatalytic water treatment: solar energy applications," *Solar Energy*, vol. 77, no. 5, pp. 445–459, 2004.

[2] J.-M. Herrmann, "Heterogeneous photocatalysis: state of the art and present applications," *Topics in Catalysis*, vol. 34, no. 1–4, pp. 49–65, 2005.

[3] M. R. Hoffmann, S. T. Martin, W. Choi, and D. W. Bahnemann, "Environmental applications of semiconductor photocatalysis," *Chemical Reviews*, vol. 95, no. 1, pp. 69–96, 1995.

[4] D. Li, H. Haneda, S. Hishita, and N. Ohashi, "Visible-light-driven nitrogen-doped TiO2 photocatalysts: effect of nitrogen precursors on their photocatalysis for decomposition of gas-phase organic pollutants," *Materials Science and Engineering B*, vol. 117, no. 1, pp. 67–75, 2005.

[5] M. Maeda and T. Yamada, "Photocatalytic activity of metal-doped titanium oxide films prepared by sol-gel process," *Journal of Physics*, vol. 61, no. 1, article 151, pp. 755–759, 2007.

[6] M. Maeda and T. Watanabe, "Visible light photocatalysis of nitrogen-doped titanium oxide films prepared by plasma-enhanced chemical vapor deposition," *Journal of the Electrochemical Society*, vol. 153, no. 3, pp. C186–C189, 2006.

[7] D. Noguchi, Y. Kawamata, and T. Nagatomo, "The response of TiO2 photocatalysts codoped with nitrogen and carbon to visible light," *Journal of the Electrochemical Society*, vol. 152, no. 9, pp. D124–D129, 2005.

[8] S. Sakthivel and H. Kisch, "Daylight photocatalysis by carbon-modified titanium dioxide," *Angewandte Chemie*, vol. 42, no. 40, pp. 4908–4911, 2003.

[9] A. Kubacka, M. Fernández-García, and G. Colón, "Nanostructured Ti-M mixed-metal oxides: toward a visible light-driven photocatalyst," *Journal of Catalysis*, vol. 254, no. 2, pp. 272–284, 2008.

[10] J. Yu, H. Yu, C. H. Ao, S. C. Lee, J. C. Yu, and W. Ho, "Preparation, characterization and photocatalytic activity of in situ Fe-doped TiO2 thin films," *Thin Solid Films*, vol. 496, no. 2, pp. 273–280, 2006.

[11] J. P. Wang, H. C. Yang, and C. T. Hsieh, "Visible-light photodegradation of dye on Co-doped Titania nanotubes prepared by hydrothermal synthesis," *International Journal of Photoenergy*, vol. 2012, Article ID 206534, 10 pages, 2012.

[12] C. H. Huang, Y. M. Lin, I.-K. Wang, and C. M. Lu, "Photocatalytic activity and characterization of carbon-modified titania for visible-light-active photodegradation of nitrogen oxides," *International Journal of Photoenergy*, vol. 2012, Article ID 548647, 13 pages, 2012.

[13] O. Mekasuwandumrong, P. Pawinrat, P. Praserthdam, and J. Panpranot, "Effects of synthesis conditions and annealing post-treatment on the photocatalytic activities of ZnO nanoparticles in the degradation of methylene blue dye," *Chemical Engineering Journal*, vol. 164, no. 1, pp. 77–84, 2010.

[14] R. Ullah and J. Dutta, "Photocatalytic degradation of organic dyes with manganese-doped ZnO nanoparticles," *Journal of Hazardous Materials*, vol. 156, no. 1–3, pp. 194–200, 2008.

[15] H. F. Lin, S. C. Liao, and S. W. Hung, "The dc thermal plasma synthesis of ZnO nanoparticles for visible-light photocatalyst," *Journal of Photochemistry and Photobiology A*, vol. 174, no. 1, pp. 82–87, 2005.

[16] D. Li and H. Haneda, "Synthesis of nitrogen-containing ZnO powders by spray pyrolysis and their visible-light photocatalysis in gas-phase acetaldehyde decomposition," *Journal of Photochemistry and Photobiology A*, vol. 155, no. 1–3, pp. 171–178, 2003.

[17] D. Li and H. Haneda, "Photocatalysis of sprayed nitrogen-containing Fe2O3-ZnO and WO3-ZnO composite powders in gas-phase acetaldehyde decomposition," *Journal of Photochemistry and Photobiology A*, vol. 160, no. 3, pp. 203–212, 2003.

[18] H. Wang, S. Baek, J. Lee, and S. Lim, "High photocatalytic activity of silver-loaded ZnO-SnO2 coupled catalysts," *Chemical Engineering Journal*, vol. 146, no. 3, pp. 355–361, 2009.

[19] S. Anandan, Y. Ikuma, and V. Murugesan, "Highly active rare-earth metal La-doped photocatalysts: fabrication, characterization and their photocatalytic activity," *International Journal of Photoenergy*, vol. 2012, Article ID 921412, 10 pages, 2012.

[20] T. Parvin, N. Keerthiraj, I. A. Ibrahim, S. Phanichphant, and K. Byrappa, "Photocatalytic degradation of municipal wastewater and brilliant blue dye using hydrothermal synthesized surface-modified silver-doped ZnO designer particles," *International Journal of Photoenergy*, vol. 2012, Article ID 670610, 8 pages, 2012.

[21] Z. Liu, H. Bai, and D. Delai Sun, "Hierarchical CuO/ZnO Mambranes for environmental applications under the irradiation of visible light," *International Journal of Photoenergy*, vol. 2012, Article ID 804840, 11 pages, 2012.

[22] M. Bizarro, "High photocatalytic activity of ZnO and ZnO:Al nanostructured films deposited by spray pyrolysis," *Applied Catalysis B*, vol. 97, no. 1-2, pp. 198–203, 2010.

[23] H. Al-Ekabi and N. Serpone, "Kinetic studies in heterogeneous photocatalysis. 1. Photocatalytic degradation of chlorinated phenols in aerated aqueous solutions over TiO2 supported on a glass matrix," *Journal of Physical Chemistry*, vol. 92, no. 20, pp. 5726–5731, 1988.

[24] S. Mridha and D. Basak, "Aluminium doped ZnO films: electrical, optical and photoresponse studies," *Journal of Physics D*, vol. 40, no. 22, pp. 6902–6907, 2007.

[25] F. K. Shan and Y. S. Yu, "Band gap energy of pure and Al-doped ZnO thin films," *Journal of the European Ceramic Society*, vol. 24, no. 6, pp. 1869–1872, 2004.

[26] M. Bizarro, A. Sánchez-Arzate, I. Garduño-Wilches, J. C. Alonso, and A. Ortiz, "Synthesis and characterization of ZnO and ZnO:Al by spray pyrolysis with high photocatalytic properties," *Catalysis Today*, vol. 166, no. 1, pp. 129–134, 2011.

[27] B. E. Sernelius, K. F. Berggren, Z. C. Jin, I. Hamberg, and C. G. Granqvist, "Band-gap tailoring of ZnO by means of heavy Al doping," *Physical Review B*, vol. 37, no. 17, pp. 10244–10248, 1988.

[28] Y. Liu, H. Zhang, X. An et al., "Effect of Al doping on the visible photoluminescence of ZnO nanofibers," *Journal of Alloys and Compounds*, vol. 506, no. 2, pp. 772–776, 2010.

[29] B. K. Sharma, N. Khare, and D. Haranath, "Photoluminescence lifetime of Al-doped ZnO films in visible region," *Solid State Communications*, vol. 150, no. 47-48, pp. 2341–2345, 2010.

[30] M. A. Mahmood, S. Baruah, and J. Dutta, "Enhanced visible light photocatalysis by manganese doping or rapid crystallization with ZnO nanoparticles," *Materials Chemistry and Physics*, vol. 130, pp. 531–535, 2011.

[31] Y. Liu and J. Lian, "Optical and electrical properties of aluminum-doped ZnO thin films grown by pulsed laser deposition," *Applied Surface Science*, vol. 253, no. 7, pp. 3727–3730, 2007.

[32] M. Gabás, S. Gota, J. R. Ramos-Barrado et al., "Unraveling the conduction mechanism of Al-doped ZnO films by valence band soft x-ray photoemission spectroscopy," *Applied Physics Letters*, vol. 86, no. 4, Article ID Article number042104, pp. 042104–1, 2005.

Research Article

Photocatalytic Degradation of Rhodamine B with $H_3PW_{12}O_{40}/SiO_2$ Sensitized by H_2O_2

Shuijin Yang, Yongkui Huang, Yunzhi Wang, Yun Yang, Mingbo Xu, and Guohong Wang

*Hubei Key Laboratory of Pollutant Analysis & Reuse Technology, College of Chemistry and Environmental Engineering,
Hubei Normal University, Huangshi 435002, China*

Correspondence should be addressed to Guohong Wang, wanggh2003@163.com

In order to remove aquatic organic dye contaminants by utilizing the inexpensive and inexhaustible solar energy, the Keggin-type $H_3PW_{12}O_{40}$ was loaded on the surface of SiO_2 with the sol-gel method and sensitized by H_2O_2 solution. The photocatalytic degradation of rhodamine B (RhB) by $H_3PW_{12}O_{40}/SiO_2(x)$ under simulated natural light irradiation was investigated. The effects of the initial RhB concentration, the solution pH, and catalyst dosage on the photocatalytic degradation rate of RhB were also studied. The results demonstrated that at optimal condition (initial concentration of methyl orange is 10 mg/L, catalyst dosage is 0.8 g, and the pH is 2.5) the degradation rate of RhB is as high as 97.7% after 2 h under simulated natural light irradiation. The reaction of photocatalysis for RhB can be expressed as a first-order kinetic model.

1. Introduction

Environmental pollution caused by organic dyes has become a worldwide problem. Those dyes are often used in textiles, papers, leathers, food, and cosmetics. It is essential to develop methods that can lead to destruction of such compounds. A variety of common treatment techniques including condensation, ultrafiltration, membrane separation, and adsorption have become the main technology for treatment of organic pollutants [1, 2]. However, these methods often transferred organic pollutants to the other phases and not degraded completely to nontoxic substances [3–5]. So, the development of advanced low cost and high efficiency water treatment technologies is desirable.

Advanced oxidation processes (AOPs) in organic pollutants degradation have shown outstanding advantages, which have the potential to completely oxidize organic compounds to CO_2, H_2O, and other inorganic substances [6–8]. Among these AOPs, photocatalytic degradation by semiconductor catalysts has been investigated widely during the past decade. A number of semiconductor materials such as TiO_2 [9, 10], ZnO [11], Fe_2O_3 [12], Bi_2WO_6 [13], $H_2WO_4 \cdot H_2O/Ag/AgCl$ [14], Ag_2O [15], and $SrTiO_3$ [16] were used in photocatalytic degradation of organic pollutants. Among them, the use of TiO_2 as a photocatalyst to degrade organic pollutants has recieved extensive attention due to its high activity, low cost, chemical stability, and non-toxicity [17, 18]. But this photocatalyst is activated only by ultraviolet (UV) light (wavelength < 387 nm) due to its band gap of 3.2 eV. Since UV light only accounts for less than 5% of the solar energy that reaches the surface of the earth, the photocatalytic activity of pure TiO_2 cannot be effectively activated under solar light irradiation, which limits its practical application [19, 20].

In recent years, the development of photocatalysts with a visible light response has been extensively studied. For this purpose, TiO_2 has been modified by various ways such as impurity doping inorganic compound [21, 22] and dye sensitization [23] to obtain visible light reactivity [24, 25]. Polyoxometalates (POMs) have also attracted much attention as photocatalysts because they generally share the same photochemical characteristics of semiconductor photocatalysts such as TiO_2 [26, 27]. The excited POMs, produced after light absorption is able to completely degrade organic compounds, either directly or via OH radicals-mediated oxidations [28]. A problem of POMs catalysts used to degrade pollutants in homogeneous systems is that they are difficult to separate from the reaction system at the end of the reaction,

which precludes their recovery and reuse. POMs should be supported on a support to improve the catalytic performance in the reaction [29]. SiO_2 was an ideal support because it exhibits higher surface area, chemical inertness, controlled porosity and well disperses for POMs while retaining the structure. Unfortunately, the photocatalysis of POMs/SiO_2 are concentrated on UV irradiation [30]. Aiming at utilizing the inexpensive and inexhaustible solar energy, we attempted to use a simple and efficient method to improve their photocatalytic activity.

In this paper, $H_3PW_{12}O_{40}$/SiO_2 was prepared by a sol-gel technique, and sensitized by H_2O_2 solution. The photocatalytic degradation of RhB with the catalyst under simulated natural light irradiation was investigated.

2. Experimental

2.1. Preparation of Samples. $H_3PW_{12}O_{40}$/SiO_2 was synthesized according to references [26, 30] by a sol-gel technique. An amount of $H_3PW_{12}O_{40}$ was dissolved in 26 mL of H_2O, and a stoichiometric amount of TEOS was mixed with 1-BuOH. The latter was added dropwise to the aqueous solution. The resultant was allowed to stir at room temperature for 1 h, at 45°C for 1 h, and then at 80°C until a uniform gel was formed. The hydrogel obtained was dehydrated slowly at 45°C for 16 h in vacuum, and then at 90°C for 3.5 h. Thus, the silica network was fastened and the removal of the $H_3PW_{12}O_{40}$ molecules from it was avoided. The particulate gel was washed with hot water for several times until the filtrate was neutral, and then the products were calcined for the required duration. The acetalization of cyclohexanone with 1, 2-propanediol was used as a probe to study the preparation conditions of catalyst, and the optimum conditions are as follows the loading of $H_3PW_{12}O_{40}$ is 30 wt% calcination temperature is 200°C; and calcination time is 4 h.

$H_3PW_{12}O_{40}$/SiO_2 was treated by H_2O_2 as follows [17]: 1 g $H_3PW_{12}O_{40}$/SiO_2 was added into 15 mL 30% H_2O_2 solution and sonicated the mixture for 20 min. The slurry mixture was filtrated and dried at room temperature. This catalyst is denoted as $H_3PW_{12}O_{40}$/SiO_2(x).

2.2. Characterization. The FT-IR spectra of the samples in KBr matrix were recorded on a Nicolet 5700 FT-IR spectrometer in the range 400–4000 cm^{-1}. The X-ray powder diffraction pattern of the samples was measured by a Bruker AXS D8-Advanced diffractometer (Bruker, Germany) employing Cu K_α radiation. The UV-vis diffuse reflectance spectra (UV-vis/DRS) were recorded on a spectrophotometer with an integrating sphere (Shmadzu UV-2550), and $BaSO_4$ was used as a reference sample.

2.3. Activity Test. For the evaluation of catalyst activity, the catalyst was suspended in an aqueous solution of rhodamine B (RhB) in a Pyrex reactor. The photoreactor was designed with a light source surrounded by a quartz jacket. Simulated sunlight irradiation was provided by a 500 W xenon lamp (Nanjing Xujiang Electromechanical Factory, China), and the intensity of the lamp was 1200 $\mu mol \cdot m^{-2} \cdot s^{-1}$. Solution pH was adjusted with dilute aqueous HCl and NaOH
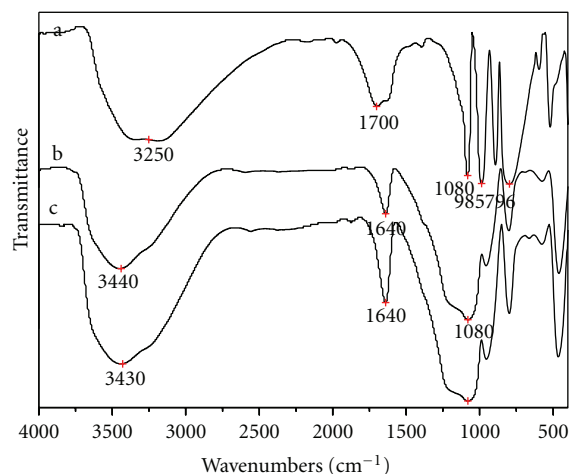
Figure 1: FT-IR spectra of $H_3PW_{12}O_{40}$ (a), $H_3PW_{12}O_{40}$/SiO_2 (b), and $H_3PW_{12}O_{40}$/SiO_2(x) (c).

solutions. The system was cooled by circulating water and maintained at room temperature. Before irradiation, the suspensions were magnetically stirred in the dark for 30 min to reach the adsorption–desorption equilibrium of organic dyes on catalyst surface. At given time intervals, about 3 mL suspension was continually taken from the photoreactor for subsequent RhB concentration analysis after centrifuging. Decreases of the RhB concentrations were monitored via a UV-visible spectrometer (Hitachi U-3010, Japan). The degradation yield of organics was calculated by the following formula:

$$\text{degradation yield (\%)} = \left(\frac{(A_0 - A)}{A_0} \right) \times 100, \quad (1)$$

where A_0 and A referred to the absorbance of RhB before and after reaction, respectively.

3. Results and Discussion

3.1. Characterization of the Catalysts. The FT-IR spectra of $H_3PW_{12}O_{40}$ (a), $H_3PW_{12}O_{40}$/SiO_2 (b), and $H_3PW_{12}O_{40}$/SiO_2(x) (c) are shown in Figure 1. As shown in Figure 1, pure $H_3PW_{12}O_{40}$ gives peaks due to the Keggin structure at 1080, 985, 890, and 794 cm^{-1}. In addition, the band at 1662 cm^{-1}, which is the bending mode of the water, indicates the presence of the water. When $H_3PW_{12}O_{40}$ is supported on SiO_2, these bands have somewhat changed. The bands at 1080 and 890 cm^{-1} are overlapped by the characteristic band of SiO_2, while these bands at 985 and 794 cm^{-1} shift to 950 and 803 cm^{-1}, respectively. The spectrum of $H_3PW_{12}O_{40}$/SiO_2(x) is similar to that of $H_3PW_{12}O_{40}$/SiO_2. It can be concluded that the Keggin geometry of $H_3PW_{12}O_{40}$ is still kept [31]. Meanwhile, it indicates that a strong chemical interaction exists between the $H_3PW_{12}O_{40}$ and silica.

POMs could be supported as molecules or aggregates on the supports. Figure 2 shows the X-ray diffraction patterns of $H_3PW_{12}O_{40}$ (a), $H_3PW_{12}O_{40}$/SiO_2 (b), and $H_3PW_{12}O_{40}$/SiO_2(x) (c). The characteristic diffraction peaks of $H_3PW_{12}O_{40}$ at 8–10°, 17–20°, 26–30°, and 32–35° can be
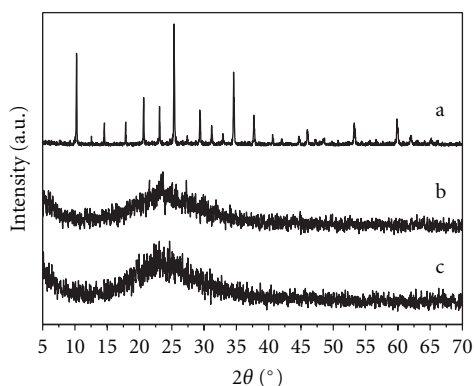
FIGURE 2: XRD patterns of $H_3PW_{12}O_{40}$ (a), $H_3PW_{12}O_{40}/SiO_2$(b), and $H_3PW_{12}O_{40}/SiO_2$(x) (c).

FIGURE 3: UV-vis/DRS of $H_3PW_{12}O_{40}/SiO_2$ and $H_3PW_{12}O_{40}/SiO_2$(x).

FIGURE 4: Comparison of photocatalytic activity before and after treatment of catalysts, and under no light or without catalyst.

assigned to the diffraction characteristic peaks of crystalline $H_3PW_{12}O_{40}$ Keggin structure [31]. For $H_3PW_{12}O_{40}/SiO_2$ and $H_3PW_{12}O_{40}/SiO_2$(x), only a broad band at $2\theta = 24°$ that can be assigned to the diffraction peaks of amorphous silica is observed, and the signals of $H_3PW_{12}O_{40}$ are disappeared. So it is reasonable to consider that $H_3PW_{12}O_{40}$ is highly dispersed on the surface of silica support without any aggregation.

The diffusing reflectance UV-Vis spectra (UV-DRS) of the catalysts are directly related to their photochemical behavior. The UV-DRS of the samples were characterized, and the results are shown in Figure 3. From the Figure 3, it can be seen clearly the characteristic absorption peaks at 260 nm which was attributed to O-W charge transfer of the Keggin unit at W-O-W bond. Their characteristics are similar to pure $H_3PW_{12}O_{40}$.This can be assigned to the Keggin geometry of $H_3PW_{12}O_{40}$ [31]. It is worthy to note that an absorption tail extending from the UV to the visible region in the UV-DRS of $H_3PW_{12}O_{40}/SiO_2$(x). Therefore, it is concluded that the sensitizing effect maybe have obvious influence on the photocatalytic activity of catalyst.

3.2. Investigation of Photocatalytic Activity of Catalysts

3.2.1. Comparison of Photocatalytic Activity of Catalysts. In order to observe the effect of H_2O_2 treatment on the catalytic activity of $H_3PW_{12}O_{40}/SiO_2$, comparison of photocatalytic activity of catalysts was carried out at the initial RhB concentration of 10 mg/L, pH 2.5, and 0.5 g of catalyst, and the results are shown in Figure 4.

As seen from Figure 4, after 2 h irradiation under the same conditions, no obvious RhB degradation was observed without any catalyst or light. However, in the presence of $H_3PW_{12}O_{40}/SiO_2$, the degradation yield of RhB is about 44.0%, while with $H_3PW_{12}O_{40}/SiO_2$(x) the degradation yield can reach to 92.7%. Since the $H_3PW_{12}O_{40}/SiO_2$ is illuminated by ultraviolet light, which represents 3 to 5% of the total solar radiation. This is consistent with previous reports [26, 30]. So the photodegradation reaction of RhB in the presence of $H_3PW_{12}O_{40}/SiO_2$(x) is more effectively than that of $H_3PW_{12}O_{40}/SiO_2$.
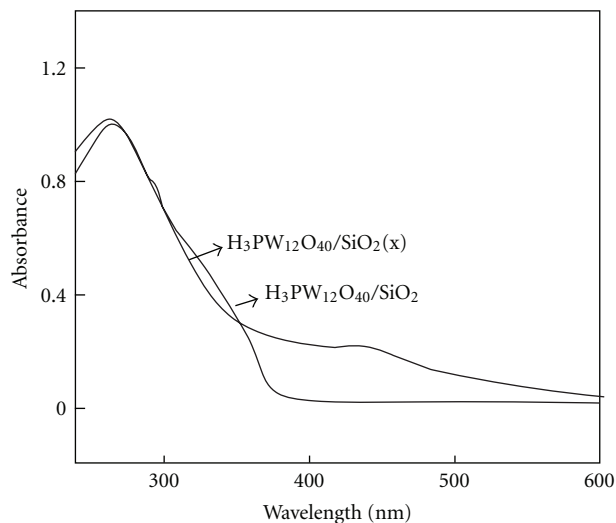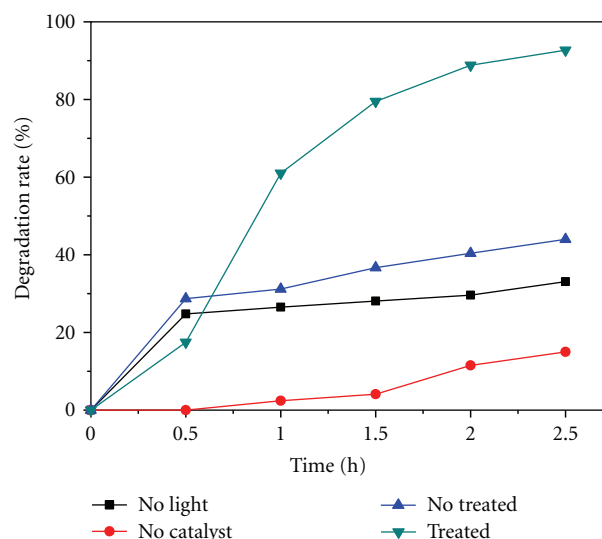
3.2.2. Effect of the Initial Concentration of Dye. To investigate the influence of initial concentration on the degradation efficiency of RhB, the initial concentration was varied from 5 to 20 mg/L, keeping the other experimental conditions constant.

As can be seen in Figure 5, the degradation rate decreased with increase of initial concentration of RhB. This might be due to the excessive adsorption of the RhB molecules on the surface of catalyst at higher concentration. Moreover, light through the solution is reduced significantly. Thus, the efficiency of degradation was decreased in the higher concentration. It was further observed that the activity decreased slightly from 5 to 10 mg/L of the initial concentration of dye. From the practical point of wastewater treatment, the initial concentration of the 10 mg/L is more appropriate.
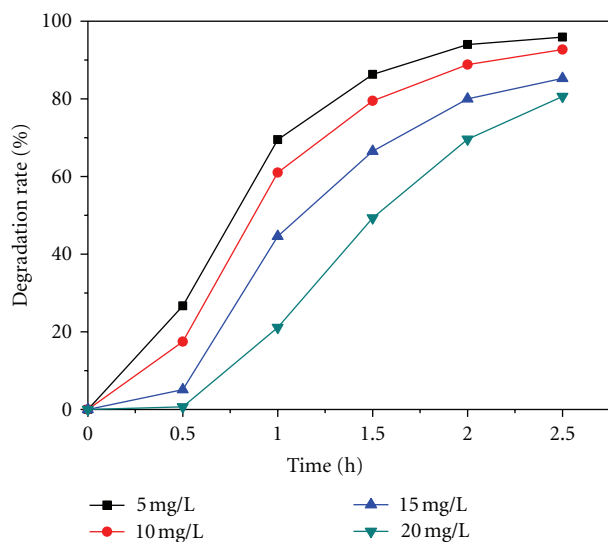
FIGURE 5: Effect of the initial RhB concentration on the photocatalytic degradation rate of RhB.

FIGURE 7: Effect of catalyst dosage on the photocatalytic degradation rate of RhB.

FIGURE 6: Effect of the solution pH on the photocatalytic degradation rate of RhB.
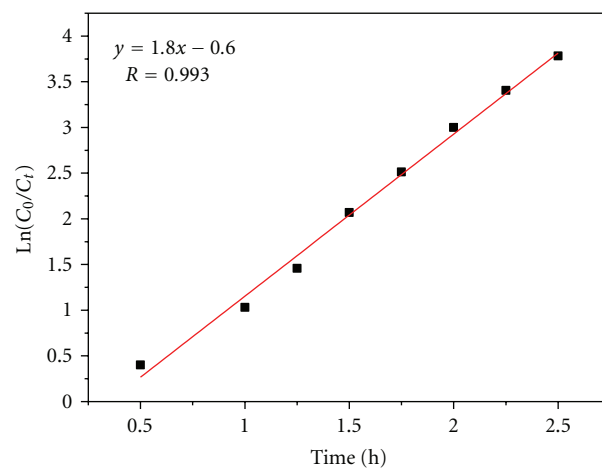
FIGURE 8: Relation curve of $\ln(C_0/C_t)$ and time (t).

3.2.3. Effect of pH. It is well known that the pH of the solution is one of the most important parameters in the photocatalytic degradation of organic compounds. This is attributed to that the pH does not only determine chemical properties of the photocatalyst but also influences adsorption behaviour of the pollutants. Therefore, the effect of pH on the degradation of RhB was studied at pH range from 2.5 to 12.

As shown in Figure 6, the most effective pH condition is at 2.5. This may be ascribed to the fact that the pH value could influence the amount of hydroxyl radicals (OH·) formed [21] and the stable of $H_3PW_{12}O_{40}$. So the optimum pH of the solution is 2.5.

3.2.4. Effect of Catalyst Dosage. The catalyst dosage is also an important parameter for optimizing the operational conditions. Therefore, the effect of catalyst dosage on the

degradation of RhB was investigated in the catalyst dosage from 0.2 to 1.2 g, and the result shown was in Figure 7. The results indicated that the degradation rate gradually increased with increase of catalyst dosage from 0.2 to 0.8 g. However, the degradation efficiency decreased slightly with increase of catalyst dosage from 0.8 to 1.2 g. This may be attributed to the fact that the surplus catalyst can scatter the photons in the photoreaction system.

3.3. Kinetic Analysis. It is well known that the photodegradation of organic dyes mainly follows first-order kinetics. The kinetics of photocatalytic degradation of RhB was also studied under optimized conditions. The results are shown in Figure 8.

The results showed that the photocatalytic degradation of RhB over $H_3PW_{12}O_{40}/SiO_2$ (x) under simulated sunlight irradiation can be described by the first order kinetic model, $\ln(C_0/C_t) = kt$, where k is the rate constant (h^{-1}), C_0 is

the initial concentration, and C_t is the concentration of dye at time t. It can be seen for Figure 8 that the plots represented a straight line. The correlation constant for the line was 0.993. The rate constant was $1.8 \, h^{-1}$.

4. Conclusion

$H_3PW_{12}O_{40}/SiO_2$ was prepared by a sol-gel method and sensitized by H_2O_2 solution and significantly improved its catalytic activity under simulated natural light irradiation. The photocatalytic degradation of RhB by $H_3PW_{12}O_{40}/SiO_2$ (x) under simulated natural light irradiation was investigated. The results demonstrated that at optimal condition (initial concentration of methyl orange is 10 mg/L, catalyst dosage is 0.8 g, and the pH is 2.5), the degradation rate of RhB is as high as 97.7% after 2 h under simulated natural light irradiation. The reaction of photocatalysis for RhB can be expressed as first-order kinetic model.

Acknowledgments

References

[1] F. H. Hussein, "Comparison between solar and artificial photocatalytic decolorization of textile industrial wastewater," *International Journal of Photoenergy*, vol. 2012, Article ID 793648, 10 pages, 2012.

[2] M. N. Chong, B. Jin, C. W. K. Chow, and C. Saint, "Recent developments in photocatalytic water treatment technology: a review," *Water Research*, vol. 44, no. 10, pp. 2997–3027, 2010.

[3] M. Muruganandham and M. Swaminathan, "Decolourisation of reactive orange 4 by fenton and photo-Fenton oxidation technology," *Dyes and Pigments*, vol. 63, no. 3, pp. 315–321, 2004.

[4] E. Sahinkaya, N. Uzal, U. Yetis, and F. B. Dilek, "Biological treatment and nanofiltration of denim textile wastewater for reuse," *Journal of Hazardous Materials*, vol. 153, no. 3, pp. 1142–1148, 2008.

[5] H. Lachheb, E. Puzenat, A. Houas et al., "Photocatalytic degradation of various types of dyes (Alizarin S, Crocein Orange G, Methyl Red, Congo Red, Methylene Blue) in water by UV-irradiated titania," *Applied Catalysis B*, vol. 39, no. 1, pp. 75–90, 2002.

[6] S. H. S. Chan, T. Y. Wu, J. C. Juan, and C. Y. Teh, "Recent developments of metal oxide semiconductors as photocatalysts in advanced oxidation processes (AOPs) for treatment of dye waste-water," *Journal of Chemical Technology & Biotechnology*, vol. 86, no. 9, pp. 1130–1158, 2011.

[7] C. C. Hsueh and B. Y. Chen, "Comparative study on reaction selectivity of azo dye decolorization by Pseudomonas luteola," *Journal of Hazardous Materials*, vol. 141, no. 3, pp. 842–849, 2007.

[8] C. McCullagh, N. Skillen, M. Adams, and P. K. Robertson, "Photocatalytic reactors for environmental remediation: a review," *Journal of Chemical Technology & Biotechnology*, vol. 86, no. 8, pp. 1002–1017, 2011.

[9] M. Y. Guo, A. M. C. Ng, F. Liu, A. B. Djurišić, and W. K. Chan, "Photocatalytic activity of metal oxides-the role of holes and OH radicals," *Applied Catalysis B*, vol. 107, no. 1-2, pp. 150–157, 2011.

[10] L. N. Wang, F. Lu, and F. M. Meng, "Synthesis and photocatalytic activity of TiOX powders with different oxygen defects," *International Journal of Photoenergy*, vol. 2012, Article ID 208987, 7 pages, 2012.

[11] J. Fenoll, P. Hellín, C. M. Martínez et al., "Semiconductor oxides-sensitized photodegradation of fenamiphos in leaching water under natural sunlight," *Applied Catalysis B*, vol. 115-116, pp. 31–37, 2012.

[12] X. M. Zhou, J. Y. Lan, G. Liu et al., "Facet-mediated photodegradation of organic dye over hematite architectures by visible light," *Angewandte Chemie*, vol. 124, no. 1, pp. 182–186, 2012.

[13] H. G. Yu, R. Liu, X. F. Wang et al., "Enhanced visible-light photocatalytic activity of Bi_2WO_6 nanoparticles by Ag_2O cocatalyst," *Applied Catalysis B*, vol. 111-112, pp. 326–333, 2012.

[14] X. F. Wang, S. F. Li, Y. Q. Ma, H. Yu, and J. Yu, "$H_2WO_4 \cdot H_2O/Ag/AgCl$ composite nanoplates: a plasmonic Z-scheme visible-light photocatalyst," *Journal of Physical Chemistry C*, vol. 115, no. 30, pp. 14648–14655, 2011.

[15] X. F. Wang, S. F. Li, H. G. Yu et al., "Ag_2O as a new visible-light photocatalyst: self-stability and high photocatalytic activity," *Chemistry*, vol. 17, no. 28, pp. 7777–7780, 2011.

[16] X. Wei, G. Xu, Z. Ren et al., "Single-crystal-like mesoporous $SrTiO_3$ spheres with enhanced photocatalytic performance," *Journal of the American Ceramic Society*, vol. 93, no. 5, pp. 1297–1305, 2010.

[17] J. Zou, J. Gao, and Y. Wang, "Synthesis of highly active H_2O_2-sensitized sulfated titania nanoparticles with a response to visible light," *Journal of Photochemistry and Photobiology A*, vol. 202, no. 2-3, pp. 128–135, 2009.

[18] S. Yanagida, A. Nakajima, T. Sasaki, T. Isobe, Y. Kameshima, and K. Okada, "Preparation and photocatalytic activity of Keggin-ion tungstate and TiO_2 hybrid layer-by-layer film composites," *Applied Catalysis A*, vol. 366, no. 1, pp. 148–153, 2009.

[19] Q. J. Xiang, J. G. Yu, and M. Jaroniec, "Graphene-based semiconductor photocatalysts," *Chemical Society Reviews*, vol. 41, pp. 782–796, 2012.

[20] Q. Zhang, D. Q. Lima, I. Lee, F. Zaera, M. Chi, and Y. Yin, "A highly active titanium dioxide based visible-light photocatalyst with nonmetal doping and plasmonic metal decoration," *Angewandte Chemie*, vol. 50, no. 31, pp. 7088–7092, 2011.

[21] Q. J. Xiang, J. G. Yu, W. G. Wang, and M. Jaroniec, "Nitrogen self-doped nanosized TiO_2 sheets with exposed 001 facets for enhanced visible-light photocatalytic activity," *Chemical Communications*, vol. 47, no. 24, pp. 6906–6908, 2011.

[22] Z. H. Xu and J. G. Yu, "Visible-light-induced photoelectrochemical behaviors of Fe-modified TiO_2 nanotube arrays," *Nanoscale*, vol. 3, pp. 3138–3144, 2011.

[23] J. G. Yu, J. J. Fan, and B. Cheng, "Dye-sensitized solar cells based on anatase TiO_2 hollow spheres/carbon nanotube composite films," *Journal of Power Sources*, vol. 196, no. 18, pp. 7891–7898, 2011.

[24] H. R. Jafry, M. V. Liga, Q. Li, and A. R. Barron, "Simple route to enhanced photocatalytic activity of P 25 titanium dioxide nanoparticles by silica addition," *Environmental Science & Technology*, vol. 45, no. 4, pp. 1563–1568, 2011.

[25] H. Li, D. Wang, P. Wang, H. Fan, and T. Xie, "Synthesis and studies of the visible-light photocatalytic properties of near-monodisperse Bi-doped TiO_2 nanospheres," *Chemistry*, vol. 15, no. 45, pp. 12521–12527, 2009.

[26] Y. H. Guo and C. W. Hu, "Heterogeneous photocatalysis by solid polyoxometalates," *Journal of Molecular Catalysis A*, vol. 262, no. 1-2, pp. 136–148, 2007.

[27] P. X. Lei, C. C. Chen, J. Yang, W. Ma, J. Zhao, and L. Zang, "Degradation of dye pollutants by immobilized polyoxometalate with H_2O_2 under visible-light irradiation," *Environmental Science & Technology*, vol. 39, no. 21, pp. 8466–8474, 2005.

[28] I. Arslan-Alaton, "Homogenous photocatalytic degradation of a disperse dye and its dye bath analogue by silicadodecatungstic acid," *Dyes and Pigments*, vol. 60, no. 2, pp. 167–176, 2004.

[29] S. J. Jiang, Y. H. Guo, C. H. Wang, X. Qu, and L. Li, "One-step sol-gel preparation and enhanced photocatalytic activity of porous polyoxometalate-tantalum pentoxide nanocomposites," *Journal of Colloid and Interface Science*, vol. 308, no. 1, pp. 208–215, 2007.

[30] Y. H. Guo, C. W. Hu, S. C. Jiang, C. Guo, Y. Yang, and E. Wang, "Heterogeneous photodegradation of aqueous hydroxy butanedioic acid by microporous polyoxometalates," *Applied Catalysis B*, vol. 36, no. 1, pp. 9–17, 2002.

[31] E. B. Wang, C. W. Hu, and L. Xu, *Polyhydric Chemistry Introduction*, Chemical Industry Press, Beijing, China, 1998.

Research Article

Hydrothermal Synthesis of Iodine-Doped Bi$_2$WO$_6$ Nanoplates with Enhanced Visible and Ultraviolet-Induced Photocatalytic Activities

Jiang Zhang,[1] Zheng-Hong Huang,[1] Yong Xu,[2] and Feiyu Kang[1]

[1] *Laboratory of Advanced Materials, Department of Materials Science and Engineering, Tsinghua University, Beijing 100084, China*
[2] *Beijing Tongfang Puri-tech Co., Ltd, Beijing 100083, China*

Correspondence should be addressed to Zheng-Hong Huang, zhhuang@mail.tsinghua.edu.cn
and Feiyu Kang, fykang@mail.tsinghua.edu.cn

The iodine-doped Bi$_2$WO$_6$ (I-BWO) photocatalyst was prepared via a hydrothermal method using potassium iodide as the source of iodine. The samples were characterized by X-ray diffraction (XRD), scanning electron microscope (SEM), transmission electron microscopy (TEM) and selected area electron diffraction (SAED), X-ray photoelectron spectroscopy (XPS), UV-vis diffuse reflectance spectroscopy (DRS), and photoluminescence (PL) spectroscopy. The photocatalytic activity of I-BWO for the degradation of rhodamine B (RhB) was higher than that of pure BWO and I$_2$-BWO regardless of visible light (>420 nm) or ultraviolet light (<400 nm) irradiation. The results of DRS analysis showed that the I-BWO and I$_2$-BWO catalysts had narrower band gaps. XPS analysis proved that the multivalent iodine species including I^0 and I$^-$ were coadsorbed on the defect surface of Bi$_2$WO$_6$ in I-BWO. The enhanced PL intensity revealed that a large number of defects of oxygen vacancies were formed by the doping of iodine. The enhanced photocatalytic activity of I-BWO for degradation of RhB was caused by the synergetic effect of a small crystalline size, a narrow band gap, and plenty of oxygen vacancies.

1. Introduction

To decompose the organic pollutants existing in water and air, the advanced oxidation technique of photocatalysis was applied to deal with the serious environmental problems. Among all kinds of photocatalysts, the UV-induced TiO$_2$ as an effective photocatalyst have been applied widely in the conversion of photon energy into chemical energy and the decomposition of organic pollutants in air and water. For example, the photocatalytic technology had been used to disinfect water utilizing the solar energy [1]. In earlier researches, to develop visible-light-driven photocatalysts, in the case of TiO$_2$, the doping with nonmetal elements was regarded as a feasible modification to expand the photoresponsive range greatly and to inhibit the recombination of photoinduced electrons and holes efficiently [2–4]. In the past decades, the nitrogen-doped titanium dioxide was regarded as an effective case to improve the visible light photoresponsivity and to shift the optical absorption edge of TiO$_2$ towards a lower energy, thereby increasing the photoactivity. Among these nonmetal dopants, iodine-doping was paid more attentions owing to altering the surface charge, shifting the photoresponse from UV to visible region and acting as a conduction-band electron scavenger capable of inhibiting the rapid recombination of photoinduced electron-hole pairs [5–17].

Bi$_2$WO$_6$ is thought to be a promising visible-light-induced photocatalyst owing to its narrow band gap, presenting intrinsic photoabsorption and photoresponsivity from UV to visible light with wavelength of shorter than ca. 450–460 nm [18–22]. However, the photocatalytic efficiency of Bi$_2$WO$_6$ is very low owing to its drawbacks, such as limited visible light photoresponse, poor adsorption performance, poor dispersivity in water and high recombination opportunities of photoinduced electron-hole pairs. To improve the photoactivity of Bi$_2$WO$_6$, many efforts

on micro/nano-structures of Bi_2WO_6 had been made by solution self-assembly of nanoplates, such as hierarchical nest-like superstructure [20, 23] and hierarchical flower-like superstructure [24]. These superstructures with high surface area and porous structure are beneficial to the adsorption of organic molecules, improving the adsorption performance of Bi_2WO_6. In addition, the hollow structure of Bi-containing multimetal oxides [25, 26] has large specific surface area and special multiple scattering of UV-vis light within hollow frameworks, improving the visible light photocatalytic activity. It is well known that high photoinduced charge recombination is harmful to the photocatalytic activity of Bi_2WO_6. Therefore, it is necessary to take some measures to improve the migration efficiency of photoinduced electrons and suppress the recombination of photoinduced electrons and holes effectively. Recently, the modification of Bi_2WO_6 with Cu nanoparticles [27] exhibited a Fenton-like synergistic effect on improving the visible-light induced photocatalytic activity. Besides, Ag nanoparticles [28], C [29, 30], TiO_2 [31–33], $PtCl_4$ [34], Bi_2O_3 [35], Ag_2O [36], and $ZnWO_4$ [37] were also used to modify the Bi_2WO_6 catalyst, which can inhibit the recombination of photoinduced electrons and holes effectively and improve the photocatalytic performance greatly. The similar $BiVO_4$ modified $Bi_2O_2CO_3$ nanosheets hierarchical structure [38] exhibits an enhanced visible light photocatalytic activity. However, few studies have been focused on the UV-induced photocatalytic performance.

In the present study, the nonmetal element of iodine was used to modify the photophysical and photochemical performances of Bi_2WO_6. Herein, the iodine-doped Bi_2WO_6 nanoplates were synthesized by a hydrothermal process, and the photocatalytic activity was evaluated in terms of the decoloration of rhodamine B (RhB) under UV and visible light irradiation. The influences of iodine doping on the structure, optical properties, and morphologies of Bi_2WO_6 were investigated. And the corresponding mechanism of enhanced photocatalytic activity of I-BWO was also proposed in this work. In addition, I_2-loaded Bi_2WO_6 was also prepared to analyze the mechanism for higher photocatalytic activity of iodine-doped Bi_2WO_6 photocatalyst.

2. Experimental

2.1. Preparation of the Iodine-Doped Bi_2WO_6 Photocatalyst.
The iodine-doped Bi_2WO_6 catalyst was synthesized by a hydrothermal reaction. In a typical process, $Bi(NO_3)_3 \cdot 5H_2O$ (10 mmol) and Na_2WO_4 (5 mmol) were dissolved in 50 mL deionized water under magnetic stirring for 2 h to obtain a homogeneous white suspension. Subsequently, KI (1 mmol) was dissolved into the above suspension under magnetic stirring. Finally, the mixture was sealed into 100 mL Teflon autoclave and maintained at 160°C for 24 h. The as-obtained precipitate was filtrated, washed, and dried at 80°C for 5 h. The as-prepared iodine-doped Bi_2WO_6 was denoted as I-BWO. For comparison, the pure Bi_2WO_6 sample was also synthesized in the absence of iodine ions, and the corresponding catalyst was abbreviated as pure BWO.

In addition, I_2-loaded Bi_2WO_6 sample was also prepared by a simple method of impregnation as following: 16 mg I_2 was dissolved into 3 mL absolute ethanol. Subsequently, the above I_2-containing solution was dropped into 0.4 g pure BWO to form a mixed slurry by grinding in an agate mortar. Finally, the absolute ethanol was volatilized in the grinding procedure to obtain the dry powders, and this sample was marked as I_2-BWO.

2.2. Characterization of Photocatalysts.
The crystalline phases of the as-prepared catalysts were confirmed by powder X-ray diffraction (XRD). The XRD patterns of the samples were obtained by using a Rigaku Multiflex diffractometer at 40 kV and 200 mA with monochromated high-intensity Cu $K\alpha$ radiation. X-ray photoelectron spectra (XPS) were performed with a VG scientific ESCA Lab Mark II spectrometer which was equipped with a monochromatic Mg $K\alpha$ ($h\nu$ = 1253.6 eV) excitation source. The binding energies obtained in the XPS spectral analysis were calibrated for specimen charging by referencing C 1s to 284.8 eV. The surface morphology of the as-synthesized samples was observed by a field emission scanning electron microscope (FE-SEM). High-resolution transmission electron microscopy (HRTEM) was performed to determine the microstructure of the samples on JEOL-2010F operated at 200 kV. To prepare the transmission electron microscopy (TEM) sample, a small amount of catalyst was ultrasonically dispersed in ethanol. A drop of such suspension was placed on a 200-mesh Cu grid with holey carbon film and dried completely in air. The UV-vis diffuse reflectance spectra (DRS) were acquired on a Shimadzu UV-2450 spectrophotometer with ISR-240A integrating sphere assembly in the range of 200–800 nm. $BaSO_4$ was used as a reflectance standard. The photoluminescence (PL) spectra of the samples were recorded with a fluorescence spectrophotometer F-4500 at the range of 400–700 nm.

2.3. Evaluation of Photocatalytic Properties.
Photocatalytic activities of the samples were evaluated by the photocatalytic degradation of rhodamine B (RhB). A 300 W Xe lamp was used as the light source with a 420 nm cutoff filter and an ultraviolet reflected filter (<400 nm) to provide visible and ultraviolet light irradiation, respectively. In the typical process, 0.05 g of photocatalyst was dispersed into a beaker, which was filled with 100 mL of 4×10^{-5} mol/L RhB solution. The as-obtained suspension was stirred for 2 h in the dark in order to establish the adsorption and desorption equilibrium between the photocatalyst and RhB. Then the suspension was irradiated under ultraviolet light (<400 nm) or visible light (>420 nm). At the given intervals, a 4 mL solution was sampled and centrifuged to remove the suspended solid photocatalyst. The concentration of RhB solution was determined by measuring the absorbance at the characteristic band of 553 nm using a Shimadzu UV-2450 spectrophotometer.

3. Results and Discussion

3.1. XRD Analysis.
The crystal phase compositions of as-prepared photocatalysts were characterized by the powder X-ray diffraction, and the corresponding XRD patterns of pure

BWO, I-BWO, and I_2-BWO samples are shown in Figure 1. All diffraction peaks of as-prepared samples appear to be in accordance with the standard orthorhombic phase of Bi_2WO_6 (JCPDS no. 39-0256). New crystal orientations or changes in preferential orientations are not observed in I-BWO and I_2-BWO comparing with pure BWO. This result indicates that the crystal phase of Bi_2WO_6 has not been influenced by the doping of I^- ions or the loading of I_2. In addition, the diffraction peaks of I-BWO and I_2-BWO are obviously weaker and broader, which indicate smaller crystalline sizes comparing with pure BWO. The average crystalline sizes calculated by the half-width of the maximum diffraction peak of the (131) crystallographic plane according to the scherrer equation for the pure BWO, I-BWO and I_2-BWO are 20.67 nm, 13.64 nm and 18.6 nm, respectively (listed in Table 1). It can be seen that compared with pure BWO, the crystalline sizes of I-BWO and I_2-BWO samples decrease. It is obvious that the crystallite growth can be inhibited by the iodine doping owing to the enhanced the energy barrier of mutual diffusion among the grains in the presence of potassium iodide caused by the repulsion among the adsorbed iodine species. However, the smaller crystalline size for I_2-BWO sample was caused by the small crystalline size of I_2. By careful comparison in Figure 1(b), the diffracted intensity of the (131) crystallographic plane in the range of $2\theta = 26$–$30°$ decreases drastically as a result of doping with I^- ions. This indicates that the crystallinity of Bi_2WO_6 becomes lower with the introducing of iodine dopant. Moreover, the diffraction peak of the (131) crystallographic plane becomes much wider by the doping of I^- ions. Table 1 compares the lattice parameters of pure BWO and I-BWO as determined by rietveld refinement of the relevant X-ray powder diffraction patterns. The lattice parameter along b-axis orientation increases owing to the doping of I^- ions.

3.2. Morphologies and Microstructures of Photocatalysts.

The typical scanning electron microscopy images of as-synthesized pure BWO, I-BWO, and I_2-BWO photocatalysts are shown in Figure 2. The pure BWO sample is composed of well-dispersed nanoplates, as shown in Figure 2. The edges of nanoplates are irregular and a slight aggregation is observed among the Bi_2WO_6 nanoplates. By contrast with pure Bi_2WO_6, the I-BWO sample is composed of sheet-like morphological nanoplates. As shown in Figure 2, the diameter of I-BWO nanoplates is smaller than that of pure BWO, and the dispersivity of nanoplates in I-BWO is better than that of pure BWO owing to the repulsion among the negatively charged iodine species adsorbed on the surface of nanoplates. However, the I_2-BWO sample is composed of the aggregated nanoplates and nanoparticles loading on the surface of Bi_2WO_6. It can be deduced that the nanoparticles are ascribed to I_2 loading on the Bi_2WO_6 nanoplates compared with the pure BWO sample. The rough surfaces of I_2-BWO are different from the smooth surfaces of pure BWO and I-BWO samples. The microstructure of the iodine-doped Bi_2WO_6 sample was investigated by TEM. Figure 3(a) shows the morphology of I-BWO synthesized by a hydrothermal reaction at 160°C for 24 h. The I-BWO sample is composed of two-dimensional nanoplates

(a)

(b)
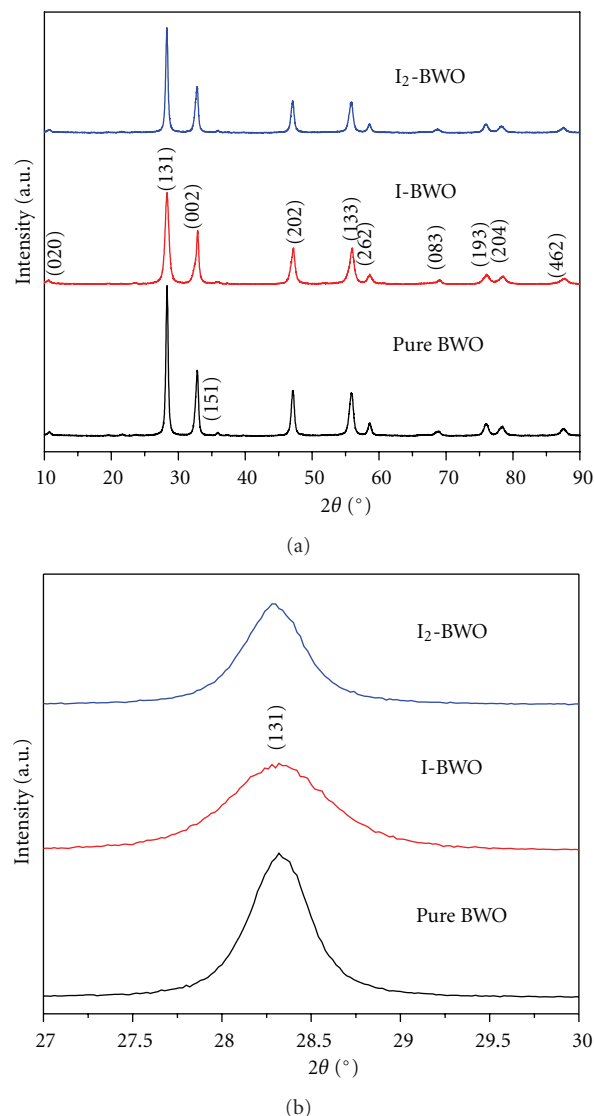
Figure 1: XRD patterns of the as-prepared pure BWO, I-BWO and I_2-BWO samples.

with the diameter of 50–100 nm. An HRTEM image of I-BWO is shown in Figure 3(b). The distance between two planes in I-BWO is about 0.248 nm, which is similar to the d-spacing of (151) plane of orthorhombic Bi_2WO_6. The selective area electron diffraction (SAED) pattern of I-BWO sample in Figure 3(c) shows the irregular electron diffraction spots, highlighting the microcrystalline nature of the I-BWO sample. The different electron diffraction spots have been indexed by measuring the interplanar crystal spacings. The characteristic spots of the SAED pattern for I-BWO were assigned to the diffractions from the (131), (262), (174), (351), and (241) planes. The microcrystalline nature of I-BWO indicates that the I-BWO sample is a transient state from polycrystalline nature to monocrystalline nature.

To further confirm the composition of the iodine-doped Bi_2WO_6, the energy dispersive spectrum was measured to analyze the elements and contents of the as-prepared I-BWO.

TABLE 1: The average crystalline sizes and lattice parameters of the as-prepared samples.

Sample	D (131)/nm	Lattice parameters		
		a/Å	b/Å	c/Å
Pure BWO	20.67	5.452	16.426	5.444
I-BWO	13.64	5.459	16.446	5.441
I_2-BWO	18.6	5.455	16.414	5.443
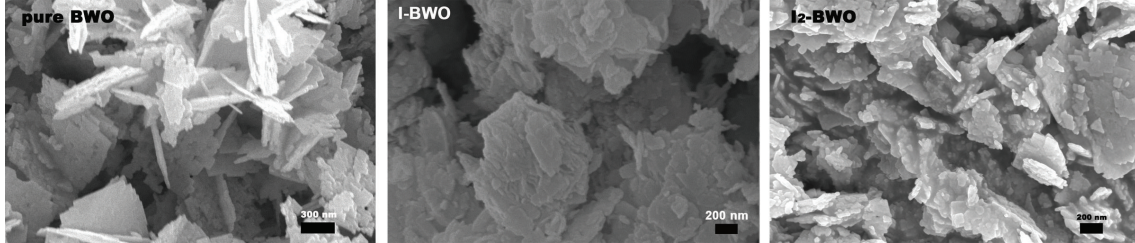
FIGURE 2: The typical SEM images of the as-prepared pure BWO, I-BWO and I_2-BWO samples.

Figure 4 shows that the main peaks of Bi, W, O, and Cu elements are exhibited in the spectrum of I-BWO, while the peak of iodine element is not observed owing to the trace doping of iodine. Herein, the peak of Cu element was ascribed to the background signal of Cu grid. There are several additional peaks of Cr, Re, Os, and Th species which are attributed to the instrumental error.

3.3. Optical Property.
The UV-visible diffuse reflectance spectra of pure BWO, I-BWO, and I_2-BWO samples are shown in Figure 5. The pure BWO sample exhibits the absorption edge around 440 nm. As shown in Figure 5(a), the I-BWO sample exhibits much stronger absorbance in the region of 200–450 nm comparing to pure BWO and its absorption band has an obvious red shift owing to the doping of I^- ions. However, the enhanced absorption in the range from 440 to 700 nm are not observed, indicating that the doping of I^- ions is formed by the surface adsorption instead of the lattice doping of Bi_2WO_6. The I_2-BWO sample has a larger red shift of absorption edge. By comparison, the I-BWO sample has a stronger ultraviolet light absorption than pure BWO and I_2-BWO. The steep shape of UV-vis diffuse spectra indicates that the absorption for visible light is not caused by the transition from the impurity level of I^- ions but is induced by the intrinsic band gap transition of Bi_2WO_6. For a crystalline semiconductor, the optical absorption near the band edge could be estimated by the equation $ah\nu = A(h\nu - E_g)^{n/2}$, where a, ν, E_g, and A are absorption coefficient, light frequency, band gap, and a constant, respectively. Herein, the value of n for Bi_2WO_6 was 1. To estimate the band gap of samples, a modified plot of Kubelka-Munk function versus the energy of exciting light was shown in Figure 5(b). The band gap energy can be estimated from a plot of $(ah\nu)^{1/2}$ versus photon energy $(h\nu)$. The intercept of the tangent to the plot will give a good approximation of the band gap energy for indirect band gap materials. The estimated band gaps for pure BWO, I-BWO, and I_2-BWO from the intercepts of the tangents to the plots were 2.57, 2.48, and 2.33 eV, respectively. This result reveals that a narrower band gap is obtained by the iodine doping, indicating that the I-BWO sample possesses a suitable band gap for utilizing visible light and photocatalytic decomposition of organic contaminants under visible light irradiation. The I_2-BWO sample has a narrower band gap than I-BWO, improving the visible light absorption by I_2 loading.

3.4. XPS Analysis.
To analyze the surface compositions and chemical states of the as-prepared iodine-doped Bi_2WO_6 sample, X-ray photoelectron spectra were obtained as shown in Figure 6. The XPS measurement for I-BWO reveals the presence of Bi, W, O, I, and C elements. The binding energies given in the XPS analysis were calibrated for specimen charging by referencing C 1s to 284.80 eV. As shown in Figure 6, the high-resolution XPS spectra of the C 1s orbit has a peak at 284.8 eV. This was attributed to the surface amorphous carbon of the referenced C 1s from the XPS instrument itself. The O 1s core level spectrum of I-BWO could be fitted by the peak at binding energy of around 530.2 eV [34] in Figure 6, indicating that the oxygen species are assigned to the lattice oxygen ions and hydroxyl oxygen on the surface [39]. The high-resolution XPS spectrum of I 3d5 core level on the surface of I-BWO is shown in Figure 6. The I 3d5 core level spectrum of I-BWO was composed of two peaks at 632.0 eV and 619.4 eV, which were ascribed to I $3d_{3/2}$ and I $3d_{5/2}$, respectively, which were different from the binding energies of 630.1 and 618.3 eV relating to the characteristic bands of iodine in I_2 [40]. Herein, the peak at 619.4 eV should be ascribed to the negatively charged iodine (I^-) species, while the other peak at 632.0 eV can be attributed to I_2 (631.0 eV). The chemical shift of 1.0 eV was caused by the surface adsorption of Bi_2WO_6 for I_2. It is probable that the I^- ions may undergo the following chemical reaction to form I_2 during the hydrothermal process: $4I^- + O_2 + 4H^+ \rightarrow 2I_2 + 2H_2O$. The trace amount of iodine dopant was measured in I-BWO by the elementary

(a)   (b)   (c)
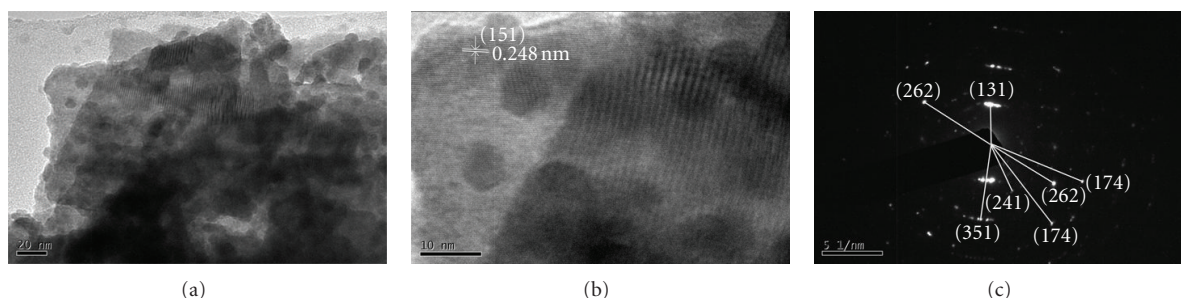
FIGURE 3: (a) TEM microphotograph of the iodine-doped Bi_2WO_6 (I-BWO); (b) high-resolution TEM photograph of I-BWO; (c) SEAD pattern of I-BWO.
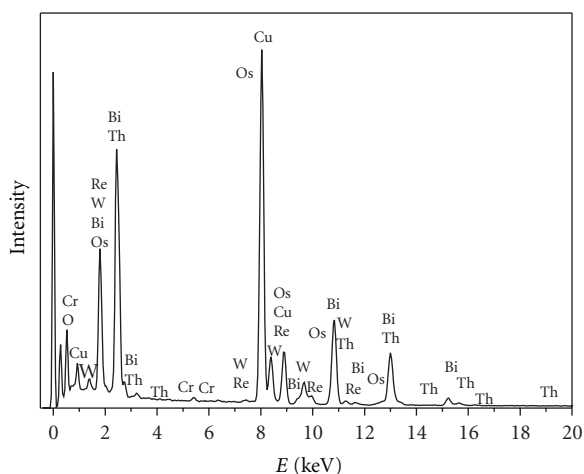
FIGURE 4: Energy dispersive spectrum for the as-prepared I-BWO.

analysis, and the atomic content of iodine dopant was 0.31%. Since the ionic radius of I^- (0.216 nm) is much larger than that of O^{2-} (0.124 nm), the substitution of O^{2-} ions in the lattice by I^- would occur difficultly. Thus I_2 and I^- species were probably adsorbed on the surface defect sites of Bi_2WO_6 nanoplates, since the position of the diffraction peaks of I-BWO are exactly the same as that of pure BWO. To determine the oxidation state of Bi, the Bi 4f XPS peak for sample I-BWO was shown in Figure 6. The characteristic spin-orbit split of Bi $4f_{5/2}$ and Bi $4f_{7/2}$ signals [41–43] at approximately 164.4 eV and 159.2 eV in I-BWO sample demonstrates that the main chemical state of bismuth in the iodine-doped sample was trivalence (Bi^{3+}), which is similar to the reported values of pure Bi_2WO_6 [44, 45]. The XPS spectrum of W 4f (Figure 6) in I-BWO shows a resolved doublet due to the tungsten W $4f_{5/2}$ and W $4f_{7/2}$ components observed at binding energies of 37.4 eV and 35.4 eV, respectively. The difference in binding energy of the resolved doublet is 2.0 eV, corresponding to the W^{6+} oxidation state. An additional resolved doublet due to the tungsten W $4f_{5/2}$ and W $4f_{7/2}$ components is observed at binding energies of 29.2 eV and 26.2 eV, respectively. The difference in binding energy of the resolved doublet is 3.0 eV, corresponding to the W^{4+} oxidation state [23, 46]. The appearance of W^{4+} valence

indicates that a lower oxidation state of tungsten element is formed by the doping of iodine. It is possible that the coordination environment of tungsten was changed owing to the coadsorption of I^- and I_2 species on the surface defect sites of sheet-like Bi_2WO_6 nanoplates.

3.5. Photocatalytic Activity for RhB under Ultraviolet and Visible Light Irradiation. After the dark adsorption, the RhB adsorption of pure BWO is only 3.5%, while that of I-BWO is up to 16%. In addition, the RhB adsorption of I_2-BWO is similar to pure BWO. Therefore, the I-BWO sample displays a higher adsorption capability for RhB than that of pure BWO and I_2-BWO. Then the photocatalytic activities of the as-prepared samples were evaluated by the degradation of RhB under ultraviolet (<400 nm) or visible light (>420 nm) irradiation. As can be seen in Figure 7, the I-BWO sample displays a higher photocatalytic activity than that of pure BWO and I_2-BWO under ultraviolet light or visible light irradiation. The photodegradation efficiencies of RhB over pure BWO, I-BWO, and I_2-BWO samples are up to 49%, 80%, and 84% after 120 minutes visible light irradiation, respectively. However, the corresponding UV-induced photodegradation efficiencies of RhB are up to 35%, 85%, and 58%, respectively. The photodegradation efficiency of RhB for I_2-BWO under visible light irradiation is slightly higher than that for I-BWO, which is caused by a lower amount of RhB owing to the strong adsorption of I-BWO for RhB. This result proved that the enhanced visible-light-induced and ultraviolet-light-induced photocatalytic activities were obtained by the doping of iodine. Furthermore, it is found that the photocatalytic activities of all photocatalysts induced by ultraviolet light are higher than that induced by visible light. To obtain the same removal rate for RhB, the visible-light-induced photodecomposition process would take much more time than the ultraviolet-light-induced photodecomposition process. As shown in Figure 7, the doping of I^- ions is more efficient to improve the photocatalytic activity of Bi_2WO_6 than the loading of I_2. The visible-light-induced photocatalytic activity of I-BWO sample is similar to that of I_2-BWO, while the UV-induced photocatalytic activity of I-BWO sample is greatly higher than that of I_2-BWO sample. The photodegradation

(a)

(b)
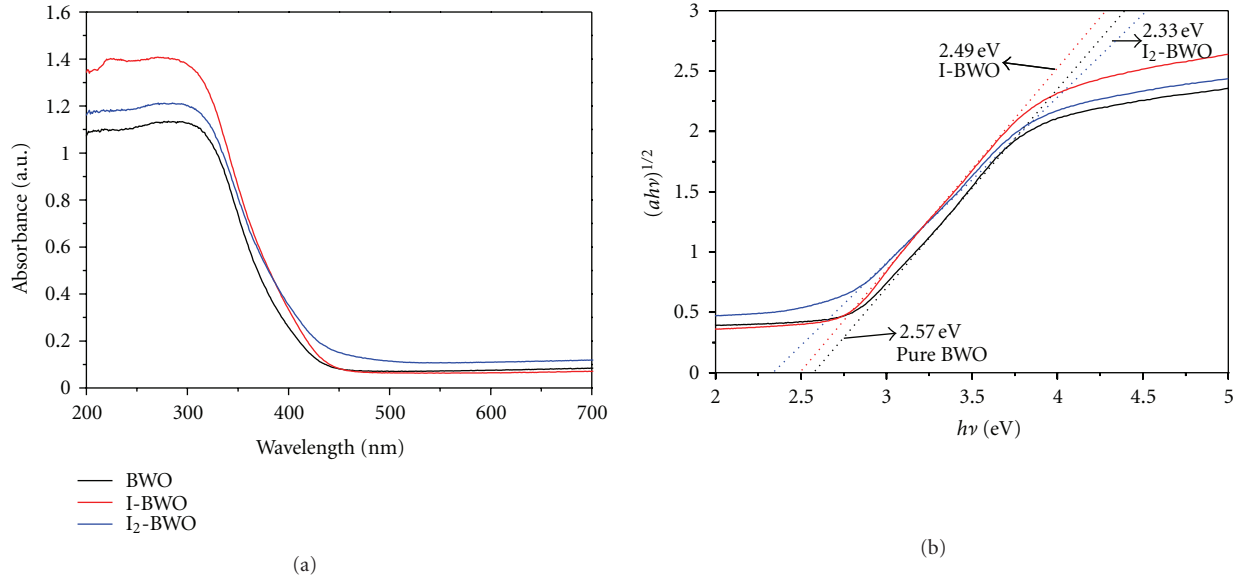
FIGURE 5: (a) UV-vis diffuse reflectance spectra for pure BWO, I-BWO, and I$_2$-BWO samples. (b) The relationship between $(ah\nu)^{1/2}$ and photon energy.

TABLE 2: The values of the photodegradation rate constant k for RhB and linearly dependent coefficient R^2.

Sample	Ultraviolet light		Visible light	
	k (mol L^{-1} min^{-1})	R^2	k (mol L^{-1} min^{-1})	R^2
Pure BWO	6.27×10^{-3}	0.929	5.97×10^{-3}	0.931
I-BWO	6.30×10^{-2}	0.947	4.03×10^{-2}	0.962
I$_2$-BWO	1.39×10^{-2}	0.994	1.72×10^{-2}	0.987

efficiency of I-BWO is 1.47 times larger than that of I$_2$-BWO. These results revealed that as-prepared catalysts were regarded as bifunctional photocatalysts, exhibiting excellent photocatalytic performances under ultraviolet and visible light irradiation.

To distinguish the photocatalytic activities of the as-prepared samples, the kinetic fitted curve plots for photodegradation of RhB under different light source with various wavelength ranges are shown in Figure 8. The corresponding values of the photodegradation rate constant k for RhB and linearly dependent coefficient R^2 were listed in Table 2. The value of $-\mathrm{Ln}(C_t/C_0)$ increased linearly with time, indicating that the photodegradation of RhB under both ultraviolet and visible light irradiation over the as-prepared samples could be described as first-order reaction [47]. The photocatalytic activities of as-prepared samples can be evaluated by the values of k, that is, the higher the value of k is, the higher the photocatalytic activity is [48]. Moreover, the larger the coefficient R^2 is, the better the linear dependence relation is. As shown in Table 2, under UV illumination, the order of the values of k was $6.27 \times 10^{-3} < 1.39 \times 10^{-2} < 6.30 \times 10^{-2}$, corresponding to the slopes of kinetic fitted curves of pure BWO, I$_2$-BWO, and I-BWO, respectively. The photodegradation rate of I-BWO is 4.53 times larger than that of I$_2$-BWO under UV

irradiation. For comparison, under visible light irradiation, the order of the values of k was $5.97 \times 10^{-3} < 1.72 \times 10^{-2} < 4.03 \times 10^{-2}$, corresponding to the slopes of kinetic fitted curves of pure BWO, I$_2$-BWO and I-BWO, respectively. The photodegradation rate of I-BWO is 2.34 times larger than that of I$_2$-BWO under visible light irradiation. As above-mentioned, the photodegradation rate for RhB under ultraviolet light irradiation was higher than that under visible light irradiation in cases of I-BWO and pure BWO. However, the photodegradation rate for RhB under ultraviolet light irradiation is lower than that under visible light irradiation in case of I$_2$-BWO. Moreover, the photodegradation rates of the I-BWO and I$_2$-BWO for RhB are higher than that of pure Bi$_2$WO$_6$, regardless of ultraviolet or visible light irradiation. It can be deduced that during the photocatalytic reaction, I^0 acted as an electron acceptor and was reduced to I$^-$, and I$^-$ was also oxidized to I^0 by photoinduced holes. Hence, an efficient separation of electron-hole pairs was obtained by surface iodine species containing I^0 and I$^-$. Thus, it is reasonable that I-BWO shows a higher photocatalytic activity than pure BWO. Different from I-BWO, the improved photocatalytic activity of I$_2$-BWO was obtained by the role of electron acceptor of I$_2$. In addition, the values of R^2 for visible-light-induced photocatalysis are higher than that for ultraviolet-light-induced photocatalysis in cases of pure
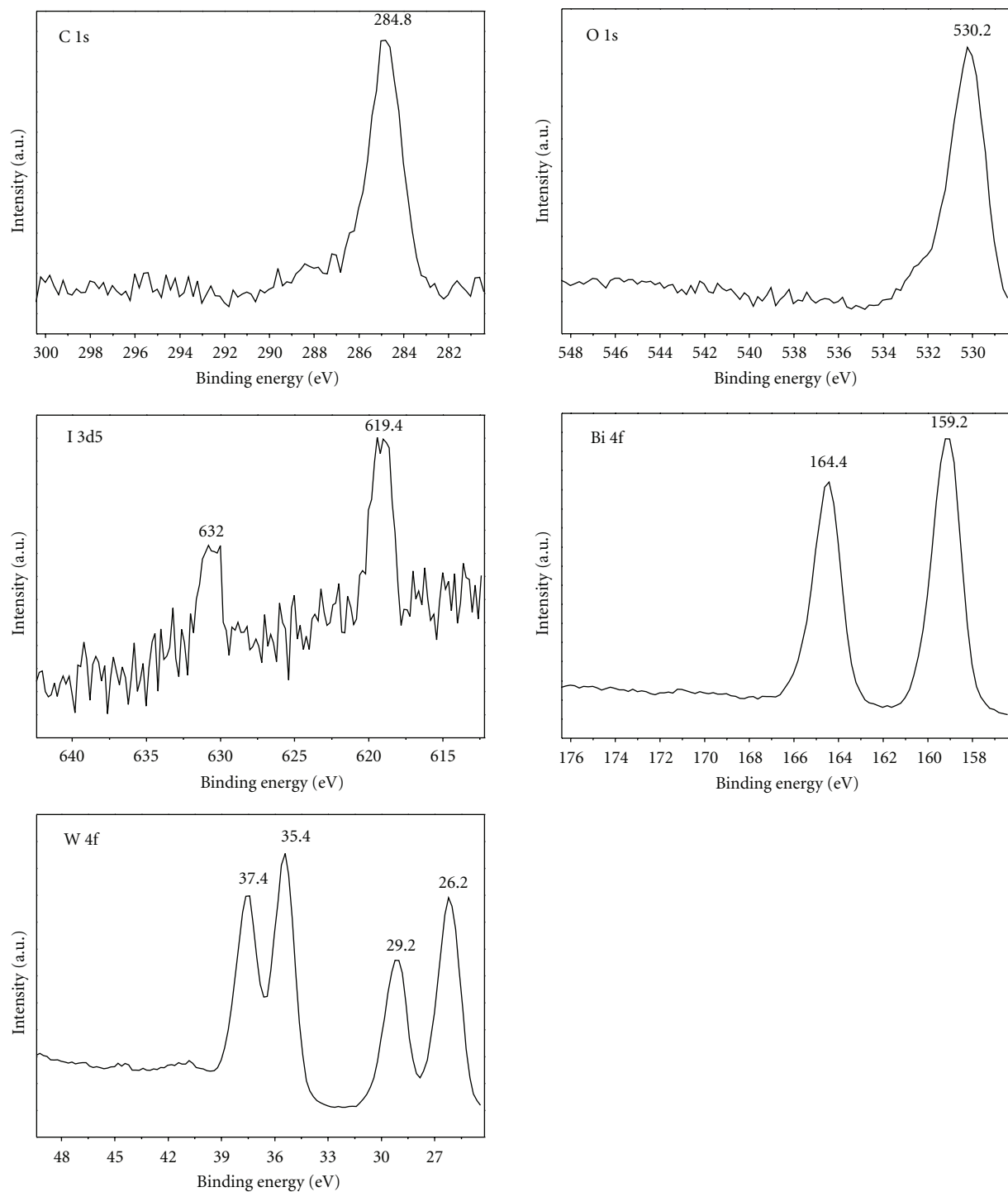
Figure 6: High-resolution XPS spectra analysis of C 1s, O 1s, I 3d5, Bi 4f, and W 4f.

BWO and I-BWO. This result proved that the linear dependence relation of visible-light-induced photocatalysis was better than that of ultraviolet-light-induced photocatalysis. And the visible-light-induced photodegradation for RhB using the as-prepared photocatalysts was even more similar to the first-order reaction.

3.6. Mechanism Discussion.

The photoluminescence (PL) spectroscope, as one of the most powerful tools, has been utilized to investigate the carrier transfer, energy transportation, and energy conversion during the photochemical and photophysical processes. According to the results of Wen's group [49], the emission of fluorescence is related to the surface
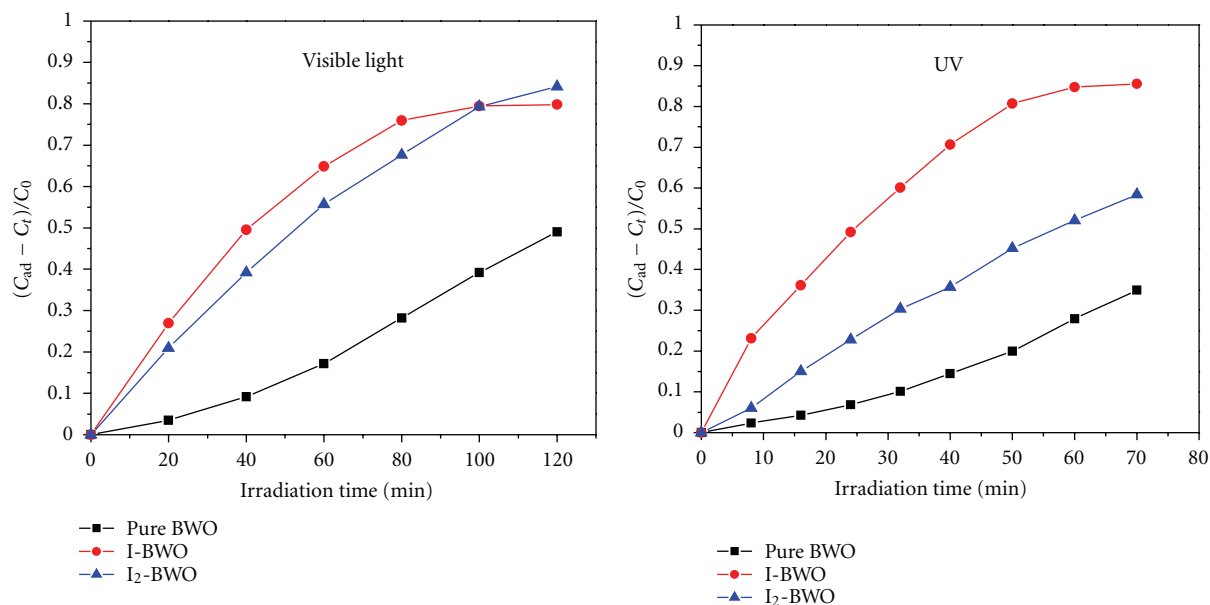
FIGURE 7: Photocatalytic activity for decomposition of rhodamine B (4×10^{-5} mol L^{-1}) under visible light (>420 nm) and ultraviolet light (<400 nm) irradiation at room temperature in air using pure BWO, I-BWO, and I$_2$-BWO as photocatalysts. C_{ad}: the concentration of RhB after dark adsorption, C_t: the concentration of RhB during the photocatalytic reaction, and C_0: the initial concentration of RhB before dark adsorption.
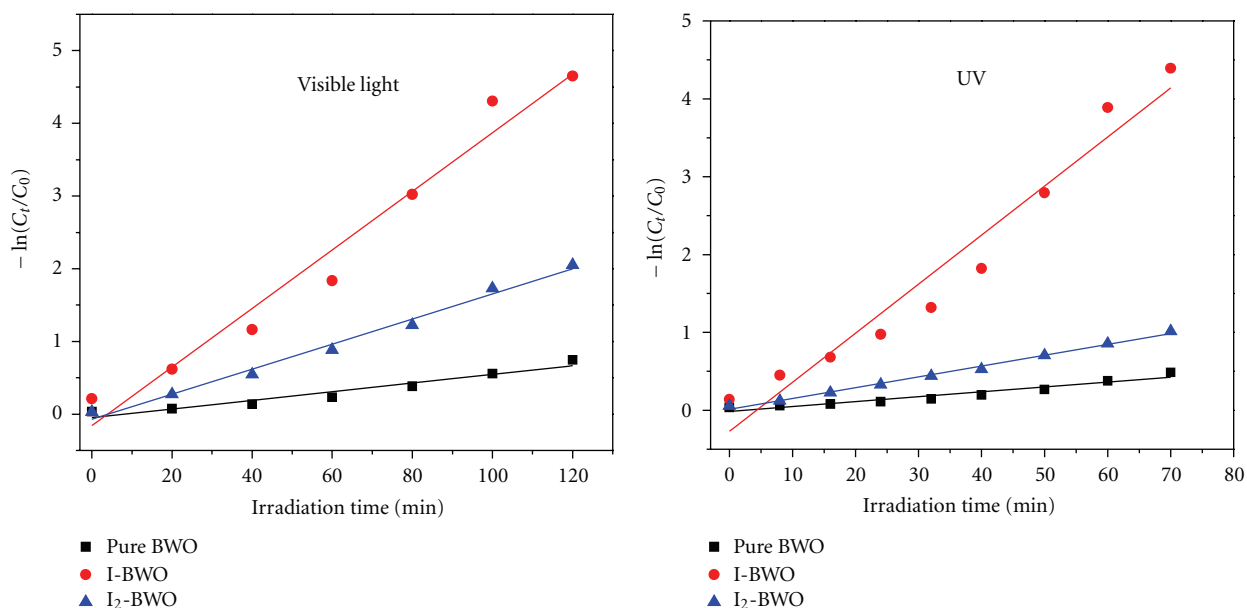
FIGURE 8: Kinetic fitted curve plots of photocatalytic degradation of RhB (4×10^{-5} mol L^{-1}) under visible light (>420 nm) and ultraviolet light (<400 nm) irradiation at room temperature in air over the as-prepared photocatalysts.

states or the density of defects. And the PL intensity originates from the number of recombination of the photoexcited electron-hole pairs; low intensity of fluorescence means a low recombination rate for the photoexcited electrons and holes. Figure 9 exhibits the PL spectra of pure BWO and I-BWO excited at different wavelengths. Figure 9(a) shows the PL spectra of the as-prepared samples excited by light with a wavelength of 338 nm in UV region. An obvious

visible band is obtained in the range of 430–520 nm, which is ascribed to a broad blue-green emission. The iodine-doped Bi$_2$WO$_6$ sample displays a large enhancement in the visible luminescence. And the PL intensity of I-BWO is greatly higher than that of pure BWO, indicating that the PL enhancement effect is caused by the doping of iodine species. However, the positions of PL peaks do not shift and there is no new PL peaks observed owing to the introduction
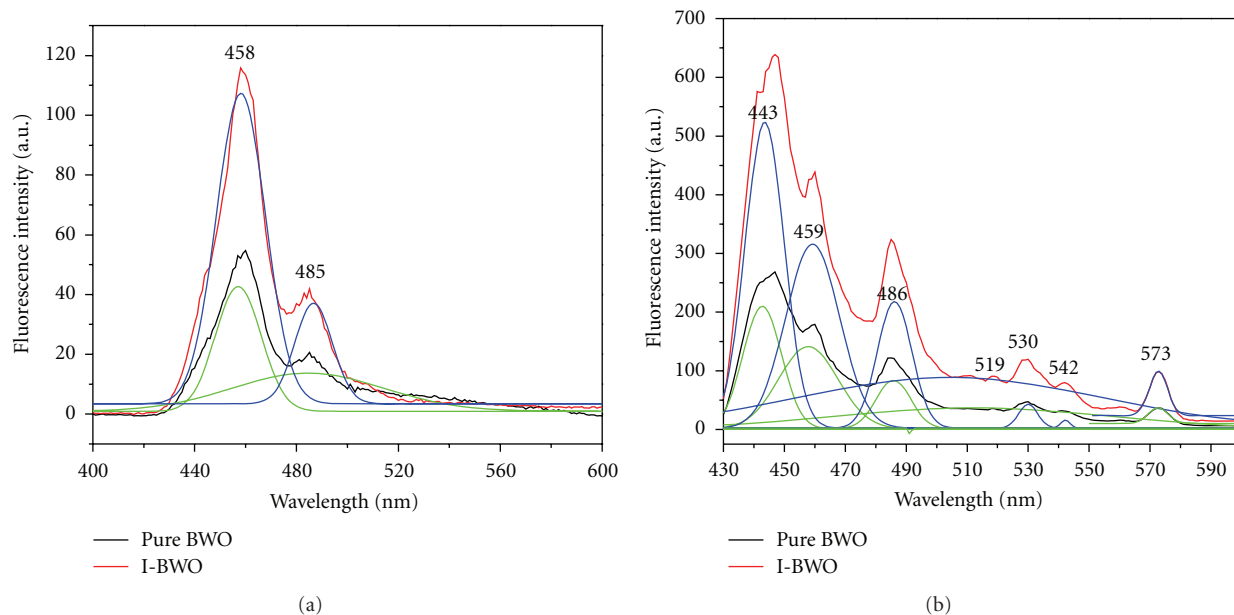
FIGURE 9: The room temperature Photoluminescence spectra of pure BWO and I-BWO (a) monitored at 338 nm, (b) monitored at 420 nm.

of iodine dopant. The visible band can be easily fitted with two broad Gaussian bands (Figure 9(a)), located in the blue (2.82–2.64 eV; 440–470 nm) and in the blue-green parts of the visible spectrum (2.70–2.38 eV; 460–520 nm) [14]. The strongest blue-emitting peaks at 458 nm were attributed to the intrinsic blue luminescence of Bi_2WO_6, which originates from the charge-transfer transitions between the hybrid orbital of Bi 6s and O 2p(VB) and the empty W 5d orbital (CB) in the $[WO_6]^{2-}$ complex. In addition, this emission peak reveals the spectral dependence of the intrinsic band-edge absorption for Bi_2WO_6. The redundant emitting peak at 485 nm (green) is ascribed to the defects of metal atoms and oxygen vacancies during the crystal growth process, which will become many defect centers, and thus affect the optical properties of Bi_2WO_6 [8]. For comparison, Figure 9(b) shows the PL spectra of the as-prepared samples excited by light with a wavelength of 420 nm in visible light region. Different from the situation of UV-excitation, there are several additional visible Gaussian bands around 443, 519, 530, 542, and 573 nm besides the above-mentioned two visible bands around 459 and 486 nm. The strong blue emission band centered at 443 nm is attributed to the intrinsic transition of Bi^{3+} ions from the 3P1 (6s6p) excited state to the 1S0 (6S2) ground state. The four visible bands around 519, 530, 542, and 573 nm are ascribed to the defects of oxygen vacancies caused by the doping of iodine. The enhanced visible PL intensity is also observed in the situation of visible light excitation in I-BWO. From the results of XRD, I-BWO possesses a smaller crystallite size than pure BWO, indicating a higher density of surface defects or oxygen vacancies. In the case of light excitation, the transition of photoinduced electrons increased with the increasing light absorption caused by surface defect, resulting in the enhancement of responding PL intensity [49].

According to the previous theoretical calculations [50], the coadsorption of I^- and IO_4^- ions on the defect surface of TiO_2 would result in the formation of new energy bands between the conduction band bottom and the valence band top of TiO_2. In the same way, the new energy bands was also introduced into the energy band structure of Bi_2WO_6 by the coadsorption of I^0 and I^- ions on the defect surface of Bi_2WO_6. The redox potential $E^0(I^0/I^-)$ = 0.54 V lies between the conduction band E_{cb} (Bi_2WO_6) = 0.46 V and the valence band E_{vb} (Bi_2WO_6) = 3.26 V [51]; hence the excitation of an electron from the valence band of Bi_2WO_6 to the surface adsorbed I^0 is qualified as practical. The photoinduced electrons are captured by the surface I^0 to produce I^-, while the holes left on the valence band of Bi_2WO_6 can induce the production of hydroxyl radicals (•OH) and further degrade the organic pollutants. In addition, the photocatalytic activity of I-BWO is higher than I_2-BWO. This indicates that the photoinduced electron is also utilized to accelerate the photodegradation of RhB via the capture of hole by surface I^- ions. Based on the results of XRD analysis, the crystallinity of the I-BWO was lower than that of pure BWO, which was not beneficial to improving the photocatalytic activity. However, it was found that the photocatalytic activity of I-BWO was higher than that of pure BWO. Therefore, we deduced that the crystallinity was not the decisive factor controlling photocatalytic activity. According to the results of UV-vis absorption spectra, a slight red shift of absorption spectrum for I-BWO was caused by the doping of I^- ions. The band gap estimated from absorption spectrum for I-BWO is slightly lower than that of pure BWO, indicating that the energy band structure becomes narrower by the doping of iodine. Although the light absorption had never been improved greatly, the doping of iodine resulted in the formation of an

impurity energy level at the bottom of conduction band of Bi_2WO_6. The narrowing band gap of I-BWO was beneficial to increasing the transfer rate of electrons to the photocatalyst surface, improving the separation efficiency of photoinduced electrons and holes. The small crystalline size of I-BWO is beneficial to the fast transfer of photoinduced electrons, improving the photocatalytic activity for the degradation of RhB. By comparison with I_2-BWO, the photoinduced electrons and holes are utilized efficiently to improve the photocatalytic activity of I-BWO. In the XPS analysis, the appearance of W^{4+} was caused by the lattice distortion of Bi_2WO_6 crystal owing to the surface adsorbed I^- species, resulting in the rearrangement of the internal electric field of Bi_2WO_6. In addition, the enhanced PL intensity of I-BWO proved the existence of defects of oxygen vacancies due to the doping of iodine, facilitating the effective separation of photoinduced electrons and holes and even enhancing the photocatalytic activity for the degradation of RhB.

4. Conclusion

The iodine-dope Bi_2WO_6 nanopaltes were synthesized via a hydrothermal process. The band gaps of I-BWO and I_2-BWO were narrower than that of pure BWO, resulting in the enhanced photoabsorption and photoresponsivity for visible light, increasing the number of photoinduced electron-hole pairs. The defects of oxygen vacancies caused by the doping of iodine were proved to be responsible for the enhanced PL intensity. As shown in XPS analysis, the multivalency iodine species including I^0 and I^- were coadsorbed on the defect surface of Bi_2WO_6. I^0 can be regarded as the acceptor of photoinduced electrons, while I^- can act as the acceptor of photoinduced holes. Hence, I-BWO exhibits more effective separation of the photoinduced electron-hole pairs than I_2-BWO. The as-prepared I-BWO exhibited the highest photocatalytic activities for photodegradation of RhB regardless of UV or visible light irradiation. The above-mentioned factors were responsible for the enhanced photocatalytic activity during the photodegradation of RhB. Moreover, the UV-induced photocatalytic activity was much higher than the visible-induced photoactivity. The iodine-doped Bi_2WO_6 could be regarded as a bifuncitonal photocatalyst to deal with the pollutants existing in water and air.

Acknowledgment

References

[1] J. A. Byrne, P. A. Fernandez-Ibañez, P. S. M. Dunlop, D. M. A. Alrousan, and J. W. J. Hamilton, "Photocatalytic enhancement for solar disinfection of water: a review," *International Journal of Photoenergy*, vol. 2011, Article ID 798051, 12 pages, 2011.

[2] R. Kun, S. Tarján, A. Oszkó et al., "Preparation and characterization of mesoporous N-doped and sulfuric acid treated anatase TiO_2 catalysts and their photocatalytic activity under UV and Vis illumination," *Journal of Solid State Chemistry*, vol. 182, no. 11, pp. 3076–3084, 2009.

[3] G. Liu, X. Wang, L. Wang et al., "Drastically enhanced photocatalytic activity in nitrogen doped mesoporous TiO_2 with abundant surface states," *Journal of Colloid and Interface Science*, vol. 334, no. 2, pp. 171–175, 2009.

[4] J. Yu, M. Jaroniec, and G. Lu, "TiO_2 photocatalytic materials," *International Journal of Photoenergy*, vol. 2012, Article ID 206183, 5 pages, 2012.

[5] Y. Ma, J. W. Fu, X. Tao, X. Li, and J. F. Chen, "Low temperature synthesis of iodine-doped TiO_2 nanocrystallites with enhanced visible-induced photocatalytic activity," *Applied Surface Science*, vol. 257, no. 11, pp. 5046–5051, 2011.

[6] Z. He, L. Zhan, F. Hong et al., "A visible light-responsive iodine-doped titanium dioxide nanosphere," *Journal of Environmental Sciences*, vol. 23, no. 1, pp. 166–170, 2011.

[7] R. Long, Y. Dai, and B. Huang, "Structural and electronic properties of iodine-doped anatase and rutile TiO_2," *Computational Materials Science*, vol. 45, no. 2, pp. 223–228, 2009.

[8] C. Wen, L. Sun, J. M. Zhang, H. Deng, and P. Wang, "Effect of iodine-doping on photocatalytic activity of TiO_2 photocatalyst," *Chemical Journal of Chinese Universities*, vol. 27, no. 12, pp. 2408–2410, 2006.

[9] W. Su, Y. Zhang, Z. Li et al., "Multivalency iodine doped TiO_2: preparation, characterization, theoretical studies, and visible-light photocatalysis," *Langmuir*, vol. 24, no. 7, pp. 3422–3428, 2008.

[10] S. Tojo, T. Tachikawa, M. Fujitsuka, and T. Majima, "Iodine-doped TiO_2 photocatalysts: correlation between band structure and mechanism," *Journal of Physical Chemistry C*, vol. 112, no. 38, pp. 14948–14954, 2008.

[11] G. Liu, C. Sun, X. Yan et al., "Iodine doped anatase TiO_2 photocatalyst with ultra-long visible light response: correlation between geometric/electronic structures and mechanisms," *Journal of Materials Chemistry*, vol. 19, no. 18, pp. 2822–2829, 2009.

[12] Y. Su, Y. Xiao, X. Fu, Y. Deng, and F. Zhang, "Photocatalytic properties and electronic structures of iodine-doped TiO_2 nanotubes," *Materials Research Bulletin*, vol. 44, no. 12, pp. 2169–2173, 2009.

[13] Z. He, L. Xie, J. Tu et al., "Visible light-induced degradation of phenol over iodine-doped titanium dioxide modified with platinum: role of platinum and the reaction mechanism," *Journal of Physical Chemistry C*, vol. 114, no. 1, pp. 526–532, 2010.

[14] F. Barka-Bouaifel, B. Sieber, N. Bezzi et al., "Synthesis and photocatalytic activity of iodine-doped ZnO nanoflowers," *Journal of Materials Chemistry*, vol. 21, no. 29, pp. 10982–10989, 2011.

[15] Q. Hou, Y. Zheng, J. F. Chen, W. Zhou, J. Deng, and X. Tao, "Visible-light-response iodine-doped titanium dioxide nanocrystals for dye-sensitized solar cells," *Journal of Materials Chemistry*, vol. 21, no. 11, pp. 3877–3883, 2011.

[16] Y. Z. Zheng, X. Tao, Q. Hou, D. T. Wang, W. L. Zhou, and J. F. Chen, "Iodine-doped ZnO nanocrystalline aggregates for improved dye-sensitized solar cells," *Chemistry of Materials*, vol. 23, no. 1, pp. 3–5, 2011.

[17] W. A. Wang, Q. Shi, Y. P. Wang, J. L. Cao, G. Q. Liu, and P. Y. Peng, "Preparation and characterization of iodine-doped mesoporous TiO_2 by hydrothermal method," *Applied Surface Science*, vol. 257, no. 8, pp. 3688–3696, 2011.

[18] Z. Zhang, W. Wang, J. Xu, M. Shang, J. Ren, and S. Sun, "Enhanced photocatalytic activity of Bi_2WO_6 doped with upconversion luminescence agent," *Catalysis Communications*, vol. 13, no. 1, pp. 31–34, 2011.

[19] L. Zhang, Y. Man, and Y. Zhu, "Effects of Mo replacement on the structure and visible-light-induced photocatalytic performances of Bi_2WO_6 photocatalyst," *ACS Catalysis*, vol. 1, no. 8, pp. 841–848, 2011.

[20] L. Zhang, H. Wang, Z. Chen, P. K. Wong, and J. Liu, "Bi_2WO_6 micro/nano-structures: synthesis, modifications and visible-light-driven photocatalytic applications," *Applied Catalysis B*, vol. 106, no. 1-2, pp. 1–13, 2011.

[21] Y. J. Chen, Y. Q. Zhang, C. Liu, A. M. Lu, and W. H. Zhang, "Photodegradation of malachite green by nanostructured Bi_2WO_6 visible light-induced photocatalyst," *International Journal of Photoenergy*, vol. 2012, Article ID 510158, 6 pages, 2012.

[22] J. Yu, J. Xiong, B. Cheng, Y. Yu, and J. Wang, "Hydrothermal preparation and visible-light photocatalytic activity of Bi_2WO_6 powders," *Journal of Solid State Chemistry*, vol. 178, no. 6, pp. 1968–1972, 2005.

[23] J. Wu, F. Duan, Y. Zheng, and Y. Xie, "Synthesis of Bi_2WO_6 nanoplate-built hierarchical nest-like structures with visible-light-induced photocatalytic activity," *Journal of Physical Chemistry C*, vol. 111, no. 34, pp. 12866–12871, 2007.

[24] S. Liu and J. Yu, "Cooperative self-construction and enhanced optical absorption of nanoplates-assembled hierarchical Bi_2WO_6 flowers," *Journal of Solid State Chemistry*, vol. 181, no. 5, pp. 1048–1055, 2008.

[25] B. Cheng, W. G. Wang, L. Shi, J. Zhang, J. R. Ran, and H. G. Yu, "One-pot template-free hydrothermal synthesis of monoclinic $BiVO_4$ hollow microspheres and their enhanced visible-light photocatalytic activity," *International Journal of Photoenergy*, vol. 2012, Article ID 797968, 10 pages, 2012.

[26] D. Wu, H. Zhu, C. Zhang, and L. Chen, "Novel synthesis of bismuth tungstate hollow nanospheres in water-ethanol mixed solvent," *Chemical Communications*, vol. 46, no. 38, pp. 7250–7252, 2010.

[27] J. Xu, W. Wang, E. Gao, J. Ren, and L. Wang, "Bi_2WO_6/Cu^0: a novel coupled system with enhanced photocatalytic activity by Fenton-like synergistic effect," *Catalysis Communications*, vol. 12, no. 9, pp. 834–838, 2011.

[28] J. Ren, W. Wang, S. Sun, L. Zhang, and J. Chang, "Enhanced photocatalytic activity of Bi_2WO_6 loaded with Ag nanoparticles under visible light irradiation," *Applied Catalysis B*, vol. 92, no. 1-2, pp. 50–55, 2009.

[29] Y. Li, J. Liu, X. Huang, and J. Yu, "Carbon-modified Bi_2WO_6 nanostructures with improved photocatalytic activity under visible light," *Dalton Transactions*, vol. 39, no. 14, pp. 3420–3425, 2010.

[30] E. Gao, W. Wang, M. Shang, and J. Xu, "Synthesis and enhanced photocatalytic performance of graphene-Bi_2WO_6 composite," *Physical Chemistry Chemical Physics*, vol. 13, no. 7, pp. 2887–2893, 2011.

[31] S. Murcia López, M. C. Hidalgo, J. A. Navío, and G. Colón, "Novel Bi_2WO_6-TiO_2 heterostructures for rhodamine B degradation under sunlike irradiation," *Journal of Hazardous Materials*, vol. 185, no. 2-3, pp. 1425–1434, 2011.

[32] M. Shang, W. Wang, L. Zhang, S. Sun, L. Wang, and L. Zhou, "3D Bi_2WO_6/TiO_2 hierarchical heterostructure: controllable synthesis and enhanced visible photocatalytic degradation performances," *Journal of Physical Chemistry C*, vol. 113, no. 33, pp. 14727–14731, 2009.

[33] J. Zhang, Z. H. Huang, Y. Xu, and F. Y. Kang, "Sol-gel-hydrothermal synthesis of the heterostructured TiO_2/N-Bi_2WO_6 composite with high-visible-light- and ultraviolet-light-induced photocatalytic performances," *International Journal of Photoenergy*, vol. 2012, Article ID 469178, 12 pages, 2012.

[34] F. Duan, Y. Zheng, and M. Chen, "Flowerlike $PtCl_4/Bi_2WO_6$ composite photocatalyst with enhanced visible-light-induced photocatalytic activity," *Applied Surface Science*, vol. 257, no. 6, pp. 1972–1978, 2011.

[35] M. Ge, Y. Li, L. Liu, Z. Zhou, and W. Chen, "Bi_2O_3-Bi_2WO_6 composite microspheres: hydrothermal synthesis and photocatalytic performances," *Journal of Physical Chemistry C*, vol. 115, no. 13, pp. 5220–5225, 2011.

[36] H. G. Yu, R. Liu, X. F. Wang, P. Wang, and J. G. Yu, "Enhancedvisible-lightphotocatalyticactivity of Bi_2WO_6 nanoparticles by Ag_2O cocatalyst," *Applied Catalysis B*, vol. 111-112, pp. 326–333, 2012.

[37] Q. Zhang, X. Chen, Y. Zhou, G. Zhang, and S. H. Yu, "Synthesis of $ZnWO_4@MWO_4$ (M = Mn, Fe) core-shell nanorods with optical and antiferromagnetic property by oriented attachment mechanism," *Journal of Physical Chemistry C*, vol. 111, no. 10, pp. 3927–3933, 2007.

[38] P. Madhusudan, J. R. Ran, J. Zhang, J. G. Yu, and G. Liu, "Novel urea assisted hydrothermal synthesis of hierarchical $BiVO_4/Bi_2O_2CO_3$ nanocomposites with enhanced visible-light photocatalytic activity," *Applied Catalysis B*, vol. 110, pp. 286–295, 2011.

[39] J. Bi, L. Wu, Z. Li, Z. Ding, X. Wang, and X. Fu, "A facile microwave solvothermal process to synthesize $ZnWO_4$ nanoparticles," *Journal of Alloys and Compounds*, vol. 480, no. 2, pp. 684–688, 2009.

[40] Z. Zheng, Z. H. Ai, M. Wang, and L. Z. Zhang, "Doping iodine in CdS for pure hexagonal phase, narrower band gap, and enhanced photocatalytic activity," *Journal of Materials Research*, vol. 26, no. 5, pp. 710–719, 2011.

[41] L. Wu, J. Bi, Z. Li, X. Wang, and X. Fu, "Rapid preparation of Bi_2WO_6 photocatalyst with nanosheet morphology via microwave-assisted solvothermal synthesis," *Catalysis Today*, vol. 131, no. 1–4, pp. 15–20, 2008.

[42] X. Chang, J. Huang, C. Cheng et al., "Photocatalytic decomposition of 4-t-octylphenol over $NaBiO_3$ driven by visible light: catalytic kinetics and corrosion products characterization," *Journal of Hazardous Materials*, vol. 173, no. 1–3, pp. 765–772, 2010.

[43] Y. Guo, X. Yang, F. Ma et al., "Additive-free controllable fabrication of bismuth vanadates and their photocatalytic activity toward dye degradation," *Applied Surface Science*, vol. 256, no. 7, pp. 2215–2222, 2010.

[44] D. Wu, H. Zhu, C. Zhang, and L. Chen, "Novel synthesis of bismuth tungstate hollow nanospheres in water-ethanol mixed solvent," *Chemical Communications*, vol. 46, no. 38, pp. 7250–7252, 2010.

[45] L. Ge and J. Liu, "Efficient visible light-induced photocatalytic degradation of methyl orange by QDs sensitized CdS-Bi_2WO_6," *Applied Catalysis B*, vol. 105, no. 3-4, pp. 289–297, 2011.

[46] H. Fu, C. Pan, W. Yao, and Y. Zhu, "Visible-light-induced degradation of rhodamine B by nanosized Bi_2WO_6," *Journal of Physical Chemistry B*, vol. 109, no. 47, pp. 22432–22439, 2005.

[47] C. Zhang and Y. Zhu, "Synthesis of square Bi_2WO_6 nanoplates as high-activity visible-light-driven photocatalysts," *Chemistry of Materials*, vol. 17, no. 13, pp. 3537–3545, 2005.

[48] S. Zhang, C. Zhang, Y. Man, and Y. Zhu, "Visible-light-driven photocatalyst of Bi_2WO_6 nanoparticles prepared via amorphous complex precursor and photocatalytic properties," *Journal of Solid State Chemistry*, vol. 179, no. 1, pp. 62–69, 2006.

[49] C. Wen, L. Sun, J. M. Zhang, H. Deng, and P. Wang, "Effect of iodine-doping on photocatalytic activity of TiO_2 photocatalyst," *Chemical Journal of Chinese Universities*, vol. 27, no. 12, pp. 2408–2410, 2006.

[50] W. Su, Y. Zhang, Z. Li et al., "Multivalency iodine doped TiO_2: preparation, characterization, theoretical studies, and visible-light photocatalysis," *Langmuir*, vol. 24, no. 7, pp. 3422–3428, 2008.

[51] Z. Zhang, W. Wang, L. Wang, and S. Sun, "Enhancement of visible-light photocatalysis by coupling with narrow-band-gap semiconductor: a case study on Bi_2S_3/Bi_2WO_6," *Acs Applied Materials & Interfaces*, vol. 4, no. 2, pp. 593–597, 2012.

Research Article

Rapid Decolorization of Cobalamin

Falah H. Hussein and Ahmed F. Halbus

Chemistry Department, College of Science, Babylon University, P.O. Box 51002, Hilla, Iraq

Correspondence should be addressed to Falah H. Hussein, abohasan_hilla@yahoo.com

The photocatalytic decolorization of cobalamin was carried out in aqueous solution of different types of catalysts including ZnO, TiO_2 (Degussa P25), TiO_2 (Hombikat UV100), TiO_2 (Millennium PC105), and TiO_2 (Koronose 2073) by using UVA source of irradiation. The effect of various parameters such as photocatalyst amount, cobalamin concentration, type of catalyst, pH of aqueous solution, light intensity, addition of H_2O_2, flow rate of O_2, type of current gas, and temperature on photocatalytic oxidation was investigated. The results indicated that the photocatalytic decolorization of cobalamin was well described by pseudo-first-order kinetics according to the Langmuir-Hinshelwood model. The effect of temperature on the efficiency of photodecolorization of cobalamin was also studied in the range 278–298 K. The activation energy was calculated according to Arrhenius plot and was found equal to 28 ± 1 kJ·mol^{-1} for ZnO and 22 ± 1 kJ·mol^{-1} for TiO_2 (Degussa P25). The results of the total organic carbon (TOC) analysis indicate that the rate of decolorization of dye was faster than the total mineralization. Decolorization and mineralization of cobalamin in the absence of light and/or catalyst were performed to demonstrate that the presence of light and catalyst is essential for the decolorization of this cobalamin. The results show that the activity of different types of catalysts used in this study was of the sequence: ZnO > TiO_2 (Degussa P25) > TiO_2 (Hombikat UV100) > TiO_2 (Millennium PC105) > TiO_2 (Koronose 2073).

1. Introduction

Frank and Bard in 1977 stated that it was possible to use TiO_2 to degrade the organic compound in water [1]. Photodegradation of organic and inorganic pollutants on different types of semiconductors has been studied by several researchers. Dyes have become one of the important industry pollutants that lead to environmental contamination. To find a general process for treatmentof the color of dye used in dyeing processes is very difficult due to the complexity and variety of these types of industrial wastewater [2]. In recent years, the interest has been focused on the use of semiconductor in photocatalytic decolorization of different types of wastewater where the band gap for zinc oxide is ($\sim$3.2 e.V). In addition, their photocatalytic activities are shown only under UV irradiations. However, the presence of colored compounds on the surface of the semiconductor can absorb a radiation in the visible range and then is excited by a process called photosensitization process. The hydroxyl group radical ($^{\bullet}$OH), which is formed by the photocatalytic process, from the photosensitization processes, will oxidize all the organic compounds to CO_2 and H_2O (mineralization) [3]. Several processes were used for the treatment of pollutants such as biodegradation, catalytic oxidation, chemical treatment (chlorine, ozone, hydrogen peroxide), and degradation by high-energy ultraviolet light [4, 5]. One of the active methods to treat the colored wastewater is advance oxidation process (AOP) including photocatalysis degradation systems which use a semiconductor (TiO_2 or ZnO) and UV light [6]. Titanium dioxide is one of the best materials which have good ability to destroy the organic materials and active species to un-harmful material by using light/semiconductor system [7].

The photocatalytic activity of semiconductors can be enhanced by using different techniques [8–15]. Zhou et al. showed that doping of titanium dioxide with gold (Au–TiO_2) nanocomposites gives higher activity in visible-light for degradation of Rhodamine-B (RhB) in water [8].

Wang et al. observed that the calcination temperature of TiO_2 (P25) at 500°C caused to double the activity of TiO_2
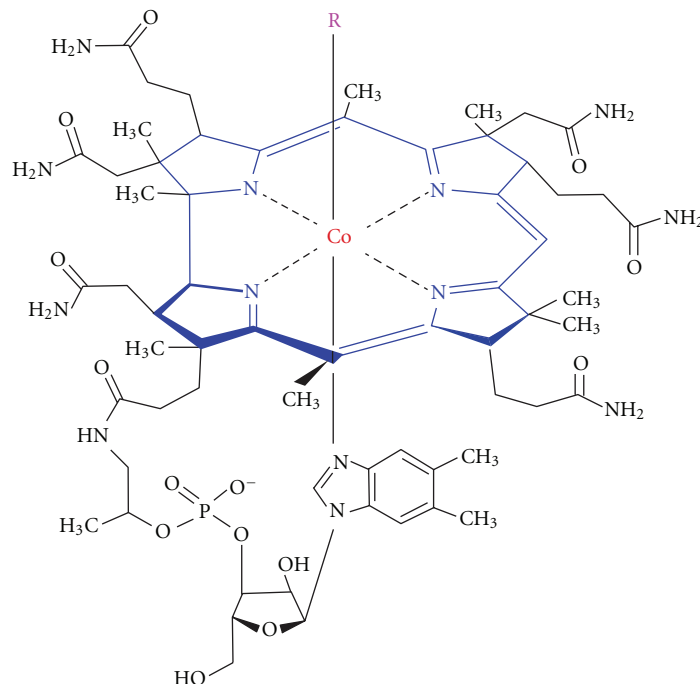
FIGURE 1: Structure of cobalamin.

(P25) for photocatalytic degradation of methyl orange (MO) [9]. Wu et al. studied a comparison between the photocatalytic activity (PC) and photoelectrocatalytic activity (PEC) of methylene blue (MB) [11]. They have noticed that the photoelectrocatalytic activity is more efficient than photocatalytic activity. There are different studies using doped metal on TiO_2 surface to enhance the activity of catalyst or to reduce the band gab of semiconductor [10–15].

Heterogeneous photocatalysis is a method used for the degradation of various types of organic pollutants in water and wastewater [16]. Different types of semiconductors such as TiO_2, ZnO, CdS, and ZnS and irradiation source of UV or visible lights can be used in photocatalysis systems. In the process of irradiation of the semiconductor with energy equal or greater than the band gap, the electrons in valence band are promoted to the conduction band leaving a hole behind. The holes at the valence bond have an oxidation potential of +2.6 V with normal hydrogen electrode (NHE) at pH = 7. This energy is enough to oxidize water molecule or hydroxide and produce hydroxyl radicals or oxidize wastewater containing various types of dyes [17, 18]. The photosensitization process is defined in summary term as photocatalytic decolorization of dyes, and this process also follows the mechanism of free radical, where the adsorbed dyes molecules on the semiconductor surface have ability to absorb a radiation in with short wavelength or in the visible region [19–21]. Therefore the excited colored dye either in singlet or triplet states shall inject an electron to the conduction band for the chosen semiconductor [22].

Porphyrins are aromatic compounds that have a highly conjugated system and composed of four smaller 5-membered heterocycles. They are called pyrroles that contain one nitrogen and four carbon atoms. In porphyrins, one carbon is typically referred to as the mesocarbon, serving the connection of each of the four pyrrole rings [23]. Porphyrins are intensely colored cyclic molecules which occur in nature as in green leaves and red blood cells. Porphyrins are characterized by the presence of four modified pyrrole subunits interconnected at their α carbon atoms with methane bridges (=CH–) [24].

Cobalamin, also known as vitamin B_{12}, is a complex organometallic compound which is formed by the situated cobalt atom in a corrin ring [25]. The structure of cobalamin is shown in Figure 1.

The central metal ion in the cobalamin is cobalt. While four of the six coordination sites are provided by the corrin ring, the fifth is provided by a dimethylbenzimidazole group. The sixth coordination site, the center of reactivity, is variable as it can be a cyano group (–CN), a hydroxyl group (–OH), a methyl group (–CH_3), or a 5′-deoxyadenosyl group (here the C5′ atom of the deoxyribose forms the covalent bond with Co), respectively, to yield the four cobalamin forms mentioned above [26].

Cobalamin is soluble in water and has the molecular formula $C_{63}H_{88}CoN_{14}O_{14}P$, mole mass 1355.37 g/mol. The systematic (IUPAC) name is α-(5,6-dimethylbenzimidazolyl) cobamidcyanide. It can be produced industrially only through bacterial fermentation-synthesis. Cobalamin consists of a class of chemically-related compounds (vitamers) such as cyanocobalamin, methylcobalamin, adenosylcobalamin, and hydroxocobalamin. The various forms of isomers of B_{12} are all deeply red colored, due to the color of the cobalt-corrin complex [27]. Photolysis of cobalamin in aqueous solution produced hydroxocobalamin. The kinetics

of photolysis was found to follow zero-ordar kinetics at different pH and the rate was catalysed by both hydrogen and hydroxyl ions [28].

The idea of this work was derived from the announcement of NineSigma company in October 2010 about decolorization of porphyrin species proposal number 66645 (rapid decolorization of porphyrin species). The company aimed to decolorize porphyrin species to prevent staining or noticeable transfer to cloth and other absorbant surfaces. The aim of this study was to investigate the photocatalyst decolorization of cobalamin using different types of catalyst, namely, ZnO, TiO$_2$ (Degussa P25), TiO$_2$ (Hombikat UV100), TiO$_2$ (Millennium PC105), and TiO$_2$ (Koronose 2073). The effect of different parameters was studied to estimate the best condition for decolorization of cobalamin.

2. Experimental

Photocatalytic reactions were carried out in a batch photoreactor with the radiation source type Philips (CLEO), Poland, mercury lamps containing 6 lamps with 15 W for each. Aqueous suspensions of zinc oxide (ZnO) or titanium dioxide (TiO$_2$) containing cobalamin in beaker, under magnetic stirring, were irradiated in light of wavelength 365 nm with an irradiation intensity of (0.5–3 mW·cm^{-2}). In all experiments, the required amount of the catalyst was suspended in 100 cm^3 of aqueous solution of cobalamin. After illumination, 2 mL was taken from the reaction suspension, centrifuged at 4,000 rpm for 15 minutes in an 800 B centrifuge, and filtered to remove the particles. The second centrifuge was found necessary to remove fine particle of the zinc oxide or titanium dioxide (TiO$_2$). After the second centrifuge, the absorbance of the cobalamin was measured at 361 nm and 550 nm, respectively, using Cary 100Bio UV-visible spectrophotometer shimadzu. The measurements at the two wavelength produced equivalent results, when compared with the prepared calibration curves.

The photocatalytic decolorization rate of cobalamin is described by pseudo-first-order kinetics according to the Langmuir-Hinshelwood model, so the rate of photocatalytic decolorization of cobalamin could be expressed by the following:

$$C_t = C_o e^{-kt}, \qquad (1)$$

where C_t represents cobalamin concentration at time t of irradiation, C_o is the initial concentration, k is the apparent reaction rate constant of the pseudo-first-order kinetics, and t is irradiation exposure time [3]:

$$\frac{C_t}{C_o} = e^{-kt},$$

$$\ln \frac{C_t}{C_o} = -kt, \qquad (2)$$

$$\text{or} \quad \ln \frac{C_o}{C_t} = kt.$$
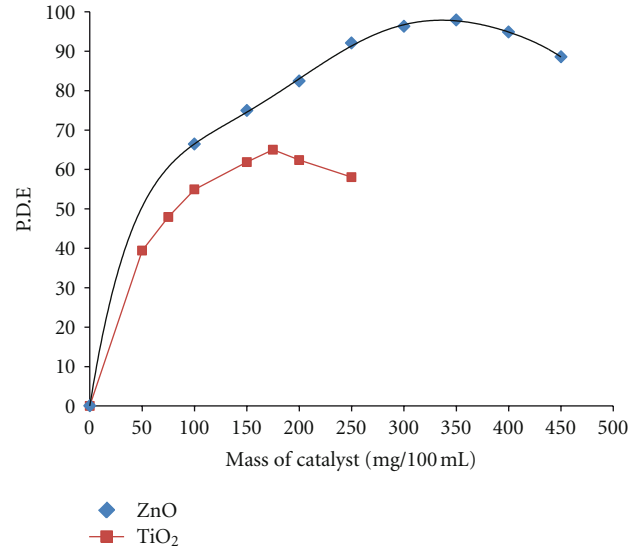
Figure 2: Effect of the masses of catalyst on photodecolorization efficiency of cobalamin.

The photodecolorization efficiency (P.D.E) of cobalamin was calculated from a mathematical equation adapted from measurements of decolorization used before [29]:

$$\text{P.D.E} = \frac{C_o - C_t}{C_o} \times 100, \qquad (3)$$

where C_o is the initial concentration of cobalamin, C_t represents cobalamin concentration at time t of irradiation.

3. Results and Discussion

3.1. Effect of Mass Catalyst of ZnO or TiO$_2$. The photodegradation efficiency of cobalamin increased with the increase of the amount of catalyst up to an optimum value and then decreased slightly with the increase of the amount of catalyst as shown in Figure 2. One possible explanation for such behavior is that it is believed that an increase in the number of catalyst will increase the number of photons absorbed and the number of cobalamin molecules adsorbed. Therefore, the photodegradation rate can be expected to be enhanced on increasing the amount of catalyst due to the increase in total surface area available for contaminant adsorption. However, a further increase of the catalyst concentration may cause light-screening effects [30]. These screening effects reduce the specific activity of the catalyst [31].

3.2. Effect of Initial Dye Concentration of ZnO or TiO$_2$. The effect of the initial concentration of cobalamin on the photocatalytic decolorization was studied by varying the initial concentration over a wide range. At a fixed pH and amount of catalyst, photocatalytic experiments were carried out at different initial concentrations of cobalamin. The results in Figure 3 show that the rate constant of photodecolorization decreased with increasing the initial cobalamin concentration [32]. This behavior can have the explanation that
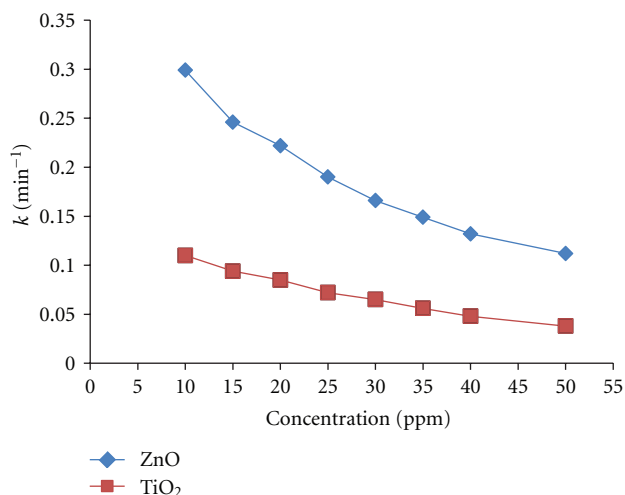
FIGURE 3: Effect of initial dye concentration on rate constant.

FIGURE 4: Effect of initial pH of solution on rate constant.

the initial concentration of the cobalamin increases because the path length of the photons log in the solution decreases and in low concentration the reverse effect is observed, thereby increasing the number of photon absorption by the catalyst in lower concentration [33].

3.3. Effect of pH. The results in Figure 4 show that the photodecolorization efficiency increased with the increase of the pH value of solution to pH 9.01 for ZnO and pH 6.59 for TiO$_2$ (Degussa P25) and then decreases. The production of hydroxyl radicals is also a function of pH. Therefore, pH is an important parameter in photocatalytic reactions. The photodecolorization of cobalamin was studied at different pH. In all the experiments, pH was adjusted by using appropriate amounts of base (NaOH) or acid (HCl) solutions [34–37]. The zero point charge (ZPC) is equal to 9.01 for ZnO and 6.59 for TiO$_2$ (Degussa P25) and the semiconductor surface will remain positively charged in acidic medium and negatively charged in alkaline medium, because the ionization state of the surface of semiconductor is according to the following reactions:

$$ZnOH + H^+ \longrightarrow ZnOH_2{}^+$$
$$ZnOH + OH^- \longrightarrow ZnO^- + H_2O \qquad (4)$$
$$TiOH + H^+ \longrightarrow TiOH_2{}^+ \qquad (5)$$
$$TiOH + OH^- \longrightarrow TiO^- + H_2O. \qquad (6)$$

This behavior can be explained when the pH value of the solution is increased up to a maximum value and then decreased, this is because in alkaline medium the surface area of photocatalyst possesses much negative charge [38–41].

3.4. Effect of Temperature. The effect of temperature on photocatalytic decolorization of cobalamin in water solution was investigated in the range of 278.15–298.15 K. The results in Figure 5 show that the degradation efficiency of cobalamin

FIGURE 5: Arrhenius plot.

gradually increased with increase in the temperature. The increase in temperature would lead to generating the free radicals [42]. Therefore, the rise in temperature helped the reaction to compete more efficiently than electron-hole recombination [43]. The increasing of temperature may increase the oxidation rate of cobalamin and also reduce the adsorption capacities associated with cobalamin and dissolved oxygen [44]. Generally the rise in temperature can affect the amount of adsorption [45]. Arrhenius plot shows that the activation energy for photocatalytic decolorization of cobalamin is equal to 28 ± 1 kJ mol^{-1} for ZnO and 22 ± 1 kJ mol^{-1} for TiO$_2$ [46].

3.5. Effect of Light Intensity. The effect of light intensity on the decolorization efficiency for cobalamin was examined at constant initial cobalamin concentration (40 ppm). It is
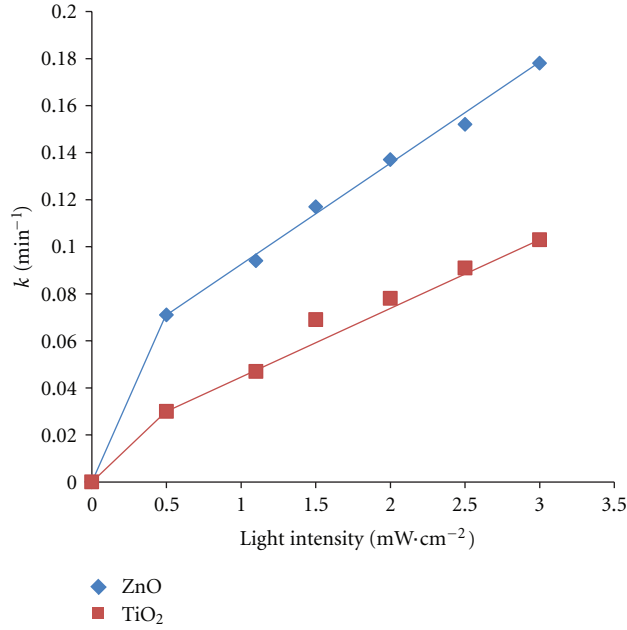
FIGURE 6: Effect of initial light intensity on the rate constant.

FIGURE 7: Effect of type of gas on photodecolorization of cobalamin by ZnO.

FIGURE 8: Effect of type of gas on photodecolorization of cobalamin by TiO$_2$.

found that the percentage of decolorization and photodecolorization for cobalamin increases with increasing the light intensity as shown in Figure 6. The light intensity was studied in the range $(0.5–3)$ mW·cm^{-2} by changing the high and lowering the lamps. From these results it is found that the decolorization rate for cobalamin increased with increase in the light intensity [47]. This behavior can be explained that the UV irradiation production the photons required for the electron transfer from the valence band to the conduction band in the catalyst. photocatalyst and the energy of a photon is related to its wavelength and the overall energy input to a photocatalytic process is dependent on light intensity. The rate of decolorization for cobalamin increases when more radiations fall on the catalyst surface and hence more $^\bullet$OH radicals are generated on catalyst surface [48, 49].

3.6. Effect of Current Gas. The results in Figures 7 and 8 show that the photodecolorization efficiency for cobalamin increased with the presence of the oxygen gas (O_2) but decreased or was extremely slow in the presence of the nitrogen gas (N_2). This behavior can be explained that in the presence of nitrogen gas (N_2) and TiO$_2$ (Degussa P25) will production grey-blue in color may be attributed to the sharing of lattice oxygen from the surface. The results indicated that the presence of oxygen is necessary [50, 51]. The presence of oxygen in the solution plays an important role in the photocatalytic decolorization of cobalamin. This behavior can be explained that the oxygen molecule acts as an electron acceptor and minimizes the chance of electron-hole pair recombination [52].

3.7. Effect of Addition of H_2O_2. Hydrogen peroxide (H_2O_2) plays an important role in the production of hydroxyl radicals. The effect of addition of hydrogen peroxide H_2O_2
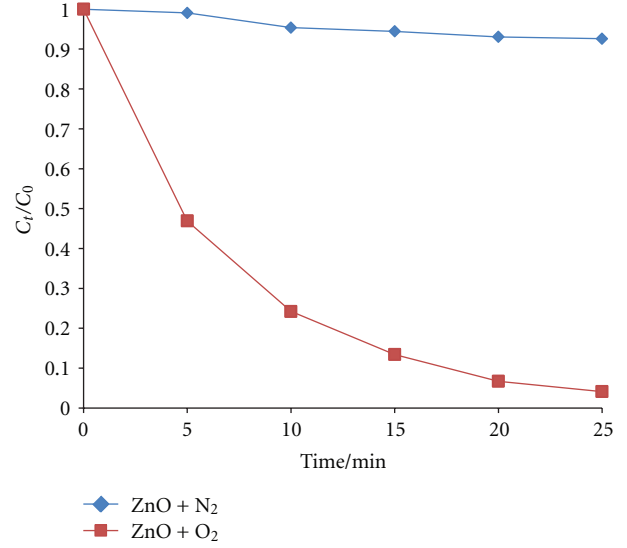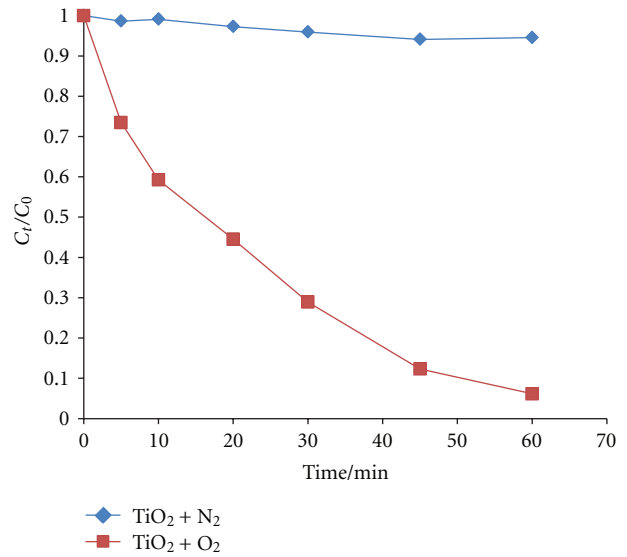
on the decolorization rate was studied for photocatalytic decolorization of the cobalamin. The results in Figure 9 show that the decolorization rate increase in with increases concentration of hydrogen peroxide H_2O_2 from 0.1 to 1.5 mmol/L, becomes maximum at 1.5 mmol/L and then $^\bullet$OH starts decreasing from 1.5 to 4.0 mmol/L with increase in the concentration of hydrogen peroxide H_2O_2 [53].

This behavior is due to increasing the concentration of hydroxyl radical since it inhibits the hole-electron recombination according to the following equations:

$$H_2O_2 + e_{cb}^- \longrightarrow {}^\bullet OH + OH \tag{7}$$

$$H_2O_2 + {}^\bullet O_2 \longrightarrow {}^\bullet OH + OH + O_2. \tag{8}$$
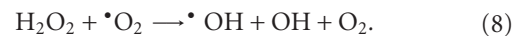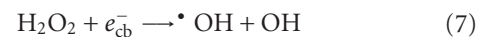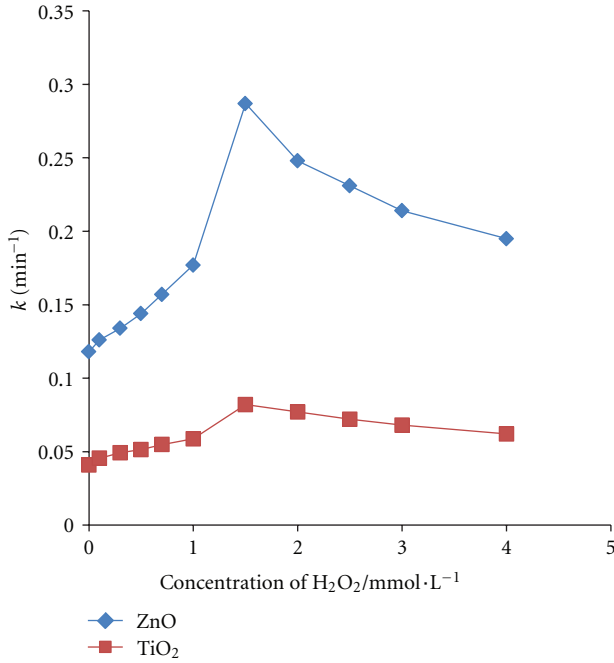
FIGURE 9: Effect of addition of H_2O_2 on rate constant.

FIGURE 10: Photodecolorization of cobalamin by different types of TiO_2.

At high concentration of hydrogen peroxide H_2O_2 the photocatalytic processes decrease because of its hydroxyl radical scavenging effect, according to the following equations [54]:

$$H_2O_2 + {}^{\bullet}OH \longrightarrow H_2O + HO_2^{\bullet} \qquad (9)$$

$$HO_2^{\bullet} + {}^{\bullet}OH \longrightarrow H_2O + O_2 \qquad (10)$$
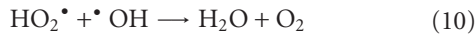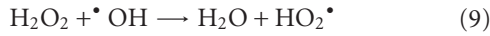
3.8. Type of Catalyst. The results in Figure 10 show the relationship between the photodecolorization of cobalamin with irradiation time in the existence of oxygen gas by using different types of TiO_2, under the experimental conditions, initial cobalamin concentration of 40 ppm, solution pH equal to 7.8, light intensity equal to $1.3 \, mW \cdot cm^{-2}$, TiO_2 concentration 175 (mg/100 mL), and the temperature equal to 298.15 K. The results show that the activity of different types of catalyst used in this study was of the sequence:

$$TiO_2 (Degussa \ P25) > TiO_2 (Hombikat \ UV100) >$$

$$TiO_2 \ (Millennium \ PC105) > TiO_2 \ (Koronose \ 2073).$$

$$\qquad (11)$$

3.9. Mineralization of Cobalamin. The results in Figures 11, 12, and 13 show the relationship between the TOC degradation % with irradiation time and it is found that the TOC degradation % increased with the increase of the irradiation time. These results indicate that the color photodegradation for cobalamin is faster than the decrease of total organic carbon (TOC). From these results it is found that the ZnO

FIGURE 11: Mineralization of cobalamin.

is more active than the TiO_2 (Degussa P25). The efficiency of these catalyst arrangements is as follows:

$$ZnO > TiO_2 (Degussa \ P25). \qquad (12)$$

4. Conclusions

Complete decolorization of cobalamin was achieved in less than thirty minutes. PH was changed at the end of reaction
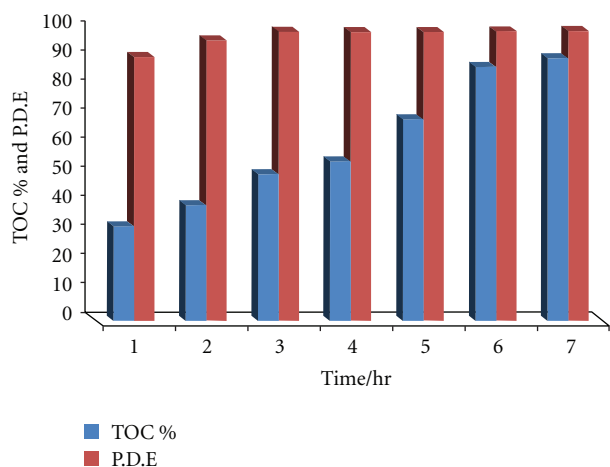
FIGURE 12: TOC degradation % and P.D.E for cobalamin by ZnO.
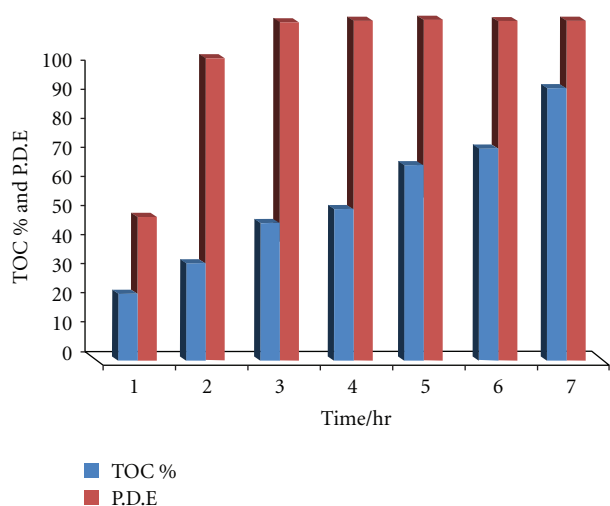
FIGURE 13: TOC degradation % and P.D.E for cobalamin by TiO$_2$ (Degussa P25).

towards 7 (neutral). The photocatalytic process can be expressed by both the pseudo-first-order reaction kinetics and the Langmuir-Hinshelwood kinetic model.

The controlled experiment indicates that the presence of UV light, oxygen, and catalyst was essential for the effective destruction of cobalamin. It is important to choose optimum degradation parameters to obtain a high photocatalytic decolorization rate.

The enhancement of decolorization efficiency of cobalamin increasing masses of catalysts is attributed to the increase of the availability of photocatalytic sites. Nevertheless, the decrease of catalytic activity often the plateau region is related to a shielding effect of excess partials and resulted in a reduced performance.

The photocatalytic decolorization of cobalamin using different types of catalysts like photocatalyst strongly depends on the amount of catalyst, cobalamin concentration, pH of solution, light intensity, type of current gas, and addition of H$_2$O$_2$.

The phenomenon of increasing the photodecolorization efficiency of cobalamin with decreasing the concentration of solution is due to the decrease of the concentration of OH$^-$ adsorbed on catalyst surface. The increasing of cobalamin concentration increases the competitions between OH$^-$ and cobalamin to adsorb on active site of catalyst.

The photocatalytic decolorization efficiency of cobalamin increases with the increase of the pH of solution up to a maximum value and then decreases. This behavior could be explained on the basis of zero point charge (ZPC).

The decolorization of cobalamin increases with the increase of light intensity. Nevertheless, the increase of light intensity leads to the increase of the number of electron–hole pair and, hence, increases the decolorization efficiency of cobalamin.

The temperature is the factor that has the smallest effect on the photocatalytic decolorization of cobalamin. Photocatalytic decolorazation of cobalamin is faster than the decrease of total organic carbon (TOC).

Acknowledgments

References

[1] S. N. Frank and A. J. Bard, "Heterogeneous photocatalytic oxidation of cyanide ion in aqueous solutions at TiO$_2$ powder," *Journal of the American Chemical Society*, vol. 99, no. 1, pp. 303–304, 1977.

[2] C. Belver, R. Bellod, A. Fuerte, and M. Fernández-García, "Nitrogen-containing TiO$_2$ photocatalysts. Part 1. Synthesis and solid characterization," *Applied Catalysis B*, vol. 65, no. 3-4, pp. 301–308, 2006.

[3] F. H. Hussein, A. F. Halbus, H. A. K. Hassan, and W. A. K. Hussein, "Photocatalytic degradation of bismarck brown G using irradiated ZnO in aqueous solutions," *E-Journal of Chemistry*, vol. 7, no. 2, pp. 540–544, 2010.

[4] D. F. Ollis, E. Pelizzetti, and N. Serpone, *Photocatalysis: Fundamentals and Applications*, Wiley, New York, NY, USA, 1989.

[5] D. Robert and S. Malato, "Solar photocatalysis: a clean process for water detoxification," *Science of the Total Environment*, vol. 291, no. 1–3, pp. 85–97, 2002.

[6] A. Fujishima, T. N. Rao, and D. A. Tryk, "Titanium dioxide photocatalysis," *Journal of Photochemistry and Photobiology C*, vol. 1, no. 1, pp. 1–21, 2000.

[7] J. A. Byrne, P. A. Fernandez-Ibañez, P. S. M. Dunlop, D. M. A. Alrousan, and J. W. J. Hamilton, "Photocatalytic enhancement for solar disinfection of water: a review," *International Journal of Photoenergy*, vol. 2011, Article ID 798051, 12 pages, 2011.

[8] M. Zhou, J. Zhang, B. Cheng, and H. Yu, "Enhancement of visible-light photocatalytic activity of mesoporous Au-TiO$_2$ nanocomposites by surface plasmon resonance," *International Journal of Photoenergy*, vol. 2012, Article ID 532843, 10 pages, 2012.

[9] G. Wang, L. Xu, J. Zhang, T. Yin, and D. Han, "Enhanced photocatalytic activity of TiO₂ powders (P25) via calcination treatment," *International Journal of Photoenergy*, vol. 2012, Article ID 265760, 9 pages, 2012.

[10] H. Znad, M. H. Ang, and M. O. Tade, "Ta/TiO₂-and Nb/TiO₂-mixed oxides as efficient solar photocatalysts: preparation, characterization, and photocatalytic activity," *International Journal of Photoenergy*, vol. 2012, Article ID 548158, 9 pages, 2012.

[11] X. Wu, Z. Huang, Y. Liu, and M. Fang, "Investigation on the photoelectrocatalytic activity of well-aligned TiO₂ nanotube arrays," *International Journal of Photoenergy*, vol. 2012, Article ID 832516, 7 pages, 2012.

[12] X. Cheng, X. Yu, Z. Xing, and L. Yang, "Enhanced visible light photocatalytic activity of mesoporous anatase TiO₂ codoped with nitrogen and chlorine," *International Journal of Photoenergy*, vol. 2012, Article ID 593245, 6 pages, 2012.

[13] C. H. Huang, Y. M. Lin, I. K. Wang, and C. M. Lu, "Photocatalytic activity and characterization of carbon-modified titania for visible-light-active photodegradation of nitrogen oxides," *International Journal of Photoenergy*, vol. 2012, Article ID 548647, 13 pages, 2012.

[14] Q. Wang, D. Gao, C. Gao et al., "Removal of a cationic dye by adsorption/photodegradation using electrospun PAN/O-MMT composite nanofibrous membranes coated with TiO₂," *International Journal of Photoenergy*, vol. 2012, Article ID 680419, 8 pages, 2012.

[15] J. Wang, Q. Cai, H. Li, Y. Cui, and H. Wang, "A reviewon TiO₂ nanotube film photocatalysts prepared by liquid-phase deposition," *International Journal of Photoenergy*, vol. 2012, Article ID 702940, 11 pages, 2012.

[16] M. A. Behnajady, N. Modirshahla, M. Shokri, and B. Rad, "Enhancement of photocatalytic activity of TiO₂ nanoparticles by Silver doping: photodeposition versus liquid impregnation methods," *Global Nest Journal*, vol. 10, no. 1, pp. 1–7, 2008.

[17] M. A. Behnajady, N. Modirshahla, and R. Hamzavi, "Kinetic study on photocatalytic degradation of C.I. Acid Yellow 23 by ZnO photocatalyst," *Journal of Hazardous Materials*, vol. 133, no. 1–3, pp. 226–232, 2006.

[18] M. Saquib and M. Muneer, "TiO₂/mediated photocatalytic degradation of a triphenylmethane dye (gentian violet), in aqueous suspensions," *Dyes and Pigments*, vol. 56, no. 1, pp. 37–49, 2003.

[19] P. Fernández-Ibáñez, J. Blanco, S. Malato, and F. J. de las Nieves, "Application of the colloidal stability of TiOM₂ particles for recovery and reuse in solar photocatalysis," *Water Research*, vol. 37, no. 13, pp. 3180–3188, 2003.

[20] T. Ohno, "Preparation of visible light active S-doped TiO₂ photocatalysts and their photocatalytic activities," *Water Science and Technology*, vol. 49, no. 4, pp. 159–163, 2004.

[21] A. N. Alkhateeb, F. H. Hussein, and K. A. Asker, "Photocatalytic decolonization of industrial wastewater under natural weathering conditions," *Asian Journal of Chemistry*, vol. 17, no. 2, pp. 1155–1159, 2005.

[22] F. H. Hussein and A. N. Alkhateeb, "Photo-oxidation of benzyl alcohol under natural weathering conditions," *Desalination*, vol. 209, no. 1–3, pp. 350–355, 2007.

[23] J. L. Sessler, E. Karnas, and E. Sedenberg, "Porphyrins and expanded porphyrins as receptors," *Supramolecular Chemistry*, vol. 1, pp. 1–29, 2012.

[24] Y. Bai, *Photoelectron Spectroscopic Investigations of Porphyrins and Phthalocyanines on Ag(111) and Au(111): Adsorption and Reactivity*, Friedrich-Alexander-Universität Erlangen-Nürnberg, 2010.

[25] L. Quaroni, J. Reglinski, and W. E. Smith, "Surface enhanced resonance raman scattering from cyanocobalamin and 5′-deoxyadenosylcobalamin," *Journal of Raman Spectroscopy*, vol. 26, pp. 1075–1076, 1995.

[26] G. Jaouen, *Bioorganometallics: Biomolecules, Labeling, Medicine*, Wiley-VCH, Weinheim, Germany, 2006.

[27] V. Herbert, "Vitamin B-12: plant sources, requirements, and assay," *The American Journal of Clinical Nutrition*, vol. 48, no. 3, pp. 852–858, 1988.

[28] I. Ahmad, W. Hussain, and A. A. Fareedi, "Photolysis of cyanocobalamin in aqueous solution," *Journal of Pharmaceutical and Biomedical Analysis*, vol. 10, no. 1, pp. 9–15, 1992.

[29] F. H. Hussein and T. A. Abassa, "Photocatalytic treatment of textile industrial wastewater," *International Journal of Chemical Sciences*, vol. 8, no. 3, pp. 1353–1364, 2010.

[30] M. A. Rahman and M. Muneer, "Photocatalysed degradation of two selected pesticide derivatives, dichlorvos and phosphamidon, in aqueous suspensions of titanium dioxide," *Desalination*, vol. 181, no. 1–3, pp. 161–172, 2005.

[31] Y. Abdollahi, A. H. Abdullah, Z. Zainal, and N. A. Yusof, "Photocatalytic degradation of p-Cresol by zinc oxide under UV irradiation," *International Journal of Molecular Sciences*, vol. 13, pp. 302–315, 2012.

[32] C. S. Turchi and D. F. Ollis, "Photocatalytic degradation of organic water contaminants: mechanisms involving hydroxyl radical attack," *Journal of Catalysis*, vol. 122, no. 1, pp. 178–192, 1990.

[33] R. J. Davis, J. L. Gainer, G. O'Neal, and I. W. Wu, "Photocatalytic decolorization of wastewater dyes," *Water Environment Research*, vol. 66, no. 1, pp. 50–53, 1994.

[34] M. Abu Tariq, M. Faisal, and M. Muneer, "Semiconductor-mediated photocatalysed degradation of two selected azo dye derivatives, amaranth and bismarck brown in aqueous suspension," *Journal of Hazardous Materials*, vol. 127, no. 1–3, pp. 172–179, 2005.

[35] C. N. Chang, Y. S. Ma, G. C. Fang, A. C. Chao, M. C. Tsai, and H. F. Sung, "Decolorizing of lignin wastewater using the photochemical UV/TiO₂ process," *Chemosphere*, vol. 56, no. 10, pp. 1011–1017, 2004.

[36] A. Aguedach, S. Brosillon, J. Morvan, and E. K. Lhadi, "Photocatalytic degradation of azo-dyes reactive black 5 and reactive yellow 145 in water over a newly deposited titanium dioxide," *Applied Catalysis B*, vol. 57, no. 1, pp. 55–62, 2005.

[37] A. T. Toor, A. Verma, C. K. Jotshi, P. K. Bajpai, and V. Singh, "Photocatalytic degradation of direct yellow 12 dye using UV/TiO₂ in a shallow pond slurry reactor," *Dyes and Pigments*, vol. 68, no. 1, pp. 53–60, 2006.

[38] J. M. Herrmann, "Heterogeneous photocatalysis: fundamentals and applications to the removal of various types of aqueous pollutants," *Catalysis Today*, vol. 53, no. 1, pp. 115–129, 1999.

[39] Y. Wang, "Solar photocatalytic degradation of eight commercial dyes in TiO₂ suspension," *Water Research*, vol. 34, no. 3, pp. 990–994, 2000.

[40] Y. C. Chung and C. Y. Chen, "Degradation of azo dye reactive violet 5 by TiO₂ photocatalysis," *Environmental Chemistry Letters*, vol. 7, no. 4, pp. 347–352, 2009.

[41] E. Evgenidou, K. Fytianos, and I. Poulios, "Photocatalytic oxidation of dimethoate in aqueous solutions," *Journal of Photochemistry and Photobiology A*, vol. 175, no. 1, pp. 29–38, 2005.

[42] Z. He, S. Song, H. Zhou, H. Ying, and J. Chen, "C.I. reactive black 5 decolorization by combined sonolysis and ozonation," *Ultrasonics Sonochemistry*, vol. 14, no. 3, pp. 298–304, 2007.

[43] L. B. Reutergådh and M. Iangphasuk, "Photocatalytic decolourization of reactive azo dye: a comparison between TiO_2 and CdS photocatalysis," *Chemosphere*, vol. 35, no. 3, pp. 585–596, 1997.

[44] M. Kositzi, I. Poulios, K. Samara, E. Tsatsaroni, and E. Darakas, "Photocatalytic oxidation of cibacron yellow LS-R," *Journal of Hazardous Materials*, vol. 146, no. 3, pp. 680–685, 2007.

[45] N. Daneshvar, M. Rabbani, N. Modirshahla, and M. A. Behnajady, "Kinetic modeling of photocatalytic degradation of Acid Red 27 in UV/TiO_2 process," *Journal of Photochemistry and Photobiology A*, vol. 168, no. 1-2, pp. 39–45, 2004.

[46] K. Byrappa, A. K. Subramani, S. Ananda, K. M. Lokanatha Rai, R. Dinesh, and M. Yoshimura, "Photocatalytic degradation of rhodamine B dye using hydrothermally synthesized ZnO," *Bulletin of Materials Science*, vol. 29, no. 5, pp. 433–438, 2006.

[47] M. Tokumura, H. Tawfeek Znad, and Y. Kawase, "Modeling of an external light irradiation slurry photoreactor: UV light or sunlight-photoassisted Fenton discoloration of azo-dye Orange II with natural mineral tourmaline powder," *Chemical Engineering Science*, vol. 61, no. 19, pp. 6361–6371, 2006.

[48] I. K. Konstantinou and T. A. Albanis, "TiO_2-assisted photocatalytic degradation of azo dyes in aqueous solution: kinetic and mechanistic investigations: a review," *Applied Catalysis B*, vol. 49, no. 1, pp. 1–14, 2004.

[49] J. J. Vora, S. K. Chauhan, K. C. Parmar, S. B. Vasava, S. Sharma, and L. S. Bhutadiya, "Kinetic study of application of ZnO as a photocatalyst in heterogeneous medium," *E-Journal of Chemistry*, vol. 6, no. 2, pp. 531–536, 2009.

[50] V. Mirkhani, S. Tangestaninejad, M. Moghadam, M. H. Habibi, and A. Rostami-Vartooni, "Photocatalytic degradation of azo dyes catalyzed by Ag doped TiO_2 photocatalyst," *Journal of the Iranian Chemical Society*, vol. 6, no. 3, pp. 578–587, 2009.

[51] R. Zhang, C. Zhang, X. X. Cheng, L. Wang, Y. Wu, and Z. Guan, "Kinetics of decolorization of azo dye by bipolar pulsed barrier discharge in a three-phase discharge plasma reactor," *Journal of Hazardous Materials*, vol. 142, no. 1-2, pp. 105–110, 2007.

[52] M. I. Litter, "Heterogeneous photocatalysis: transition metal ions in photocatalytic systems," *Applied Catalysis B*, vol. 23, no. 2-3, pp. 89–114, 1999.

[53] M. A. Behnajady, N. Modirshahla, and M. Shokri, "Photodestruction of acid orange 7 (AO7) in aqueous solutions by UV/H_2O_2: influence of operational parameters," *Chemosphere*, vol. 55, no. 1, pp. 129–134, 2004.

[54] M. S. Mashkour, A. F. Al-Kaim, L. M. Ahmed, and F. H. Hussein, "Zinc oxide assisted photocatalytic decoloriztion of reactive red 2 dye," *International Journal of Chemical Sciences*, vol. 9, no. 3, pp. 969–979, 2011.

Research Article

Pretreatment of Color Filter Wastewater towards Biodegradable by Fresnel-Lens-Assisted Solar TiO$_2$ Photocatalysis

Wen-Shiuh Kuo and Min-Tian Li

Department of Safety, Health, and Environmental Engineering, National United University, Miao-Li 360, Taiwan

Correspondence should be addressed to Wen-Shiuh Kuo, wsk@nuu.edu.tw

The pretreatment of color filter wastewater towards biodegradable by Fresnel-lens-enhanced solar TiO$_2$ photocatalytic process was investigated. The experimental design of response surface methodology (RSM) was employed to assess the effect of critical process parameters (including initial pH, TiO$_2$ dosage, and reaction time) on pretreatment performance in terms of BOD$_5$/COD, COD and TOC removal efficiency. Appropriate reaction conditions were established as an initial pH of 7.5, a TiO$_2$ dosage of 1.5 g/L with a reaction time of 3 h for increasing the BOD$_5$/COD ratio to 0.15, which implied that the treated wastewater would be possibly biodegradable. Meanwhile, the efficiency of COD and TOC removals reached 32.9% and 24.4%, respectively. With the enhancement of Fresnel lens, the required reaction time for improving the biodegradability of wastewater to 0.15 was 1 h only. Moreover, the efficiency of COD and TOC removals was promoted to 37.4% and 25.8%, respectively. This could be mainly due to the concentrated effect of Fresnel lens for solar energy, including an increase of 2 times of solar irradiation and a raising of 15–20°C of wastewater temperature. Consequently, solar TiO$_2$ photocatalytic process with the use of a PMMA Fresnel lens could offer an economical and practical alternative for the pretreatment of industry wastewater containing diversified biorefractory pollutants with a high concentration of COD such as color filter wastewater.

1. Introduction

Organic wastewater from color filter industry generally contains so many residuals such as TMAH (C$_4$H$_{13}$NO), PGMEA (C$_6$H$_{12}$O$_3$), acrylic resin, and pigments, and it is variable in composition and strength at different stages of process. In the presence of biorefractory organic matter, the effluent is usually characterized by its high chemical oxygen demand (COD) and low biodegradability generally expressed as a ratio of biological oxygen demand at day 5 (BOD$_5$) to COD, that is, BOD$_5$/COD. Advanced oxidation processes (AOPs) have been previously described as a promising option to remove persistent pollutants from contaminated water [1] when conventional water treatment processes are not efficient enough. AOPs are able to produce a highly reactive, nonspecific oxidant, mainly hydroxyl radicals ($^\bullet$OH). The hydroxyl radical possesses inherent properties that enable it to attack refractory organic pollutants in water to achieve a complete mineralization. However, the production of photons with artificial light sources requires significant electrical

energy demand and UV lamp consumption, which result in a high operation cost in AOPs [2]. Alternatively, solar energy is essentially unlimited and its utilization is ecologically benign. In the wastewater treatment sector, solar technology has been extensively used as an alternative to UV lamps to reduce the operation cost in AOPs [3]. In particular, TiO$_2$ photocatalysis (as shown in (1)–(3)) using solar irradiation has been used as an economically viable process and has attracted great interest in the recent years [4–6]:

$$\text{TiO}_2 \xrightarrow{hv\ (\lambda < 382\,\text{nm})} h_{vb}^+ + e_{cb}^-$$ (1)

$$h_{vb}^+ + \text{H}_2\text{O} \longrightarrow {}^\bullet\text{OH} + \text{H}^+$$ (2)

$$h_{vb}^+ + \text{OH}^- \longrightarrow {}^\bullet\text{OH}$$ (3)
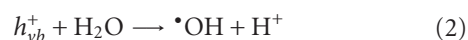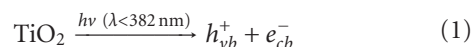
However, solar TiO$_2$ photocatalysis was usually carried out by using solar irradiation directly, resulting in a lower absorption and utilization of solar energy [7, 8]. To improve the efficiency of solar TiO$_2$ photocatalysis, it is necessary

TABLE 1: Physical and chemical properties of color filter wastewater.

Characteristic	Values
pH	9.8~10.2
COD, mg/L	924~960
BOD_5, mg/L	22~51
BOD_5/COD	0.02~0.05
TOC, mg/L	280~303
SS, mg/L	0.3~1.9
TS, mg/L	1080~1160
Color (ADMI value)	1540~1600
TMAH, mg/L	3.2~3.3
Cl^-, mg/L	1.8~2.0
NO_3^-, mg/L	4.8~5.0
SO_4^{2-}, mg/L	1.1~1.2
NH_4^+, mg/L	0.7~0.8

TABLE 2: Experimental range and levels of the process parameters in this study.

	Factor	Range and level		
Independent variable		**−1**	**0**	**+1**
Initial pH	X_1	5	7.5	10
TiO_2 dose, g/L	X_2	0.5	1.0	1.5
Reaction time, hr	X_3	1	2	3
Y (response) – BOD_5/COD				

to concentrate and maximize solar energy utilization in the process. Moreover, the combination of solar TiO_2 photocatalysis as a preliminary treatment, followed by an inexpensive biological process, seems to be a more attractive option for biorefractory organic wastewater.

In this study, pretreatment of color filter wastewater towards biodegradable using solar TiO_2 photocatalysis enhanced by a high-concentrating Fresnel lens was investigated. A factorial design according to response surface methodology (RSM) was employed to optimize the reaction conditions of critical process parameters (including initial pH of wastewater, TiO_2 dosage, and reaction time) to reach a biodegradable degree of color filter wastewater. Moreover, the effect of Fresnel lens on treatment performance in terms of COD degradation efficiency, mineralization efficiency, and biodegradability (BOD_5/COD) of color filter wastewater was examined.

2. Material and Methods

2.1. Materials. The color filter wastewater used in this study was obtained from an electrooptical industry plant located in Hsin-Chu, Taiwan, during 2009-2010. The characteristics of color filter wastewater are shown in Table 1. Basically, the color filter wastewater has the properties of high COD (924–960 mg/L), high TOC (280–303 mg/L), and low biodegradability (BOD_5/COD: 0.02–0.05). TiO_2 powder (mainly anatase form, mean particle size: 30 nm, BET surface area: 50 ± 15 m^2/g) from Degussa Co. (Frankfurt, Germany) was used in this study. All other chemicals used in this study were analytical grade and used as received.

2.2. Procedures. All experiments were carried out in a batch mode. A 1 L glass beaker containing 200 mL of color filter wastewater was used and maintained at a preset temperature in a water bath during the experiments. A 3 factors ∗ 3 levels Box-Behnken experimental design [9] with three replicates at center point according to the methodology of response surface as shown in Table 2 was performed to examine

the influence of three critical process parameters (viz., initial pH, TiO_2 dosage and reaction time) on the biodegradability, COD and TOC degradation of wastewater. Moreover, the regression analysis of Minitab R14 software (Minitab Co., USA) was used to figure out the reaction conditions for improving the biodegradability of wastewater. At the RSM runs, the initial pH of wastewater was adjusted to the desired pH by adding 1 N H_2SO_4. The wastewater was then placed into the photoreactor and irradiated by a 1500 W Xe lamp in an ATLAS Suntest CPS+ solar simulator (ATLAS Co., USA) emitting artificial solar light with a spectral distribution resembling the solar spectrum (300–800 nm) in which the $UV_{280–400\,nm}$ intensity is around 66.5 ± 0.5 W/m^2. In addition, the wastewater was maintained at $25 \pm 0.5°C$ in a water bath. During the experiments, the pH of the solution was monitored using a pH meter (SP-701LI 120, Suntex Co., Taiwan) equipped with a glass electrode. Samples were withdrawn from the reactor at preset time intervals and then tested for COD, TOC, and BOD_5.

As the appropriate values of the process parameters were developed on the basis of RSM application and related regression equation of biodegradability, a Fresnel lens made of PMMA (thickness: 2 mm, pitch: 0.5 mm, facet depth: 0.2 mm, Fresnel circles: 395) was added into solar TiO_2 photocatalytic system with a distance of 16 cm above the level of wastewater in a clear sky condition to investigate the effect of Fresnel lens. The solar irradiation was measured with a LI-250 radiation indicator (LI-COR Co., USA) of pyranometer LI-200SA and a $UV_{280–400\,nm}$ detector of PMA 2100 (Solar Light Co., USA). The irradiated solar irradiation during the experimental run with Fresnel lens was in the range of 900–1000 W/m^2 ($UV_{280–400\,nm}$: 52.4–57.4 W/m^2). In addition, two blank experiments including direct photolysis reaction and adsorption on TiO_2 only under the experimental conditions of this study were performed. The result indicated that the COD and TOC removal efficiency of color filter wastewater was less than 1%, which implied that the removal of organic pollutants of color filter wastewater due to these effects was negligible in this study.

2.3. Analysis

2.3.1. Chemical Oxygen Demand (COD) Measurement. COD of solution via a DR 4000 photometer (HACH Co., USA) by using a $K_2Cr_2O_7$ as the reacting reagent was measured in order to understand the changes on degree of oxidation for color filter wastewater.

2.3.2. Total Organic Carbon (TOC) Measurement. TOC of solution was measured by using a Shimadzu VCPH analyzer (Shimadzu Co., Japan) in order to know the amount of organics in color filter wastewater degraded to CO_2 during oxidation.

2.3.3. BOD_5 Measurement. BOD_5 test was measured according to the procedures described in Standard methods 10 [Section 5210D, 10].

The bacteria (2000~4000 mgMLSS/L) used in this test were obtained from a local activation sludge system, operating at industrial wastewater treatment plant. The data showed that the BOD_5 value of untreated color filter wastewater in this study was in the range of 0.02~0.05, indicating that the color filter wastewater was hardly biodegradable.

3. Results and Discussion

3.1. Effect of Initial pH and Dosage of TiO_2. Figure 1 displays the two-dimensional contour plots for the biodegradability (BOD_5/COD), COD, and TOC degradation of color filter wastewater as a function of initial pH and concentration of TiO_2. As shown in Figure 1, when the pH of wastewater was varied from 10 (the original pH of wastewater) to 5 at the same TiO_2 dosage, the biodegradability of wastewater decreased with decreasing initial pH of wastewater to around a pH of 7.5 and then gradually increased with decreasing initial pH of wastewater to pH 5. This phenomenon was also observed in the degradation of COD and TOC in all the TiO_2 concentration range studied. This can be explained by the surface charge of TiO_2 as a function of pH. The zero point of charge (ZPC) for TiO_2-P25 is around pH 6.3–6.8 [11]. Therefore, at more acidic pH values (pH < pH_{ZPC}), the TiO_2 surface is positively charged as expressed by (4) and at alkaline pH, the surface (pH > pH_{ZPC}) is negatively charged as expressed by (5) [12, 13]. Therefore, at pH values below 6.3, the adsorption of wastewater is favourable due to the electrostatic attraction between the organic pollutants of wastewater and positively charged TiO_2 on the surface, leading to a better efficiency with the $^{\bullet}$OH generated on the surface of TiO_2. A similar phenomenon was found in the study of Xiang et al. [14]. Moreover, the study of Wang et al. [15] indicated that the positively charged TiO_2 could prompt the transfer of photoinduced electrons to the oxygen adsorbed on the surface of TiO_2. Consequently, the superoxide ion would be produced as shown in (6) and the recombination of electron hole on the surface of TiO_2 would be probably inhibited:

$$\text{TiOH} + \text{H}^+ \longrightarrow \text{TiOH}_2{}^+ \tag{4}$$

$$\text{TiOH} + \text{OH}^- \longrightarrow \text{TiO}^- + \text{H}_2\text{O} \tag{5}$$

$$\text{e}^- + \text{O}_2 \longrightarrow \text{O}_2{}^{\bullet-} \tag{6}$$
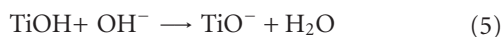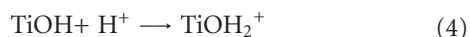
As the pH was above 6.8, the organic pollutants of wastewater were subjected to electrostatic repulsion between themselves and the negative surface of TiO_2. Hence, the adsorption of the organic pollutants of wastewater is less, leading to a decrease in degradation efficiency. Similar results were also observed in the TiO_2 photocatalytic degradation of a power station effluent [16] and the adsorption of Congo red on the surface of NiO [17]. Nevertheless, Barka et al. [18] pointed out that more OH^- may react with the holes generated from the photoexcitation of TiO_2 and produced more $^{\bullet}$OH radicals as described by (3), leading to a higher degradation efficiency. Hence, the biodegradability and degradation efficiency of color filter wastewater treated in the alkaline condition (pH 10) was found to be higher than those treated in the neutral pH. In general, the biodegradability and degradation efficiency of color filter wastewater was in the order of pH 5 > pH 10 > pH 7.5 under all TiO_2 concentration range studied.

On the other hand, as shown in Figure 1, the concentration of TiO_2 also showed an obvious effect on the biodegradability and degradation efficiency of color filter wastewater. Ordinarily, more catalyst will substantially result in more generation of hydroxyl radicals until an optimum catalyst concentration is achieved. Hence, the results showed that, under all pH range studied (5–10), the increase of catalyst concentration from 0.5 to 1.5 g/L increased the degradation efficiency. This fact may be due to the increase in the number of organic pollutants adsorbed and more oxidation of organics [19].

In addition, the experimental results allow the development of a second-order polynomial multiple regression equation as described by (7), which could be used to assess the effect of critical process parameters (viz., initial pH, TiO_2 dosage and reaction time) on pretreatment performance in terms of the biodegradability of wastewater. The regression model had a high value of coefficient of determination ($r^2 > 0.96$). This implies that the process efficiency could be predicted well by the second order polynomial regression equations under the conditions studied. Moreover, a neutral pH must be considered for a better operation of the following biological treatment. Accordingly, an appropriate reaction condition was established as an initial pH value of 7.5, a TiO_2 dosage of 1.5 g/L with a reaction time of 3 h for increasing the ratio of BOD_5/COD ratio to 0.15, which means the treated wastewater reaching a possibly biodegradable level [20]:

$$\begin{aligned} Y_{\text{BOD5/COD}} = {} & 0.166 - 0.010X_1 + 0.035X_2 \\ & + 0.027X_3 - 0.033X_1{}^2 - 0.026X_2{}^2 \\ & - 0.051X_3{}^2 - 0.027X_1X_2 - 0.015X_1X_3 \\ & - 0.003X_2X_3, \quad r^2 = 0.962. \end{aligned} \tag{7}$$

3.2. Effect of Fresnel Lens. Table 3 showed the effect of Fresnel lens on the degradation efficiency and biodegradability of color filter wastewater under the reaction condition with an initial pH of 7.5 and a TiO_2 dosage of 1.5 g/L. It was found that the concentrating effect of Fresnel lens for solar energy could result in an increase of 2 times of solar light intensity as indicated by an increase in $UV_{280-400\,\text{nm}}$ intensity from 54.9 W/m² to 110.3 W/m², accompanied with a raising of

TABLE 3: Effect of Fresnel lens on the degradation efficiency and biodegradability of color filter wastewater.

Solar light source and reaction time	$UV_{280-400\,nm}$ Intensity, W/m^2	Wastewater temperature, °C	COD removal, %	TOC removal, %	AOS	BOD_5/COD
Solar light + Fresnel lens, 1 h	110.3	35–45	37.4	25.8	0.01	0.150
Suntest 500 W/m^2, 1 h	66.5	25	25.9	20.3	−0.40	0.112
Suntest 500 W/m^2, 2 h	66.5	25	29.1	22.6	−0.15	0.120
Suntest 500 W/m^2, 3 h	66.5	25	32.9	24.4	−0.02	0.145

(a)

(b)

(c)
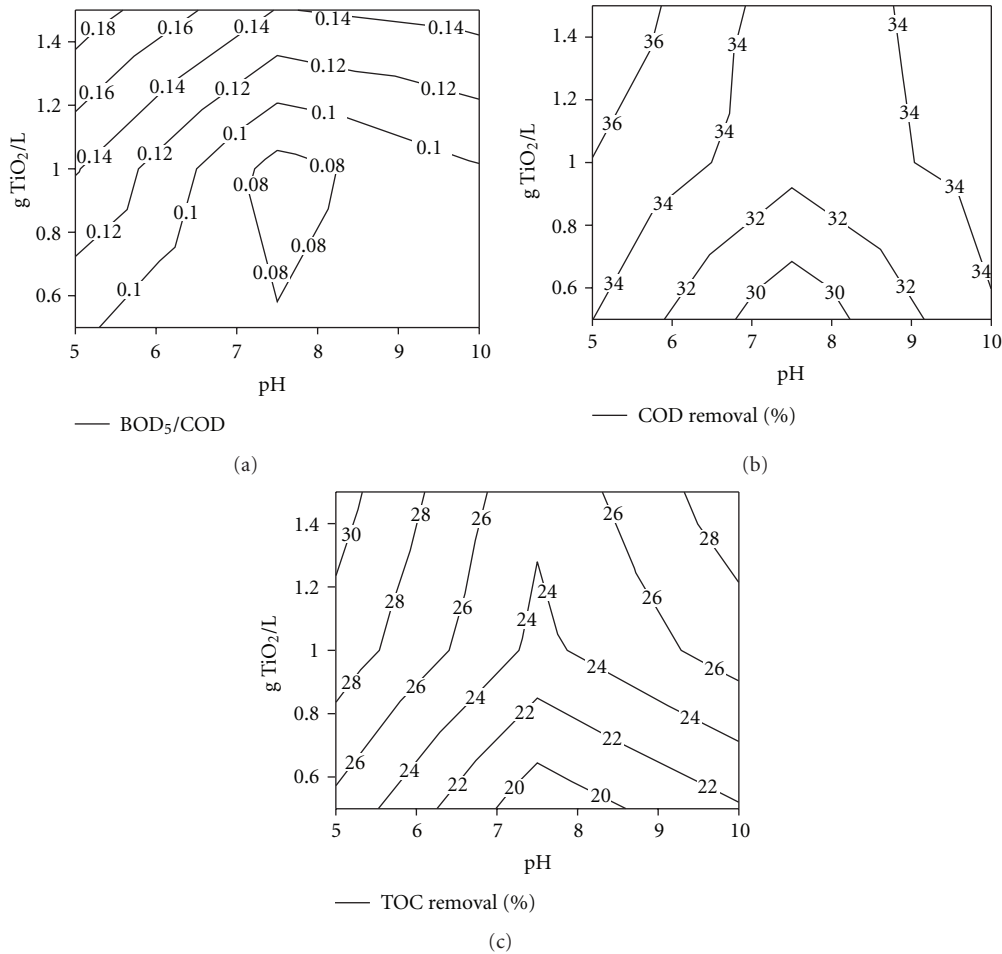
FIGURE 1: Contour of the biodegradability (a) and degradation efficiency (b) and (c) of color filter wastewater as a function of initial pH and TiO_2 dosage (reaction time: 3 h).

heat irradiation in terms of 15~20°C increase in wastewater temperature in this study. Consequently, a 37.4% of COD and a 25.8% of TOC degradation of color filter wastewater were achieved in a reaction time of 1 h with the assistance of Fresnel lens, in contrast to a 32.9% of COD and a 24.4% of TOC degradation in 3 h reaction by an artificial solar irradiation with an $UV_{280-400\,nm}$ intensity of 66.5 W/m^2.

Moreover, the degree of oxidation of color filter wastewater during solar photocatalysis could significantly affect the biodegradability of solution. The average oxidation state (AOS) of organic carbon could be used to monitor the change in the degree of oxidation of pollutants [1]. The

average oxidation state of the organic carbon was calculated by.

$$AOS = 4 - 1.5 \times \frac{COD}{TOC}, \qquad (8)$$

in which the unit of COD and TOC is mg/L. The AOS value indicates how chemical substances in the effluent become more oxidized. A higher AOS value implies a higher degree of oxidation. Theoretically, the AOS has a value of +4 for CO_2, the most oxidized state of C, and −4 for CH_4, the most reduced state of carbon. As shown in Table 3, the AOS values increased from −0.73 for untreated color filter wastewater

(a)

(b)

(c)

- ● 250 W/m² (UV$_{280–400\,nm}$ = 27.5 W/m²)
- ○ 500 W/m² (UV$_{280–400\,nm}$ = 66.5 W/m²)
- ▼ 750 W/m² (UV$_{280–400\,nm}$ = 114 W/m²)
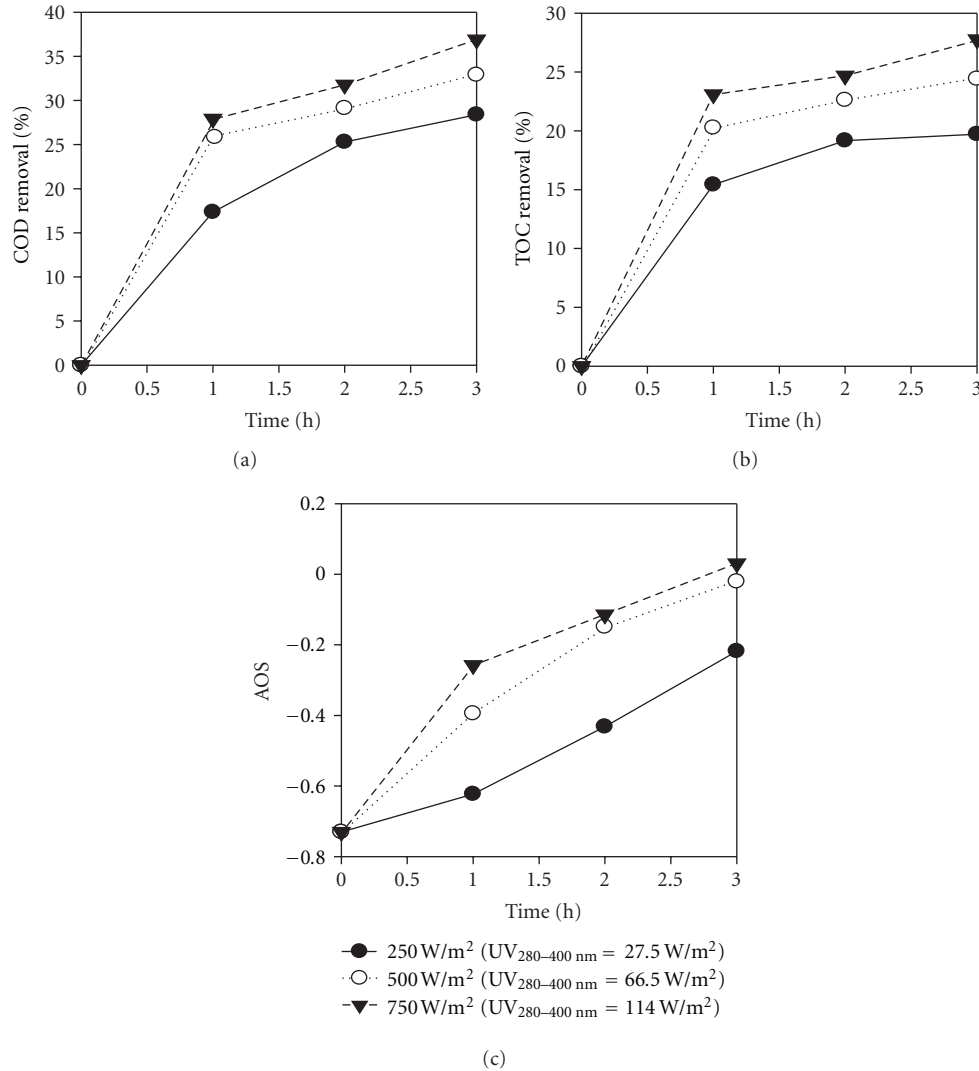
Figure 2: Effect of solar light intensity on the degradation of color filter wastewater (wastewater temperature: $25 \pm 0.5°C$).

to 0.01 and -0.42 for treated color filter wastewater at a reaction time of 1 h with and without using Fresnel lens, respectively. This result implied that a higher degree of oxidation happened, leading to a further improvement in the biodegradability of color filter wastewater in Fresnel-lens-assisted system. The required reaction time to reach the criteria of a possible biodegradability of wastewater, which a BOD$_5$/COD value of 0.15 was usually selected, and it was, therefore much less for the Fresnel-lens-assisted system.

Basically, the degradation efficiency of wastewater increased with increasing light intensity in the TiO$_2$ photocatalytic process [21]. As shown in Figure 2, the result illustrated that the higher the solar light intensity, the higher the COD and TOC degradation was. A 10% increase of the COD and TOC degradation was observed with raising solar light intensity from 250 (UV$_{280–400\,nm}$: 27.5 W/m²) to 750 W/m² (UV$_{280–400\,nm}$: 114 W/m²). This could be becuase a higher light irradiation increased the generation of electron-hole pairs and then produced more oxidizing species such as •OH

radical. A similar phenomenon was observed in the study of Liu et al. [22]. Their result indicated that the TOC degradation efficiency of Acid Yellow 17 solution increased from 5.1% to 53.2% as the intensity of UV light increased from 12.4 to 31.5 W/m², indicating a positive effect of increasing light irradiation.

Furthermore, the degradation efficiency of wastewater probably increased with increasing the temperature of wastewater. The study of Daneshvar et al. [23] indicated that the effect of wastewater temperature on the degradation efficiency of wastewater may not be significant because the adsorption capability of TiO$_2$ may decrease and the recombination of electron hole may accelerate. However, the study of Barka et al. [24] found that the degradation efficiency of dye wastewater increased with raising the wastewater temperature from 20 to 40°C due to the enhanced motivation energy of wastewater, leading to increasing the frequency of collision between pollutants and •OH. As shown in Figure 3, a 10% increase of the COD and TOC degradation was

(a)

(b)

(c)
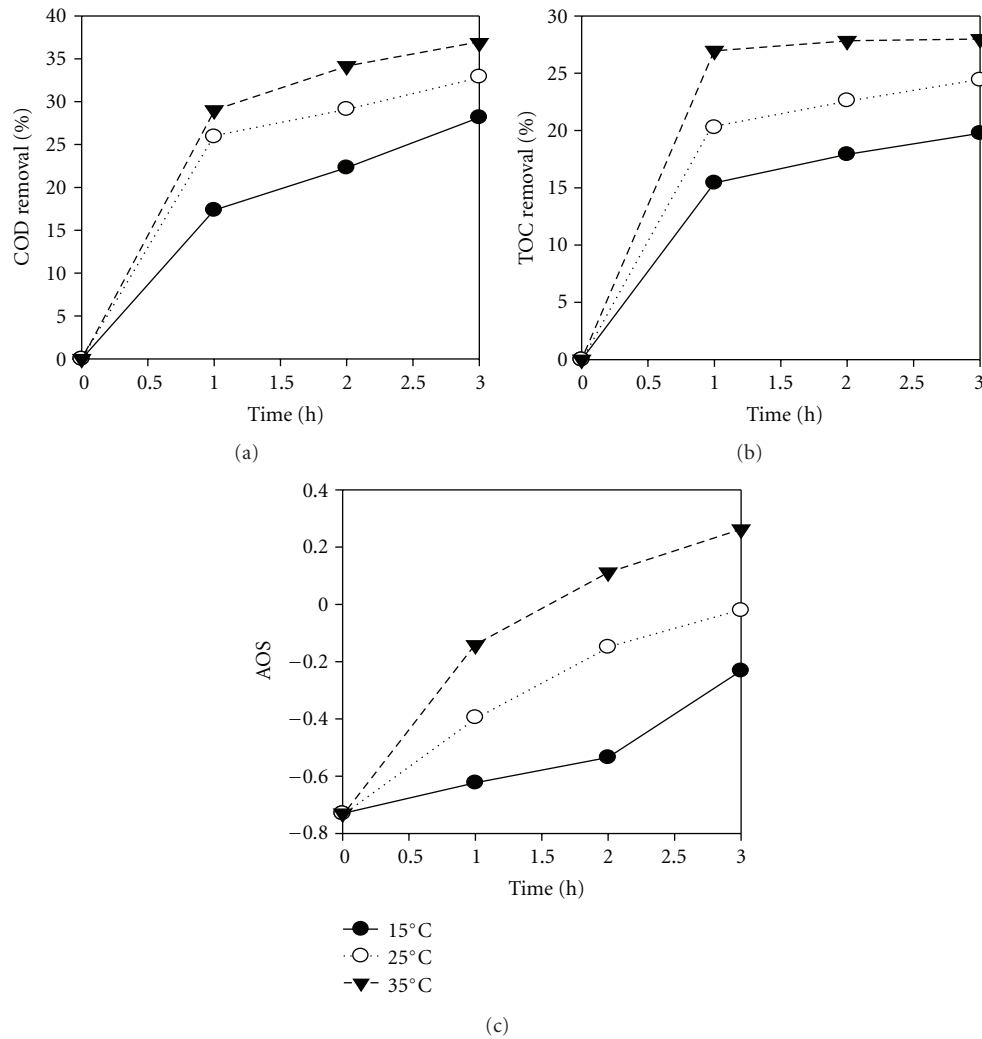
FIGURE 3: Effect of wastewater temperature on the degradation of color filter wastewater (solar light intensity: 500 W/m^2 (UV$_{280-400\,nm}$: 66.5 W/m^2)).

observed with raising wastewater temperature from 15 to 35°C. Similarly, the results of Lin and Lee [25] illustrated that the degradation efficiency of MX-5B dye wastewater improved 15% while the temperature of water was increased from 22 to 40°C in a TiO$_2$ photocatalytic process. This is because a higher water temperature increased the reaction rate between $^{\bullet}$OH and organic molecules. Accordingly, two promotion effects were found with the assistance of Fresnel lens. First, the increase of solar light irradiation could enhance the excitation of electron-hole and then persistent promotion of $^{\bullet}$OH production. Secondly, the raise of water temperature would be higher due to the effect of solar heat irradiation, which provides additional positive effect on the performance of solar photocatalytic process. By the way, quantitative determination of the concentration of hydroxyl radicals produced during photocatalysis may provide more solid explanation for the promotion effect with the assistance of Fresnel lens. Xiang et al. [26] reported that the photolumi-nescence (PL) technique using coumarin as a probe molecule of $^{\bullet}$OH radicals is an effectively probing method for indirect

determination of hydroxyl radical concentration. However, hydroxyl radicals had a short lifetime and high reactivity influencing its detection efficiency. Newton and Milligan [27] had reported that the trapping efficiency of $^{\bullet}$OH formed in the TiO$_2$ photocatalysis was about 5–11% even by the PL technique. Therefore, though the measurement of $^{\bullet}$OH concentration was not performed in this study, the promo-tion effect of Fresnel lens on solar TiO$_2$ photocatalysis is still clear according to the results, namely, the increase of biodeg-radability, COD, and TOC removal efficiency of wastewater.

To quantitatively analyze the effect of solar light intensity and solar heat irradiation in terms of wastewater temperature on the degradation of color filter wastewater, a pseudo-first-order model was applied to obtain the rate constants as shown in Tables 4 and 5, respectively. It was found that both the COD and TOC degradation rate of color filter wastewater increased significantly with increasing solar light intensity and wastewater temperature. The effect of wastewater tem-perature was more obvious than that of solar light intensity on the degradation rate of color filter wastewater.

TABLE 4: Effect of solar light intensity on the degradation rate constant of color filter wastewater[a].

Solar Light Intensity	$^{b}k_{COD}$, hr^{-1}	$^{c}k_{TOC}$, hr^{-1}
250 W/m^2 (UV$_{280-400\,nm}$: 27.5 W/m^2)	0.154	0.118
500 W/m^2 (UV$_{280-400\,nm}$: 66.5 W/m^2)	0.197	0.147
750 W/m^2 (UV$_{280-400\,nm}$: 114 W/m^2)	0.218	0.165

[a]Wastewater temperature: $25 \pm 0.5°C$.
[b]k_{COD}: pseudo-first-order rate constant based on the degradation of COD in solution.
[c]k_{TOC}: pseudo-first-order rate constant based on the degradation of TOC in solution.

TABLE 5: Effect of water temperature on the degradation rate constant of color filter wastewater[a].

Wastewater temperature	$^{a}k_{COD}$, hr^{-1}	$^{b}k_{TOC}$, hr^{-1}
15°C	0.140	0.116
25°C	0.197	0.147
35°C	0.235	0.193

[a]solar light intensity: 500 W/m^2 (UV$_{280-400\,nm}$: 66.5 W/m^2).
[b]k_{COD}: pseudo-first-order rate constant based on the degradation of COD in solution.
[c]k_{TOC}: pseudo-first-order rate constant based on the degradation of TOC in solution.

4. Conclusions

Solar energy could be concentrated efficiently by using Fresnel lens and had a significant effect on the increase of UV$_{280-400\,nm}$ light intensity of solar irradiation and the temperature of wastewater, leading to a positive effect on the performance of solar photocatalytic process. A biodegradability of 0.15 and a COD degradation of 27.4% and a TOC degradation of 25.8% of color filter wastewater were achieved in 1 h reaction under the reaction conditions of an initial pH of 7.5, a TiO$_2$ concentration of 1.5 g/L, and an assistance of Fresnel lens. Consequently, the solar TiO$_2$ photocatalytic process with the use of a PMMA Fresnel lens can offer an economical and practical alternative for the pretreatment of color filter wastewater towards biodegradable, making color filter wastewater be treated effectively by a biological process possible.

Acknowledgments

References

[1] F. Al Momani, "Impact of photo-oxidation technology on the aqueous solutions of nitrobenzene: degradation efficiency and biodegradability enhancement," *Journal of Photochemistry and Photobiology A*, vol. 179, no. 1-2, pp. 184–192, 2006.

[2] L. A. Pérez-Estrada, S. Malato, A. Agüera, and A. R. Fernández-Alba, "Degradation of dipyrone and its main intermediates by solar AOPs. Identification of intermediate products and toxicity assessment," *Catalysis Today*, vol. 129, no. 1-2, pp. 207–214, 2007.

[3] M. I. Maldonado, P. C. Passarinho, I. Oller et al., "Photocatalytic degradation of EU priority substances: a comparison between TiO$_2$ and Fenton plus photo-Fenton in a solar pilot plant," *Journal of Photochemistry and Photobiology A*, vol. 185, no. 2-3, pp. 354–363, 2007.

[4] S. Malato, P. Fernández-Ibáñez, M. I. Maldonado, J. Blanco, and W. Gernjak, "Decontamination and disinfection of water by solar photocatalysis: recent overview and trends," *Catalysis Today*, vol. 147, no. 1, pp. 1–59, 2009.

[5] J.-C. Sin, S.-M. Lam, A. R. Mohamed, and K.-T. Lee, "Degrading endocrine disrupting chemicals from wastewater by TiO$_2$ photocatalysis: a review," *International Journal of Photoenergy*, vol. 2012, Article ID 185159, 23 pages, 2012.

[6] J. A. Byrne, P. A. Fernandez-Ibañez, P. S. M. Dunlop, D. M. A. Alrousan, and J. W. J. Hamilton, "Photocatalytic enhancement for solar disinfection of water: a review," *International Journal of Photoenergy*, vol. 2011, Article ID 798051, 12 pages, 2011.

[7] M. S. T. Gonçalves, E. M. S. Pinto, P. Nkeonye, and A. F. Oliveira-Campos, "Degradation of *C.I. Reactive Orange* 4 and its simulated dyebath wastewater by heterogeneous photocatalysis," *Dyes and Pigments*, vol. 64, no. 2, pp. 135–139, 2005.

[8] A. Durán and J. M. Monteagudo, "Solar photocatalytic degradation of reactive blue 4 using a Fresnel lens," *Water Research*, vol. 41, no. 3, pp. 690–698, 2007.

[9] G. E. P. Box, W. G. Hunter, and J. S. Hunter, *Statistics For Experimenters: An Introduction to Design, Data Analysis and Model Building*, Wiley, New York, NY, USA, 1st edition, 1978.

[10] APHA, AWWA, and WEF, *Standard Methods For the Examination of Water and Wastewater*, American Public Health Association, Washington, DC, USA, 20th edition, 2000.

[11] E. Evgenidou, K. Fytianos, and I. Poulios, "Semiconductor-sensitized photodegradation of dichlorvos in water using TiO$_2$ and ZnO as catalysts," *Applied Catalysis B*, vol. 59, no. 1-2, pp. 81–89, 2005.

[12] G. Li, X. S. Zhao, and M. B. Ray, "Advanced oxidation of orange II using TiO$_2$ supported on porous adsorbents: the role of pH, H$_2$O$_2$ and O$_3$," *Separation and Purification Technology*, vol. 55, no. 1, pp. 91–97, 2007.

[13] Y. Zhang, J. Wan, and Y. Ke, "A novel approach of preparing TiO$_2$ films at low temperature and its application in photocatalytic degradation of methyl orange," *Journal of Hazardous Materials*, vol. 177, no. 1–3, pp. 750–754, 2010.

[14] Q. Xiang, J. G. Yu, and M. Jaroniec, "Tunable photocatalytic selectivity of TiO$_2$ films consisted of flower-like microspheres with exposed {001} facets," *Chemical Communications*, vol. 47, no. 15, pp. 4532–4534, 2011.

[15] D. Wang, J. Zhang, Q. Luo, X. Li, Y. Duan, and J. An, "Characterization and photocatalytic activity of poly(3-hexylthiophene)-modified TiO$_2$ for degradation of methyl orange under visible light," *Journal of Hazardous Materials*, vol. 169, no. 1–3, pp. 546–550, 2009.

[16] J. M. Monteagudo, A. Durán, J. Guerra, F. García-Peña, and P. Coca, "Solar TiO$_2$-assisted photocatalytic degradation of IGCC power station effluents using a Fresnel lens," *Chemosphere*, vol. 71, no. 1, pp. 161–167, 2008.

[17] B. Cheng, Y. Le, W. Q. Cai, and J. G. Yu, "Synthesis of hierarchical Ni(OH)$_2$ and NiO nanosheets and their adsorption kinetics and isotherms to Congo red in water," *Journal of Hazardous Materials*, vol. 185, no. 2-3, pp. 889–897, 2011.

[18] N. Barka, A. Assabbane, A. Nounah, J. Dussaud, and Y. A. Ichou, "Photocatalytic degradation of methyl orange with immobilized TiO$_2$ nanoparticles: effect of pH and some inorganic anions," *Physical and Chemical News*, vol. 41, pp. 85–88, 2008.

[19] M. S. T. Gonçalves, A. M. F. O. Campos, E. M. M. S. Pinto, P. M. S. Plasência, and M. J. R. P. Queiroz, "Photochemical treatment of solutions of azo dyes containing TiO_2," *Chemosphere*, vol. 39, no. 5, pp. 781–786, 1999.

[20] Y. C. Hsu, H. C. Yang, and J. H. Chen, "The enhancement of the biodegradability of phenolic solution using preozonation based on high ozone utilization," *Chemosphere*, vol. 56, no. 2, pp. 149–158, 2004.

[21] D. Gumy, C. Morais, P. Bowen et al., "Catalytic activity of commercial of TiO_2 powders for the abatement of the bacteria (*E. coli*) under solar simulated light: influence of the isoelectric point," *Applied Catalysis B*, vol. 63, no. 1-2, pp. 76–84, 2006.

[22] C. C. Liu, Y. H. Hsieh, P. F. Lai, C. H. Li, and C. L. Kao, "Photodegradation treatment of azo dye wastewater by UV/TiO_2 process," *Dyes and Pigments*, vol. 68, no. 2-3, pp. 191–195, 2006.

[23] N. Daneshvar, M. Rabbani, N. Modirshahla, and M. A. Behnajady, "Kinetic modeling of photocatalytic degradation of Acid Red 27 in UV/TiO_2 process," *Journal of Photochemistry and Photobiology A*, vol. 168, no. 1-2, pp. 39–45, 2004.

[24] N. Barka, A. Assabbane, A. Nounah, and Y. A. Ichou, "Photocatalytic degradation of indigo carmine in aqueous solution by TiO_2-coated non-woven fibres," *Journal of Hazardous Materials*, vol. 152, no. 3, pp. 1054–1059, 2008.

[25] Y. C. Lin and H. S. Lee, "Effects of TiO_2 coating dosage and operational parameters on a TiO_2/Ag photocatalysis system for decolorizing Procion red MX-5B," *Journal of Hazardous Materials*, vol. 179, no. 1–3, pp. 462–470, 2010.

[26] Q. J. Xiang, J. G. Yu, and P. K. Wong, "Quantitative characterization of hydroxyl radicals produced by various photocatalysts," *Journal of Colloid and Interface Science*, vol. 357, no. 1, pp. 163–167, 2011.

[27] G. L. Newton and J. R. Milligan, "Fluorescence detection of hydroxyl radicals," *Radiation Physics and Chemistry*, vol. 75, no. 4, pp. 473–478, 2006.

Review Article

Heterogeneous Photo-Fenton Reaction Catalyzed by Nanosized Iron Oxides for Water Treatment

Chuan Wang,[1] Hong Liu,[1] and Zhimin Sun[2]

[1] *Chongqing Institute of Green and Intelligent Technology, Chinese Academy of Sciences, Chongqing 401122, China*
[2] *Guangzhou Municipal Engineering Design & Research Institute, Guangzhou 510060, China*

Correspondence should be addressed to Hong Liu, liuhong@cigit.ac.cn

Great efforts have been exerted in overcoming the drawbacks of the Fenton reaction for water treatment applications. The drawbacks include pH confinement, handling of iron sludge, slow regeneration of Fe(II), and so forth. This paper highlights the recent developments in the heterogeneous photo-Fenton reaction which utilizes nanosized iron oxides as catalyst for maximizing the activity due to the enhanced physical or chemical properties brought about by the unique structures. This paper also summarizes the fundamentals of the Fenton reaction, which determine the inherent drawbacks and associated advances, to address the advantages of iron oxides and nanosized iron oxides. Tips for applying this method in water treatment are also provided. Given that the environmental effect of nanosized iron oxides is not yet well established, rapid research growth may occur in the near future to advance this promising technology toward water treatment once it is smartly coupled with conventional technologies.

1. Introduction

Large amounts of wastewater from industries, agriculture, and households are produced every day, and organic wastewater has a dominant proportion. The organic content must be reduced to a sufficiently low level acceptable for the receiving waters. Organic pollutants are highly toxic and need to be subjected to physicochemical approaches such as advanced treatment or pretreatment.

The Fenton reaction is frequently investigated as a physicochemical technology because it involves highly oxidative activity of hydroxyl radicals ($\bullet$OH) with respect to the substrates [1]. The $\bullet$OH is the second most powerful oxidizing species after fluorine in aqueous media, and it is believed to destroy or even mineralize most organic substrates nonselectively in advanced oxidation processes [2–5].

Fenton reaction uses H_2O_2 and ferrous ion (Fe^{2+}) to produce $\bullet$OH, as shown in the following reactions [1]:

$$Fe^{2+} + H_2O_2 \longrightarrow Fe^{3+} + {}^\bullet OH + OH^-, \quad k_1 = 76\,M^{-1}S^{-1} \tag{1}$$

$$Fe^{3+} + H_2O_2 \longrightarrow Fe^{2+} + HO_2{}^\bullet + H^+, \quad k_2 = 0.02\,M^{-1}S^{-1} \tag{2}$$

$$Fe^{2+} + HO_2{}^\bullet \longrightarrow Fe^{3+} + {}^\bullet OH_2{}^-, \quad k_3 = 1.3 \times 10^6\,M^{-1}S^{-1} \tag{3}$$

$$Fe^{3+} + HO_2{}^\bullet \longrightarrow Fe^{2+} + O_2 + H^+, \quad k_4 = 1.2 \times 10^6\,M^{-1}S^{-1} \tag{4}$$

$$H_2O_2 + HO^\bullet \longrightarrow HO_2{}^\bullet + H_2O, \quad k_5 = 2.7 \times 10^7\,M^{-1}S^{-1} \tag{5}$$
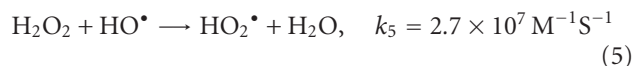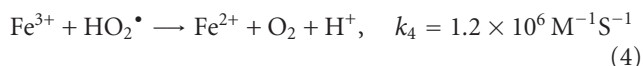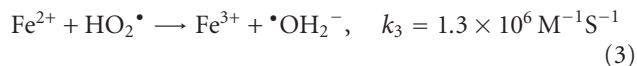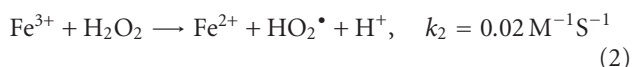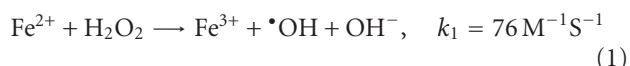
During the process, Fe^{2+} is oxidized to ferric ion (Fe^{3+}) and then reduced back to Fe^{2+}. Thus, iron is considered to function as a catalyst. Several studies indicate that Fe^{3+} can also mediate the Fenton reaction [6–8]. In practice, an Fe^{2+} solution almost inevitably contains Fe^{3+}; thus, the Fenton reaction is actually mediated by the mixture of Fe^{2+} and Fe^{3+}.

Apart from its well-established high efficiency, the Fenton reaction has attracted much attention because of its environmental friendliness, that is, nontoxic products (1)–(6) However, engineers encounter two drawbacks when implementing the Fenton reaction in water treatment. First, the working pH for the reaction is confined to 2.0–4.0, and the highest efficiency of the Fenton reaction occurs at pH 2.8–3.0 [9, 10]. At pH higher than 4.0, the Fenton reaction appears to terminate due to the precipitation of Fe^{3+}. Second,

the amount of iron ions decreases because Fe^{3+} precipitates after use due to its extremely low solubility product constant even at the pH 4.0.

The escape of iron ions can be prevented and the range of the working pH can be widened once the Fenton reaction evolves into a heterogeneous Fenton reaction that utilizes solid iron oxides as a catalyst instead of free iron ions [10, 11]. A light source can also elevate the reaction efficiency by enhancing the generation of $^{\bullet}OH$ and recycling Fe(II)/Fe(III). Nanosized iron oxides further exhibit improved catalytic activity because of their large surface area, which potentially provides more active sites for the generation of $^{\bullet}OH$ [12–19].

This review focuses on the heterogeneous photo-Fenton reaction catalyzed by nanosized iron oxides. Iron oxides are commonly found in nature and can be easily prepared in the laboratory. They are commonly considered to be nontoxic, environmentally friendly compounds similar to free iron ions, in contrast to other Fenton-like ions such as cobalt ions [20, 21]. In particularly, the nanosized iron oxides have been acknowledged to have unique properties including stronger adsorptive and catalytic activities. Moreover, the solid iron oxides are subjected to manipulate to achieve special physical and chemical structures, which serve to bring added advantages to the target reactions. Consequently, the Fenton reaction using nanosized iron oxides should be paid, as it is, great attention. Besides, UV-based technologies [22–24] have also been widely tested and already implemented in wastewater treatment plants. Thus, the utilization of a light source in the heterogeneous photo-Fenton reaction, which aids to enhance the Fenton reaction by generating more radicals, is expected to be widespread as it has already been. From an economic point of view, once the solid iron oxides become reusable, the operation cost of the Fenton reaction can be considerably reduced. However, the heterogeneous photo-Fenton reaction is rarely studied compared with other types of Fenton reactions, and thus deserves further investigations. To arouse the attention of readers regarding the importance of heterogeneous photo-Fenton reaction using the nanosized iron oxides for water treatment, this review starts with the brief development of the Fenton reaction, then has a special interest in the iron oxides as catalysts for the heterogeneous Fenton reaction, emphasizing the nanosized iron oxides including their preparation, associated Fenton matrix, and working mechanism. After that, the reusability of nanosized iron oxide and coupling of heterogeneous Fenton reaction with conventional water treatment technologies are addressed because the two topics are significant in real applications. Ahead of the concluding remarks, the potential environmental effect of nanoiron oxides is covered.

2. Developments of the Fenton Reaction

The classic Fenton process begins with the production of short-lived, extremely reactive $^{\bullet}OH$ with a potential of 2.8 V [1] from the interaction between Fe^{2+} and H_2O_2 (1). $^{\bullet}OH$ then attacks the substrate, which results in substrate decomposition [1, 25].

$^{\bullet}OH$ generation occurs with the concurrent transformation of Fe(II) to Fe(III), whose kinetics relies on the pH, partial pressure of oxygen, and initial concentration of Fe^{2+}, as expressed in the following equation [26]:

$$\frac{d[Fe^{2+}]}{dt} = k[OH^-]^2 P_{O_2}[Fe^{2+}] \qquad (6)$$

This indicates that the pH plays an important role in Fe(II) transformation, and a high pH favors Fe(II) oxidation. pH higher than 4.0 induces Fe(II) oxidation and its subsequent rapid precipitation, which adversely terminates the Fenton reaction. Therefore, the classic Fenton reaction is limited by a narrow pH range.

Under the narrow pH range, iron must be separated from water after use by adding alkali to form iron sludge, which is an awkward process in real applications. Thus, a heterogeneous Fenton reaction using solid iron oxides to extend the pH range and prevent the formation of iron sludge was needed.

The Fenton reaction is sustained by the redox recycling of the Fe(II)/Fe(III) couple, although Fe^{3+} can also initiate a Fenton-like reaction [27]. Equations (1) and (2) suggest that the reduction of Fe^{3+} to Fe^{2+} occurs much more slowly than the backward process. Thus, any measure to accelerate the Fe(II) regeneration is desired in the Fenton-based reaction. The phototreatment of solid iron oxides can accelerate the recycling of Fe(II)/Fe(III), as illustrated by [28]

$$Fe^{3+} + H_2O + h\nu \longrightarrow HO^{\bullet} + Fe^{2+} + H^+ \qquad (7)$$

Thus, the heterogeneous photo-Fenton reaction is established [29]. Given the difficult transportation and storage of H_2O_2, H_2O_2 is produced electrochemically instead of chemically. The in situ electrochemical production of H_2O_2 is performed via the cathodic reduction of oxygen from ambient air to establish the electro-Fenton reaction [25, 30–34]:

$$O_2 + 2e + 2H^+ \longrightarrow H_2O_2 \qquad (8)$$
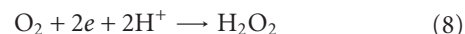
At the same time, the anodic reaction occurs to produce oxygen:

$$H_2O \longrightarrow \frac{1}{2}O_2 + 2H^+ + 2e \qquad (9)$$
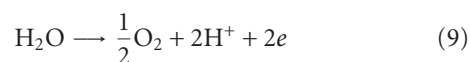
H^+ consumption (cathodic reaction) and production (anodic reaction) is an equilibrium process. Liu et al. [35] utilizes this inherent consumption and production of H^+ to adjust the pH automatically for the Fenton reaction instead of chemical addition.

Following the fundamental research of Fenton reaction, remarkable developments have been made to advance its application in water treatment [13, 26, 36]. A variety of Fenton reactions are outlined in Table 1.

Table 1 shows that the efforts exerted to develop the Fenton reaction focused on pH extension, in situ supply of H_2O_2 via the cathodic reduction of oxygen, in situ supply of Fe^{2+} via the electrochemical anodic oxidation of elemental iron, avoidance of iron loss, and Fe(II) regeneration by

TABLE 1: Varieties of Fenton reactions.

	Reagents	pH	Iron loss	Light
Classic Fenton	H_2O_2, Fe^{2+}	2–4	Yes	No
Fenton-like	H_2O_2, Fe^{3+}	2–4	Yes	No
Photo-Fenton	H_2O_2, iron complex, free iron ions	Acidic to neutral	Yes	Yes
Heterogeneous Fenton	H_2O_2, solid iron oxide	Wide range	No	No
Electro-Fenton	Electrogenerated H_2O_2, free iron ions; H_2O_2, electrogenerated Fe^{2+}	2–4	Yes	
Heterogeneous photo-Fenton	H_2O_2, solid iron oxide	Wide range	No	Yes
Heterogeneous photoelectro-Fenton	Electrogenerated H_2O_2, solid iron oxide	Wide range	No	Yes

illuminating the sludge iron sources [37]. Although all these modifications of the classic Fenton reaction cannot be coupled in one system, the heterogeneous photo-Fenton reaction unifies most of them and poses a promising Fenton-based technology. Obviously, it overcomes the pH limitation, prevents the iron loss after use like that in the reaction using free iron ions as the iron sources, and utilizes light to favor Fe(II) generation from Fe(III). The in situ supply of electrogenerated H_2O_2 can also be coupled into this system to form a photoelectro-Fenton system [31, 33]. Fe-oxalate can also be utilized in a heterogeneous photo-Fenton system by fixing the Fe ions on silica fabric [37]. Therefore, the heterogeneous photo-Fenton reaction covers almost all developments of the Fenton reaction and has certainly attracted much attention in recent years.

3. Iron Oxides as Catalysts for the Heterogeneous Fenton Reaction

Iron oxides are found abundantly in nature and easily synthesized in the laboratory. There are some iron oxides that exist in nature, hematite, magnetite (Fe_3O_4), maghemite, β-Fe_2O_3, ε-Fe_2O_3, goethite, ferrihydrite, lepidocrocite, and wüstite (FeO). Oxide-hydroxides can be dehydroxylated to their oxide counterparts under specific conditions such as thermal treatment. In most iron oxides, iron is present in the trivalent state, and three compounds of green rusts, magnetite, and wüstite contain Fe(II).

Although all iron oxides are crystalline, their degrees of structural order and crystallinities differ depending on the conditions for crystal formation. Ferrihydrite and schwetmannite are poorly crystalline. The structures of the iron oxides are well defined [38], and particularly interesting, determine the activities for the degradation of organic substrates.

Iron oxides are semiconductors. For instance, stoichiometric hematite is an n-type semiconductor, with the conduction band composed of empty Fe^{3+} d orbitals and the valence band consisting of full $2t_{2g}$ orbitals. Photocatalysts such as n-type TiO_2 with a bandgap of 3.2 eV that outputs holes and electrons upon UV excitation have been frequently investigated [39–41]. During the TiO_2 photocatalytic process to decompose organic substrates, photogenerated holes can attack H_2O molecules to produce $^\bullet OH$, which further oxidizes the organic substrates. Likewise, the bandgap of stoichiometric hematite is commonly considered to be 2.2 eV [42]; thus, it can be photoexcited by light for the decomposition of organic pollutants in waters [43–45] and the splitting of H_2O to extract hydrogen energy [46] or disinfect the water [47]. Apparently, poorly crystalline iron oxides release iron ions more readily than their good-crystalline counterparts particularly in acidic media.

4. Nanosized Iron Oxides as Catalysts for the Heterogeneous Photo-Fenton Reaction

Under sunlight irradiation, iron minerals are known to undergo reductive dissolution into Fe^{2+} species with the concomitant oxidation of organic compounds on solid-liquid surfaces [48]. These heterogeneous photo-Fenton reactions with iron oxides as catalysts can be mimicked and applied in water treatment. Some mineral iron oxides such as Fe_3O_4 and FeO [49] have been reported to mediate the photo-Fenton reaction. To obtain desired properties, iron oxides are often prepared artificially; thus, extensive efforts have been exerted to the synthesis of iron oxides in the last decade.

Iron oxides are readily prepared using different methods, and their size, orientation, dimensionality, and morphology can be manipulated. Table 2 shows that, in recent years, various interesting architectures of nanoparticles, nanorods, nanoplates, nanosheets, and nanotubes for potential electronic, magnetic, optoelectronic, biomaterial, and catalytic applications have been developed. Nanoparticles have at least one dimension in size of less than 100 nm, and the activity of solid catalysts depends on their particle size and fine structure. With decreased catalyst particle size to the nanometer scale, the particles exhibit unique catalytic activity due to their increased surface areas and number of active sites.

Nanoiron oxides have also been intensively fabricated, and the nanostructures of α-Fe_2O_3, γ-Fe_2O_3, and Fe_3O_4 have attracted remarkable interest due to their potential applications in nanodevices. Among iron oxides, nanohematite is the most widely prepared probably because of its scientific and technological importance as the most stable iron oxide under ambient conditions. Several methods for hematite preparation are listed in Table 2.

For the large-scale production of nanoiron oxides, a low operational cost is highly expected. Generally, the hydrothermal method involves high pressure and temperature, and is thus an energy-intensive route. A method that utilizes a template or substrate to control direct growth often suffers from high cost, heterogeneous impurity, and complexity. For

TABLE 2: Preparation methods of iron oxides.

Nomenclature	Chemical	Preparation methods	Reference
Nanorod, nanosphere, and nanohexagon	α-Fe$_2$O$_3$	Hydrothermal	[50]
Nanohematite	α-Fe$_2$O$_3$	Hydrothermal	[51, 52]
—	α-Fe$_2$O$_3$	Chemical precipitation	[53]
—	—	High-energy ball milling	[54]
Nanocomposite	Fe$_2$O$_3$/SiO$_2$	Sol-gel method	[16, 55]
Maghemite (7-8 nm)	—	Microemulsion method	[56]
Fe/SBA-15	Hematite	Two solvent impregnation technique	[57]
	α-Fe$_2$O$_3$	Solvent thermal	[45]
Flower-like hierarchical α-Fe$_2$O$_3$	α-Fe$_2$O$_3$	Vapor-solid growth	[58]
	α-Fe$_2$O$_3$	Solution-combustion	[59]
Flower-like hematite	—	Complexation-mediated oxidation-hydrolysis	[60]
Nanocrystals	α-Fe$_2$O$_3$	Convenient organic phase process	[61]
Nanoparticle	α-Fe$_2$O$_3$	conducting controlled oxidation reactions	[62]
Nanocube	α-Fe$_2$O$_3$	—	[63]
Nanospindle	α-Fe$_2$O$_3$	—	[64]
Nanorod	α-Fe$_2$O$_3$	Ethylenediamine-(EDA-) assisted method	[65, 66]
Nanowire	α-Fe$_2$O$_3$	Oxidation of pure iron	[67]
Nanotube	—	Solutionphase approach	[52, 68]
Nanobelt	α-Fe$_2$O$_3$	Direct thermal oxidation	[69]
Nanoflake	α-Fe$_2$O$_3$	Deposition	[70]

example, in hematite nanotube preparation using an Al$_2$O$_3$ anodic membrane, the hard template needs to be removed by chemical etching in aqueous NaOH, an extremely basic solution [68].

To overcome the disadvantages of the conventional hydrothermal and template methods for the synthesis of nanosized iron oxides, Zhou and Wong [71] reported a facile synthesis of α-Fe$_2$O$_3$ hierarchical nanoarchitectures by a solvent thermal process (isopropyl alcohol-mediated self-assembly) without any template or matrix. The formation of 3D porous flower-like α-Fe$_2$O$_3$ involves a few sequential steps, including nucleation and aggregation, secondary growth (self-assembly), further growth (also self-assembly), and Ostwald ripening (coarsening) [45]. Similarly, Wang et al. [72] prepared flower-like porous hematite nanoarchitectures by annealing the iron oxide precursor formed via the oxidation-hydrolysis reaction between Fe(II) ions and Tris(hydroxymethyl) aminomethane (Tris). They proposed

a formation mechanism of "complex-assembly-aggregation-etching," wherein as-prepared flower-like nanostructures are nucleated by the self-assembly of Fe(II)-Tris complexes via hydrogen bonds. A simple solution-combusting method to prepare nano-α-Fe$_2$O$_3$ particles has been reported. Using a mixture solvent of ethanol and ethyleneglycol, FeCl$_3$ as iron source, and atmospheric oxygen gas as oxidant, nano-α-Fe$_2$O$_3$ particles can be rapidly obtained in one step. This method is cost effective, safe, easily reproducible, and high yielding [72].

Aside from one-component iron oxides, iron oxides with two or more components can be prepared [12] with each component having its specialized function. The composite iron oxides exhibits unique chemical and physical properties.

Chemically, the combination of two oxides exerts a synergistic effect that outweighs the sum of the effects of all individual components. Mazille et al. [73, 74] prepared polymer films that contain titanium oxide and iron oxide (PVF^f-TiO$_2$-Fe). Experiments on the photocatalytic degradation of a few organic substrates (e.g., phenol, nalidixic acid, pesticide mixtures, etc.) demonstrated that the composite oxides have synergistic photocatalytic activity at neutral pH. The high activity is attributed to the photo-Fenton reaction (10) and photocatalytic reaction (11) occurring both on the iron oxide and TiO$_2$ surfaces. In particular, the synergistic activity (12) between the two components is believed to accelerate Fe(II) regeneration, which is the rate-determining step in the Fenton reaction [75]. The simplified mechanism can be outlined as follows:

$$=\!Fe(III) + H_2O_2 \longrightarrow =\!Fe(II) + H^+ + HO_2^{\bullet}$$

$$=\!Fe(II) + H_2O_2 \longrightarrow =\!Fe(III) + OH^- + OH^{\bullet} \quad (10)$$

$$=\!Fe(III)L_n + h\nu \longrightarrow =\!Fe(II)L_{n-1} + L_{ox}^{\bullet+}$$

$$Fe\ oxide + h\nu \longrightarrow Fe\ oxide\ (e^- + h^+)$$

$$TiO_2 + h\nu \longrightarrow TiO_2(e^- + h^+) \quad (11)$$

$$=\!Fe(III) + h\nu + TiO_2 \longrightarrow =\!Fe(IV) + TiO_2(e^-)$$

$$Fe\ oxide + TiO_2 \longrightarrow Fe\ oxide\ (e^-) + TiO_2 \quad (12)$$

$$Fe\ oxide\ (e^-) + =\!Fe(III) \longrightarrow Fe\ oxide + =\!Fe(II)$$
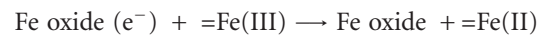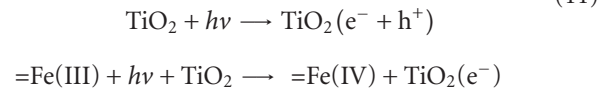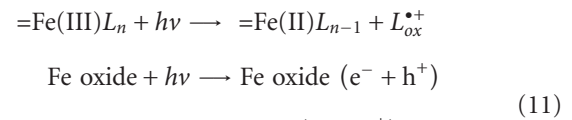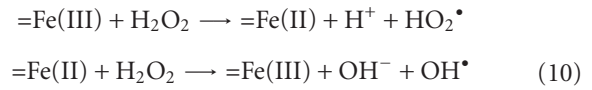
In all the above equations, $=\!Fe(II)$ and $=\!Fe(III)$ are iron species in the solid phase or at the solid-liquid interface.

In some circumstances, the cocomponent assists the immobilization and dispersion of fine particles of iron oxides, which are not trivial tasks. Rasoulifarda et al. [76] prepared nanosized Fe$_2$O$_3$/SiO$_2$ composites by the sol-gel method and calcination. Fe$_2$O$_3$ induces the photo-Fenton decolorization of azo dye from contaminated water, and SiO$_2$ immobilizes the iron oxides. Ho et al. [77] applied solid waste comprising iron oxides that is immobilized on SiO$_2$ in the photo-Fenton degradation of reactive black B in a fluidized reactor. SiO$_2$ also ensures the recovery of the catalyst with continued activity after three successive tests. Chhabra et al. [51] used a single SBA-15 silica with a mesopore diameter of 7.1 nm and two solvent impregnation techniques to

deposit the iron ions into silica pores. Interesting, a spatial location of the iron oxides are observed to be trapped inside the silica pores or dispersed outside silica grains. The external hematite particles are significantly less active and react less rapidly than the internally trapped iron species in the photo-Fenton decomposition. Wang et al. [78] observed that, the dispersion of α-Fe$_2$O$_3$ on silica minimizes particle growth during the sintering process. Fe$_2$O$_3$ crystallites also have larger surface areas and smaller sizes of around 8 nm than unsupported Fe$_2$O$_3$ (>30 nm). They also observed through X-ray diffraction that the phase transformation from β-FeOOH to α-Fe$_2$O$_3$ upon thermal treatment is inhibited on silica. In the presence of silica, newly formed ferric (hydr)oxides via photodissolution are preferably redeposited onto the silica instead of α-Fe$_2$O$_3$ due to the negatively charged surface. Ferric (hydr)oxides are mostly amorphous and less photoactive; thus, α-Fe$_2$O$_3$/SiO$_2$ is more photoactive than α-Fe$_2$O$_3$.

Another type of two-component iron oxide is formed by the modification of iron oxides using a metal such as gold. Gao et al. [46] described an Au/Fe$_2$O$_3$ aerogel for the photodegradation of azo dye. Due to the addition of gold species to the Fe$_2$O$_3$, the light absorption spectrum shifts toward the red visible region and reduces the band gap energy. Accordingly, enhanced photocatalytic activity is obtained.

Sometimes, coexisting organic substance, such as organic acids, especially oxalic acid, serves as an indispensable component of the heterogeneous Fenton reaction. The organic acid interacts with the iron oxide under the excitation of photoenergy to produce s serials of radicals including hydroxyl radicals, and then the target substrates are decomposed [79–81].

5. Reuse of NanoIron Oxides

In the photo-Fenton process, the use of Fe(II)/Fe(III) as a homogeneous catalyst suffers from a major disadvantage, that is, the need to remove the iron sludge after water treatment. This drawback can be overcome by solid iron oxides. The development of nanosized iron oxides increases their activity in the heterogeneous photo-Fenton reaction, whereas the fine particles of nanosized iron oxides necessitate catalyst reusability. The process of separating nanosized particles from the aqueous phase after the reactions is also complicated [82].

For easy separation, magnetic iron oxides [83] that can settle at the bottom of a reactor by the aid of a magnetic field placed under the reactor have been designed. Obviously, this separation method is limited to iron oxides with magnetic force. For other types of nanosized iron oxides without magnetic force, the separation of fine particles from aqueous solution must resort to an alternative technology.

A simple and effective alternative to the prevention of runoff of nanosized catalysts is the immobilization of fine particles on a support. There are various available materials that can serve as supports, such as silica [77, 84, 85], polymer [86, 87], SBA [57], zeolitic Fe(III)-Y and Fe(II)-3X materials [88], alumina [89], and pillared clays [90].

Once immobilized onto support materials, the associated catalytic efficiency may decrease even if there is a synergetic effect. Generally, nanosized iron oxides in powder form can ensure fine contact between light and iron oxide particles. The illumination of the iron oxide surface is a prerequisite for Fe(II)/Fe(III) recycling to sustain the Fenton reaction. Unfortunately, after the particles of iron oxides are immobilized onto a support, particularly onto a porous one, adequate illumination enjoyed by a naked particle system, may be impeded. To date, whether such illumination loss actually occurs is not known.

In TiO$_2$ photocatalysis, Li et al. [82] reported a type of TiO$_2$ microspheres fabricated from TiO$_2$-nanosized particles and their sol precursor. They observed that the microspheres possess larger pore volumes and surface areas, and consequently, comparable activity with the nanosized particle counterpart. Microspheres with sizes of 30–160 μm can also be suspended readily by air bubbling to ensure sufficient illumination. These microspheres can settle quickly at the bottom of the reactor when the air supply stops after use for easy separation from the aqueous solution and reuse. This design concept also appears to be applicable in the heterogeneous photo-Fenton system with nanosized iron oxides.

On the other hand, support materials sometimes have adverse effects on the photo-Fenton reaction. For example, after the support of iron oxides on zeolite, the iron exchange of iron species within the zeolite framework slows down and the stability decreases compared with those in unsupported iron oxides, and some supports such as Nafion are very costly because perfluorosulphonic polymer is used [91]. Thus, its large-scale application in water treatment is hindered.

6. Coupling of Iron Oxide-Based Heterogeneous Photo-Fenton Technology with an Integrated Process of Water Treatment

Effluents discharged from industrial processes usually contain recalcitrant pollutants that are nonbiodegradable and destroyed only by chemical approaches. Fenton-based processes are highly effective chemical means that offer simple and cost-effective sources of $^{\bullet}$OH to decompose recalcitrant pollutants [92–94]. The heterogeneous photo-Fenton reaction addresses the drawbacks that arise from the classic Fenton reaction, and it is a promising chemical technology for destroying and mineralizing recalcitrant pollutants. Following the successful development of the heterogeneous photo-Fenton technology with iron oxides as catalyst, an incorporation of this technology into an overall process for water treatment becomes essential, given that any individual technology has its own inherent disadvantages and compatible conditions. Water purification demands the coupling of diverse technologies to achieve an integrated process.

Technically, the heterogeneous photo-Fenton process is applicable when two prerequisites are satisfied. One is the transparency of water that ensures the transmission of light. The other is the nonbiodegradability of water that has to be treated by the abiotic method. This method is expected to

improve the biodegradability of water as a pretreatment unit or to decompose recalcitrant pollutants as an advanced unit.

Along with the heterogeneous photo-Fenton process are conventional technologies that work together to purify the polluted influent. At the front-end of the integrated process, the influent can be pretreated by a physical unit such as filtration or grilling to separate the solids present in it. A physicochemical process such as coagulation is subsequently performed to remove colloidal substances. A biological process such as aerobic or anaerobic oxidation is performed to degrade most of the biodegradable organic molecules. Thus, the water quality is usually improved in terms of indices such as chemical oxygen demand (COD) and NH_3-N. If the effluent requires further purification to destroy nondegradable organic pollutants, the heterogeneous photo-Fenton technology follows the biological process. Advanced treatment is believed to increasingly important with the increased requirement of wastewater reclamation.

Alternatively, heterogeneous photo-Fenton technology is used prior to the biochemical process to improve biodegradability for better biological oxidization of the organic substrates in the subsequent process. In this regard, the organic pollutants are highly toxic to the biotas; thus, they are decomposed by the heterogeneous photo-Fenton technology [91].

If the heterogeneous photo-Fenton process is followed by another process, further measures must be taken in some cases. For example, if there is H_2O_2 residue (even in small amounts) in the effluent and a membrane process follows for further treatment, the residual H_2O_2 must be decomposed to protect the membrane from oxidation.

The smart coupling of the heterogeneous photo-Fenton technology with conventional technologies results in an integrated process for water treatment. The enhanced degradation of polycyclic aromatic hydrocarbons by biodegradation combined with a modified Fenton's reaction [95] is expected to have progress based on a comprehensive assessment of technique and economic feasibility. A pilot-scale test is extremely necessary to verify such data because related reports are very limited.

7. Potential Environmental Effect of Nanoiron Oxides

Nanoparticles are increasingly used for industrial and commercial purposes due to their unique characteristics, such as large specific surface areas and unique surface structures that cause high surface reactivity. The widespread use of nanoparticles leads to their inevitable release into the environment during manufacturing, transportation, use, and/or disposal. Therefore, the potential health and environmental risks posed by nanoparticles have drawn significant attention in recent years [96]. In aqueous environments, many nanoparticles such as nano-TiO_2 [97, 98] and nano-Al_2O_3 have been confirmed to pose biological risks. Consequently, the bioaccumulation of nanoparticles in aquatic organisms is a very important process that affects the overall toxicity of nanoparticles in a realistic environment.

Iron oxides are commonly considered to be nontoxic, whereas some studies suggest that *C. dubia* significantly accumulate on nano-Fe_2O_3 through ingestion and that nano-Fe_2O_3 serves as a carrier of As(V) to enhance As(V) toxicity [99]. Some studies reported the cytotoxicity of nano-Fe_2O_3 toward different types of cell lines, such as human MSTO cells [100] and PC12 cells [101], or toward different bacteria, such as *Escherichia coli* [102]. Katsnelson et al. also observed that at equal mass doses, Fe_3O_4 nanoparticles possess considerably higher systemic toxicity than microparticles [103].

Nanoiron oxides can also be formed via secondary formation. For example, nanoscale zerovalent iron that is often used for groundwater remediation because of its reducing ability can be oxidized over time to magnetite, maghemite, hematite, and goethite. Such surface oxidation tends to reduce the activity, agglomeration, sedimentation rate, and toxicity to mammalian cells [104].

Primary tests on the toxicity of nanoiron oxides indicate that great care must be taken when handling nanosized iron oxides during their life cycle from manufacturing to disposal. When used in water treatment, nanoiron oxides can be reused by gravity-induced settlement and immobilization onto a support material that enables their fast separation. Although long-term utilization is possible under illumination, the nanoparticles may undergo photocorrosion and escape from the system into the aquatic environment. In this case, further efforts are recommended to improve the photostability of the iron oxides for the heterogeneous photo-Fenton reaction.

8. Concluding Remarks

The heterogeneous photo-Fenton reaction combines most efforts to overcome the drawbacks of the classic Fenton reaction. This combination extends the working pH range using a solid iron source instead of free iron ions. The method also prevents the formation of iron sludge by immobilizing iron oxides, accelerates Fe(II) regeneration by light illumination, and enables the reusability of iron oxides after separation by rapid settlement. The preparation and utilization of nanosized iron oxides pave the way for technological advancement by allowing the manipulation of their architectures and chemical compositions. Consequently, unique physical and chemical properties are exhibited by these nanoiron oxides.

Following the successful development of the heterogeneous photo-Fenton process, a smart coupling of this technology with conventional ones such as filtration, coagulation, biological oxidation, and membrane technology becomes essential. Thus, pilot-scale and field tests are necessary to develop a well-established integrated water treatment process that involves the heterogeneous photo-Fenton reaction and determine technical and economical parameters.

Research on the heterogeneous photo-Fenton process is expected to grow rapidly in the near future prompted by the increasing amount of released recalcitrant pollutants. Future investigations may center on the fabrication of finer physical architectures and well-defined chemical compositions of

nanosized irons oxides. The degradation pathway of organic substrates and evolution of toxicity during the treatment process should be determined. Attention must also be paid to the potential environmental effect of nanosized iron oxides. The mechanism that governs the catalytic reactions occurring on the surface or in the pores of nanosized iron oxides remains to be elucidated as well.

Acknowledgment

References

[1] E. Neyens and J. Baeyens, "A review of classic Fenton's peroxidation as an advanced oxidation technique," *Journal of Hazardous Materials*, vol. 98, no. 1–3, pp. 33–50, 2003.

[2] J. J. Pignatello, "Dark and photoassisted Fe^{3+}-catalyzed degradation of chlorophenoxy herbicides by hydrogen peroxide," *Environmental Science & Technology*, vol. 26, no. 5, pp. 944–951, 1992.

[3] Y. Sun and J. J. Pignatello, "Photochemical reactions involved in the total mineralization of 2,4-D by $Fe^{3+}/H_2O_2/UV$," *Environmental Science & Technology*, vol. 27, no. 2, pp. 304–310, 1993.

[4] N. Miguel, M. P. Ormad, R. Mosteo, and J. L. Ovelleiro, "Photocatalytic degradation of pesticides in natural water: effect of hydrogen peroxide," *International Journal of Photoenergy*, vol. 2012, Article ID 371714, 11 pages, 2012.

[5] F. Z. Shi, Y. G. Li, Q. H. Zhang, and H. Z. Wang, "Synthesis of $Fe_3O_4/C/TiO_2$ magnetic photocatalyst via vapor phase hydrolysis," *International Journal of Photoenergy*, vol. 2012, Article ID 365401, 8 pages, 2012.

[6] J. De Laat, T. G. Le, and B. Legube, "A comparative study of the effects of chloride, sulfate and nitrate ions on the rates of decomposition of H_2O_2 and organic compounds by $Fe(II)/H_2O_2$ and $Fe(III)/H_2O_2$," *Chemosphere*, vol. 55, no. 5, pp. 715–723, 2004.

[7] J. D. Laat and T. G. Le, "Kinetics and modeling of the $Fe(III)/H_2O_2$ system in the presence of sulfate in acidic aqueous solutions," *Environmental Science & Technology*, vol. 39, no. 6, pp. 1811–1818, 2005.

[8] B. Ensing, F. Buda, and E. J. Baerends, "Fenton-like chemistry in water: oxidation catalysis by Fe(III) and H_2O_2," *Journal of Physical Chemistry A*, vol. 107, no. 30, pp. 5722–5731, 2003.

[9] H. Zhang, D. Zhang, and J. Zhou, "Removal of COD from landfill leachate by electro-fenton method," *Journal of Hazardous Materials*, vol. 135, no. 1–3, pp. 106–111, 2006.

[10] H. Zhang, H. J. Choi, and C. P. Huang, "Optimization of Fenton process for the treatment of landfill leachate," *Journal of Hazardous Materials*, vol. 125, no. 1–3, pp. 166–174, 2005.

[11] M. M. Cheng, W. H. Ma, J. Li et al., "Visible-light-assisted degradation of dye pollutants over Fe(III)-loaded resin in the presence of H_2O_2 at neutral pH values," *Environmental Science & Technology*, vol. 38, no. 5, pp. 1569–1575, 2004.

[12] X. L. Liang, Y. H. Zhong, S. Y. Zhu et al., "The contribution of vanadium and titanium on improving methylene blue decolorization through heterogeneous UV-Fenton reaction catalyzed by their co-doped magnetite," *Journal of Hazardous Materials*, vol. 199-200, pp. 247–254, 2012.

[13] C. Cornu, J. L. Bonardet, S. Casale et al., "Identification and location of iron species in Fe/SBA-15 catalysts: interest for catalytic Fenton reaction," *Journal of Physical Chemistry C*, vol. 116, no. 5, pp. 3437–3448, 2012.

[14] M. Fang, T. V. Volotinen, S. K. Kulkarni, L. Belova, and K. V. Rao, "Effect of embedding Fe_3O_4 nanoparticles in silica spheres on the optical transmission properties of three-dimensional magnetic photonic crystals," *Journal of Applied Physics*, vol. 108, no. 10, Article ID 103501, 6 pages, 2010.

[15] S. P. Sun and A. T. Lemley, "*p*-nitrophenol degradation by a heterogeneous Fenton-like reaction on nano-magnetite: process optimization, kinetics, and degradation pathways," *Journal Molecular Catatalysis A*, vol. 349, no. 1-2, pp. 71–79, 2011.

[16] M. H. Rasoulifard, M. H. Hosseini, and S. Masoudian, "Photo-assisted hetero-Fenton decolorization of azo dye from contaminated water by Fe-Si mixed oxide nanocomposite," *Environmental Technology*, vol. 32, no. 14, pp. 1627–1635, 2011.

[17] E. G. Garrido-Ramírez, B. K. G. Theng, and M. L. Mora, "Clays and oxide minerals as catalysts and nanocatalysts in Fenton-like reactions—a review," *Applied Clay Science*, vol. 47, no. 3-4, pp. 182–192, 2010.

[18] F. Martínez, G. Calleja, J. A. Melero, and R. Molina, "Heterogeneous photo-Fenton degradation of phenolic aqueous solutions over iron-containing SBA-15 catalyst," *Applied Catalysis B*, vol. 60, no. 3-4, pp. 181–190, 2005.

[19] A. Jitianu, M. Crisan, A. Meghea, I. Rau, and M. Zaharescu, "Influence of the silica based matrix on the formation of iron oxide nanoparticles in the Fe_2O_3-SiO_2 system, obtained by sol-gel method," *Journal of Materials Chemistry*, vol. 12, no. 5, pp. 1401–1407, 2002.

[20] Q. Han, S. Y. Yang, X. Yang et al., "Cobalt catalyzed peroxymonosulfate oxidation: a review of mechanisms and applications on degradating organic pollutants in water," *Progress in Chemistry*, vol. 24, no. 1, pp. 144–156, 2012.

[21] G. Q. Zhang, S. Wang, and F. L. Yang, "Efficient adsorption and combined heterogeneous/homogeneous Fenton oxidation of amaranth using supported nano-FeOOH as cathodic catalysts," *Journal of Physical Chemistry C*, vol. 116, no. 5, pp. 3623–3634, 2012.

[22] F. Yuan, C. Hu, X. X. Hu, D. Wei, Y. Chen, and J. Qu, "Photodegradation and toxicity changes of antibiotics in UV and UV/H_2O_2 process," *Journal of Hazardous Materials*, vol. 185, no. 2-3, pp. 1256–1263, 2011.

[23] M. S. Lucas, J. A. Peres, and P. G. Li, "Treatment of winery wastewater by ozone-based advanced oxidation processes (O_3, O_3 and $O_3/UV/H_2O_2$) in a pilot-scale bubble column reactor and process economics," *Separation and Purification Technology*, vol. 72, no. 3, pp. 235–241, 2010.

[24] M. Muneer, I. A. Bhatti, E. Ehsan-Ul-Haq, M. Safdar, and F. Fazal-Ur-Rehman, "Applications of advanced oxidation process for industrial wastewater treatment," *Asian Journal of Chemistry*, vol. 22, no. 4, pp. 3087–3093, 2010.

[25] E. Brillas, I. Sirés, and M. A. Oturan, "Electro-fenton process and related electrochemical technologies based on Fenton's reaction chemistry," *Chemical Reviews*, vol. 109, no. 12, pp. 6570–6631, 2009.

[26] W. Sung and J. J. Morgan, "Kinetics and product of ferrous iron oxygenation in aqueous systems," *Environmental Science & Technology*, vol. 14, no. 5, pp. 561–568, 1980.

[27] H. D. Basheer, A. A. R. Abdul, and D. W. M. A. Wan, "Oxidative mineralisation of petroleum refinery effluent

using Fenton-like process," *Chemical Engineering Research and Design*, vol. 90, no. 2, pp. 298–307, 2012.

[28] K. S. Mihir, "Degradation and mineralization, of organic contaminants by Fenton and photo-Fenton processes: review of mechanisms and effects of organic and inorganic additives," *Research Journal of Chemistry and Environment*, vol. 15, no. 2, pp. 96–112, 2011.

[29] C. Cezar, A. Daniela, and A. Petru, "Degradation of 4-chlorophenol from wastewater through heterogeneous Fenton and photo-Fenton process, catalyzed by Al-Fe PILC," *Applied Clay Science*, vol. 58, pp. 96–101, 2012.

[30] E. Brillas, R. Sauleda, and J. Casado, "Degradation of 4-chlorophenol by anodic oxidation, electro-fenton, photoelectro-fenton, and peroxi-coagulation processes," *Journal of the Electrochemical Society*, vol. 145, no. 3, pp. 759–765, 1998.

[31] B. Boye, M. M. Dieng, and E. Brillas, "Degradation of herbicide 4-chlorophenoxyacetic acid by advanced electrochemical oxidation methods," *Environmental Science & Technology*, vol. 36, no. 13, pp. 3030–3035, 2002.

[32] E. Brillas and J. Casado, "Aniline degradation by electro-Fenton and peroxi-coagulation processes using a flow reactor for wastewater treatment," *Chemosphere*, vol. 47, no. 3, pp. 241–248, 2002.

[33] E. Brillas, M. A. Baños, and J. A. Garrido, "Mineralization of herbicide 3,6-dichloro-2-methoxybenzoic acid in aqueous medium by anodic oxidation, electro-Fenton and photoelectro-Fenton," *Electrochimica Acta*, vol. 48, no. 12, pp. 1697–1705, 2003.

[34] E. Brillas, J. C. Calpe, and J. Casado, "Mineralization of 2,4-D by advanced electrochemical oxidation processes," *Water Research*, vol. 34, no. 8, pp. 2253–2262, 2000.

[35] H. Liu, C. Wang, X. Z. Li, X. L. Xuan, C. Jiang, and H. N. Cui, "A novel electro-Fenton process for water treatment: reaction-controlled pH adjustment and performance assessment," *Environmental Science & Technology*, vol. 41, no. 8, pp. 2937–2942, 2007.

[36] C. Walling, "Fenton's reagent revisited," *Accounts of Chemical Research*, vol. 8, no. 4, pp. 125–131, 1975.

[37] A. Bozzi, T. Yuranova, J. Mielczarski, and J. Kiwi, "Evidence for immobilized photo-Fenton degradation of organic compounds on structured silica surfaces involving Fe recycling," *New Journal of Chemistry*, vol. 28, no. 4, pp. 519–526, 2004.

[38] R. M. Cornell and U. Schwertmann, *The Iron Oxides*, Willy, 2003.

[39] Q. J. Xiang, J. G. Yu, and P. K. Wong, "Quantitative characterization of hydroxyl radicals produced by various photocatalysts," *Journal of Colloid and Interface Science*, vol. 357, no. 1, pp. 163–167, 2011.

[40] X. X. Yu, S. W. Liu, and J. G. Yu, "Superparamagnetic γ-Fe_2O_3@SiO_2@TiO_2 composite microspheres with superior photocatalytic properties," *Applied Catalysis B*, vol. 104, no. 1-2, pp. 12–20, 2011.

[41] T. X. Liu, Y. Liu, Z. J. Zhang, F. B. Li, and X. Z. Li, "Comparison of aqueous photoreactions with TiO_2 in its hydrosol solution and powdery suspension for light utilization," *Industrial & Engineering Chemistry Research*, vol. 50, no. 13, pp. 7841–7848, 2011.

[42] A. Kay, I. Cesar, and M. Grätzel, "New benchmark for water photooxidation by nanostructured α-Fe_2O_3 films," *Journal of the American Chemical Society*, vol. 128, no. 49, pp. 15714–15721, 2006.

[43] S. K. Maji, N. Mukherjee, A. Mondal, and B. Adhikary, "Synthesis, characterization and photocatalytic activity of α-Fe_2O_3 nanoparticles," *Polyhedron*, vol. 33, no. 1, pp. 145–149, 2012.

[44] S. Hu, G. L. Liu, D. W. Zhu, C. Chen, and S. Liao, "Synthesis, characterization, and evaluation of boron-doped iron oxides for the photocatalytic degradation of atrazine under visible light," *International Journal of Photoenergy*, vol. 2012, Article ID 598713, 4 pages, 2012.

[45] L. P. Zhu, N. C. Bing, L. L. Wang et al., "Self-assembled 3D porous flowerlike α-Fe_2O_3 hierarchical nanostructures: synthesis, growth mechanism, and their application in photocatalysis," *Dalton Transaction*, vol. 2012, no. 41, pp. 2959–2965, 2012.

[46] H. W. Gao, C. Liu, H. E. Jeong, and P. D. Yang, "Plasmon-enhanced photocatalytic activity of iron oxide on gold nanopillars," *ACS Nano*, vol. 6, no. 1, pp. 234–240, 2012.

[47] J. A. Byrne, P. A. Fernandez-Ibanez, P. S. M. Dunlop, D. M. A. Alrousan, and J. W. J. Hamilton, "Photocatalytic enhancement for solar disinfection of water: a review," *International Journal of Photoenergy*, vol. 2011, Article ID 798051, 12 pages, 2011.

[48] U. Schwertmann and R. M. Cornell, *Iron Oxides in the Laboratory: Preparation and Characterization*, John Wiley & Sons, 2008.

[49] E. Expósito, C. M. Sánchez-Sánchez, and V. Montiel, "Mineral iron oxides as iron source in electro-fenton and photoelectro-fenton mineralization processes," *Journal of the Electrochemical Society*, vol. 154, no. 8, pp. E116–E122, 2007.

[50] G. K. Pradhan and K. M. Parida, "Fabrication, growth mechanism, and characterization of α-Fe_2O_3 nanorods," *ACS Applied Materials & Interfaces*, vol. 3, no. 2, pp. 317–323, 2011.

[51] V. Chhabra, P. Ayyub, S. Chattopadhyay, and A. N. Maitra, "Preparation of acicular γ-Fe_2O_3 particles from a microemulsion-mediated reaction," *Materials Letters*, vol. 26, no. 1-2, pp. 21–26, 1996.

[52] C. J. Jia, L. D. Sun, Z. G. Yan et al., "Single-crystalline iron oxide nanotubes," *Angewandte Chemie*, vol. 44, no. 28, pp. 4328–4333, 2005.

[53] X. Q. Su and B. Yan, "The synthesis and luminescence of $YP_xV_{1-x}O_4$:Dy^{3+} microcrystalline phosphors by in situ co-precipitation composition of hybrid precursors," *Materials Chemistry and Physics*, vol. 93, no. 2-3, pp. 552–556, 2005.

[54] Y. H. Ni, X. F. Cao, G. G. Wu, G. Hu, Z. Yang, and X. Wei, "Preparation, characterization and property study of zinc oxide nanoparticles via a simple solution-combusting method," *Nanotechnology*, vol. 18, no. 15, Article ID 155603, 2007.

[55] X. Wang, X. Y. Chen, L. S. Gao et al., "Synthesis of β-FeOOH and α-Fe_2O_3 nanorods and electrochemical properties of β-FeOOH," *Journal of Materials Chemistry*, vol. 14, no. 5, pp. 905–907, 2004.

[56] Z. M. Li, X. Y. Lai, H. Wang, D. Mao, C. Xing, and D. Wang, "Direct hydrothermal synthesis of single-crystalline hematite nanorods assisted by 1,2-propanediamine," *Nanotechnology*, vol. 20, no. 24, Article ID 245603, 2009.

[57] C. Cornu, J. L. Bonardet, S. Casale et al., "Identification and location of iron species in Fe/SBA-15 catalysts: interest for catalytic Fenton reactions," *Journal of Physical Chemistry C*, vol. 116, pp. 3437–3448, 2012.

[58] Y. Y. Fu, R. M. Wang, J. Xu et al., "Synthesis of large arrays

of aligned α-Fe$_2$O$_3$ nanowires," *Chemical Physics Letters*, vol. 379, no. 3-4, pp. 373–379, 2003.

[59] X. H. Wang, L. Zhang, Y. H. Ni, J. Hong, and X. Cao, "Fast preparation, characterization, and property study of α-Fe$_2$O$_3$ nanoparticles via a simple solution-combusting method," *Journal of Physical Chemistry C*, vol. 113, no. 17, pp. 7003–7008, 2009.

[60] X. Huang, J. G. Guan, Z. D. Xiao, G. Tong, F. Mou, and X. Fan, "Flower-like porous hematite nanoarchitectures achieved by complexation-mediated oxidation-hydrolysis reaction," *Journal of Colloid and Interface Science*, vol. 357, no. 1, pp. 36–45, 2011.

[61] S. Sun, H. Zeng, D. B. Robinson et al., "Monodisperse MFe$_2$O$_4$ (M = Fe, Co, Mn) Nanoparticles," *Journal of the American Chemical Society*, vol. 126, no. 1, pp. 273–279, 2004.

[62] H. Deng, X. L. Li, Q. Peng, X. Wang, J. Chen, and Y. Li, "Monodisperse magnetic single-crystal ferrite microspheres," *Angewandte Chemie*, vol. 44, no. 18, pp. 2782–2785, 2005.

[63] S. Hamada and E. Matijević, "Ferric hydrous oxide sols. IV. Preparation of uniform cubic hematite particles by hydrolysis of ferric chloride in alcohol-water solutions," *Journal of Colloid And Interface Science*, vol. 84, no. 1, pp. 274–277, 1981.

[64] M. Ozaki, S. Kratohvil, and E. Matijević, "Formation of monodispersed spindle-type hematite particles," *Journal of Colloid and Interface Science*, vol. 102, no. 1, pp. 146–151, 1984.

[65] K. G. Pradhan and K. M. Parida, "Fabrication, growth mechanism, and characterization of α-Fe$_2$O$_3$ nanorods," *ACS Appied Materials & Interfaces*, vol. 3, pp. 317–323, 2011.

[66] L. P. Zhu, G. H. Liao, N. C. Bing, X. Zhao, and Y. Y. Gu, "Synthesis of monodisperse shuttle-like α-Fe$_2$O$_3$ nanorods via the EDA-assisted method," *Materials Letters*, vol. 65, no. 9, pp. 1287–1290, 2011.

[67] R. M. Wang, Y. F. Chen, Y. Y. Fu, H. Zhang, and C. Kisielowski, "Bicrystalline hematite nanowires," *Journal of Physical Chemistry B*, vol. 109, no. 25, pp. 12245–12249, 2005.

[68] X. Qu, N. Kobayashi, and T. Komatsu, "Solid nanotubes comprising α-Fe$_2$O$_3$ nanoparticles prepared from ferritin protein," *ACS Nano*, vol. 4, no. 3, pp. 1732–1738, 2010.

[69] X. G. Wen, S. H. Wang, Y. Ding, Z. L. Wang, and S. Yang, "Controlled growth of large-area, uniform, vertically aligned arrays of α-Fe$_2$O$_3$ nanobelts and nanowires," *Journal of Physical Chemistry B*, vol. 109, no. 1, pp. 215–220, 2005.

[70] Y. W. Zhu, T. Yu, C. H. Sow et al., "Efficient field emission from α- Fe$_2$O$_3$ nanoflakes on an atomic force microscope tip," *Applied Physics Letters*, vol. 87, no. 2, Article ID 023103, 3 pages, 2005.

[71] H. J. Zhou and S. S. Wong, "A facile and mild synthesis of 1-D ZnO, CuO, and α-Fe$_2$O$_3$ nanostructures and nanostructured arrays," *ACS Nano*, vol. 2, no. 5, pp. 944–958, 2008.

[72] X. H. Wang, L. Zhang, Y. H. Ni, J. Hong, and X. Cao, "Fast preparation, characterization, and property study of α-Fe$_2$O$_3$ nanoparticles via a simple solution-combusting method," *Journal of Physical Chemistry C*, vol. 113, no. 17, pp. 7003–7008, 2009.

[73] F. Mazille, T. Schoettl, N. Klamerth, S. Malato, and C. Pulgarin, "Field solar degradation of pesticides and emerging water contaminants mediated by polymer films containing titanium and iron oxide with synergistic heterogeneous photocatalytic activity at neutral pH," *Water Research*, vol. 44, no. 10, pp. 3029–3038, 2010.

[74] F. Mazille, A. Lopez, and C. Pulgarin, "Synergistic effect of TiO$_2$ and iron oxide supported on fluorocarbon films. Part 2: long-term stability and influence of reaction parameters on photoactivated degradation of pollutants," *Applied Catalysis B*, vol. 90, no. 3-4, pp. 321–329, 2009.

[75] N. Murakami, T. Chiyoya, T. Tsubota, and T. Ohno, "Switching redox site of photocatalytic reaction on titanium(IV) oxide particles modified with transition-metal ion controlled by irradiation wavelength," *Applied Catalysis A*, vol. 348, no. 1, pp. 148–152, 2008.

[76] M. H. Rasoulifarda, H. H. Monfareda, and S. Masoudiana, "Photo-assisted hetero-Fenton decolorization of azo dye from contaminated water by Fe-Si mixed oxide nanocomposite," *Environmental Technology*, vol. 32, no. 14, pp. 1627–2635, 2011.

[77] C. H. Ho, Y. J. Huang, and Y. H. Huang, "Degradation of azo dye reactive black b using an immobilized iron oxide in a batch photo-fluidized bed reactor," *Environmental Engineering Science*, vol. 27, no. 12, pp. 1043–1048, 2010.

[78] Y. Wang, W. P. Du, and Y. M. Xu, "Effect of sintering temperature on the photocatalytic activities and stabilities of hematite and silica-dispersed hematite particles for organic degradation in aqueous suspensions," *Langmuir*, vol. 25, no. 5, pp. 2895–2899, 2009.

[79] Q. Lan, F. Li, C. Liu, and X. Z. Li, "Heterogeneous photodegradation of pentachlorophenol with maghemite and oxalate under UV illumination," *Environmental Science & Technology*, vol. 42, no. 21, pp. 7918–7923, 2008.

[80] F. B. Li, X. Z. Li, X. M. Li, T. X. Liu, and J. Dong, "Heterogeneous photodegradation of bisphenol A with iron oxides and oxalate in aqueous solution," *Journal of Colloid and Interface Science*, vol. 311, no. 2, pp. 481–490, 2007.

[81] Y. Wang, C. S. Liu, F. B. Li, C. P. Liu, and J. B. Liang, "Photodegradation of polycyclic aromatic hydrocarbon pyrene by iron oxide in solid phase," *Journal of Hazardous Materials*, vol. 162, no. 2-3, pp. 716–723, 2009.

[82] X. Z. Li, H. Liu, L. F. Cheng, and H. J. Tong, "Photocatalytic oxidation using a new catalyst—TiO$_2$ microsphere—for water and wastewater treatment," *Environmental Science & Technology*, vol. 37, no. 17, pp. 3989–3994, 2003.

[83] B. H. Lai, C. C. Yeh, and D. H. Chen, "Surface modification of iron oxide nanoparticles with polyarginine as a highly positively charged magnetic nano-adsorbent for fast and effective recovery of acid proteins," *Process Biochemistry*, vol. 47, no. 5, pp. 799–805, 2012.

[84] D. Das, S. Roy, J. W. Chen, and D. Chakravorty, "Interface controlled electrical and magnetic properties in Fe-Fe$_3$O$_4$-silica gel nanocomposites," *Journal of Applied Physics*, vol. 91, no. 7, pp. 4573–4579, 2002.

[85] T. Nakamura, Y. Yamada, and K. Yano, "Novel synthesis of highly monodispersed γ-Fe$_2$O$_3$/SiO$_2$ and ε-Fe$_2$O$_3$/SiO$_2$ nanocomposite spheres," *Journal of Materials Chemistry*, vol. 16, no. 25, pp. 2417–2419, 2006.

[86] L. F. González-Bahamón, F. Mazille, L. N. Benítez, and C. Pulgarín, "Photo-Fenton degradation of resorcinol mediated by catalysts based on iron species supported on polymers," *Journal of Photochemistry and Photobiology A*, vol. 217, no. 1, pp. 201–206, 2011.

[87] J. Fernandez, J. Bandara, A. Lopez, P. Buffat, and J. Kiwi, "Photoassisted Fenton degradation of nonbiodegradable azo dye (Orange II) in Fe-free solutions mediated by cation transfer membranes," *Langmuir*, vol. 15, no. 1, pp. 185–192,

1999.

[88] M. Rios-Enriquez, N. Shahin, C. D. Bazua et al., "Optimization of the heterogeneous Fenton-oxidation of the model pollutant 2,4-xylidine using the optimal experimental design methodology," *Solar Energy*, vol. 77, no. 5, pp. 491–501, 2004.

[89] C. L. Hsueh, Y. H. Huang, and C. Y. Chen, "Novel activated alumina-supported iron oxide-composite as a heterogeneous catalyst for photooxidative degradation of reactive black 5," *Journal of Hazardous Materials*, vol. 129, no. 1–3, pp. 228–233, 2006.

[90] S. Azabou, W. Najjar, A. Gargoubi, A. Ghorbel, and S. Sayadi, "Catalytic wet peroxide photo-oxidation of phenolic olive oil mill wastewater contaminants. Part II. Degradation and detoxification of low-molecular mass phenolic compounds in model and real effluent," *Applied Catalysis B*, vol. 77, no. 1-2, pp. 166–174, 2007.

[91] M. I. Pariente, F. Martínez, J. A. Melero et al., "Heterogeneous photo-Fenton oxidation of benzoic acid in water: effect of operating conditions, reaction by-products and coupling with biological treatment," *Applied Catalysis B*, vol. 85, no. 1-2, pp. 24–32, 2008.

[92] X. R. Zhao, L. H. Zhu, Y. Y. Zhang et al., "Removing organic contaminants with bifunctional iron modified rectorite as efficient adsorbent and visible light photo-Fenton catalyst," *Journal Hazardours Materials*, vol. 215, pp. 57–64, 2012.

[93] X. M. Zhou, J. Y. Lan, G. Liu et al., "Facet-mediated photodegradation of organic dye over hematite architectures by visible light," *Angewandte Chemie*, vol. 51, pp. 178–182, 2012.

[94] A. Dhakshinamoorthy, S. Navalon, M. Alvaro, and H. Garcia, "Metal nanoparticles as heterogeneous Fenton catalysts," *ChemSusChem*, vol. 5, no. 1, pp. 46–64, 2012.

[95] K. Nam, W. Rodriguez, and J. J. Kukor, "Enhanced degradation of polycyclic aromatic hydrocarbons by biodegradation combined with a modified Fenton reaction," *Chemosphere*, vol. 45, no. 1, pp. 11–20, 2001.

[96] D. H. Lin, X. L. Tian, F. C. Wu, and B. S. Xing, "Fate and transport of engineered nanomaterials in the environment," *Journal of Environmental Quality*, vol. 39, no. 6, pp. 1896–1908, 2010.

[97] W. H. Fan, M. M. Cui, H. Liu et al., "Nano-TiO_2 enhances the toxicity of copper in natural water to Daphnia magna," *Environmental Pollution*, vol. 159, no. 3, pp. 729–734, 2011.

[98] D. M. Wang, J. Hu, D. R. Irons, and J. M. Wang, "Synergistic toxic effect of nano-TiO_2 and As(V) on Ceriodaphnia dubia," *Science of the Total Environment*, vol. 409, no. 7, pp. 1351–1356, 2011.

[99] J. Hu, D. Wang, J. T. Wang, and J. M. Wang, "Bioaccumulation of Fe_2O_3(magnetic) nanoparticles in Ceriodaphnia dubia," *Environmental Pollution*, vol. 162, pp. 216–222, 2012.

[100] T. J. Brunner, P. Wick, P. Manser et al., "In vitro cytotoxicity of oxide nanoparticles: comparison to asbestos, silica, and the effect of particle solubility," *Environmental Science & Technology*, vol. 40, no. 14, pp. 4374–4381, 2006.

[101] T. R. Pisanic II, J. D. Blackwell, V. I. Shubayev, R. R. Fiñones, and S. Jin, "Nanotoxicity of iron oxide nanoparticle internalization in growing neurons," *Biomaterials*, vol. 28, no. 16, pp. 2572–2581, 2007.

[102] H. Schwegmann, A. J. Feitz, and F. H. Frimmel, "Influence of the zeta potential on the sorption and toxicity of iron oxide nanoparticles on S. cerevisiae and E. coli," *Journal of Colloid and Interface Science*, vol. 347, no. 1, pp. 43–48, 2010.

[103] B. A. Katsnelson, T. D. Degtyareva, I. I. Minigalieva et al., "Subchronic systemic toxicity and bioaccumulation of Fe_3O_4 nano- and microparticles following repeated intraperitoneal administration to rats," *International Journal of Toxicology*, vol. 30, no. 1, pp. 59–68, 2011.

[104] T. Phenrat, T. C. Long, G. V. Lowry, and B. Veronesi, "Partial oxidation ("aging") and surface modification decrease the toxicity of nanosized zerovalent iron," *Environmental Science & Technology*, vol. 43, no. 1, pp. 195–200, 2009.

Review Article

Electrochemical Techniques in Textile Processes and Wastewater Treatment

Mireia Sala and M. Carmen Gutiérrez-Bouzán

Institut d'Investigació Tèxtil i Cooperació Industrial de Terrassa (INTEXTER),
Universitat Politècnica de Catalunya (UPC), C/Colom 15, 08222 Terrassa, Spain

Correspondence should be addressed to Mireia Sala, mireia.sala@intexter.upc.edu

The textile industry uses the electrochemical techniques both in textile processes (such as manufacturing fibers, dyeing processes, and decolorizing fabrics) and in wastewaters treatments (color removal). Electrochemical reduction reactions are mostly used in sulfur and vat dyeing, but in some cases, they are applied to effluents discoloration. However, the main applications of electrochemical treatments in the textile sector are based on oxidation reactions. Most of electrochemical oxidation processes involve indirect reactions which imply the generation of hypochlorite or hydroxyl radical in situ. These electrogenerated species are able to bleach indigo-dyed denim fabrics and to degrade dyes in wastewater in order to achieve the effluent color removal. The aim of this paper is to review the electrochemical techniques applied to textile industry. In particular, they are an efficient method to remove color of textile effluents. The reuse of the discolored effluent is possible, which implies an important saving of salt and water (i.e., by means of the "UVEC Cell").

1. Introduction

Traditionally, the electrochemical techniques have been used for the synthesis of compounds or for metal recovery treatments. But more recently, a wide range of other applications have been proposed. Some of them are proposed to solve several technical problems of the textile industry. This is the case of a recent application to produce smart textiles [1–28] by obtaining functionalized fabrics. These textiles with specific properties are prepared by using the electrochemistry in the synthesis of conductive polymers, especially conductive fibers.

Another interesting use of the electrochemical techniques is the bleaching of cotton fibers [29] and the bleaching of finished denim fabrics [30–37]. In order to achieve the visual effect in jeans, the generation in situ of hypochlorite by electrochemical reaction has been proposed, instead of its addition.

Their application in sulfur- and vat-dyeing processes [38–61] is also interesting. In this case, dyes are reduced by means of an electrochemical reaction (instead of sodium dithionite). In this way, sulfur and vat dyeing become cleaner processes as the addition of chemical reagents is not required.

Although the electrochemical methods play an important role in the different textile processes listed above, their wider range of applications are related to color removal in wastewater treatments [62–115], in particular, in the degradation of nonbiodegradable dyes (such as reactive dyes). This kind of dyes requires additional treatments to obtain uncolored effluents. In general, the electrochemical methods are cleaner than physicochemical and membrane technologies (the current methods for color removal) because they use the electron as unique reagent and they do not produce solid residues.

The objective of this paper is to review the main applications of electrochemical techniques in textile industry (production processes and wastewater treatments). Nowadays, there are only few applications at industrial scale as most of electrochemical treatments are still being studied at laboratory scale. Therefore, it is convenient to encourage the research on new applications of these techniques because they provide some important benefits. As far as we know,

this is the first review article dealing with the use of the electrochemical methods in the textile industry. Other authors have discussed these techniques focused on the wastewater decoloration treatments [71–73, 75, 76], or even specifically focused on heterogeneous catalysis method [62], but the review of the different electrochemical applications in the whole textile sector has not been considered.

2. The Electrochemistry in the Textile Production Processes

2.1. Textile Process. The textile industry is a very important sector because textile materials are used in many different ways: wearing clothes which change every season following the new tendencies or technical fabrics (waterproof, medical textiles, etc.) which are extended to new areas of application with some different functions. Textile development normally aimed in how it can enhance the comfort to the users.

Figure 1 summarizes the textile process which starts with fibers (which can be natural, that is, silk or cotton, or synthetic such as polyester). Then the fibers preparation process is carried out, where the fibers are treated to be spuin (as carding process for wool fibers, or bleaching process for cotton fibers). The spinning process transforms the fibers into yarns, followed by the weaving of those yarns. After that, a finishing process is applied. It is based on giving color to the fabric by means of dyeing or printing processes and on other processes such us softening or bleaching denim fabrics to obtain the degraded visual effect. The dyeing process produces highly colored effluents, which have to be treated and then, they could be reused in a new dyeing process, as it is shown in Figure 2. The next step is the clothing process and finally the textile commercial product is obtained.

2.2. Functionalization of Synthetic Textile Fibers to Obtain "Smart Textiles". Smart textiles are those which can note external stimuli and produce a controlled effect to these stimuli. The basis to obtain these materials is on the fibers preparation, where the electrochemistry is applied to obtain functionalized synthetic fibers, such as conductive polymers [1].

Table 1 summarizes some relevant papers about the synthesis of conductive fibers. The references are classified according to the aim of the electrochemical process:

Manufacturing of the polymers. An electrochemical method is applied to obtain a stable conducing material as product. Depending on the character of the monomers, the reaction could be a polymerization (same monomer) or copolymerization (different monomers).

Grafting. This process is based on the modification of the fibers by inserting different organic compounds using an electrochemical reaction.

Superficial Treatment. A complex reaction between a metal (M+) and the chemical structure of the fiber takes place (this process is mainly used with metals). The first step is an approximation of the metal to the fibrous surface, and then an electrochemical reaction (mainly reduction) gives fibers with conductive properties.

As indicated, smart textiles can react to environmental stimulus or mechanical forces which produce an electrical impulse that goes through the fiber. The response to this stimulus will be different depending on its function [21]. Examples of these applications are:

(i) Clothing and home indoors, where the stimulus reaction is a change on the aesthetics of the textiles, that is color, texture, shape, and so forth.

(ii) Computer, electronic, and communication systems, where the textiles can transfer data to the body or to entertainment products.

Nowadays, these conductive polymers are used mostly as electrodes in fuel cells and batteries. Carbon fibers and nanofibers are the most common materials (references listed in Table 2).

Lopes et al. [28] compared three different anode materials: iron, conducting polymer (Polypyrrole- (Ppy-) doped with chromium in wool textile), and boron doped diamond (BDD) electrode applied to degradation of a direct dye (Direct Red 80). With all of them, 99% of dye degradation was obtained, but BDD electrode also achieved 87% of COD removal instead of 45–50% achieved with the other electrodes (namely, iron and Ppy).

The functionalization of synthetic textile fibers to obtain smart textiles is a priority research area of national and European projects calls due to its interest in the energetic sector. However, it has not been widely considered in this section because it is mainly studied from the point of view of material science. This paper is mainly focused on the textile mill production processes.

2.3. Fibers Preparation: Bleaching of Cotton Fibers. Cotton bleaching takes place after the scouring process with the aim of destroying the natural raw color of this fiber. The most common reactive to provide whiteness to cotton is hydrogen peroxide. Chong and chu [29] reported the use of electrochemical techniques to generate in situ this oxidant required for cotton bleaching by the electrolysis of oxygen in the presence of an alkaline electrolyte. This electrolyte proceeds from the scouring process. They propose the use of the electrolysis process in a combined scouring and bleaching process, and they concluded that the whiteness obtained in the combined method is comparable to that obtained with conventional methods.

2.4. Bleaching of Denim Fabrics. Although the electrochemical techniques have been applied to bleach raw fibers, their main application in bleaching field is the discoloration of indigo–denim-dyed fabrics. An important step in the processing of indigo-dyed textiles is the finishing of the garment to obtain the required visual effect (as age-worn). The removal or destruction of part of indigo requires a combination of mechanical agitation and chemical attack, mainly with oxidizing agents.
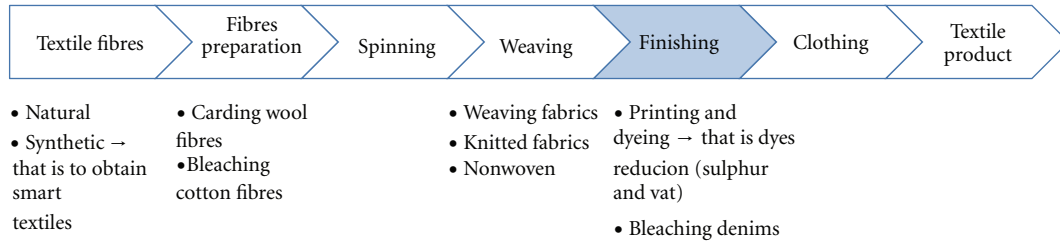
FIGURE 1: Textile process.

TABLE 1: Summary of methods to obtain conductive materials.

Method	Subject	Reference
Copolymerization	Amines	[2–4]
Copolymerization	PSPMS and polypyrrole	[5]
Copolymerization	Thiophenes	[6–9]
Copolymerization	Polypyrrole and polyaniline in polyester textiles	[10]
Polymerization	Benzene + pyridine compounds	[11]
Polymerization	Pyrrole on polyester textiles	[12]
Grafting	Cotton + methyl metacrylate	[13]
Grafting	Rayon viscose + vinyl acetate	[14]
Grafting	Natural fibers	[15]
Grafting	Rayon viscose with different electrodes	[16]
Superficial treatment	General proceeding	[17]
Superficial treatment	Polyacrylonitril + Ni	[18]
Superficial treatment	Polypyrrole	[19]
Superficial treatment	Ion-exchanger fibers with Cu	[20]
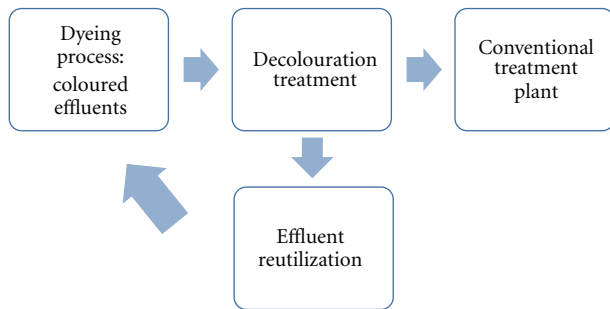
FIGURE 2: Dyeing effluent treatment and optional reuse.

TABLE 2: Materials and application of textiles and related conductive polymers.

Material	Application	Reference
Carbon fibers	Fuel cells	[22]
Carbon fibers	Fuel cells	[23]
Carbon fibers	Semifuel cells	[24]
Carbon nanofibers	Lithium batteries	[25]
Carbon nanotubes	Double layer capacitors	[26]
Carbon fibers	Lithium batteries	[27]

The most useful oxidant for bleaching indigo denims is hypochlorite. The conventional method to obtain the decolorized effect of these denims is based on the addition of this chemical reagent to the dye bath, but recently the generation in situ of the hypochlorite by an electrochemical oxidation is becoming a more attractive method, because it offers several advantages with respect to the conventional method [30]:

(i) Improvement in the process control and consistency,

(ii) Lower-process costs due to the production of more regular shades, the possibility of bleaching bath regeneration and the lower amount of effluent generated.

The addition of other chemical products or its presence in the solution, such as bromide, can increase the bleaching effect because of the stronger oxidants formation (as hypobromite [31–33]) but this could affect the shade bleach [34]. The same authors in a previous study [35] noted that electrochemical method showed more intensive bleach effects than the classical one and described in their paper that the electrochemical bleaching was due to both oxidation and reduction processes.

Bechtold et al. [36] attempted to bleach denim indigo fabrics using BDD electrodes and peroxodisulfate as oxidant (coming from sodium sulfate oxidation) and the results showed that this method was not effective enough for indigo discoloration.
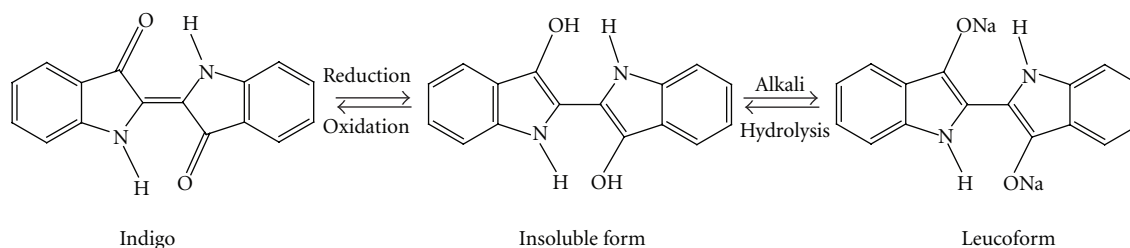
FIGURE 3: Reaction of indigo dye to leucoform (soluble form).

The use of photocatalysis methods [37] also showed good bleaching results in indigo carmine denims. In this case, the oxidation took place via hydroxyl radicals, and the presence of bromide and carbonate also affected the efficiency of the oxidative reaction.

2.5. Dyeing Process: Dyes Reduction. Vat dyes, especially indigo, play an important role in textile industry. This kind of dyes can be used in printing [38], but they are mostly applied in dyeing processes. They are insoluble in water and cannot dye fibers directly. They must be reduced in alkali medium to become soluble in water, as it is showed in Figure 3. When the dyes are absorbed onto the fiber, they return to their original form by a subsequent reoxidation.

Sulfur dyes also are water-insoluble dyes, containing sulfur as an integral part of the chromophore group. The alkaline-reduced form is required for the dyeing process and subsequently, when they are added to the fiber, they are oxidized to the insoluble form.

In attempt to increase the ecoefficiency of these dyeing processes, electrochemical techniques have been investigated in the reduction of such dyes, which avoids the addition of reducing agents as sodium dithionite.

Predominantly, they are used for cellulosic fabrics, mainly cotton, but there are some papers showing their availability for biodegradable fibers such as poly (lactic acid) [39], and in synthetic fibers as polyester blends [40] or nylon 6.6 [41–43].

Sodium dithionite ($Na_2S_2O_4$) is the most used reducing agent in the industrial dyeing process with this kind of dyes, but after its reaction, it cannot be recycled. It also produces large amounts of sodium sulfate and toxic sulfite products. For this reason, the treatment of dyeing effluents requires the addition of hydrogen peroxide [44], which also causes high costs and other additional problems (high-salt load, depletion of dissolved oxygen, nasal nuisance, toxicity of sulfide, etc.) [45]. In order to reduce these pollutants, some tests at laboratory scale pilot have been done to obtain an alternative less harmful process. There are three investigation paths based on: (a) more eco-friendly chemical reducing agents (thiourea dioxide [46], hydroxiketones [47, 48], sodium borohydride [49], etc.); (b) on physical methods [50] like ultrasound, magnetic fields or UV, but they only could be useful as accelerators of classic oxidation or reduction methods; (c) the most attractive new procedures to reduce vat and sulfur dyes are electrochemical reduction methods, because the addition of reducing agents is not required. This last method also avoids the generation of toxic products due to the reaction between the added reagents and the dye molecules. For all these reasons, electrochemical reduction processes are considered more suitable: no reagents addition is required, no byproducts are formed and no tertiary treatments are necessary to treat the final effluents. The energy is the only requirement of electrochemical methods.

The electrochemical reduction of textile dyes can be divided into direct and indirect reduction. Schrott [51] indicated that sulfur dyes can be reduced directly, but in the case of vat dyes and indigo, the reaction probably occurs by indirect reduction because of their low solubility in water (consequently they have low contact to the surface of the cathode).

The electrochemical reduction processes studied are:

(i) Indirect reduction, where sometimes iron complexes act as mediators [52, 53].

(ii) Direct reduction via radical, for sulfur dyes (using a multicathode cell made of stainless steel electrodes) [54] or indigo dye (using a nickel cathode electrode) [55]. Both of them have effectiveness between 70–90%. A radical anion, formed by a comproportionation reaction between the insoluble dye and the leucoform is the responsible of the electrochemical reduction [56].

(iii) Direct reduction on graphite electrodes [57], which are extensively used because of their high surface area [56].

(iv) Electrolytic hydrogenation, which is based on the hydrogen formation, produced in situ by water electrolysis. The hydrogen reacts with dyes adsorbed at the electrode surface. Different electrodes and catalysts have been studied [58].

According to Roessler and Jin [56], the direct electrochemical reduction of vat dyes by graphite granules is the most attractive method because of its stability, cost, and availability. Roessler and Crettenand [45] studied the kinetic rates of some vat dyes and they noted that graphite electrodes were suitable for all them. Also, they concluded that the reduction rate decreased with the increase of dyes lipophility because of aggregates formation.

To improve these methods in order to be applied at industrial scale, some investigations have been carried out,
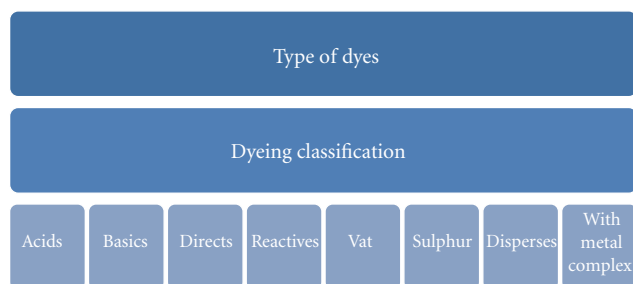
FIGURE 4: Dyes classification.

that is, several reviews [59, 60] are available on functionalizing the surface of carbon electrodes to obtain higher reduction rates with the same color intensity and washing fastness than traditional methods [61]. Furthermore the possibility of reusing these electrodes is a subject of the study.

The reuse of the reducing agent (by regeneration in a cathodic reduction) and also the dyeing bath in the indirect reduction electrochemical method, using a mediator, has been studied [53] but the final color was poorer than the one obtained by the traditional method with sodium dithionite.

Taking into account all these studies, we can conclude that the use of electrochemical techniques constitute a promising field for the different steps of textile process, but their application to the dyeing of vat and sulfur dyes is specially interesting to avoid the use of reducing reagents.

3. Wastewater Color Removal

3.1. Textile Wastewater Concern. The textile industry produces large volumes of wastewater in its dyeing and finishing processes. These effluents have as common characteristic their high coloration. Colorants, the additive substances that cause a variation in color, can be divided in dyes or pigments. Pigments in general are insoluble substances which have not the chemical affinity to the substrate to be colored; otherwise, dyes are generally soluble (or partially soluble) organic compounds, which interact with the fiber or leather imparting color [62]. Figure 4 summarizes the different textile dyes according to their dyeing behavior.

Most of electrochemical discoloration studies are focused on reactive dyes. They represent about 20–30% of the total market [63], because of their solidity and brilliant color. Their structure consists on a *reactive group* (which reacts with the fiber), and a *chromophore group* (which gives the color). The most used chromophore group is the "azo" (R–N=N–R′), followed by the anthraquinone group [64]. Azo group constitute, more than half of worldwide production [65], approximately 65% [66–68]. Moreover, this kind of dyes produces toxic aromatic products in their degradation.

The dyeing reaction, when a triazine is the reactive group, occurs by a nucleophilic displacement of the chlorine atom from the reactive group to the hydroxyl group from the cellulose in alkaline medium, as it is shown below [69].

Reaction 2:

$$dye\text{-}Cl + HO\text{-}cellulose \longrightarrow dye\text{-}O\text{-}cellulose + HCl \quad (1)$$
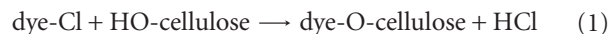
The competitive reaction between dye and water produces dyes hydrolysis (reaction 3). The hydrolyzed dyes cannot react with the fiber, being the element responsible for the colored effluents.

Reaction 3:

$$dye\text{-}Cl + H_2O \longrightarrow dye\text{-}OH + HCl \quad (2)$$

The high consumption of reactive dyes, mainly in the cotton industry, increases this environmental and aesthetic problem, due to their low degree of exhaustion, and their presence both in dyeing and soaping effluents.

Other chemical products present in the dyeing process (such as Na_2CO_3 used to set the pH in the dyeing bath which has an important role in dyes fixation to the fiber and color fastness; or NaCl added to transfer the dyestuff to the fabric) can influence the electrochemistry process as they can scavenge $^\bullet OH$ and h_{vb}^+) [70].

Several methods are used for the removal of organic dyes from wastewaters. Most of dyes are only partially removed under aerobic conditions in conventional biological treatments. As biological treatment is insufficient to remove color and to accomplish with current regulations, the application of specific treatments is required. The effluent color regulations are very variable depending on the Country. In UK, the color value is calculated from some absorbance measurements. State and USA federal agencies have been requiring low effluent color limits (<200 units of the American Dye Manufacturers Institute, ADMI). While the implementation of the Cluster Rules did not place regulatory limits on color, the U.S. EPA left the option open for regulatory authorities to establish limits on color based on the individual circumstances of each holder and watershed. In Spain, the colored effluents are allowed to be discharged if no color is observed after a 1/20 dilution (Real Decreto 849/1986), although each regional authority can restrict this value.

The different techniques to achieve effective color removal, according to Martínez-Huitle and Brillas [71], are schematically indicated in Figure 5.

Some electrochemical color removal methods have been applied to industrial effluents. The current physico-chemical methods, based on the separation of dyes from the effluents, produce a residue which requires an additional treatment to be destroyed. Also, the absorbent materials (such as active carbon, silica gel, or alumina) require their regeneration after several treatments [72], and the filtration and membranes methods need cleaning treatments. Chemical oxidation methods are rather expensive and involve some operational difficulties [73, 74]. Biological treatments are a simple method but supply inefficient results in discoloration because dyes have aromatic rings in their large molecules that provide them chemical stability and resistance to the microbiological attack [75]. Enzymatic decomposition requires
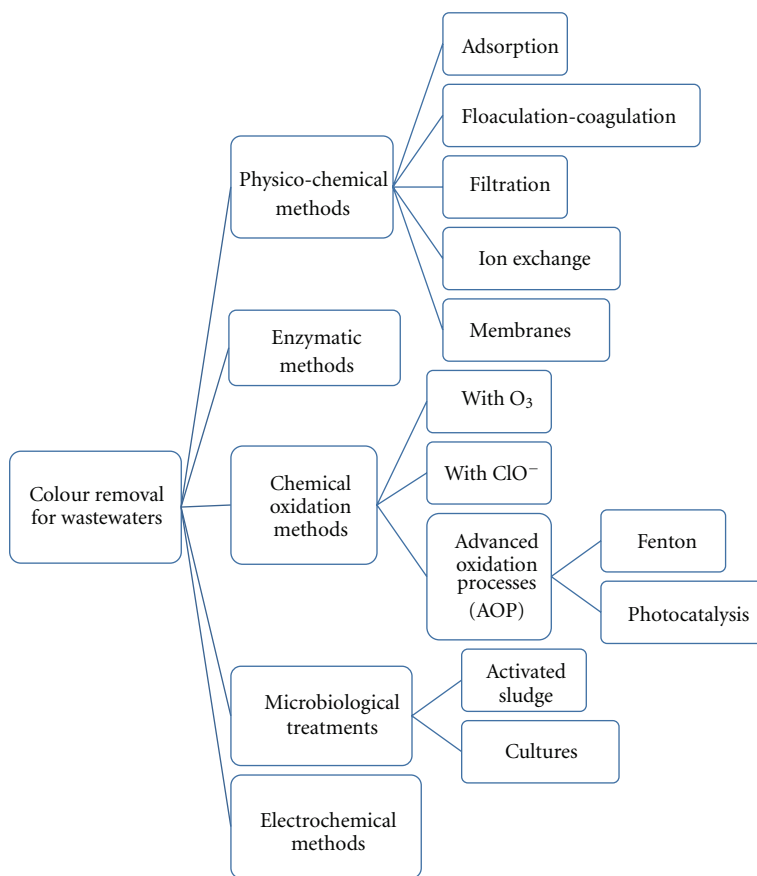
FIGURE 5: Methods for textile wastewater color removal.

further investigation in order to know which enzymatic process takes place [76]; moreover, temperature and pressure have to be controlled to avoid enzymes denaturalization.

For these reasons, the electrochemical methods are nowadays the subject of a wide range of investigations at laboratory and pilot-plant scale. The advantage of these electrochemical techniques is that electron is a clean reagent. They also have good versatility and high-energy efficiency. They are easy for automation and safety because it is possible to operate at smooth conditions [77]. Figure 6 represents the main types of electrochemical methods applied to wastewater treatment, briefly described below.

3.2. Electrocoagulation Methods. Electrocoagulation systems provide electrochemical aggregation of heavy metals, organic and inorganic pollutants, to produce a coagulated residue to be separated or removed from water.

This technique is an indirect electrochemical method which produces coagulant agents (Fe^{3+} or Al^{3+}) from the electrode material (Fe or Al) in hydroxide medium. These species, that is, $Fe(OH)_3$, can remove dissolved dyes by precipitation or by flotation [78, 79]. These complexed compounds are attached to the bubbles of $H_{2(gas)}$ evolved at the cathode and transported to the top of solution. The inconvenient of the electrocoagualtion in comparison to the other electrochemical methods is that it produces secondary residues (the complex formed with pollutant and hydroxide) which implies the use of tertiary treatments.

3.3. Electrochemical Reduction Methods. The electrochemical reduction method has been discussed in a restricted number of papers because its yield in pollutants degradation is poor in comparison to direct and indirect electro-oxidation methods [71]. Bechtold et al. [80], consider that this method is particularly suitable for the treatment of highly colored wastewaters such as the residual pad-batch dyeing bath with reactive dyes. The dye reduction takes place producing hydrazine (in the partial reduction) and its total reduction generates amino compounds (scheme in Figure 7). They remark the importance of a divided cell in the case of dye baths containing chlorides; this division is important to avoid the formation of chlorine and chlorinated products.

In the same way, Vanerkova et al. [81] proposed a reduction mechanism for the azo dyes degradation with platinated titanium electrodes (Pt/Ti) in the presence of NaCl. In this study, the action of hypochlorite generated by oxidation of chloride is also discussed Zanoni et al. [69] studied the hydrolysis under reduction process of two anthraquinone reactive dyes. They demonstrate that the acidic medium provides the best conditions, and that the presence of borate in the solution modifies the reduction process.
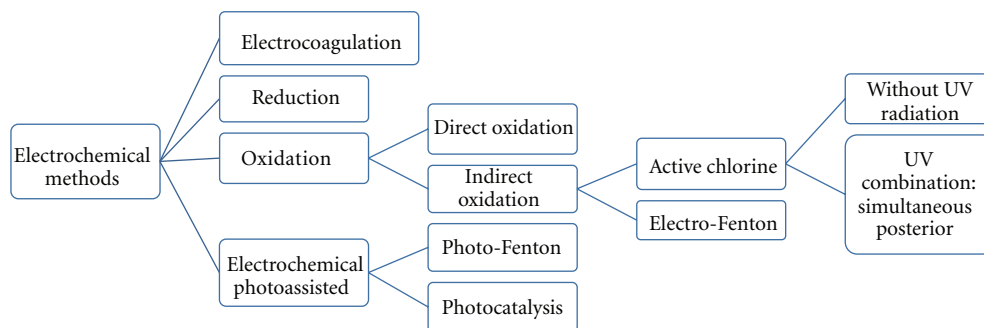
FIGURE 6: Electrochemical methods.

- Hydrolysed azo dye   - Hidrazine   - Amines
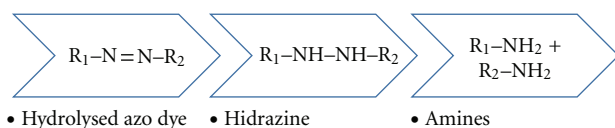
FIGURE 7: Reduction process for azo dyes.

3.4. Electrochemical Oxidation Methods. The electrochemical oxidation is a process based on pollutants removal by direct anodic oxidation (which generally produces poor decontamination) or by chemical reaction with electrogenerated species (hydroxyl radical $M[OH^{\bullet}]$ or metal oxide $[MO]$, as it is showed in the follow reaction) [71]. The reactive dyes degradation can be partial or total, according to the following mechanism:

Reaction:

$$H_2O + M \longrightarrow M[OH^{\bullet}] + H^+ + e^-$$
$$R + M[OH^{\bullet}] \longrightarrow M + RO + H^+ + e^- \tag{3}$$
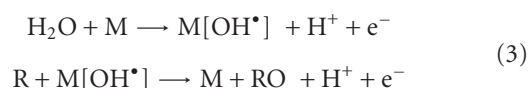
Many studies have shown that the total mineralization is possible with high efficiencies depending on the anode material (SnO_2 [82, 83], PbO_2 [84–86], BDD [87–92], $Ti/SnO_2/SbO_x/RuO_2$, and Ti/TiO_2 [63]). However, the dye solution is not decolorized effectively using both glassy and reticulated vitreous carbon electrodes [63]. The boron-doped diamond (BDD) thin-film electrodes have physical characteristics as an inert surface with low-adsorption properties, good corrosion stability, and a wide potential window in aqueous medium [93]. In spite of its high cost, the BDD electrode has much greater O_2-thovervoltage than de conventional anodes (Pt, PbO_2, etc.). Consequently, that produce generates more amount of $[OH^{\bullet}]$ which implies a faster oxidation of the pollutants [94].

In the same way, Martínez-Huitle and Brillas [71] compared different kinds of electrodes in two types of wastewaters (chloride-free dye wastewaters and effluents which contain chloride). They supported that most of the anodes tested could destroy the chromophore group (–N=N–) producing its discoloration efficiently, and when chloride was present, the destruction of dyes was accelerated by active chlorine species produced.

3.5. Indirect Oxidation Methods. The indirect electro-oxidation occurs when strong oxidants are generated in situ during the electrolysis and react with the organic pollutants such as dyestuffs, producing its total or partial degradation.

Mainly two methods one used:

(i) The first one is the electro-oxidation with active chlorine [95, 96] which is the major oxidizing agent. In this case, free-chlorine gaseous and/or the generated chlorine-oxygen species such as hypochlorous acid (HClO) or hypochlorite ions (ClO^-) depending on the pH, oxidize the organic matter present in the effluents, according to the following reactions:

Reactions:

$$2Cl^- \longrightarrow Cl_{2(aq)} + 2e^-$$
$$Cl_{2(aq)} + H_2O \longrightarrow ClO^- + Cl^- + H^+$$
$$Dye + ClO^- \longrightarrow \text{dye intermediates} \longrightarrow CO_2 + H_2O + Cl^- \tag{4}$$
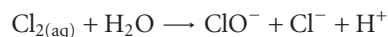
(ii) The second one is the electro-Fenton process [97], where organics degradation occurs by hydroxyl radicals ($OH^{\bullet}$) formed from Fenton's reaction between catalytic Fe^{2+} and H_2O_2, this hydrogen peroxide is also electrogenerated from O_2 reduction.

Reactions:

$$O_{2(g)} + 2H^+ + 2e^- \longrightarrow H_2O_2 \tag{5}$$
$$O_{2(g)} + Fe^{2+} \longrightarrow Fe^{3+} + OH^{\bullet} + OH^- \tag{6}$$
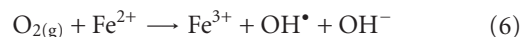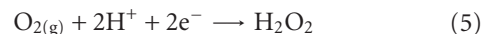
Thus, Fe^{2+} is continuously regenerated from the reduction of Fe^{3+}:

$$Fe^{3+} + e^- \longrightarrow Fe^{2+} \tag{7}$$

This technique has an important inconvenience: a strong acidic medium is required. As the reactive dyeing process is carried out in basic medium (generally pH > 10),

a high amount of acid has to be added before the treatment. Subsequently, the treated effluent must be neutralized to be discharged. Consequently, the whole process produces a high increase of the wastewater salinity.

As some industrial wastewaters contain large amounts of chloride, the first approach is more suitable to treat this kind of effluents, because the addition of any chemical product is not required whereas in second case, Fenton reagent is needed. In contrast, the combination of electrochemistry and chloride can produce haloforms such as chloroform, although it is not an inconvenient if the treated water is degraded lately in a biological plant to accomplish its mineralization. In fact, it has been verified that the concentration of haloforms is very low and they do not show any toxic effect on the plant microorganisms [98]. Otherwise it is possible to remove the haloform generated by placing a UV lamp in the electrochemical cell where the reaction takes place [99], or by adding H_2O_2 into the wastewater before the reaction had started. The first approach was studied by López-Grimau and Gutiérrez [100] and it was found to improve the kinetic rates of electrochemical degradation of some reactive azo dyes with Ti/PtO_x electrodes. The electrochemistry method using chlorine has been noted to be effective in other kind of dyes, such as acid dyes [101] or disperse dyes [102], and combined with photoelectrochemistry has also obtained good results for phtalocyanine dyes degradation [103], but in this case, the metal ions liberated (as copper) have to be removed.

3.6. Photo-Assisted Methods.

3.6. Photo-Assisted Methods. The photoassisted electrochemical methods are based on the exposure of the effluent to a UV light source during the electrochemical treatment. In these procedures, the intensity and the wavelength of the incident light plays an important role on the mineralization rate.

The most studied photoassisted method is the photoFenton [105], which consists in the simultaneous use of UV light and H_2O_2 (electrogenerated in situ with the presence of Fe^{2+}); followed by the heterogeneous TiO_2 photocatalysis method [106]. Although several photocatalysts (TiO_2, WO_3, SnO_2, ZnO, $CdS...$) act via hydroxyl radical and generate powerful oxidants, the TiO_2 under UV radiation has been the preferred catalyst, due to its low cost, nontoxicity, water insolubility and wide band gap, which consequently implies a good stability and prevents photocorrosion [62, 70, 107–112]).

Moreover, Carneiro et al. [70] noted that the use of photocatalysis with Ti/TiO_2 electrodes achieves efficiently discoloration with both electrolytes, $NaCl$ and Na_2SO_4. Their efficiency depend on the pH.

Xie and Li [113] reported the coupling of electro-Fenton with electrocatalysis for the removal of an azo dye. With respect to other electro-oxidation and photoassisted methods, their results showed a better removal of the dye in the coupled system. The major disadvantage of these methods was the excessive energy cost of the artificial UV light used. However, this problem is easy to solve by using sunlight [114, 115] as inexpensive energy source although it had less catalytic power.

Additionally, the combination between the indirect oxidation methods with the UV irradiation has been the subject of recent investigations. According to Sala [116], the energy consumption is around $5.7\,kW\cdot h/m^3$ to achieve discoloration higher than 90% when the photoelectrochemical treatment is applied to real industrial effluents by means of a semi-industrial pilot. The discoloration process follows a pseudo-first-order kinetic in the case of monochromies and a second order kinetics in the case of trichromie, evaluated at the maximum absorbance wavelength of the trichromie, which corresponds mainly to the contribution of two dyes (due to the low absorbance of the third dye at the selected wavelength).

By another hand, the actual policies concerning water and energy consumption conduce to recycling and reuse treatments. In this sense, recent studies [104] demonstrate the possibility of reusing these discolored effluents for new dyeing processes. The reuse of 70% of discolored dyebaths, after electrochemical treatment assisted by UV irradiation, provides in most of cases, low color differences ($DE_{CMC(2:1)} \leq 1$) with respect to the original dyeing with decalcified tap water. This value increases from the first step until the 4th or 5th cycle of electrochemical treatment and reuse, where $DE_{CMC(2:1)}$ become constant. In some cases, when the bath is reused, an extra amount of dye must be added to obtain the required color.

Numerous studies can be found about the electrochemical discoloration of textile wastewater, but some authors have advanced a further step: in the case of indirect oxidation with active chlorine, the conditions for the effluents reutilization have also been optimized [99, 100, 104]. In this sense, Gutierrez-Bouzan et al. in a recent patent (ES201131159) claimed a process "UVEC Cell" for the discoloration and reuse of reactive dyes effluents in a new dyeing process. Both prototype and procedure are patented, based on an electrochemical cell combined with UV source for the treatment and reuse of textile effluents saving more than 60% water and electrolyte.

4. Conclusions

The electrochemical techniques have been proved to be efficient in different oxidation or reduction steps of the textile processes such as: bleaching denim fabrics or reduction of sulfur and vat dyes, where their applications are available in both natural and synthetic fibers. They constitute a less harmful alternative than the traditional processes. They also have been studied in new textile fields, such as in the production of conductive polymers used as fibers which are applied in smart textiles to produce fabrics with new functions.

In addition, the electrochemical treatments have been extensively applied to the decontamination of wastewaters from the textile processes. They have been mainly used in the removal of residual reactive dyes, but also in the discoloration of acid and disperse dyes effluents. Taking into account the considerable amount of salt contained in the reactive dyes residual dyebath, the best method for the treatment of these

effluents is the indirect oxidation with chlorine, because of the following:

(i) The degradation takes place in the same bath.

(ii) The addition of chemical reagents is not required (the residual salts act as electrolyte).

(iii) The modification of the pH is not necessary.

(iv) No solid waste is generated.

(v) The reuse of the treated effluent for new dyeing is possible, which implies a saving of 70% water and 60% salt.

The combination with UV and solar irradiation improved the discoloration kinetic rates in different electrochemical techniques, and in some cases, the UV light exposure also removes the undesirable compounds (such as chloroform) or avoids their generation according to the patent ES201131159 ("UVEC Cell").

The possibility of reusing dyeing effluents treated by electrochemical methods is particularly interesting and it implies an important saving of water and salt. This kind of studies are especially important in Mediterranean countries, where the river flow rates are low and their salinity is nowadays an increasing environmental problem.

The bases of electrochemistry are simple but, as showed in this review, it is possible to find the application of these techniques in a wide range of textile processes.

Acknowledgment

References

[1] S. Baurley, "Interactive and experiential design in smart textile products and applications," *Personal and Ubiquitous Computing*, vol. 8, no. 3-4, pp. 274–281, 2004.

[2] F. Cases, F. Huerta, R. Lapuente, C. Quijada, E. Morallón, and J. L. Vázquez, "Conducting films obtained by electro-oxidation of p-aminodiphenylamine (ADPA) in the presence of aniline in buffer aqueous solution at pH 5," *Journal of Electroanalytical Chemistry*, vol. 529, no. 1, pp. 59–65, 2002.

[3] S. Beaupré, J. Dumas, and M. Leclerc, "Toward the development of new textile/plastic electrochromic cells using triphenylamine-based copolymers," *Chemistry of Materials*, vol. 18, no. 17, pp. 4011–4018, 2006.

[4] M. A. Cotarelo, F. Huerta, C. Quijada, F. Cases, and J. L. Vázquez, "The electrochemical co-polymerization of p-aminodiphenylamine and aniline: effect of pH," *Synthetic Metals*, vol. 148, no. 1, pp. 81–85, 2005.

[5] Y. H. Park, H. C. Shin, Y. Lee, Y. Son, and D. H. Baik, "Electrochemical preparation of polypyrrole copolymer films from PSPMS precursor," *Macromolecules*, vol. 32, no. 14, pp. 4615–4618, 1999.

[6] J. Tarábek, E. Jähne, P. Rapta, D. Ferse, H. J. Adler, and L. Dunsch, "New acetophenone-functionalized thiophene monomer for conducting films on electrodes in chemical ion-sensorics: the synthesis and spectroelectrochemical study," *Russian Journal of Electrochemistry*, vol. 42, no. 11, pp. 1169–1176, 2006.

[7] S. Tanaka, M. A. Sato, and K. Kaeriyama, "Electrochemical polymerization of thiophenes containing a methoxy group," *Polymer communications Guildford*, vol. 26, no. 10, pp. 303–306, 1985.

[8] K. Kaeriyama, M. Sato, and S. Tanaka, "Electrochemical preparation of conducting polyalkylthiophene films," *Synthetic Metals*, vol. 18, no. 1–3, pp. 233–236, 1987.

[9] M. A. Sato, S. Tanaka, and K. Kaeriyama, "Soluble conducting polymers by electrochemical polymerization of thiophenes having long alkyl substituents," *Synthetic Metals*, vol. 18, no. 1–3, pp. 229–232, 1987.

[10] J. Molina, A. I. del Río, J. Bonastre, and F. Cases, "Electrochemical polymerisation of aniline on conducting textiles of polyester covered with polypyrrole/AQSA," *European Polymer Journal*, vol. 45, no. 4, pp. 1302–1315, 2009.

[11] S. Tanaka, M. A. Sato, and K. Kaeriyama, "Electrochemical polymerization of dithienylbenzene and dithienylpyridine," *Journal of Macromolecular Science*, vol. 24, no. 7, pp. 749–761, 1987.

[12] J. Molina, A. I. del Río, J. Bonastre, and F. Cases, "Chemical and electrochemical polymerisation of pyrrole on polyester textiles in presence of phosphotungstic acid," *European Polymer Journal*, vol. 44, no. 7, pp. 2087–2098, 2008.

[13] M. L. Dupraz and J. Rouger, "Study of the electrochemical grafting of methyl methacrylate on to cellulose. II. Study of the copolymer formed by cotton linters and polymethyl methacrylate," *Cellulose Chemistry and Technology*, vol. 7, pp. 63–76, 1973.

[14] T. Skwarsky, T. Mikolajczyk, and A. Krasinka, "Modification of viscose rayon fibers by electrochemical grafting of vinyl acetate," *Polimery*, vol. 13, pp. 301–304, 1968.

[15] S. N. Bhadani, S. K. Sen Gupta, and M. K. Gupta, "Electrically conducting natural fibres," *Indian Journal of Fibre & Textile Research*, no. 18, pp. 46–47, 1993.

[16] T. Skwarsky, T. Mikolajczyk, and T. A. Krasinka, "Effect of electrode type on electrochemical grafting of methyl methacrylate on viscose rayon fibers," *Polimery*, vol. 13, pp. 407–410, 1968.

[17] S. Gimpel, U. Möhring, H. Müller, A. Neudeck, and W. Scheibner, "Textile-based electronic substrate technology," *Journal of Industrial Textiles*, vol. 33, no. 3, pp. 179–189, 2004.

[18] D. Akbarov, B. Baymuratov, P. Westbroek, R. Akbarov, K. Declerck, and P. Kiekens, "Development of electroconductive polyacrylonitrile fibers through chemical metallization and galvanisation," *Journal of Applied Electrochemistry*, vol. 36, no. 4, pp. 411–418, 2006.

[19] M. Watanabe, "Preparation of polypyrrole film with well-ordered corrugation," *Synthetic Metals*, vol. 156, no. 7-8, pp. 597–601, 2006.

[20] G. M. Mubarakshin, B. M. Vrevskii, and L. A. Vol'f, "Preparation of fibrous electron-ion exchangers by an electrochemical method," *Journal of Applied Chemistry of the USSR*, vol. 59, no. 6, pp. 1122–1125, 1986.

[21] S. L. Baurley, "Smart textiles for future intelligent consumer products," in *Proceedings of the IEEE Eurowearable*, pp. 73–75, Birmingham, UK, September 2003.

[22] J. H. Lin, W. H. Chen, S. H. Su, Y. K. Liao, and T. H. Ko, "Carbon film coating on gas diffusion layer for proton exchange membrane fuel cells," *Journal of Power Sources*, vol. 184, no. 1, pp. 38–43, 2008.

[23] R. F. Louh, A. C. C. Chang, V. Chen, and D. Wong, "Design of electrophoretically deposited microporous layer/catalysts

layer composite structure for power generation of fuel cells," *International Journal of Hydrogen Energy*, vol. 33, no. 19, pp. 5199–5204, 2008.

[24] R. R. Bessette, M. G. Medeiros, C. J. Patrissi, C. M. Deschenes, and C. N. LaFratta, "Development and characterization of a novel carbon fiber based cathode for semi-fuel cell applications," *Journal of Power Sources*, vol. 96, no. 1, pp. 240–244, 2001.

[25] L. Ji and X. Zhang, "Generation of activated carbon nanofibers from electrospun polyacrylonitrile-zinc chloride composites for use as anodes in lithium-ion batteries," *Electrochemistry Communications*, vol. 11, no. 3, pp. 684–687, 2009.

[26] C. W. Huang, C. M. Chuang, J. M. Ting, and H. Teng, "Significantly enhanced charge conduction in electric double layer capacitors using carbon nanotube-grafted activated carbon electrodes," *Journal of Power Sources*, vol. 183, no. 1, pp. 406–410, 2008.

[27] J. F. Snyder, E. L. Wong, and C. W. Hubbard, "Evaluation of commercially available carbon fibers, fabrics, and papers for potential use in multifunctional energy storage applications," *Journal of the Electrochemical Society*, vol. 156, no. 3, pp. A215–A224, 2009.

[28] A. Lopes, S. Martins, A. Moraö, M. Magrinho, and I. Gonçalves, "Degradation of a textile dye C.I. Direct Red 80 by electrochemical process," *Portugaliae Electrochimica Acta*, vol. 22, pp. 279–294, 2004.

[29] C. L. Chong and P. M. Chu, "Bleaching cotton based on electrolytic production of hydrogen peroxide," *American Dyestuff Reporter*, vol. 87, no. 4, pp. 13–19, 1998.

[30] T. Bechtold, A. Turcanu, R. Campese, P. Maier, and W. Schrott, "On-site formation of hypochlorite for indigo oxidation—scale-up and full scale operation of an electrolyser for denim bleach processes," *Journal of Applied Electrochemistry*, vol. 36, no. 3, pp. 287–293, 2006.

[31] Y. Amano and Y. Y. Tanaka, "Treating agent for bleach processing," Japanese Patent: Application number "JP1988000226387", 1990.

[32] J. I. Friday, "Method for altering fabrics or garments to discharge dyed colors or indigo denim to create finishes," US5310409, 1994.

[33] Puttaswamy, D. S. Mahadevappa, and N. M. M. Gowda, "Kinetics and mechanism of oxidation of indigo carmine by hypohalites," *International Journal of Chemical Kinetics*, vol. 23, no. 1, pp. 27–35, 1991.

[34] T. Bechtold, P. Maier, and W. Schrott, "Bleaching of indigo-dyed denim fabric by electrochemical formation of hypohalogenites in situ," *Coloration Technology*, vol. 121, no. 2, pp. 64–68, 2005.

[35] R. Maier, W. Schrott, T. Bechtold, and R. Campese, "Electrochemical bleaching in the finishing of jeans," *Melliand Textilberichte*, vol. 85, no. 11-12, pp. 880–884, 2004.

[36] T. Bechtold, A. Turcanu, and W. Schrott, "Electrochemical decolourisation of dispersed indigo on boron-doped diamond anodes," *Diamond and Related Materials*, vol. 15, no. 10, pp. 1513–1519, 2006.

[37] H. Liao, D. Stenman, and M. Jonsson, "Study of Indigo carmine as radical probe in photocatalysis," *Journal of Photochemistry and Photobiology A*, vol. 202, no. 2-3, pp. 86–91, 2009.

[38] M. D. Teli, P. Rohera, J. Sheikh, and R. Singhal, "Use of Amaranthus (Rajgeera) starch vis-à-vis wheat starch in printing of vat dyes," *Carbohydrate Polymers*, vol. 76, no. 3, pp. 460–463, 2009.

[39] K. Sawada and M. Ueda, "Optimization of dyeing poly(lactic acid) fibers with vat dyes," *Dyes and Pigments*, vol. 74, no. 1, pp. 81–84, 2007.

[40] Y. C. Chao, Y. L. Chung, C. C. Lai, S. K. Liao, and J. C. Chin, "Dyeing of cotton-polyester blends with anthraquinonoid vat dyes," *Dyes and Pigments*, vol. 40, no. 1, pp. 59–71, 1999.

[41] S. M. Burkinshaw, S. N. Chevli, and D. J. Marfell, "The dyeing of nylon 6,6 with sulphur dyes," *Dyes and Pigments*, vol. 45, no. 1, pp. 65–74, 2000.

[42] S. M. Burkinshaw, K. Lagonika, and D. J. Marfell, "Sulphur dyes on nylon 6,6—part 2: the effects of reductant, oxidant and wash-off," *Dyes and Pigments*, vol. 58, no. 2, pp. 157–170, 2003.

[43] S. M. Burkinshaw and K. Lagonika, "Sulphur dyes on nylon 6,6. Part 3. Preliminary studies of the nature of dye-fibre interaction," *Dyes and Pigments*, vol. 69, no. 3, pp. 185–191, 2006.

[44] M. Božič and V. Kokol, "Ecological alternatives to the reduction and oxidation processes in dyeing with vat and sulphur dyes," *Dyes and Pigments*, vol. 76, no. 2, pp. 299–309, 2008.

[45] A. Roessler and D. Crettenand, "Direct electrochemical reduction of vat dyes in a fixed bed of graphite granules," *Dyes and Pigments*, vol. 63, no. 1, pp. 29–37, 2004.

[46] M. Weiss, "Thiourea dioxide: a safe alternative to hydrosulfite reduction," *American Dyestuff Reporter*, vol. 67, no. 8, pp. 35–38, 1978.

[47] E. Marte, "Dyeing with sulphur, indigo and vat dyes using the new RD process. Hydroxyacetone makes it possible," *Text Praxis International*, vol. 44, p. 737, 1989.

[48] U. Baumgarte, "Developments in vat dyes and in their application 1974–1986," *Review of Progress in Coloration*, vol. 17, pp. 29–38, 1987.

[49] N. Meksi, M. Kechida, and F. Mhenni, "Cotton dyeing by indigo with the borohydride process: effect of some experimental conditions on indigo reduction and dyeing quality," *Chemical Engineering Journal*, vol. 131, no. 1–3, pp. 187–193, 2007.

[50] D. Thetford and A. P. Chorlton, "Investigation of vat dyes as potential high performance pigments," *Dyes and Pigments*, vol. 61, no. 1, pp. 49–62, 2004.

[51] W. Schrott, "Electrochemical dyeing," *Textile Asia*, vol. 35, no. 2, pp. 45–47, 2004.

[52] B. Thomas and T. Aurora, "Iron-complexes of bis(2-hydroxyethyl)-amino-compounds as mediators for the indirect reduction of dispersed vat dyes—cyclic voltammetry and spectroelectrochemical experiments," *Journal of Electroanalytical Chemistry*, vol. 591, no. 1, pp. 118–126, 2006.

[53] M. A. Kulandainathan, A. Muthukumaran, K. Patil, and R. B. Chavan, "Potentiostatic studies on indirect electrochemical reduction of vat dyes," *Dyes and Pigments*, vol. 73, no. 1, pp. 47–54, 2007.

[54] T. Bechtold, E. Burtscher, and A. Turcanu, "Direct cathodic reduction of Leuco Sulfur Black 1 and Sulfur Black 1," *Journal of Applied Electrochemistry*, vol. 28, no. 11, pp. 1243–1250, 1998.

[55] A. Roessler, D. Crettenand, O. Dossenbach, W. Marte, and P. Rys, "Direct electrochemical reduction of indigo," *Electrochimica Acta*, vol. 47, no. 12, pp. 1989–1995, 2002.

[56] A. Roessler and X. Jin, "State of the art technologies and new electrochemical methods for the reduction of vat dyes," *Dyes and Pigments*, vol. 59, no. 3, pp. 223–235, 2003.

[57] A. Roessler, D. Crettenand, O. Dossenbach, and P. Rys, "Electrochemical reduction of indigo in fixed and fluidized beds

of graphite granules," *Journal of Applied Electrochemistry*, vol. 33, no. 10, pp. 901–908, 2003.

[58] A. Roessler, O. Dossenbach, W. Marte, and P. Rys, "Electrocatalytic hydrogenation of vat dyes," *Dyes and Pigments*, vol. 54, no. 2, pp. 141–146, 2002.

[59] R. L. McCreery, "Advanced carbon electrode materials for molecular electrochemistry," *Chemical Reviews*, vol. 108, no. 7, pp. 2646–2687, 2008.

[60] R. C. Engstrom, "Electrochemical pretreatment of glassy carbon electrodes," *Analytical Chemistry*, vol. 54, no. 13, pp. 2310–2314, 1982.

[61] M. A. Kulandainathan, K. Kiruthika, G. Christopher, K. F. Babu, A. Muthukumaran, and M. Noel, "Preparation of iron-deposited graphite surface for application as cathode material during electrochemical vat-dyeing process," *Materials Chemistry and Physics*, vol. 112, no. 2, pp. 478–484, 2008.

[62] K. Rajeshwar, M. E. Osugi, W. Chanmanee et al., "Heterogeneous photocatalytic treatment of organic dyes in air and aqueous media," *Journal of Photochemistry and Photobiology C*, vol. 9, no. 4, pp. 171–192, 2008.

[63] P. A. Carneiro, M. E. Osugi, C. S. Fugivara, N. Boralle, M. Furlan, and M. V. B. Zanoni, "Evaluation of different electrochemical methods on the oxidation and degradation of Reactive Blue 4 in aqueous solution," *Chemosphere*, vol. 59, no. 3, pp. 431–439, 2005.

[64] Y. H. Lee and S. G. Pavlostathis, "Decolorization and toxicity of reactive anthraquinone textile dyes under methanogenic conditions," *Water Research*, vol. 38, no. 7, pp. 1838–1852, 2004.

[65] G. A. R. Oliveira, E. R. A. Ferraz, F. M. D. Chequer et al., "Chlorination treatment of aqueous samples reduces, but does not eliminate, the mutagenic effect of the azo dyes Disperse Red 1, Disperse Red 13 and Disperse Orange 1," *Mutation Research*, vol. 703, no. 2, pp. 200–208, 2010.

[66] P. A. Carneiro, G. A. Umbuzeiro, D. P. Oliveira, and M. V. B. Zanoni, "Assessment of water contamination caused by a mutagenic textile effluent/dyehouse effluent bearing disperse dyes," *Journal of Hazardous Materials*, vol. 174, no. 1–3, pp. 694–699, 2010.

[67] H. Zollinger, *Color Chemistry—Synthesis, Propierties and Applications of Organic Dyes and Pigments*, V.C.H, New York, NY, USA, 1991.

[68] C. C. I. Guaratini and M. V. B. Zanoni, "Textile dyes," *Quimica Nova*, vol. 23, no. 1, pp. 71–78, 2000.

[69] M. V. B. Zanoni, A. G. Fogg, J. Barek, and J. Zima, "Electrochemical investigations of reactive dyes; cathodic stripping voltammetric determination of anthraquinone-based chlorotriazine dyes at a hanging mercury drop electrode," *Analytica Chimica Acta*, vol. 349, no. 1–3, pp. 101–109, 1997.

[70] P. A. Carneiro, M. E. Osugi, J. J. Sene, M. A. Anderson, and M. V. B. Zanoni, "Evaluation of color removal and degradation of a reactive textile azo dye on nanoporous TiO_2 thin-film electrodes," *Electrochimica Acta*, vol. 49, no. 22-23, pp. 3807–3820, 2004.

[71] C. A. Martínez-Huitle and E. Brillas, "Decontamination of wastewaters containing synthetic organic dyes by electrochemical methods: a general review," *Applied Catalysis B*, vol. 87, no. 3-4, pp. 105–145, 2009.

[72] T. Robinson, G. McMullan, R. Marchant, and P. Nigam, "Remediation of dyes in textile effluent: a critical review on current treatment technologies with a proposed alternative," *Bioresource Technology*, vol. 77, no. 3, pp. 247–255, 2001.

[73] M. C. Gutiérrez and M. Crespi, "A review of electrochemical treatments for colour elimination," *Journal of the Society of Dyers and Colourists*, vol. 115, no. 11, pp. 342–345, 1999.

[74] M. M. Naim and Y. M. El Abd, "Removal and recovery of dyestuffs from dyeing wastewaters," *Separation and Purification Methods*, vol. 31, no. 1, pp. 171–228, 2002.

[75] A. B. dos Santos, F. J. Cervantes, and J. B. van Lier, "Review paper on current technologies for decolourisation of textile wastewaters: perspectives for anaerobic biotechnology," *Bioresource Technology*, vol. 98, no. 12, pp. 2369–2385, 2007.

[76] E. Forgacs, T. Cserháti, and G. Oros, "Removal of synthetic dyes from wastewaters: a review," *Environment International*, vol. 30, no. 7, pp. 953–971, 2004.

[77] C. A. Martínez-Huitle and S. Ferro, "Electrochemical oxidation of organic pollutants for the wastewater treatment: direct and indirect processes," *Chemical Society Reviews*, vol. 35, no. 12, pp. 1324–1340, 2006.

[78] S. Raghu and C. Ahmed Basha, "Chemical or electrochemical techniques, followed by ion exchange, for recycle of textile dye wastewater," *Journal of Hazardous Materials*, vol. 149, no. 2, pp. 324–330, 2007.

[79] N. Daneshvar, A. R. Khataee, A. R. Amani Ghadim, and M. H. Rasoulifard, "Decolorization of C.I. Acid Yellow 23 solution by electrocoagulation process: investigation of operational parameters and evaluation of specific electrical energy consumption (SEEC)," *Journal of Hazardous Materials*, vol. 148, no. 3, pp. 566–572, 2007.

[80] T. Bechtold, C. Mader, and J. Mader, "Cathodic decolourization of textile dyebaths: tests with full scale plant," *Journal of Applied Electrochemistry*, vol. 32, no. 9, pp. 943–950, 2002.

[81] D. Vaněrková, A. Sakalis, M. Holčapek, P. Jandera, and A. Voulgaropoulos, "Analysis of electrochemical degradation products of sulphonated azo dyes using high-performance liquid chromatography/tandem mass spectrometry," *Rapid Communications in Mass Spectrometry*, vol. 20, no. 19, pp. 2807–2815, 2006.

[82] C. Comninellis and C. Pulgarin, "Electrochemical oxidation of phenol for wastewater treatment using SnO_2, anodes," *Journal of Applied Electrochemistry*, vol. 23, no. 2, pp. 108–112, 1993.

[83] S. Stucki, R. Kötz, B. Carcer, and W. Suter, "Electrochemical waste water treatment using high overvoltage anodes Part II: anode performance and applications," *Journal of Applied Electrochemistry*, vol. 21, no. 2, pp. 99–104, 1991.

[84] A. M. Polcaro, S. Palmas, F. Renoldi, and M. Mascia, "On the performance of Ti/SnO_2 and Ti/PbO_2 anodes in electrochemical degradation of 2-chlorophenol for wastewater treatment," *Journal of Applied Electrochemistry*, vol. 29, no. 2, pp. 147–151, 1999.

[85] J. Feng, L. L. Houk, D. C. Johnson, S. N. Lowery, and J. J. Carey, "Electrocatalysis of anodic oxygen-transfer reactions: the electrochemical incineration of benzoquinone," *Journal of the Electrochemical Society*, vol. 142, no. 11, pp. 3626–3632, 1995.

[86] N. B. Tahar and A. Savall, "Electrochemical degradation of phenol in aqueous solution on bismuth doped lead dioxide: a comparison of the activities of various electrode formulations," *Journal of Applied Electrochemistry*, vol. 29, no. 3, pp. 277–283, 1999.

[87] P. Cañizares, M. Díaz, J. A. Domínguez, J. García-Gómez, and M. A. Rodrigo, "Electrochemical oxidation of aqueous phenol wastes on synthetic diamond thin-film electrodes," *Industrial and Engineering Chemistry Research*, vol. 41, no. 17, pp. 4187–4194, 2002.

[88] L. Gherardini, P. A. Michaud, M. Panizza, C. Comninellis, and N. Vatistas, "Electrochemical oxidation of 4-chlorophenol for wastewater treatment: definition of normalized current efficiency (φ)," *Journal of the Electrochemical Society*, vol. 148, no. 6, pp. D78–D82, 2001.

[89] D. Gandini, E. Mahé, P. A. Michaud, W. Haenni, A. Perret, and C. Comninellis, "Oxidation of carboxylic acids at boron-doped diamond electrodes for wastewater treatment," *Journal of Applied Electrochemistry*, vol. 30, no. 12, pp. 1345–1350, 2000.

[90] M. Panizza, P. A. Michaud, G. Cerisola, and C. Comninellis, "Electrochemical treatment of wastewaters containing organic pollutants on boron-doped diamond electrodes: prediction of specific energy consumption and required electrode area," *Electrochemistry Communications*, vol. 3, no. 7, pp. 336–339, 2001.

[91] A. M. Polcaro, M. Mascia, S. Palmas, and A. Vacca, "Electrochemical degradation of diuron and dichloroaniline at BDD electrode," *Electrochimica Acta*, vol. 49, no. 4, pp. 649–656, 2004.

[92] M. Panizza and G. Cerisola, "Removal of colour and COD from wastewater containing acid blue 22 by electrochemical oxidation," *Journal of Hazardous Materials*, vol. 153, no. 1-2, pp. 83–88, 2008.

[93] M. Panizza and G. Cerisola, "Application of diamond electrodes to electrochemical processes," *Electrochimica Acta*, vol. 51, no. 2, pp. 191–199, 2005.

[94] C. Flox, S. Ammar, C. Arias, E. Brillas, A. V. Vargas-Zavala, and R. Abdelhedi, "Electro-Fenton and photoelectro-Fenton degradation of indigo carmine in acidic aqueous medium," *Applied Catalysis B*, vol. 67, no. 1-2, pp. 93–104, 2006.

[95] M. Panizza, A. Barbucci, R. Ricotti, and G. Cerisola, "Electrochemical degradation of methylene blue," *Separation and Purification Technology*, vol. 54, no. 3, pp. 382–387, 2007.

[96] N. Daneshvar, S. Aber, V. Vatanpour, and M. H. Rasoulifard, "Electro-Fenton treatment of dye solution containing Orange II: influence of operational parameters," *Journal of Electroanalytical Chemistry*, vol. 615, no. 2, pp. 165–174, 2008.

[97] M. Panizza and G. Cerisola, "Electro-Fenton degradation of synthetic dyes," *Water Research*, vol. 43, no. 2, pp. 339–344, 2009.

[98] M. Vilaseca, M. C. Gutiérrez, V. López-Grimau, M. López-Mesas, and M. Crespi, "Biological treatment of a textile effluent after electrochemical oxidation of reactive dyes," *Water Environment Research*, vol. 82, no. 2, pp. 176–182, 2010.

[99] M. Riera-Torres and M. C. Gutiérrez, "Colour removal of three reactive dyes by UV light exposure after electrochemical treatment," *Chemical Engineering Journal*, vol. 156, no. 1, pp. 114–120, 2010.

[100] V. López-Grimau and M. C. Gutiérrez, "Decolourisation of simulated reactive dyebath effluents by electrochemical oxidation assisted by UV light," *Chemosphere*, vol. 62, no. 1, pp. 106–112, 2006.

[101] F. H. Oliveira, M. E. Osugi, F. M. M. Paschoal, D. Profeti, P. Olivi, and M. V. B. Zanoni, "Electrochemical oxidation of an acid dye by active chlorine generated using Ti/Sn$_{(1-x)}$Ir$_x$O$_2$ electrodes," *Journal of Applied Electrochemistry*, vol. 37, no. 5, pp. 583–592, 2007.

[102] M. E. Osugi, K. Rajeshwar, E. R. A. Ferraz, D. P. de Oliveira, Â. R. Araújo, and M. V. B. Zanoni, "Comparison of oxidation efficiency of disperse dyes by chemical and photoelectrocatalytic chlorination and removal of mutagenic activity," *Electrochimica Acta*, vol. 54, no. 7, pp. 2086–2093, 2009.

[103] M. E. Osugi, G. A. Umbuzeiro, F. J. V. De Castro, and M. V. B. Zanoni, "Photoelectrocatalytic oxidation of remazol turquoise blue and toxicological assessment of its oxidation products," *Journal of Hazardous Materials*, vol. 137, no. 2, pp. 871–877, 2006.

[104] M. C. Gutierrez, V. Lopez-Grimau, M. Riera-Torres, M. Vilaseca, and M. M. Crespi, "Tratamiento electroquimico y reutilizacion de efluentes de tintura," *Revista de Química Textil*, vol. 191, pp. 40–46, 2009.

[105] L. Gomathi Devi, S. Girish Kumar, K. Mohan Reddy, and C. Munikrishnappa, "Photo degradation of Methyl Orange an azo dye by Advanced Fenton Process using zero valent metallic iron: influence of various reaction parameters and its degradation mechanism," *Journal of Hazardous Materials*, vol. 164, no. 2-3, pp. 459–467, 2009.

[106] Q. Zhang and Z. Zhang, "Preparation and characterization of nanocrystalline fe-doped TiO$_2$ film on different substrates and its application in degrading dyeing water," *Journal of Dispersion Science and Technology*, vol. 30, no. 1, pp. 110–114, 2009.

[107] J. M. Peralta-Hernández, Y. Meas-Vong, F. J. Rodríguez, T. W. Chapman, M. I. Maldonado, and L. A. Godínez, "In situ electrochemical and photo-electrochemical generation of the fenton reagent: a potentially important new water treatment technology," *Water Research*, vol. 40, no. 9, pp. 1754–1762, 2006.

[108] W. G. Kuo, "Decolorizing dye wastewater with Fenton's reagent," *Water Research*, vol. 26, no. 7, pp. 881–886, 1992.

[109] F. Zhang, J. Zhao, T. Shen, H. Hidaka, E. Pelizzetti, and N. Serpone, "TiO$_2$-assisted photodegradation of dye pollutants II. Adsorption and degradation kinetics of eosin in TiO$_2$ dispersions under visible light irradiation," *Applied Catalysis B*, vol. 15, no. 1-2, pp. 147–156, 1998.

[110] C. G. Silva and J. L. Faria, "Photochemical and photocatalytic degradation of an azo dye in aqueous solution by UV irradiation," *Journal of Photochemistry and Photobiology A*, vol. 155, no. 1–3, pp. 133–143, 2003.

[111] C. Hachem, F. Bocquillon, O. Zahraa, and M. Bouchy, "Decolourization of textile industry wastewater by the photocatalytic degradation process," *Dyes and Pigments*, vol. 49, no. 2, pp. 117–125, 2001.

[112] G. A. Epling and C. Lin, "Photoassisted bleaching of dyes utilizing TiO$_2$ and visible light," *Chemosphere*, vol. 46, no. 4, pp. 561–570, 2002.

[113] Y. B. Xie and Y. B. X. Z. Li, "Interactive oxidation of photoelectrocatalysis and electr-Fenton for azo dye degradation using TiO$_2$-Ti mesh and reticulated vitreous carbon electrodes," *Materials Chemistry and Physics*, vol. 95, no. 1, pp. 39–50, 2006.

[114] A. Duran, J. M. Monteagudo, and J. M. E. Amores, "Solar photo-Fenton degradation of reactive blue 4 in a CPC reactor," *Applied Catalysis B*, vol. 80, no. 1-2, pp. 42–50, 2008.

[115] S. Figueroa, L. Vazquez, and A. Alvarez-Gallegos, "ecolorizing textile wastewater with Fenton's reagent electrogenerated with solar photovoltaic cell," *Water Research*, vol. 43, no. 2, pp. 283–294, 2009.

[116] M. Sala, *Dissertation: Aplicació de Techniques Electroquímiques i Fotoelectroquímiques per la Degradació de Compostos poc Biodegradables en Efluents Industrials Tèxtils*, UPC, 2012.

Research Article

Synthesis and Photocatalytic Properties of One-Dimensional Composite Bi$_2$O$_3$-Bi$_2$CrO$_6$ Nanowires

Qianqian Zhang,[1] Baibiao Huang,[2] Peng Wang,[2] Xiaoyang Zhang,[2] Xiaoyan Qin,[2] and zeyan wang[2]

[1] *School of Chemistry and Chemical Engineering, Shandong University, Jinan 250100, China*
[2] *State Key Laboratory of Crystal Materials, Shandong University, Jinan 250100, China*

Correspondence should be addressed to Baibiao Huang, bbhuang@sdu.edu.cn

One-dimensional composite Bi$_2$O$_3$-Bi$_2$CrO$_6$ nanowires were successfully fabricated by a simple microwave-assistant hydrothermal method. The successful fabrication of one-dimensional Bi$_2$O$_3$-Bi$_2$CrO$_6$ nanowires can only be realized at pH value range of 1–5 of the starting solution. The fabricated nanowires were characterized by X-ray powder diffraction (XRD), scanning electron microscope (SEM), transmission electron microscopy (TEM), UV-visible diffuse reflectance spectra (UV-Vis DRS), and photoluminescence (PL), respectively. The diameter of the nanowires varies from 30 to 100 nm; the length is a few micrometers. Methylene blue (MB) solutions were used to evaluate the visible light photocatalytic activities of the fabricated samples. Compared with Bi$_2$O$_3$, the fabricated Bi$_2$O$_3$-Bi$_2$CrO$_6$ nanowires show enhanced efficiency in oxidization of MB under visible light.

1. Introduction

One-dimensional nanostructures with distinctive structures and properties play important roles in nanotechnology for their use as building blocks in nanoscale circuits, optoelectronic, electrochemical, and electromechanical devices [1, 2]. The synthesis of one-dimensional (1D) nanostructures [3–7] has gained tremendous amount of attention in recent years due to their fascinating sizes, shapes, and material-dependent properties. Nanotubes, nanobelts, nanorods, and semiconducting nanowires have been fabricated through a number of advanced nanolithographic techniques, thermal evaporations, and solution-based methods [8–11]. Among all the one-dimensional nanostructures, the composite nanowires with two different constitutions are widely investigated [12, 13]. Vomiero et al. produced radial and longitudinal nanosized In$_2$O$_3$-SnO$_2$ by applying a suitable methodology of transport and condensation [14]. Bachas's group has synthesized a new class of bimetallic nanotubes based on Pd/Fe and demonstrated their efficacy in the dechlorination of PCB 77 (a polychlorinated biphenyl) one-dimensional

iron metal nanotubes of different diameters were prepared by electroless deposition within the pores of PVP-coated polycarbonate membranes using a simple technique under ambient conditions. The longitudinal nucleation of the nanotubes along the pore walls was achieved by mounting the PC membrane between two halves of a U-shape reaction tube [15]. Coaxial SnO$_2$@TNTs, with two-fold tubular structures, are assembled by electrochemical and solvothermal embedments of SnO$_2$ nanolayers inside the pristine TiO$_2$ nanotube arrays. The excellent electrochemical properties originated from the synergistic effect with improved electronic conductivity and dual lithium storage mechanism, demonstrating that the coaxial SnO$_2$@TNT hybrid is a promising candidate for electrochemical energy storage [16]. In case of our research, microwave hydrothermal method was employed in the fabrication process. Microwave irradiation provides rapid and uniform heating of reagents and solvents [17–19]. The rapid microwave heating provides uniform nucleation and growth conditions, which conduce to homogeneous and well crystalline nanomaterials. We demonstrate a simple and efficient approach to synthesize one-dimensional nanowires

within 60 min of microwave irradiation. During the process, no organic surfactant and catalyst were used. The time and energy consumption were saved with the microwave route of syntheses. Comparative experiment was carried out the same reaction time by common hydrothermal method while keeping other synthetic parameters in same. No nanowire was obtained.

Bismuth-containing oxides have been extensively studied because of their interesting properties, including ferroelectricities [20], ionic conductivities [21], superconductivities [22], and catalytic activities [23]. As a photocatalyst [24, 25], the conduction and valence band edges of Bi_2O_3 are +0.33 and +3.13 V relative to NHE, respectively. The band structure of Bi_2O_3 accounts for its ability to oxidize organic pollution and generate highly reactive species, such as $O^- \bullet$ and $OH\bullet$ radicals. Although the Bi_2O_3 have the proper band structure, the efficiency to decompose organic pollution is still low. In order to improve the photocatalytic ability of Bi_2O_3, Bi_2CrO_6 was connected to Bi_2O_3. Bi_2CrO_6 is a novel material with narrow band gap. Upon connection of Bi_2CrO_6 to Bi_2O_3 nanowires, a unique semiconductor—semiconductor nanoscale contact can be prepared, which shows different properties from Bi_2O_3. In this paper, the Bi_2O_3 and Bi_2CrO_6 were synthesized synchronously in the same Teflon autoclave, Bi_2O_3 and Bi_2CrO_6 are in well contact, and the photo-generated electron and holes can migrate from each other freely. Compared with Bi_2O_3, the Bi_2O_3-Bi_2CrO_6 nanowires show enhanced efficiency in photodegradation of methylic blue under visible light.

2. Experimental Section

Analytic grade Bismuth nitrate $(Bi(NO_3)_3)$, sodium chromate (Na_2CrO_4), sodium hydroxide (NaOH), and hydrochloric acid (HCl) were used as received without any treatment. In a typical procedure, solutions of $Bi(NO_3)_3$ and solutions of Na_2CrO_4 in water were prepared as stock solutions in advance. 10 mL of 0.2 M $Bi(NO_3)_3$ stock solution was mixed with 10 mL of 0.1 M Na_2CrO_4 aqueous solution, and 1 M HCl solution was added to adjust the pH value of the mixed solution to 3. The solution was magnetically stirred for about 0.5 h, then transferred into a special Teflon autoclave, and heated at 180°C for 1 h under microwave radiation. The resulting precipitate was collected, washed with dilute HCl aqueous solution and deionized water until the pH value of the washing solution was about 7, and dried in air at 80°C for 8 h.

X-ray powder diffraction (XRD) patterns were obtained by a Bruker AXS D8 advance powder diffractometer. The scanning electron microscope (SEM) image of the products was examined by a Hitachi, S-4800 microscope. Transmission electron microscopy (TEM) was performed with a HITACH H-600 Electron Microscope. The UV-visible diffuse reflectance spectrum was obtained by Shimadzu UV-2550. PL spectrum measurement was performed in a fluorescence spectrophotometer (Edinburgh, FL920) at room temperature. A reference photocatalyst Bi_2O_3 was prepared using the method reported in the literature [24].
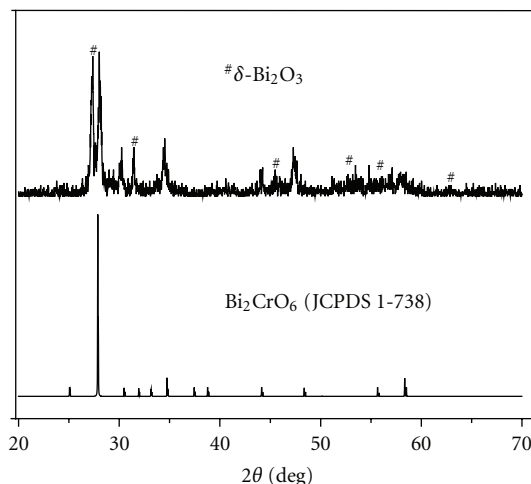

FIGURE 1: XRD pattern of the composite Bi_2O_3-Bi_2CrO_6 nanowires.

Photocatalytic activities of Bi_2O_3-Bi_2CrO_6 were evaluated by studying degradation of methylic blue (MB) dye. The photocatalytic degradation of MB dye was carried out with 0.2 g of the powdered photocatalyst suspended in 100 mL solution of MB dye prepared by dissolving 20 mg of MB powder in 1 L of distilled water in a Pyrex glass cell at room temperature under air. The optical system for detecting the catalytic reaction included a 300 W Xe arc lamp (focused through a shutter window, Chang Tuo, Beijing) with UV cutoff filter (providing visible light $\lambda \geq 400$ nm).

3. Results and Discussion

A powder XRD pattern (Figure 1) of the product initially suggests the coexistence of Bi_2O_3 (JCPDS file 16-654) and Bi_2CrO_6 (JCPDS file 1-738). The peaks in this figure can be indexed to a cubic phase of Bi_2O_3 (space group Fm-3 m (no. 225)) with lattice constants $a = 5.66$ Å. The system and lattice constants of Bi_2CrO_6 are not shown in the Joint Committee on Powder Diffraction Standards card. Figure 2 shows SEM images of Bi_2O_3-Bi_2CrO_6 nanowire. The diameter of the nanowires is about 30–100 nm, and the length is in the range of micrometers. The morphology of the nanowire is uniform.

Typical TEM images of Bi_2O_3-Bi_2CrO_6 nanowires are shown in Figures 3(a) and 3(b). According to Figure 3(a), the diameter of the nanowires varies from 30 to 100 nm, the length is a few micrometers, which is consistent with SEM results. Figure 3(b) shows TEM micrograph of a typical nanowire junction. The knots can be clearly seen in the nanowire structures. The interval between two knots is not equal and ranges from several ten to hundred of nanometers.

UV-visible diffuse reflectance spectra of commercial Bi_2O_3, fabricated Bi_2O_3 and the composite Bi_2O_3-Bi_2CrO_6 nanowires are shown in Figure 4. It can be seen that the absorbance of Bi_2O_3-Bi_2CrO_6 nanowire extends to the visible light region. The onset of the adsorption edge is 515 nm in the UV-vis diffuse reflectance spectrum. The nanowire can absorb light with wavelength $\lambda < 515$ nm, covering the region from UV through near visible light in the sunlight,

(a)

(b)
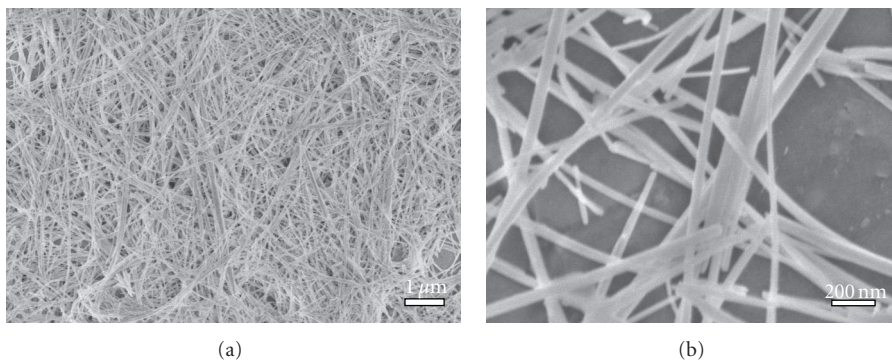
FIGURE 2: SEM images of the composite Bi_2O_3-Bi_2CrO_6 nanowires: (a) low magnification; (b) high magnification.

(a)

(b)
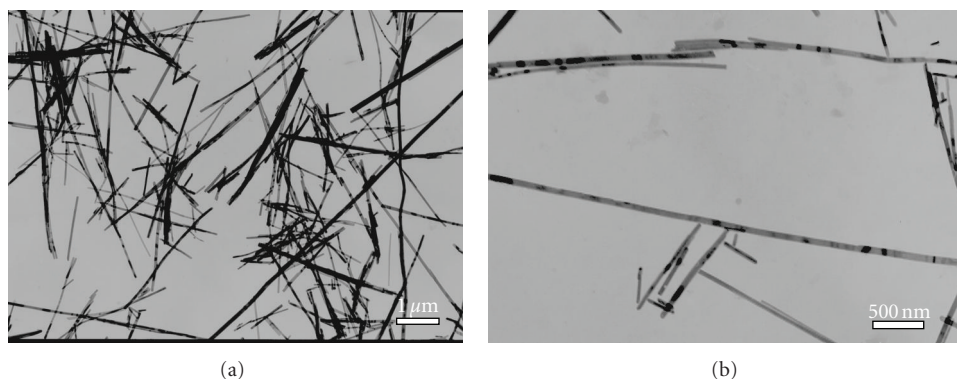
FIGURE 3: (a) TEM image of the composite Bi_2O_3-Bi_2CrO_6 nanowires; (b) a TEM image of a typical nanowire junction.
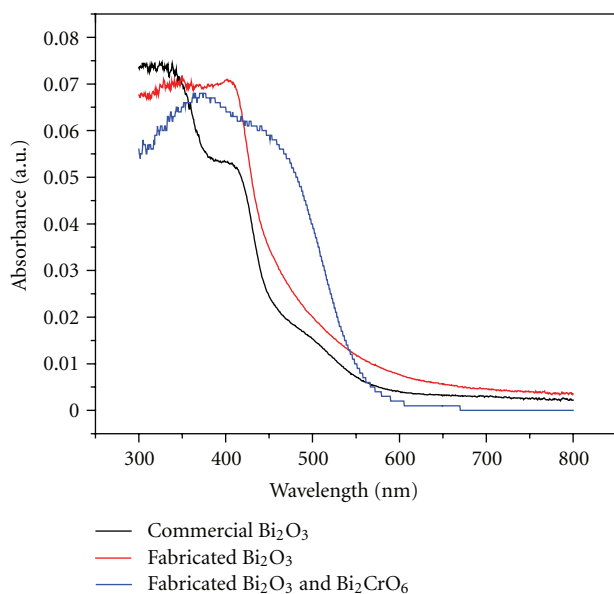
FIGURE 4: The UV-visible diffuse reflectance spectra of commercial Bi_2O_3, fabricated Bi_2O_3, and the composite Bi_2O_3-Bi_2CrO_6 nanowires.

FIGURE 5: The PL spectrum of the composite Bi_2O_3-Bi_2CrO_6 nanowires.

and can be used as a visible light photocatalyst to decompose the organic pollution. Compared with commercial and fabricated Bi_2O_3, the light absorption of Bi_2O_3-Bi_2CrO_6

in 440 nm to 540 nm is strongest. The PL spectrum of the sample is presented in **Figure 5**. Two peaks, 535 and 651 nm in the PL spectrum can be seen, which meant two recombined semiconductors. Both of them are in visible light region; one is attributed to Bi_2O_3, and the other is due to Bi_2CrO_6. The excitation wavelength was set at 430 nm.
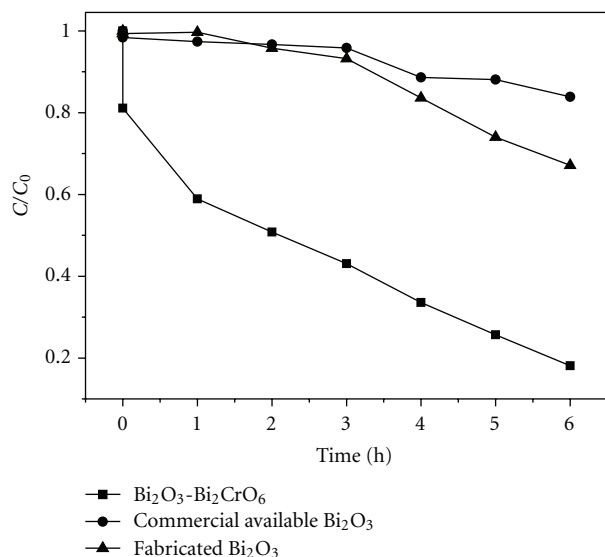
FIGURE 6: Photodecomposition of MB dye in solution (20 mg/L) over Bi_2O_3-Bi_2CrO_6 composite nanowires, commercial available Bi_2O_3 and fabricated Bi_2O_3, under visible-light irradiation ($\lambda \geq$ 400 nm). C is the concentration of MB dye at time t, and C_0 is the original concentration before it is irradiated.

FIGURE 7: XRD pattern of the sample synthesized in different pH value of starting solution: (a) pH = 1; (b) pH = 2; (c) pH = 3; (d) pH = 4; (e) pH = 5; (f) pH = 6; (g) pH = 7; (h) pH = 11.

To probe the photocatalytic activity of the composite Bi_2O_3-Bi_2CrO_6 nanowire in visible part of the solar spectrum, the bleaching of MB was carried out under irradiation of a Xe arc lamp with UV cutoff filter (providing visible light $\lambda \geq 400$ nm). An aliquot (2 mL) of MB solution was removed at interval times and placed in the UV-vis spectrometer for analysis. The results were shown in Figure 6. As shown in Figure 6, the photocatalytic activity of Bi_2O_3-Bi_2CrO_6 nanowires is higher than fabricated Bi_2O_3 and the commercial available Bi_2O_3; more than 82% of MB molecules were decomposed in 6 h, while the reference photocatalysts Bi_2O_3 and the commercial available Bi_2O_3, only 33% and 17% of the MB dye, were decomposed in 6 h, respectively. (As pure Bi_2CrO_6 phase cannot be obtained, so we just choose the Bi_2O_3 as the reference photocatalysts.) The valence band of Bi_2O_3 is composed of O2p, and the conduction band is consisted of Bi5d. The import of Cr element leads to the band positions of Bi_2CrO_6 different from the band positions of Bi_2O_3. (Since the pure Bi_2CrO_6 phase and the crystal structure and lattice constants of Bi_2CrO_6 cannot be obtained, we cannot use the plane-wave-based density functional method to clarify whether Cr^{6+} contributed to valence- or conduction-band formation in Bi_2CrO_6). The photogenerated electrons and holes can transfer between Bi_2O_3 and Bi_2CrO_6, the different band positions of Bi_2O_3 and Bi_2CrO_6, enhance the separation of photogenerated electrons and holes, leading to higher efficiency in degradation of MB.

The successful fabrication of one-dimensional composite Bi_2O_3-Bi_2CrO_6 nanowires can only be realized at the pH value range of 1–5 of starting solution. Comparative experiments were made by adjusting the starting solution's pH value 6, 7, and 11 while keeping other synthetic parameters
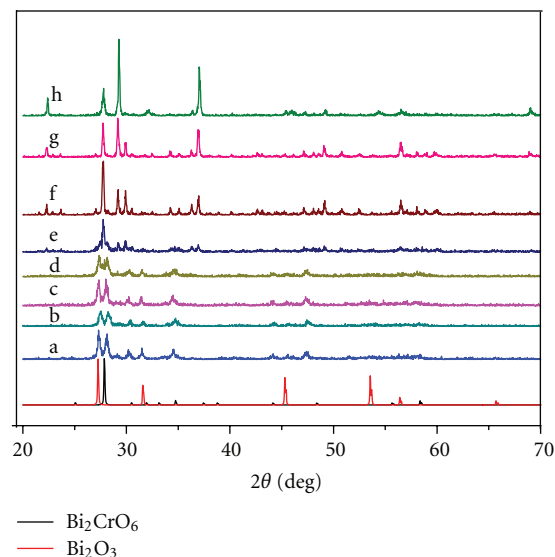
in the same condition. Figure 7 shows the XRD pattern of as-synthesized products. The XRD measurements show that the composition and structure changed drastically along with the increasing of the pH value. Below pH 5, the XRD pattern exhibits the product is composed of Bi_2O_3 (JCPDS file 16–654) and Bi_2CrO_6 (JCPDS file 1-738). The peaks belonged to Bi_2O_3 and Bi_2CrO_6 become weakened till disappeared, and subsequent peaks of newly formed crystals structure start to emerge above pH 5. At pH 11, the sample is mainly composed of $Bi_2O_{2.33}$ (JCPDS file 27-51), $Bi(OH)_3$ (JCPDS file 1-898), and CrOOH (JCPDS file 70-1115). Seen from Figure 7, the pH values of the starting solution greatly affect the fabrication of composite Bi_2O_3-Bi_2CrO_6 nanowires, and the composite Bi_2O_3-Bi_2CrO_6 nanowires can be obtained at starting solution's pH value below 5.

In conclusion, one-dimensional Bi_2O_3-Bi_2CrO_6 nanowires were synthesized by a simple microwave-assistant hydrothermal method. The diameter of the wires is about 30–100 nm, and the length is in range of micrometers. The sample can absorb visible light ($\lambda < 515$ nm), covering the region from UV through near visible light in the sunlight, showing high efficiency in degradation of MB under visible light irradiation. The work of Bi_2O_3-Bi_2CrO_6 nanowires on water splitting is still in process.

Acknowledgments

References

[1] J. Li, Y. Zhang, S. To, L. You, and Y. Sun, "Effect of nanowire number, diameter, and doping density on nano-FET biosensor sensitivity," *ACS Nano*, vol. 5, no. 8, pp. 6661–6668, 2011.

[2] A. R. Rathmell, M. Nguyen, M. Chi, and B. J. Wiley, "Synthesis of oxidation-resistant cupronickel nanowires for transparent conducting nanowire networks," *Nano Letters*, vol. 12, no. 6, pp. 3193–3199, 2012.

[3] S. Deng, V. Tjoa, H. M. Fan et al., "Reduced graphene oxide conjugated Cu_2O nanowire mesocrystals for high-performance NO_2 gas sensor," *Journal of the American Chemical Society*, vol. 134, no. 10, pp. 4905–4917, 2012.

[4] S. Hoang, S. P. Berglund, N. T. Hahn, A. J. Bard, and C. B. Mullins, "Enhancing visible light photo-oxidation of water with TiO_2 nanowire arrays via cotreatment with H_2 and NH_3: synergistic effects between Ti^{3+} and N," *Journal of the American Chemical Society*, vol. 134, no. 8, pp. 3659–3662, 2012.

[5] H. W. Liang, S. Liu, and S. H. Yu, "Controlled synthesis of one-dimensional inorganic nanostructures using pre-existing one-dimensional nanostructures as templates," *Advanced Materials*, vol. 22, no. 35, pp. 3925–3937, 2010.

[6] H. Huang, B. Liang, Z. Liu, X. Wang, D. Chen, and G. Shen, "Metal oxide nanowire transistors," *Journal of Materials Chemistry*, vol. 22, no. 27, pp. 13428–13445, 2012.

[7] J. J. Hill, N. Banks, K. Haller, M. E. Orazem, and K. J. Ziegler, "An interfacial and bulk charge transport model for dye-sensitized solar cells based on photoanodes consisting of core-shell nanowire arrays," *Journal of the American Chemical Society*, vol. 133, no. 46, pp. 18663–18672, 2011.

[8] H. Geaney, C. Dickinson, C. A. Barrett, and K. M. Ryan, "High density germanium nanowire growth directly from copper foil by self-induced solid seeding," *Chemistry of Materials*, vol. 23, no. 21, pp. 4838–4843, 2011.

[9] J. Z. Liu, P. X. Yan, G. H. Yue, L. B. Kong, R. F. Zhuo, and D. M. Qu, "Synthesis of doped ZnS one-dimensional nanostructures via chemical vapor deposition," *Materials Letters*, vol. 60, no. 29-30, pp. 3471–3476, 2006.

[10] F. Wang, A. Dong, J. Sun, R. Tang, H. Yu, and W. E. Buhro, "Solution-liquid-solid growth of semiconductor nanowires," *Inorganic Chemistry*, vol. 45, no. 19, pp. 7511–7521, 2006.

[11] K. Li, H. Wang, C. Pan, J. Wei, R. Xiong, and J. Shi, "Enhanced photoactivity of Fe + N Codoped anatase-rutile TiO_2 nanowire film under visible light irradiation," *International Journal of Photoenergy*, vol. 2012, Article ID 398508, 8 pages, 2012.

[12] Z. Liu, D. D. Sun, P. Guo, and J. O. Leckie, "An efficient bi-component TiO_2/SnO_2 nanofiber photocatalyst fabricated by electrospinning with a side-by-side dual spinneret method," *Nano Letters*, vol. 7, no. 4, pp. 1081–1085, 2007.

[13] M. Müllner, T. Lunkenbein, J. Breu, F. Caruso, and A. H. E. Müller, "Template-directed synthesis of silica nanowires and nanotubes from cylindrical core-shell polymer brushes," *Chemistry of Materials*, vol. 24, no. 10, pp. 1802–1810, 2012.

[14] A. Vomiero, M. Ferroni, E. Comini, G. Faglia, and G. Sberveglieri, "Preparation of radial and longitudinal nano-sized heterostructures of In_2O_3 and SnO_2," *Nano Letters*, vol. 7, no. 12, pp. 3553–3558, 2007.

[15] E. M. Zahran, D. Bhattacharyya, and L. G. Bachas, "Development of reactive Pd/Fe bimetallic nanotubes for dechlorination reactions," *Journal of Materials Chemistry*, vol. 21, no. 28, pp. 10454–10462, 2011.

[16] X. Wu, S. Zhang, L. Wang et al., "Coaxial SnO_2@TiO_2 nanotube hybrids: from robust assembly strategies to potential application in Li^+ storage," *Journal of Materials Chemistry*, vol. 22, no. 22, pp. 11151–11158, 2012.

[17] M. N. Nadagouda and R. S. Varma, "Microwave-assisted synthesis of crosslinked poly(vinyl alcohol) nanocomposites comprising single-walled carbon nanotubes, multi-walled carbon nanotubes, and buckminsterfullerene," *Macromolecular Rapid Communications*, vol. 28, no. 7, pp. 842–847, 2007.

[18] R. S. Varma, *Microwaves in Organic Synthesis*, chapter 8, Wiley-VCH, Weinheim, Germany, 2006.

[19] Z. P. Qiao, Y. Zhang, L. T. Zhou, and Q. Xire, "Shape control of PbS crystals under microwave irradiation," *Crystal Growth and Design*, vol. 7, no. 12, pp. 2394–2396, 2007.

[20] R. V. K. Mangalam, P. Mandal, E. Suard, and A. Sundaresan, "Ferroelectricity in ordered perovskite $BaBi_{0.5}{}^{3+}(Bi_{0.2}{}^{5+}Nb_{0.3}{}^{5+})O_3$ with Bi^{3+}:$6s^2$ lone pair at the B-site," *Chemistry of Materials*, vol. 19, no. 17, pp. 4114–4116, 2007.

[21] F. Mauvy, J. C. Launay, and J. Darriet, "Synthesis, crystal structures and ionic conductivities of $Bi_{14}P_4O_{14}$ and $Bi_{50}V_4O_{85}$. Two members of the series $Bi_{18-4m}M_{4m}O_{27+4m}$ (M=P, V) related to the fluorite-type structure," *Journal of Solid State Chemistry*, vol. 178, no. 6, pp. 2015–2023, 2005.

[22] M. L. Munzarová and R. Hoffmann, "Strong electronic consequences of intercalation in cuprate superconductors: the case of a trigonal planar AuI3 complex stabilized in the $Bi_2Sr_2CaCu_2Oy$ lattice," *Journal of the American Chemical Society*, vol. 124, no. 19, pp. 5542–5549, 2002.

[23] W. J. M. van Well, M. T. Le, N. C. Schiødt, S. Hoste, and P. Stoltze, "The influence of the calcination conditions on the catalytic activity of Bi_2MoO_6 in the selective oxidation of propylene to acrolein," *Journal of Molecular Catalysis A*, vol. 256, no. 1-2, pp. 1–8, 2006.

[24] A. Hameed, T. Montini, V. Gombac, and P. Fornasiero, "Surface phases and photocatalytic activity correlation of Bi_2O_3/Bi_2O_{4-x} nanocomposite," *Journal of the American Chemical Society*, vol. 130, no. 30, pp. 9658–9659, 2008.

[25] X. Yong and M. A. A. Schoonen, "The absolute energy positions of conduction and valence bands of selected semiconducting minerals," *American Mineralogist*, vol. 85, no. 3-4, pp. 543–556, 2000.

Research Article

Feasibility of Carbonaceous Nanomaterial-Assisted Photocatalysts Calcined at Different Temperatures for Indoor Air Applications

Wan-Kuen Jo and Kun-Hwan Kim

Department of Environmental Engineering, Kyungpook National University, University Road, Bukgu, Daegu 702-701, Republic of Korea

Correspondence should be addressed to Wan-Kuen Jo, wkjo@knu.ac.kr

This study examined the characteristics and photocatalytic activity of multiwall carbon nanotube-assisted TiO_2 (MWNT-TiO_2) nanocomposites calcined at different temperatures to assess their potential indoor air applications. It was confirmed that the composites calcined at low temperatures (300 and 400°C) contained TiO_2 nanoparticles bound intimately to the MWNT networks. Meanwhile, almost no MWNTs were observed when the calcination temperature was increased to 500 and 600°C. The MWNT-TiO_2 composites calcined at low temperatures showed higher photocatalytic decomposition efficiencies for aromatic hydrocarbons at indoor concentrations than those calcined at high temperatures. The mean efficiencies for benzene, toluene, ethyl benzene, and o-xylene (BTEX) by the composite calcined at 300°C were 32, 70, 79, and 79%, respectively, whereas they were 33, 71, 78, and 78% for the composite calcined at 400°C, respectively. In contrast, the efficiencies decreased to close to zero when the calcination temperature was increased to 600°C. Moreover, the MWNT-TiO_2 exhibited superior photocatalytic performance for the decomposition efficiencies compared to TiO_2 under conventional UV-lamp irradiations. Consequently, these carbonaceous nanomaterial-assisted photocatalysts can be applied effectively to indoor air applications depending upon the calcination temperature.

1. Introduction

The photocatalytic process using titanium dioxide (TiO_2) has become an attractive advanced oxidation technology for addressing a variety of environmental problems owing to its potential to oxidize a wide range of environmental pollutants and long-term thermodynamic stability under certain operating conditions [1, 2]. However, the current bottleneck for TiO_2 photocatalysis lies in its low quantum yield and low photodegradation efficiency. Therefore, a range of modifying methods were attempted to enhance the photocatalytic properties of TiO_2 for the decomposition of several environmental pollutants. The methods include nonmetallic doping, metallic doping, cocatalysts, dye sensitization, and adsorbent assistance [3–8].

Among these methods, carbonaceous adsorbent-assisted photocatalysts have attracted considerable attention because of their superior performance. Initially, granular- and fibrous-type activated carbons (ACs) were used as TiO_2 supporters for certain environmental applications [9–11]. Later, other types of carbonaceous nanomaterials (particularly carbon nanotubes (CNTs)) were suggested as alternative supporters of mainly TiO_2 due to the combined effect of the electronic and adsorption properties [7, 12, 13]. CNTs are generally classified into multi- and single-wall carbon nanotubes (MWNTs and SWNTs). The unique electronic properties of CNTs can retard the electron-hole recombination time, thereby enhancing the photocatalytic performance of TiO_2 [7, 13]. In addition, CNTs have the potential to provide reactive surface areas approaching those

provided by ACs and to adsorb hydrophobic species, which are barely adsorbed by TiO_2 nanoparticles [14]. Accordingly, many studies [15–19] applied MWNT- or SWNT-assisted TiO_2 photocatalysts (MWNT- or SWNT-TiO_2) for the purification of environmental pollutants and reported these nanomaterials to have superior performance to that of stand-alone TiO_2. Unlike other types of photocatalysts, there are few reports on the effects of the calcination temperature of CNT-assisted TiO_2 photocatalysts on the gas-phase pollutant decomposition. In particular, the calcination temperature can be an important parameter associated with the photocatalytic activity for certain photocatalysts [20–24]. This suggests that the photocatalytic activity of CNT-assisted TiO_2 nanomaterials can vary with the calcination temperature.

Accordingly, this study examined the characteristics and heterogeneous photocatalytic activity of MWNT-assisted TiO_2 (MWNT-TiO_2) photocatalysts prepared at different calcination temperatures to assess the feasibility of their indoor air applications. Although SWNTs have a higher specific surface area, they are more expensive than MWNTs [25]. Therefore, this study used MWNTs as a cost-effective TiO_2 assistant material. The target environmental pollutants included four organic vapors (benzene, toluene, ethyl benzene, and xylene (also known as BTEX)), which are toxic or potentially toxic to humans [26]. These compounds are an important class of pollutants found frequently at high concentrations in a range of indoor environments [27]. The characteristics of BTEX have prompted the development of control means to minimize the health impacts of indoor air exposure. For indoor air applications, the surveyed concentration of each compound was chosen to be within the indoor air concentration (IAC) range (<1 ppm) [27].

2. Methods

2.1. Synthesis Route and Properties of MWNT-Assisted Photocatalyst.

The MWNT-TiO_2 nanomaterials were synthesized using a sol-gel method. For this method, 0.7 g of MWNT (95.9%, Carbon Nano-material Technology) was added to 50 mL of ethanol (99.9% Merck) and sonicated for 20 min. Subsequently, 15.5 mL of tetrabutyl orthotitanate (TBOT, Sigma-Aldrich) was added to the MWNT-ethanol solution. This mixture was sonicated for 30 min to achieve better mixing and stirred vigorously for 30 min. Afterwards, 4 mL of nitric acid (69 wt%, Junsei) and 20 mL of deionized water were added to the solution to catalyze the hydrolysis and condensation. The resulting mixture was stirred vigorously until a homogeneous gel was formed. The gel was aged in air for 4 d at room temperature, crushed into fine powders, and dried at 80°C in an oven for 12 h. The powders were calcined at 300, 400, 500, or 600°C for 5 h. The calcined CNT-TiO_2 powders were coated on the inner surface of the pyrex reactor, using the method reported by Xagas et al. [28].

Before the coating procedure, the as-prepared MWNT-TiO_2 powders were examined for their surface and morphological properties. X-ray diffraction (XRD) patterns were determined on a Rigaku D/max-2500 diffractometer with Cu K$_\alpha$ radiation operated at 40 kV and 100 mA. Thermal

gravity analysis (TGA) was done using a TA Instrument SDT Q600 TG/DTA in order to determine the carbon content in the MWNT-TiO_2 powders. The particle morphology was observed using a Hitachi S-4300&EDX-350 FE-scanning electron microscope (SEM) at an acceleration voltage of 15 kV. X-ray photoelectron spectroscope (XPS) measurements were done using a Thermo VG Scientific Escalab 250 spectrometer with monochromatized Al Ka excitation. Fourier transform infrared (FTIR) analysis was performed on a PerkinElmer Spectrum GX spectrophotometer at a resolution of 4 cm^{-1} in the spectral range of 400−4,000 cm^{-1}, using a KBR pellet for sample preparation.

2.2. Application of MWNT-Assisted TiO_2 Nanocomposites to BTEX Decomposition.

The experimental setup is illustrated in Figure 1. An annular-geometry reactor was used to evaluate the as-prepared MWNT-TiO_2 nanomaterials for the decomposition of gas-phase BTEX. The reactor consisted of a pyrex tube coated on the inner surface with a thin film of the MWNT-TiO_2 nanomaterials. A conventional cylindrical lamp or a hexahedral tube installed with light-emitting diodes (LEDs) was inserted inside another pyrex tube (outside diameter, 25 mm), whose outer surface served as the inner surface of the annular reactor. The gas flowed through the annular region. This design was particularly suited for research, because it provided a well-characterized reactive catalyst surface along the length of the reactor body and allowed uniform light distribution. Moreover, the reactor was designed to direct the flow of incoming air toward the UV light to increase the air turbulence inside the reactor, thereby enhancing the distribution of target compounds onto the catalytic surface of the reactor. The humidity was adjusted by passing zero-grade air through a charcoal filter, followed by a humidification device in a water bath. The relative humidity (RH) was measured in front of the photocatalytic reactor inlet using a humidity meter (T & D Thermo Recorder TR-72S). The flow rate (FR) measurement was carried out using identical rotameters (0–10 L min^{-1}) calibrated to a dry test meter (URG 3000-020C). The air stream was heated externally to help vaporize the BTEX injected into the mixing chamber through a syringe pump (Kd Scientific Model 210). The air stream was then finally fed to the photocatalytic reactor. The desired concentration of the standard gas was controlled by adjusting the FR and BTEX injection rate.

The major photocatalytic parameters were the input concentration (IC), RH, light source, FR, and hydraulic diameter (HD, which is defined as the inside diameter of the annular reactor tube minus the outside diameter of the lamp). The IC was fixed to 0.1 ppm for each component of BTEX to simulate the IAC condition. The RH was adjusted to 50%, which was within the American Society of Heating, Refrigerating and Air-Conditioning Engineers comfort range (40−60%). UV radiation was supplied using a conventional 8-W fluorescent black light (Sankyo Denki F8T5/BLB) with a maximum spectral intensity at 352 nm or 42 0.06-W UV-LEDs (Moksan MS-L512UVP) with a maximum spectral intensity at 380 nm. The FR was adjusted
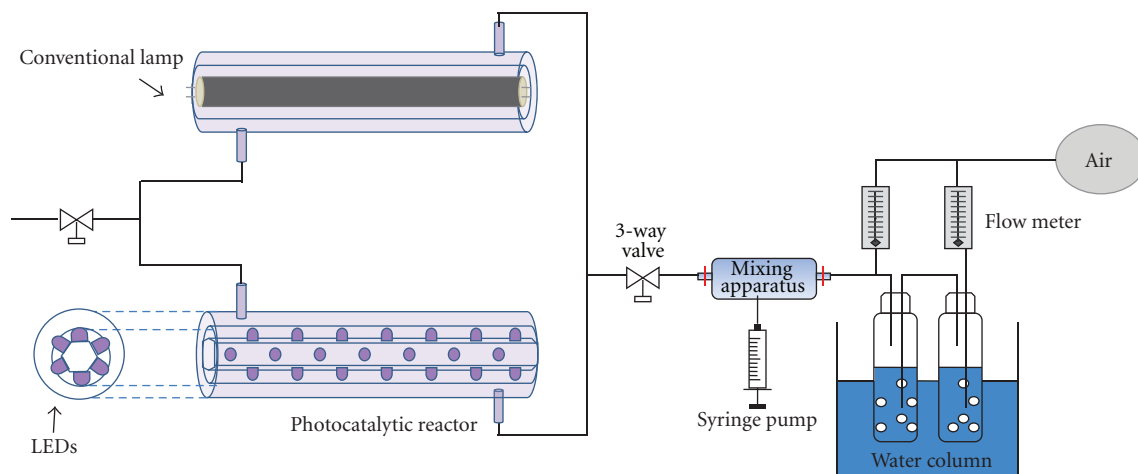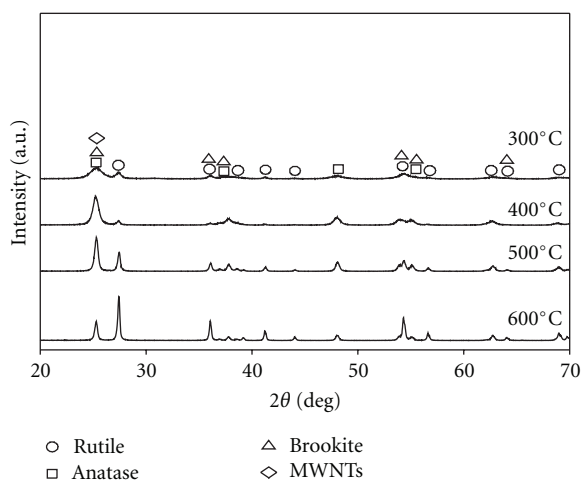
FIGURE 1: Schematic diagram of the experimental setup.

FIGURE 2: X-ray diffraction pattern of MWNT-TiO$_2$ at four different calcination temperatures (300, 400, 500, and 600°C).

to 1.0 or 4.0 L min^{-1}, giving a residence time of 7.2 and 1.8 s, respectively. The former FR was used to compare the decomposition efficiencies of the MWNT-TiO$_2$ composites irradiated using the two light-source types. The latter FR was used to examine the effects of the calcination temperature on the photocatalytic decomposition efficiency of the nanocomposites. The HD of the reactor was 10 mm.

Air measurements were performed by collecting air samples periodically at the inlet and outlet of the photocatalytic reactor and analyzing them by gas chromatography (GC, Hewlett-Packard 4890) or mass spectrometry (MS, Hewlett Packard MSD5973) coupled with a thermal desorption (TD, Donam TD-II) unit. Sampling was done by filling an evacuated Tedlar bag at a constant flow rate. The gas from this bag was then drawn through a 0.64 cm outside diameter and 18 cm long SS sorbent trap containing 0.4 g of Tenax TA using a constant flow-sampling pump (SKC Aircheck Sampler Model 224-PCXR8). The sampling time was varied from one to five min depending on the flow

rate. All samples were taken at room temperature. The gaseous species collected on the sorbent trap were analyzed by TD/GC installed with a flame ionization detector or GC/MS. The quality control program involved an analysis of the laboratory blank traps and spiked samples. At the beginning of the day, a laboratory blank trap was analyzed for contamination but no trap contamination was identified. A spiked external standard was also analyzed daily to check the quantitative response. The method detection limits ranged from 0.3 to 0.5 ppb for BTEX, depending on the compounds.

3. Results and Discussion

3.1. Properties of MWNT-Assisted TiO$_2$ Nanocomposites according to Calcination Temperature. The characteristics of the MWNT-assisted nanomaterials prepared at different calcination temperatures were investigated using a range of optical and analytical instruments. Figure 2 exhibits the XRD patterns of the MWNT-TiO$_2$ composites calcined at four different temperatures (300, 400, 500, and 600°C, for MWNT-TiO$_2$-300, MWNT-TiO$_2$-400, MWNT-TiO$_2$-500, and MWNT-TiO$_2$-600, resp.). The anatase content of the composites decreased with increasing calcination temperature and the rutile and brookite contents increased. This pattern is consistent with that reported by Wang et al. [15]. In addition, the peak at 25.3°2θ became broader with decreasing calcination temperature. The broad peaks obtained from both the MWNT-TiO$_2$-300 and MWNT-TiO$_2$-400 were assigned to overlap of the peak at 26.0°2θ, which was assigned to MWNTs [14], with the anatase peak at 25.3°2θ [29]. The sharp peaks at approximately 25.3°2θ for both MWNT-TiO$_2$-500 and MWNT-TiO$_2$-600 were attributed to the low thermal stability of MWNTs [25]. MWNTs and certain unidentified chemical species might have been destroyed during the calcination processes under such high-temperature conditions. This assertion was supported by TGA (Figure 3), in that there were no significant weight losses for the MWNT-TiO$_2$-500 and MWNT-TiO$_2$-600. Consequently, TiO$_2$ crystallites would be
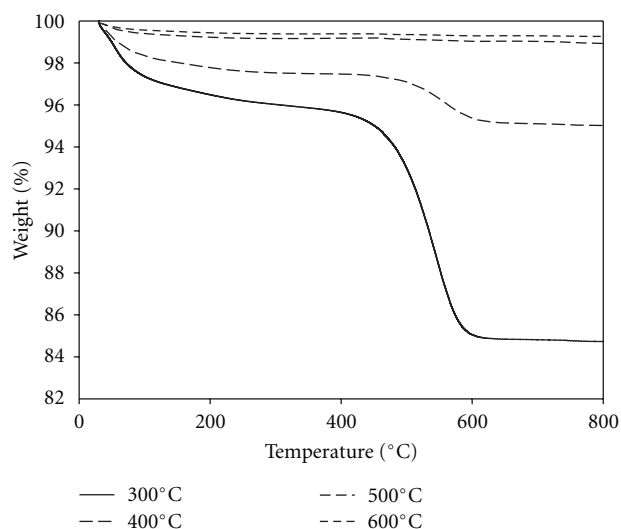
Figure 3: Thermogravimetric analysis of MWNT-TiO$_2$ at four different calcination temperatures (300, 400, 500, and 600°C).

the major component of these composites, resulting in sharp peaks at approximately 25.3°2θ.

Figure 3 also exhibits that for the MWNT-TiO$_2$-300 and MWNT-TiO$_2$-400, three-step weight losses were observed over the temperature range 20–800°C. An endothermic weight loss was observed between 20 and 500°C, which was attributed to the release of the residual TiO$_2$ precursor and organic solvent. A second sharper weight loss (11 and 2.4% for the MWNT-TiO$_2$-300 and MWNT-TiO$_2$-400, resp.) was observed between 500 and 600°C and attributed to the thermal decomposition of MWNTs and the crystallization of amorphous TiO$_2$ [14]. On the other hand, almost no weight loss was observed between 630 and 800°C, suggesting that TiO$_2$ became the major component at this temperature range.

Unlike the MWNT-TiO$_2$-300 and MWNT-TiO$_2$-400, SEM images revealed almost no MWNTs in MWNT-TiO$_2$-500 and MWNT-TiO$_2$-600 (Figure 4). This supports the assertion that MWNTs might have been destroyed during the calcination processes at high temperatures. In contrast, TiO$_2$ nanoparticles in MWNT-TiO$_2$-300 and MWNT-TiO$_2$-400 were bound intimately to the MWNT networks.

Figure 5 illustrates the XP spectra of the C 1s regions for the MWNT-TiO$_2$ composites calcined at four different temperatures. The spectra of the MWNT-TiO$_2$-300 and MWNT-TiO$_2$-400 yielded four peaks at 283.6, 284.5, 286.3, and 288.8 eV, which were assigned to graphitic carbon atoms (46 and 35% for MWNT-TiO$_2$-300 and MWNT-TiO$_2$-400, resp.), –C–O, –C=O, and –COO bonds, respectively. The –COO bond was likely formed by the oxidation of MWNT surfaces during the composite synthesis process [30]. On the other hand, for the MWNT-TiO$_2$-500 and MWNT-TiO$_2$-600, the corresponding peaks exhibited much lower intensities, were just trace, or were not shown. This again was attributed to the destruction of MWNTs and other

chemical species during the calcination processes at these high temperatures.

Pure MWNT and MWNT-TiO$_2$ powders calcined at different temperatures revealed different FTIR spectra (Figure 6). For both the pure and calcined nanocomposites, the main absorption peaks were located at 3440 and 1626 cm^{-1}, which were assigned to the O–H stretching vibration of hydroxyl groups and the O–H bending of surface adsorbed water, respectively [31]. For the calcined MWNT-TiO$_2$ powders, although their intensities differed according to the calcination temperature, other distinctive peaks were observed at low frequency bands <1,000 cm^{-1}. These peaks were assigned to the Ti–O–Ti vibration of the network [32], confirming the presence of TiO$_2$ in the calcined nanocomposites.

3.2. BTEX Decomposition Efficiencies via MWNT-TiO$_2$ Nanocomposites.

The as-prepared MWNT-TiO$_2$ nanomaterials were evaluated for the decomposition of gas-phase BTEX at an IAC level (0.1 ppm). Figure 7 illustrates the average photocatalytic decomposition efficiencies for BTEX determined using the MWNT-TiO$_2$ unit with two light sources (conventional 8-W black-light and blue LED lamps) under the FR condition of 1.0 L min^{-1}. Under similar operating conditions, the decomposition efficiencies determined using the conventional lamp/MWNT-TiO$_2$ unit were higher those of the conventional lamp/Degussa P25 TiO$_2$ unit, which were reported previously [33]. The mean efficiencies obtained from the conventional lamp/MWNT-TiO$_2$ unit were 95% for benzene and ~100% for the other target compounds (TEX). Jo and Yang [33] reported the mean degradation efficiencies for BTEX obtained from the conventional lamp/Degussa P25 TiO$_2$ unit of 56%, 76%, 92%, and 93%, respectively. Consequently, the MWNT-TiO$_2$ composite revealed superior performance in the photocatalytic decompositions of IAC-level toxic aromatic pollutants to the commercially available reference photocatalyst, Degussa P25 TiO$_2$. This was attributed to the combined electrical properties and adsorption capacity of the MWNT-TiO$_2$ composite. MWNTs have a large electron-storage capacity to store photon-excited electrons in MWNT-TiO$_2$ nanomaterials [25]. This electron-storage capacity would likely retard or hinder electron-hole recombination. In addition, at the interface of MWNT-TiO$_2$, electrons transfer from the TiO$_2$ with a higher than Fermi energy level to the MWNT with a lower Fermi energy level to adjust the Fermi energy levels [13]. This electron transfer can result in TiO$_2$ with an excess negative charge and MWNT with an excess positive charge. Thus, the MWNT would act as an electron sink. Consequently, the formation of this MWNT-TiO$_2$ junction would extend the recombination times of the photogenerated electron-hole pairs, thereby enhancing the photocatalytic activity of TiO$_2$. MWNTs also have high adsorption capacity with typical specific surface areas of 200−400 m^2 g^{-1} [25]. Therefore, MWNTs would assist the TiO$_2$ powders by concentrating the pollutants and intermediates around the powders followed by subsequent migration of these species to the surface of the photocatalyst

(a)

(b)

(c)

(d)
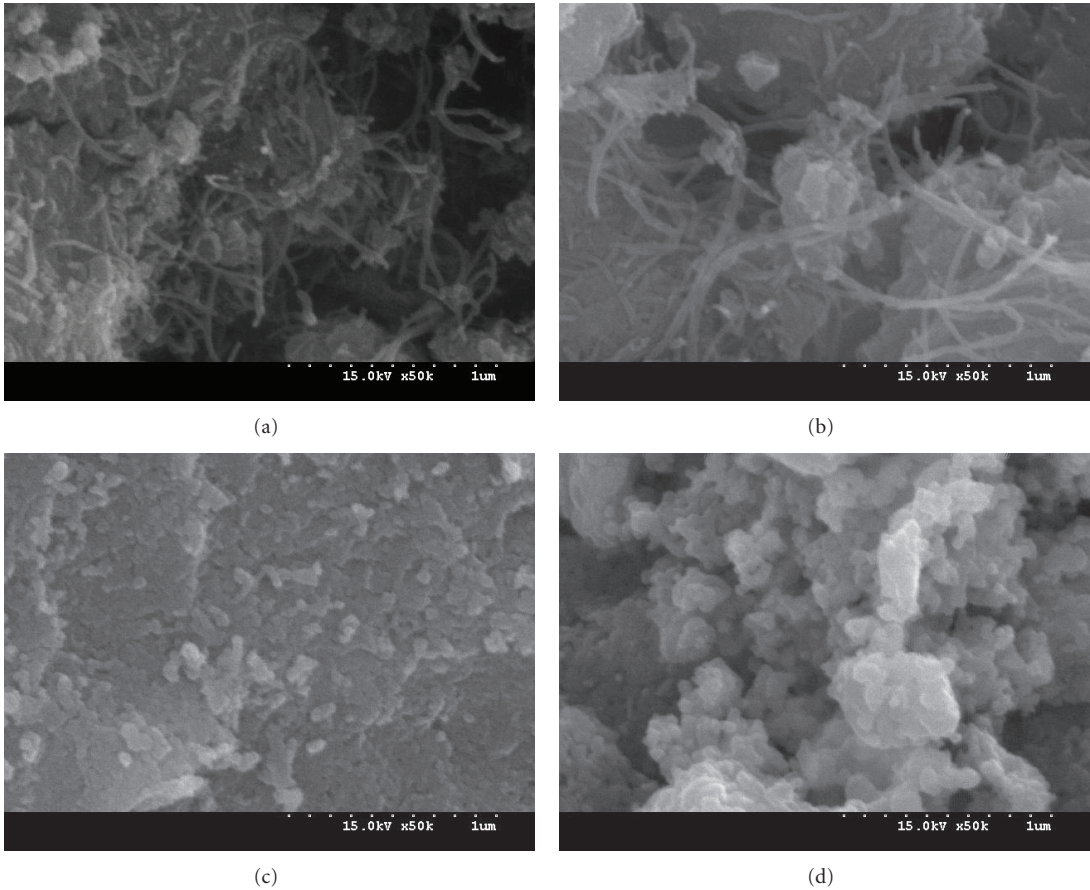
FIGURE 4: Scanning electron microscopy images of MWNT-TiO$_2$ at four different calcination temperatures (300, 400, 500, and 600°C).

(A) Graphite carbon   (C) C=O
(B) C–O   (D) COO

FIGURE 5: X-ray photoelectron spectra of MWNT-TiO$_2$ at four different calcination temperatures (300, 400, 500, and 600°C).

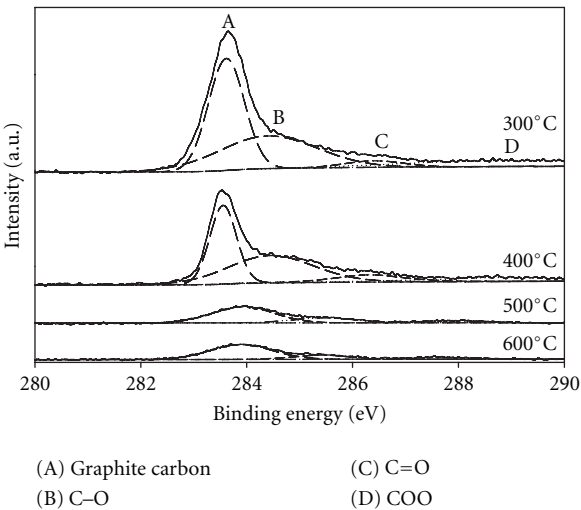FIGURE 6: Fourier transform infrared spectra of MWNT-TiO$_2$ at four different calcination temperatures (300, 400, 500, and 600°C).

via diffusion [34]. Adsorption in MWNTs would occur in the aggregated pores, inside the tube, or on the external walls [25].
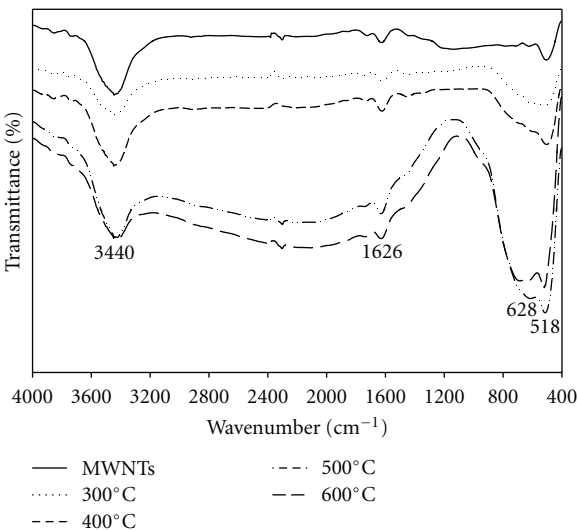
Figure 7 compares the decomposition performance of the MWNT-TiO$_2$ units using the conventional lamp with that using the blue LEDs. The decomposition efficiencies
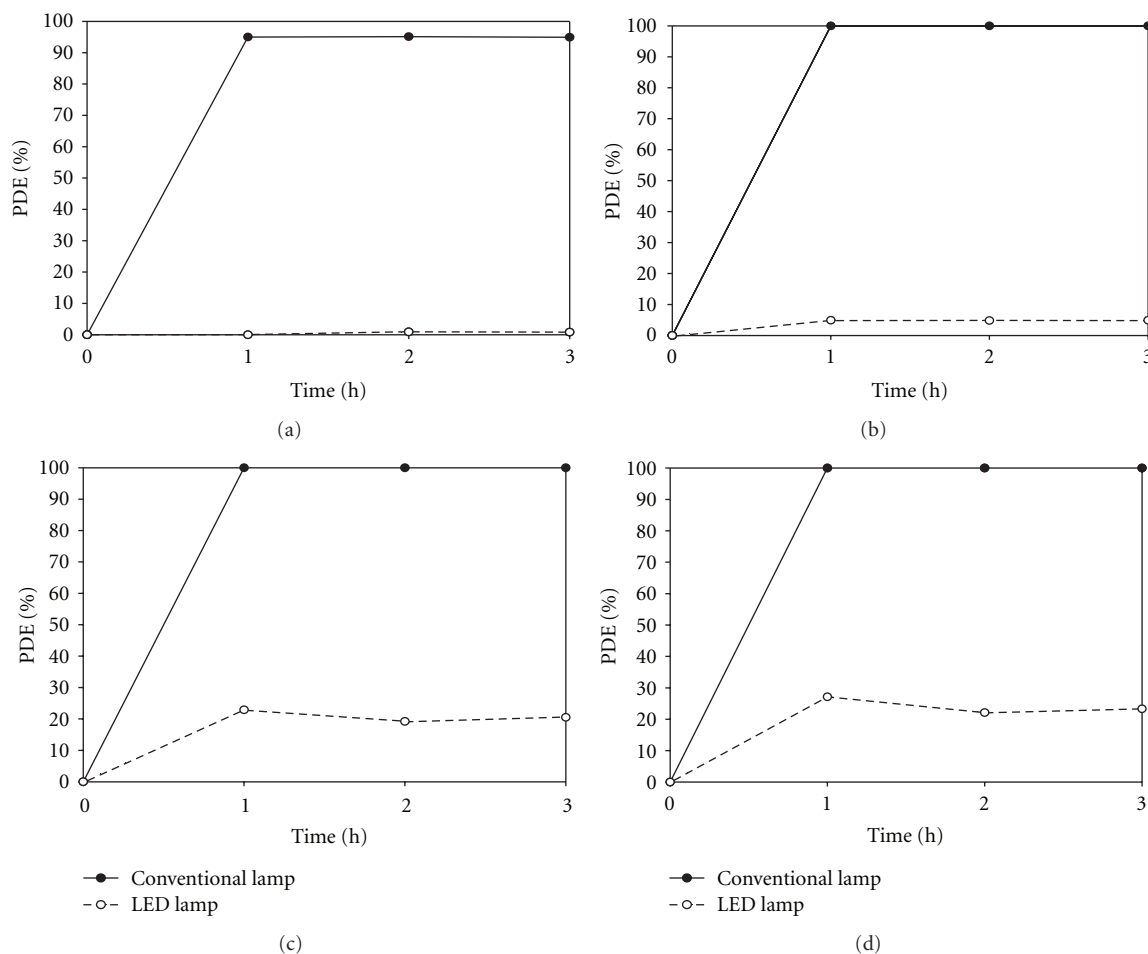
FIGURE 7: Time-series photocatalytic decomposition efficiencies determined via MWNT-TiO$_2$ irradiated using two light-source types (conventional 8-W black light lamp and blue-LEDs): benzene (a), toluene (b), ethyl benzene (c), and o-xylene (d).

for BTEX determined using the conventional lamp/MWNT-TiO$_2$ unit were higher than those of the blue LEDs/MWNT-TiO$_2$ unit. For the blue-LED/MWNT-TiO$_2$ unit, the average efficiencies for BTEX were approximately zero, 5, 23, and 28%, respectively. TiO$_2$ is a semiconductor photocatalyst with a band gap energy of 3.2 eV, meaning that only light with a wavelength ≤385 nm can overcome this barrier [35]. Since the conventional lamp and UV-LED exhibit the maximum light intensity at 352 and 380 nm, respectively, both light sources had sufficient energy to promote electrons from the valence band to the conduction band of TiO$_2$. In general, the activity of the photocatalyst depends strongly on the photon flux on the surface of the catalyst as well as the light irradiation (energy per unit area) [36, 37]. In the present study, the conventional lamp revealed higher light intensity (3.4 mW cm^{-2}) than that of the UV-LED (0.6 mW cm^{-2}). Therefore, the higher decomposition efficiency for the conventional lamp/MWNT-TiO$_2$ unit was attributed to the combined effects of the lower wavelength (higher energy) with higher light intensity.

Different calcination temperatures might yield different photocatalytic behaviors due to different morphological and electronic properties of MWNT-TiO$_2$ nanomaterials. Figure 8 represents the decomposition efficiencies as a function of the calcination temperature under the conditions of FR = 4.0 L min^{-1} and conventional UV lamp irradiation. For the target compounds, MWNT-TiO$_2$-300 and MWNT-TiO$_2$-400 showed similar decomposition efficiency. The mean efficiencies for BTEX by the MWNT-TiO$_2$-300 were 32, 70, 79, and 79%, respectively, whereas they were 33, 71, 78, and 78% for the MWNT-TiO$_2$-400, respectively. On the other hand, when the calcination temperature was increased to 500°C, the decomposition efficiencies decreased to close to zero for both benzene and toluene and to 42 and 44% for ethyl benzene and o-xylene, respectively. When the temperature was increased to 600°C, the decomposition efficiencies were all approximately zero. Higher photocatalytic activities obtained from the MWNT-TiO$_2$-300 and MWNT-TiO$_2$-400 were attributed to the combined effects of MWNTs and TiO$_2$ nanoparticles bound intimately to the MWNT networks, as
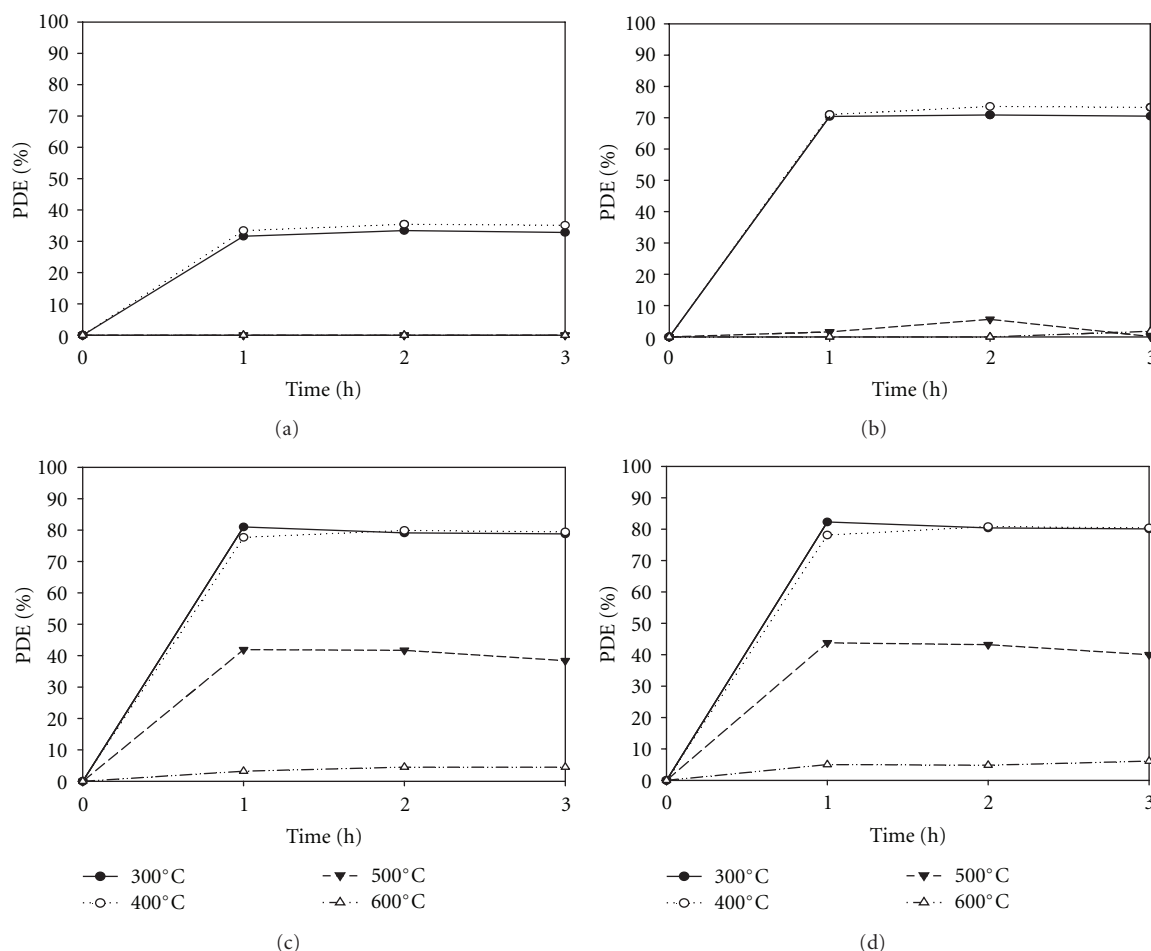
Figure 8: Time-series photocatalytic decomposition efficiencies (PDEs) determined via MWNT-TiO$_2$ according to the calcination temperatures: benzene (a), toluene (b), ethyl benzene (c), and o-xylene (d).

confirmed by the morphological and optical properties of the photocatalysts. This assertion is supported by that the carbon materials can accept photogenerated electrons and separate efficiently the charge carriers, thereby enhancing the photocatalytic activity [38–40].

4. Conclusions

This study investigated the feasibility of carbonaceous nanomaterial-assisted photocatalysts calcined at different temperatures for indoor air applications. The MWNT-TiO$_2$ composites calcined at different temperatures revealed different photocatalytic activities, morphologies, and surface properties. The optical and analytical results showed that for the composites calcined at low temperatures ($\leq 400°$C) TiO$_2$ nanoparticles were bound intimately to the MWNT networks. However, no MWNTs were observed when the calcination temperature was increased to higher values. Consistently, the MWNT-TiO$_2$ composites calcined at the low temperatures showed higher photocatalytic decomposition efficiencies for aromatic hydrocarbons at IAC levels than those calcined at high temperatures. Moreover, MWNT-TiO$_2$ exhibited superior photocatalytic performance for the decomposition efficiencies to Degussa P25 TiO$_2$ under conventional UV lamp irradiations, which was attributed to the combined electrical properties and adsorption capacity for the MWNT-TiO$_2$ composite. Overall, these carbonaceous nanomaterial-assisted photocatalysts can be applied effectively to indoor air applications, depending on the calcination temperature.

References

[1] Y. Lu, D. Wang, Y. Wu, C. Ma, X. Zhang, and C. Yang, "Synergistic effect of nanophotocatalysis and nonthermal plasma on the removal of indoor HCHO," *International Journal of Photoenergy*, vol. 2012, Article ID 354032, 8 pages, 2012.

[2] G. Wang, L. Xu, J. Zhang, T. Yin, and D. Han, "Enhanced photocatalytic activity of TiO$_2$ powders (P25) via calcination treatment," *International Journal of Photoenergy*, vol. 2012, Article ID 265760, 9 pages, 2012.

[3] G. Wang, B. Cheng, J. Zhang, L. Xu, and T. Yin, "Facile synthesis and photocatalytic property of titania/carbon composite hollow microspheres with bimodal mesoporous shells," *International Journal of Photoenergy*, vol. 2012, Article ID 976389, 9 pages, 2012.

[4] W. K. Jo and J. T. Kim, "Application of visible-light photocatalysis with nitrogen-doped or unmodified titanium dioxide for control of indoor-level volatile organic compounds," *Journal of Hazardous Materials*, vol. 164, no. 1, pp. 360–366, 2009.

[5] R. Vinu, S. Polisetti, and G. Madras, "Dye sensitized visible light degradation of phenolic compounds," *Chemical Engineering Journal*, vol. 165, no. 3, pp. 784–797, 2010.

[6] G. Yang, Z. Jiang, H. Shi et al., "Study on the photocatalysis of F-S co-doped TiO$_2$ prepared using solvothermal method," *Applied Catalysis B*, vol. 96, no. 3-4, pp. 458–465, 2010.

[7] R. Leary and A. Westwood, "Carbonaceous nanomaterials for the enhancement of TiO$_2$ photocatalysis," *Carbon*, vol. 49, no. 3, pp. 741–772, 2011.

[8] G. Veréb, Z. Ambrus, Z. Pap et al., "Comparative study on UV and visible light sensitive bare and doped titanium dioxide photocatalysts for the decomposition of environmental pollutants in water," *Applied Catalysis A*, vol. 417-418, pp. 26–36, 2012.

[9] W. Zhou, P. Zhang, and W. Liu, "Anatase TiO$_2$ nanospindle/activated carbon (ac) composite photocatalysts with enhanced activity in removal of organic contaminant," *International Journal of Photoenergy*, vol. 2012, Article ID 325902, 7 pages, 2012.

[10] S. Liu and X. Chen, "Preparation and characterization of a novel activated carbon-supported N-doped visible light response photocatalyst (TiO$_{2-x}$Ny/AC)," *Journal of Chemical Technology and Biotechnology*, vol. 82, no. 5, pp. 453–459, 2007.

[11] S.-Y. Ye, Q. M. Tian, X.-L. Song, and S.-C. Luo, "Photo-electrocatalytic degradation of ethylene by a combination of TiO$_2$ and activated carbon felts," *Journal of Photochemistry and Photobiology A*, vol. 208, no. 1, pp. 27–35, 2010.

[12] B. Ahmmad, Y. Kusumoto, S. Somekawa, and M. Ikeda, "Carbon nanotubes synergistically enhance photocatalytic activity of TiO$_2$," *Catalysis Communications*, vol. 9, no. 6, pp. 1410–1413, 2008.

[13] K. Woan, G. Pyrgiotakis, and W. Sigmund, "Photocatalytic carbon-nanotube-TiO$_2$ composites," *Advanced Materials*, vol. 21, no. 21, pp. 2233–2239, 2009.

[14] Q. Wang, D. Yang, D. Chen, Y. Wang, and Z. Jiang, "Synthesis of anatase titania-carbon nanotubes nanocomposites with enhanced photocatalytic activity through a nanocoating-hydrothermal process," *Journal of Nanoparticle Research*, vol. 9, no. 6, pp. 1087–1096, 2007.

[15] W. Wang, P. Serp, P. Kalck, and J. L. Faria, "Visible light photodegradation of phenol on MWNT-TiO$_2$ composite catalysts prepared by a modified sol-gel method," *Journal of Molecular Catalysis A*, vol. 235, no. 1-2, pp. 194–199, 2005.

[16] G. Hu, X. Meng, X. Feng, Y. Ding, S. Zhang, and M. Yang, "Anatase TiO$_2$ nanoparticles/carbon nanotubes nanofibers: preparation, characterization and photocatalytic properties," *Journal of Materials Science*, vol. 42, no. 17, pp. 7162–7170, 2007.

[17] Y. Yao, G. Li, S. Ciston, R. M. Lueptow, and K. A. Gray, "Photoreactive TiO$_2$/carbon nanotube composites: synthesis

and reactivity," *Environmental Science and Technology*, vol. 42, no. 13, pp. 4952–4957, 2008.

[18] C.-Y. Kuo, "Prevenient dye-degradation mechanisms using UV/TiO$_2$/carbon nanotubes process," *Journal of Hazardous Materials*, vol. 163, no. 1, pp. 239–244, 2009.

[19] W.-C. Oh, A.-R. Jung, and W.-B. Ko, "Characterization and relative photonic efficiencies of a new nanocarbon/TiO$_2$ composite photocatalyst designed for organic dye decomposition and bactericidal activity," *Materials Science and Engineering C*, vol. 29, no. 4, pp. 1338–1347, 2009.

[20] T. Matsumoto, N. Iyi, Y. Kaneko et al., "High visible-light photocatalytic activity of nitrogen-doped titania prepared from layered titania/isostearate nanocomposite," *Catalysis Today*, vol. 120, no. 2, pp. 226–232, 2007.

[21] K. Suriye, P. Praserthdam, and B. Jongsomjit, "Control of Ti^{3+} surface defect on TiO$_2$ nanocrystal using various calcination atmospheres as the first step for surface defect creation and its application in photocatalysis," *Applied Surface Science*, vol. 253, no. 8, pp. 3849–3855, 2007.

[22] M. A. Aramendía, V. Borau, J. C. Colmenares et al., "Modification of the photocatalytic activity of Pd/TiO$_2$ and Zn/TiO$_2$ systems through different oxidative and reductive calcination treatments," *Applied Catalysis B*, vol. 80, no. 1-2, pp. 88–97, 2008.

[23] A. Zaleska, E. Grabowska, J. W. Sobczak, M. Gazda, and J. Hupka, "Photocatalytic activity of boron-modified TiO$_2$ under visible light: the effect of boron content, calcination temperature and TiO$_2$ matrix," *Applied Catalysis B*, vol. 89, no. 3-4, pp. 469–475, 2009.

[24] A. Jia, X. Liang, Z. Su, T. Zhu, and S. Liu, "Synthesis and the effect of calcination temperature on the physical-chemical properties and photocatalytic activities of Ni,La codoped SrTiO3," *Journal of Hazardous Materials*, vol. 178, no. 1–3, pp. 233–242, 2010.

[25] P. Serp, M. Corrias, and P. Kalck, "Carbon nanotubes and nanofibers in catalysis," *Applied Catalysis A*, vol. 253, no. 2, pp. 337–358, 2003.

[26] C. S. Chen, Y. C. Hseu, S. H. Liang, J. Y. Kuo, and S. C. Chen, "Assessment of genotoxicity of methyl-tert-butyl ether, benzene, toluene, ethylbenzene, and xylene to human lymphocytes using comet assay," *Journal of Hazardous Materials*, vol. 153, no. 1-2, pp. 351–356, 2008.

[27] U. Schlink, A. Thiem, T. Kohajda, M. Richter, and K. Strebel, "Quantile regression of indoor air concentrations of volatile organic compounds (VOC)," *Science of the Total Environment*, vol. 408, no. 18, pp. 3840–3851, 2010.

[28] A. P. Xagas, E. Androulaki, A. Hiskia, and P. Falaras, "Preparation, fractal surface morphology and photocatalytic properties of TiO$_2$ films," *Thin Solid Films*, vol. 357, no. 2, pp. 173–178, 1999.

[29] W. K. Jo and J. T. Kim, "Decomposition of gas-phase aromatic hydrocarbons by applying an annular-type reactor coatedwith sulfur-doped photocatalyst under visible-light irradiation," *Journal of Chemical Technology and Biotechnology*, vol. 85, no. 4, pp. 485–492, 2010.

[30] C. Y. Yen, Y. F. Lin, C. H. Hung et al., "The effects of synthesis procedures on the morphology and photocatalytic activity of multi-walled carbon nanotubes/TiO$_2$ nanocomposites," *Nanotechnology*, vol. 19, no. 4, Article ID 045604, 2008.

[31] K. Dai, T. Peng, D. Ke, and B. Wei, "Photocatalytic hydrogen generation using a nanocomposite of multi-walled carbon

nanotubes and TiO$_2$ nanoparticles under visible light irradiation," *Nanotechnology*, vol. 20, no. 12, Article ID 125603, 2009.

[32] T. Peng, D. Zhao, K. Dai, W. Shi, and K. Hirao, "Synthesis of titanium dioxide nanoparticles with mesoporous anatase wall and high photocatalytic activity," *Journal of Physical Chemistry B*, vol. 109, no. 11, pp. 4947–4952, 2005.

[33] W. K. Jo and C. H. Yang, "Feasibility of a tandem photocatalytic oxidation-adsorption system for removal of monoaromatic compounds at concentrations in the sub-ppm-range," *Chemosphere*, vol. 77, no. 2, pp. 236–241, 2009.

[34] A. Y. Shan, T. I. M. Ghazi, and S. A. Rashid, "Immobilisation of titanium dioxide onto supporting materials in heterogeneous photocatalysis: a review," *Applied Catalysis A*, vol. 389, no. 1-2, pp. 1–8, 2010.

[35] U. I. Gaya and A. H. Abdullah, "Heterogeneous photocatalytic degradation of organic contaminants over titanium dioxide: a review of fundamentals, progress and problems," *Journal of Photochemistry and Photobiology C*, vol. 9, no. 1, pp. 1–12, 2008.

[36] W. Wang and Y. Ku, "Photocatalytic degradation of gaseous benzene in air streams by using an optical fiber photoreactor," *Journal of Photochemistry and Photobiology A*, vol. 159, no. 1, pp. 47–59, 2003.

[37] T. H. Lim and S. D. Kim, "Trichloroethylene degradation by photocatalysis in annular flow and annulus fluidized bed photoreactors," *Chemosphere*, vol. 54, no. 3, pp. 305–312, 2004.

[38] J. Yu, T. Ma, and S. Liu, "Enhanced photocatalytic activity of mesoporous TiO$_2$ aggregates by embedding carbon nanotubes as electron-transfer channel," *Physical Chemistry Chemical Physics*, vol. 13, no. 8, pp. 3491–3501, 2011.

[39] Q. Xiang, J. Yu, and M. Jaroniec, "Synergetic effect of MoS$_2$ and graphene as cocatalysts for enhanced photocatalytic H$_2$ production activity of TiO$_2$ nanoparticles," *Journal of the American Chemical Society*, vol. 134, pp. 6575–6578, 2012.

[40] J. Yu, B. Yang, and B. Cheng, "Noble-metal-free carbon nanotube-Cd$_{0.1}$Zn$_{0.9}$S composites for high visible-light photocatalytic H$_2$-production performance," *Nanoscale*, vol. 4, pp. 2670–2677, 2012.

Research Article

Impact of Preparative pH on the Morphology and Photocatalytic Activity of BiVO$_4$

Yongbiao Wan,[1,2] Sihong Wang,[3] Wenhao Luo,[1] and Lianhua Zhao[1]

[1] *Department of Chemistry, College of Science, Yanbian University, Jilin, Yanji 133002, China*
[2] *Xinxiang Institute of Occupational Disease Prevention and Control, Henan, Xinxiang 453000, China*
[3] *Analysis and Test Center, Yanbian University, Jilin, Yanji 133002, China*

Correspondence should be addressed to Lianhua Zhao, zhaolh1031@yahoo.com.cn

Adjusting pH with an ammonia solution during the synthesis, single-crystalline BiVO$_4$ has been prepared using Bi(NO$_3$)$_3 \cdot$5H$_2$O and NH$_4$VO$_3$ as starting materials through aqueous-phase precipitation at room temperature. The prepared samples are characterized by X-ray diffraction (XRD), diffuse reflectance spectroscopy (DRS), X-ray photoelectron spectroscopy (XPS), and scanning electron microscope (SEM). The impact of pH on structure, surface morphology, visible-light photocatalytic activity, and light absorption performance of BiVO$_4$ is explored and discussed. During the synthesis process, neither extremely acidic (low pH) nor basic (high pH) conditions are desirable for the formation of BiVO$_4$ in monoclinic phase. The highest photocatalytic performance on the degradation of a methylene blue solution is observed under pH $=$ 7.0 for BiVO$_4$ in monoclinic scheelite, which is attributed to its small grain size and marked surface oxygen evolution ability.

1. Introduction

Titanium dioxide and other semiconductor photocatalysts have been intensively studied for wide potential applications in water and air purification and solar energy conversion since Fujishima and Honda first reported the photocatalytic splitting of water on TiO$_2$ electrodes in 1972 [1–9]. Among the various oxide and nonoxide semiconductor photocatalysts, titanium dioxide has proven to be the most suitable for widespread environmental applications due to its chemical and biological inertness, very strong oxidizing properties, low cost-effectiveness, and long-term stability against photocorrosion and chemical corrosion [7, 8]. However, a large intrinsic band gap of TiO$_2$ (3.2 eV for anatase and 3.0 eV for rutile) allows only a small portion of the solar spectrum in the ultraviolet light region to be absorbed. Therefore, effective utilization of visible light has become one of the most difficult challenges in photocatalysis, and it is highly desirable to develop a photocatalyst that can use visible light in high efficiency under sunlight irradiation [6–9].

Bismuth vanadate (BiVO$_4$) has attracted more and more attention as visible-light-response photocatalyst [10–16]. According to previous reports, BiVO$_4$ appears in three main crystalline phases: monoclinic scheelite (s-m), tetragonal zircon (z-t), and tetragonal scheelite (s-t) [17–19]. Among these forms, BiVO$_4$ (s-m) presents strong visible-light catalytic properties [14–16], because the energy gap of BiVO$_4$ (s-m) is merely 2.41 eV, and the absorptive wavelength is 515 nm [14]. Therefore, a wide range of exciting light results in high catalytic activity. It is well known that the catalytic activity is influenced by many factors such as structure, crystallite dimension, and surface appearance [20–23]. Moreover, the activity is strongly connected to the preparation method and conditions of the catalyst.

BiVO$_4$ (s-m) is usually prepared through solid-state reaction at high temperature [24, 25]. Hydrothermal synthesis [13, 26–28], organometallic decomposition [29], and aqueous-phase precipitation [11, 12, 30, 31] have also been reported to obtain BiVO$_4$ (s-m). As discussed by Kudo and coworkers [11], it took a long time to prepare BiVO$_4$ with different structures through aqueous-phase precipitation

using particular starting materials (e.g., K_2V_5O and KV_3O_8) at room temperature. Utilizing $Bi(NO_3)_3$ and NH_4VO_3 as starting materials, Yu and coworkers obtained $BiVO_4$ (s-m) through calcination at 250°C [12], and they studied the correlation between the calcination temperature and crystalline phase in an ammonia solution. Furthermore, using the same starting materials, Ke and coworkers prepared $BiVO_4$ (s-m) through aqueous-phase precipitation mixed with carbamide at 364°C [30]. Utilizing $NaVO_3$ as the vanadium source, Gao and coworkers successfully prepared $BiVO_4$ (s-m) through aqueous-phase precipitation at 150°C [31].

$BiVO_4$ powders have also been synthesized through different templating routes. For example, Li and coworkers synthesized $BiVO_4$ (s-m) using mesoporous silica KIT-6 as a hard template [32]. Ke and coworkers selectively prepared $BiVO_4$ through a hydrothermal process using cetyltrimethyl-ammonium bromide as a template-directing agent [27]. However, the template-assisted route not only increases the cost but also makes it more difficult to scale up due to its complexity and the limited capability of a template. To our best knowledge, little has been reported on the synthesis of $BiVO_4$ (s-m) with various morphologies through regulating pH in convenient aqueous-phase precipitation, along with its visible-light photocatalytic activity. In this paper, utilizing aqueous-phase precipitation with $Bi(NO_3)_3 \cdot 5H_2O$ and NH_4VO_3 as starting materials, single-crystalline $BiVO_4$ (s-m) is successfully prepared. The impact of pH on structure, surface topography, visible-light photocatalytic activity, and light absorption performance of $BiVO_4$ (s-m) is investigated, and the results are discussed.

2. Experimental

2.1. Preparation of BiVO4. Equimolar amounts of NH_4VO_3 and $Bi(NO_3)_3 \cdot 5H_2O$ were dissolved consecutively into a nitric acid solution, and the mixture was kept stirring for 30 min. To the mixture was slowly added an NH_4VO_3 solution to give a uniform and transparent saffron yellow solution. An orange precipitate was obtained after the pH was adjusted by dropwise adding an ammonia solution under stirring. The precipitate was then filtered, rinsed with distilled water, and dried at 25, 80, or 110°C to give a final product.

2.2. Characterization. X-ray diffraction (XRD) patterns were measured on an X-ray diffractometer (Rigaku dmax/III-C) with Cu Ka radiation (tube voltage = 35 KV, tube current = 15 mA) in order to analyze the structure of $BiVO_4$. DRS patterns were obtained to appraise the light absorption performance of samples. Scanning electron microscope (SEM, HITACHI S-3500N) was used to observe the micromorphology. Absorbance for degradation of a methylene blue (MB) solution was measured on a UV-vis spectrophotometer (U-3010, Hitachi). X-ray photoelectron spectroscopy (XPS) patterns were measured using X-ray photoelectron spectroscopy (ESCALAB MK II) to analyze the surface components with Al Kα radiation, and all spectra
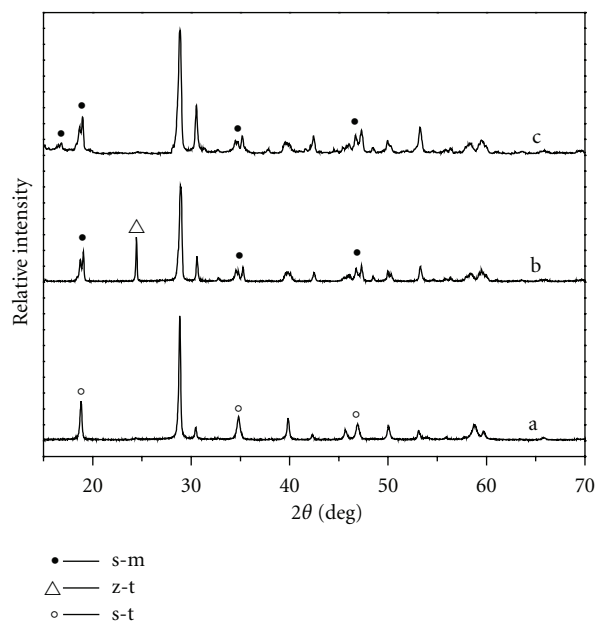
Figure 1: XRD patterns of samples at different temperature. (a): 25°C, (b): 80°C, (c): 110°C.

were referenced by setting the hydrocarbon C1s peak to 285.0 eV to compensate for residual charging effects.

2.3. Measurements of Photocatalytic Activity. Photocatalytic decomposition of a methylene blue (MB) solution was used to evaluate the photocatalytic properties of the synthesized materials. A photocatalyst powder (0.10 g) was dispersed in an MB solution (100 mL) in a reaction cell with a magnetic stirrer. A 300 W Xe-illuminator (light intensity = $3.5 \, \text{mW/cm}^2$) was used as a light source, and a cutoff filter ($\lambda > 420 \, \text{nm}$) was employed for visible-light irradiation in order to decolorate. At irradiation time intervals of 1 h, suspensions (4.0 mL) were collected and subsequently centrifuged to remove photocatalyst particles. A spectrophotometer was used to analyze the absorbance. Destruction rates were calculated with formula: $D = (C_0 - C)/C_0 \times 100\%$ (D: destruction rate; C_0: initial concentration; C: concentration in different batches).

3. Results and Discussion

3.1. Formation of BiVO4 with Different Crystal Phase. Although similar to the XRD pattern of $BiVO_4$ (s-t) due to the same scheelite structures, the XRD pattern of $BiVO_4$ (s-m) exhibits a weak diffraction peak at 15°. There are apparent splitting peaks at $2\theta = 18.5, 35,$ and $46°$, which are attributed to the Bi-O polyhedron in $BiVO_4$ (s-m) containing a $6s^2$ lone pair in Bi^{3+} [12].

Figure 1 shows XRD patterns of samples calcined at different temperatures. All the diffraction peaks of $BiVO_4$ fit well with the standard Joint Committee on Powder Diffraction Standards (JCPDS) card for $BiVO_4$ (s-t) (JCPDS

no. 75-2481, space group: I41/amd, unit cell parameters: $a = b = 5.147$ Å, $c = 11.721$ Å, $\beta = 90°$), and no other peaks from impurities are detected. The results suggest that BiVO$_4$ (s-t) can be successfully synthesized at room temperature (25°C), which is consistent with Kudo's et al. studies [11]. When the reaction temperature increases to 80°C, the diffraction peaks of the resulting powders can be indexed to BiVO$_4$ (z-t) (JCPDS no. 14-0133, space group: I41/amd, unit cell parameters: $a = b = 7.300$ Å, $c = 6.457$ Å, $\beta = 90°$) and BiVO$_4$ (s-m) (JCPDS no. 14-0688, space group: I2/amd, unit cell parameters: $a = 5.195$ Å, $b = 11.701$ Å, $c = 5.092$ Å, $\beta = 90.38°$). These findings indicate that the resulting powders are the mixtures of BiVO$_4$ (s-m) and BiVO$_4$ (s-t). As the treatment temperature increases to 110°C, BiVO$_4$ (s-m) is obtained.

In general, BiVO$_4$ (s-m) and BiVO$_4$ (s-t) are obtained at high temperatures. In this work, two different single-crystalline BiVO$_4$ (s-m) and BiVO$_4$ (s-t) are successfully prepared at low temperature. Moreover, the photocatalytic activity of BiVO$_4$ (s-m) is superior to that of BiVO$_4$ (s-t). To optimize the process conditions for BiVO$_4$ (s-m), the impact of different pH on the formation of crystalline BiVO$_4$ at 110°C is studied as shown in Figure 2.

3.2. Impact of Preparative pH on the Formation of BiVO$_4$. Figure 2 shows the XRD patterns of the samples prepared under different pH at 110°C. The peaks of the powders under pH = 1.0 and 10.0 can both be indexed to mixtures of BiVO$_4$ (z-t) and BiVO$_4$ (s-m) (JCPDS no. 14-0133 and no. 14-0688), while the samples under pH = 3.0, 5.0, and 7.0 are BiVO$_4$ (s-m) only. Therefore, BiVO$_4$ (s-m) can be selectively synthesized simply by adjusting pH. During the synthetic process, neither extreme acidic (low pH) nor basic (high pH) conditions are desirable to the formation of monoclinic phase.

The average particle size of the samples is calculated using the Scherrer equation [6],

$$D = \frac{K(\lambda \times (180°/\pi))}{\left(\sqrt{\beta^2 - S^2}\right)\cos\theta_\beta},\tag{1}$$

where D is the apparent crystallite mean size, perpendicular to the reflecting plane, K the shape factor (0.9 for spherical crystallite), λ the radiation wavelength (1.5406 A°), S the instrumental line broadening (0.001°), β the reflection width at half-maximum intensity (FWHM), and θ_β is the angle at the maximum intensity. The results are summarized in Table 1. Under extreme acidic (low pH, pH = 1.0) or basic (high pH, pH = 10.0) conditions, only BiVO$_4$ (z-t) is formed with a large particle size. The sample grain obtained in the presence of ammonia decreases gradually with an increasing amount of ammonia, and in the end it transforms into BiVO$_4$ (s-m).

According to Tokunaga's et al. view [14], although BiVO$_4$ (s-m) is thermodynamically more stable than BiVO$_4$ (z-t) at room temperature, the formation of BiVO$_4$ (z-t) seems to be favored kinetically with a sudden increase in pH by adding a base. BiVO$_4$ (z-t) with a large particle size shows no phase
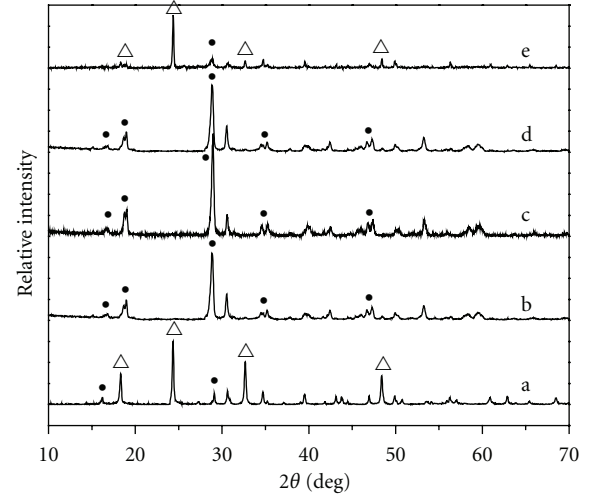
Figure 2: XRD patterns of samples under different pH. (△—tetragonal zircon type, •—monoclinic scheelite type). (a) pH = 1.0, (b) pH = 3.0, (c) pH = 5.0, (d) pH = 7.0, (e) pH = 10.0.

Table 1: Crystal size of samples different pH at 110°C.

Samples under different pH	pH = 1.0	pH = 3.0	pH = 5.0	pH = 7.0	pH = 10.0
Crystal size/nm	38.1	23.9	22.3	19.4	49.6

transform into the thermodynamically stable BiVO$_4$ (s-m) at room temperature. The particle size becomes smaller during the preparation after dissolution and recrystallization, and BiVO$_4$ (s-m) is finally formed after recrystallization and/or in the small particles, where the stress can be released.

3.3. Impact of Preparative pH on the Morphology of BiVO$_4$. Figure 3 shows SEM micrographs of BiVO$_4$ under different preparative pH at 110°C, with significant differences found in the morphology and particle shape. When the pH of the solution is approximately neutral, the particle size of the samples is 19.4 nm, while when the condition is extremely acidic or basic, the particle size becomes relatively larger. The results are consistent with Table 1. Obviously, the pH of the synthesis solution has a significant impact on the morphologies and particle size of the final products.

3.4. Impact of Preparative pH on the Optical Absorption Performance of BiVO$_4$. Figure 4 presents the DRS spectra of BiVO$_4$ prepared under different pH at 110°C. Although there are some differences in the absorption band of BiVO$_4$ under different preparative pH, all absorption bands are found in the visible range. Samples prepared under extremely acidic (pH = 1.0) or basic (pH = 10.0) conditions exhibit blue-shift in the spectra when compared with those under pH = 3.0, 5.0, and 7.0, and the optical absorption performance of the former is weaker than that of the latter. The absorption band in the visible-light region is attributed to the band transition from a Bi$_{6s}$ and O$_{2p}$ valence band to a V$_{3d}$ conduction band [29]. If an absorption band is different, both the relevant

(a)   (b)   (c)

(d)   (e)
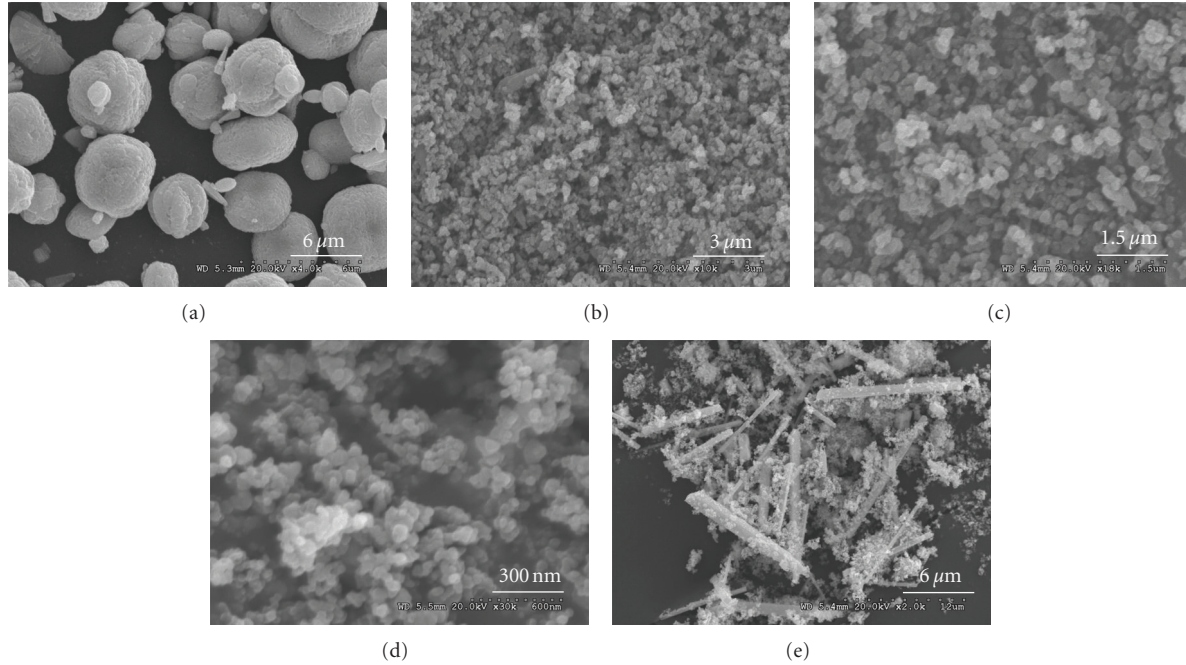
Figure 3: SEM images of BiVO$_4$ under different pH at 110°C. (a) pH = 1.0, (b) pH = 3.0, (c) pH = 5.0, (d) pH = 7.0, (e) pH = 10.0.
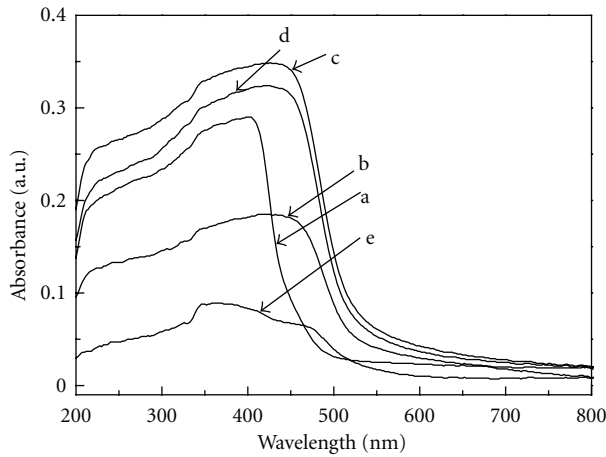
Figure 4: DRS spectra of samples under different pH at 110°C. (a) pH = 1.0, (b) pH = 3.0, (c) pH = 5.0, (d) pH = 7.0, (e) pH = 10.0.
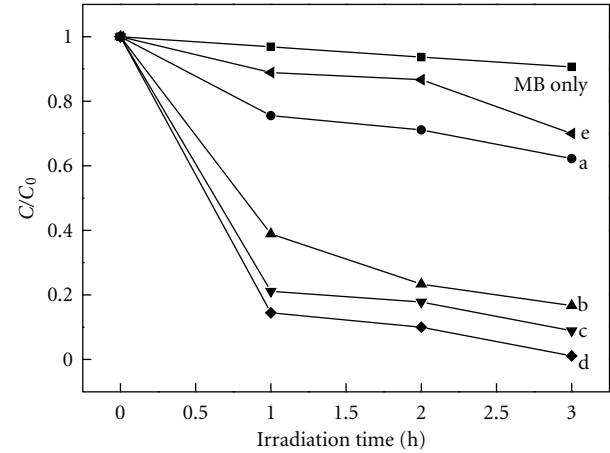
Figure 5: Photocatalytic activities of samples under different pH at 110°C. (a) pH = 1.0, (b) pH = 3.0, (c) pH = 5.0, (d) pH = 7.0, (e) pH = 10.0.

conduction and valence band energy level are also difference. The band gap (E_g, eV) is calculated using the equation $E_g = 1240/\lambda$, where λ is the wavelength of the absorption bands. The band gap of BiVO$_4$ (z-t) is slightly wider than that of BiVO$_4$ (s-m). If the BiVO$_4$ (s-m) content is low and its band gap is relatively wide, the absorption band will be blue-shifted. According to the DRS spectra, low BiVO$_4$ (s-m) contents are obtained under extremely acidic (pH = 1.0) or basic (pH = 10.0) conditions, while under pH = 3.0, 5.0, and 7.0, only BiVO$_4$ (s-m) is formed. This is consistent with the XRD results. The low optical absorption performance of the samples under extremely acidic (pH = 1.0) or basic (pH = 10.0) conditions may be attributed to their weak crystallinity.

3.5. Impact of Preparative pH on the Photocatalytic Activity of BiVO$_4$.

The photocatalytic activities of BiVO$_4$ are measured on the degradation of an MB solution in a liquid medium under a visible-light irradiation. Figure 5 presents the MB concentration (C/C_0) in a function of the irradiation time over samples under different preparative pH at 110°C. As shown in Figure 5, the photocatalytic activity of BiVO$_4$ (s-m) is generally higher than the mixtures of BiVO$_4$ (z-t) and BiVO$_4$ (s-m). Especially, the decoloration rate of MB over the sample under pH = 7.0 is 98.9% after 3 h of irradiation, and the sample also exhibits the highest photocatalytic activity. The decoloration rates are 91.2% and 84.0% over

(a)

(b)

(c)

FIGURE 6: XPS spectra of BiVO$_4$ (s-m) under different pH. (a) pH = 3.0, (b) pH = 5.0, (c) pH = 7.0.

the samples under pH = 5.0 and 3.0, respectively. However, the photocatalytic activities of the samples under pH = 1.0 and 10.0 are both low, whose decoloration rates are 38.0% and 30.0%, respectively.

It is widely believed that the photocatalytic activity is directly affected by the particle size of a catalyst. The smaller the particle size is, the larger the specific surface area becomes. The different particle size in Table 1 also explains the order for the phot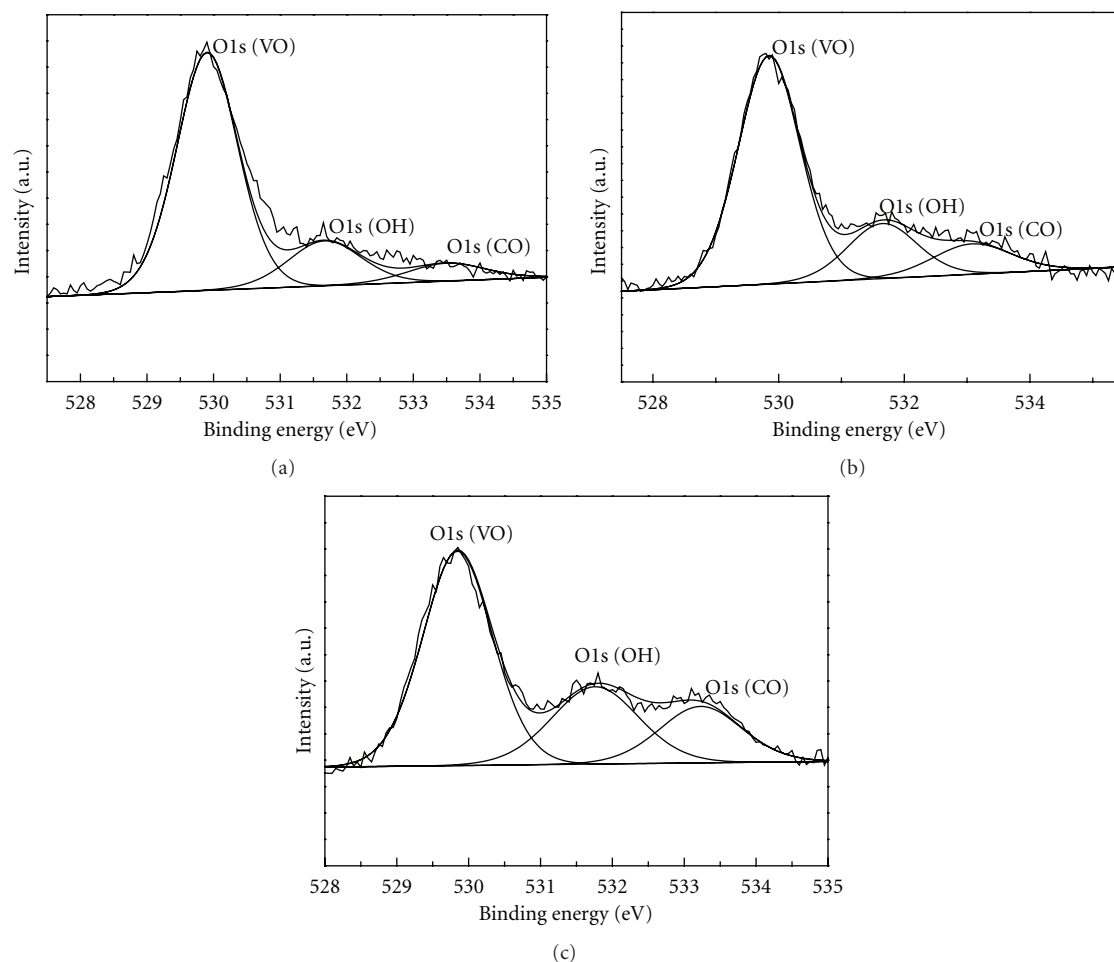ocatalytic activity of the samples under different pH. The average grain size of the sample under pH = 7.0 is the smallest, which possesses the highest photocatalytic activity.

3.6. X-Ray Photoelectron Spectroscopy Analysis. In order to explore the surface adsorption of OH$^-$ on the catalyst surface, XPS analysis was performed. The XPS spectra of BiVO$_4$ (s-m) under different pH are shown in Figure 6. The three fitting peaks of O1s are from lattice oxygen (VO), adsorbed oxygen (OH, binding energy: 532 eV), and carbon oxygen (CO, binding energy: 553 eV). A C–O bond is formed from carbon impurities in the air and adsorbed oxygen on the surface of catalyst. The percentages of the fitting peak

area on the lattice oxygen (VO), adsorbed oxygen (OH), and carbon oxygen (CO) are summarized in Table 2.

Table 2 summaries the results of the curve-fitting of the high resolution XPS spectra of BiVO$_4$ (s-m) for the O1s region under different pH. With an increasing pH, the relative content of adsorbed oxygen increases gradually. Photocatalytic reactions are usually caused by photoelectrons and holes separated, which can provide highly active OH$^\bullet$ [33]. A strong oxide free radical, OH$^\bullet$, has no selectivity toward oxidizing certain organic compounds. Therefore, the better separation between photoelectron and hole attribute to the higher surface adsorbed oxygen contents. Sequentially, the quantum efficiency of the catalyst is enhanced. Usually, adsorbed oxygen and carbon oxygen reflect the surface adsorption ability of a photocatalyst. The surface-adsorbed oxygen content of the sample under pH = 7.0 is the highest (25.57% + 17.61%), so it exhibits a high photocatalytic activity.

4. Conclusions

Single-crystalline BiVO$_4$ (s-m) has been synthesized through aqueous-phase precipitation at pH ranging from 3.0 to

TABLE 2: Binding energy and area percentage of BiVO$_4$ (s-m) for the O1s region under different pH.

Samples	Bonding energy/eV (ri/%)		
	O1s (VO)	O1s (OH)	O1s (CO)
pH = 3.0	529.90 (75.76%)	531.67 (16.67%)	533.50 (7.58%)
pH = 5.0	529.85 (69.44%)	531.65 (18.75%)	533.08 (11.82%)
pH = 7.0	529.85 (56.82%)	531.76 (25.57%)	533.23 (17.61%)

ri/%: area percentage of O1s fitting peaks.

7.0 regulated with an ammonia solution. The morphology, surface texture, and grain size of the synthesized BiVO$_4$ are significantly dependent on the preparative pH. Under pH = 1.0 and 10.0 conditions, mixtures of BiVO$_4$ (s-t) and BiVO$_4$ (s-m) are obtained, while under pH = 3.0–7.0, only BiVO$_4$ (s-m) is prepared. Therefore, BiVO$_4$ (s-m) can be selectively synthesized simply by adjusting the preparative pH. The band gap of BiVO$_4$ (s-m) is 2.4 eV when it is prepared under pH = 5.0 and 7.0.

The overlap between the Bi$_{6s}$ and O$_{2p}$ orbitals in the valence band results in an increase in hole mobility. Both the surface oxygen evolution ability and grain size have significant impacts on the photocatalytic performance for the degradation of a methylene blue solution under a visible-light irradiation.

Acknowledgment

References

[1] A. Fujishima and K. Honda, "Electrochemical photolysis of water at a semiconductor electrode," *Nature*, vol. 238, no. 5358, pp. 37–38, 1972.

[2] M. R. Hoffmann, S. T. Martin, W. Choi, and D. W. Bahnemann, "Environmental applications of semiconductor photocatalysis," *Chemical Reviews*, vol. 95, no. 1, pp. 69–96, 1995.

[3] Q. Xiang, J. Yu, and M. Jaroniec, "Graphene-based semiconductor photocatalysts," *Chemical Society Reviews*, vol. 41, no. 2, pp. 782–796, 2012.

[4] Q. Li, B. Guo, J. Yu et al., "Highly efficient visible-light-driven photocatalytic hydrogen production of CdS-cluster-decorated graphene nanosheets," *Journal of the American Chemical Society*, vol. 133, no. 28, pp. 10878–10884, 2011.

[5] J. Zhang, J. Yu, Y. Zhang, Q. Li, and J. R. Gong, "Visible light photocatalytic H$_2$-production activity of CuS/ZnS porous nanosheets based on photoinduced interfacial charge transfer," *Nano Letters*, vol. 11, no. 11, pp. 4774–4779, 2011.

[6] B. D. Cullity, *Elements of X-Ray Diffraction*, Addison-Wesley, San Francisco, Calif, USA, 1978.

[7] S. Liu, J. Yu, and M. Jaroniec, "Anatase TiO$_2$ with dominant high-energy {001} facets: synthesis, properties, and applications," *Chemistry of Materials*, vol. 23, no. 18, pp. 4085–4093, 2011.

[8] A. Kubacka, M. Fernández-García, and G. Colón, "Advanced nanoarchitectures for solar photocatalytic applications," *Chemical Reviews*, vol. 112, no. 3, pp. 1555–1614, 2012.

[9] M. Romero, J. Blanco, B. Sánchez et al., "Solar photocatalytic degradation of water and air pollutants: challenges and perspectives," *Solar Energy*, vol. 66, no. 2, pp. 169–182, 1999.

[10] X. Zhang, Z. Ai, F. Jia, L. Zhang, X. Fan, and Z. Zou, "Selective synthesis and visible-light photocatalytic activities of BiVO$_4$ with different crystalline phases," *Materials Chemistry and Physics*, vol. 103, no. 1, pp. 162–167, 2007.

[11] A. Kudo, K. Omori, and H. Kato, "A novel aqueous process for preparation of crystal form-controlled and highly crystalline BiVO$_4$ powder from layered vanadates at room temperature and its photocatalytic and photophysical properties," *Journal of the American Chemical Society*, vol. 121, no. 49, pp. 11459–11467, 1999.

[12] J. Yu, Y. Zhang, and A. Kudo, "Synthesis and photocatalytic performances of BiVO$_4$ by ammonia co-precipitation process," *Journal of Solid State Chemistry*, vol. 182, no. 2, pp. 223–228, 2009.

[13] J. Yu and A. Kudo, "Effects of structural variation on the photocatalytic performance of hydrothermally synthesized BiVO$_4$," *Advanced Functional Materials*, vol. 16, no. 16, pp. 2163–2169, 2006.

[14] S. Tokunaga, H. Kato, and A. Kudo, "Selective preparation of monoclinic and tetragonal BiVO$_4$ with scheelite structure and their photocatalytic properties," *Chemistry of Materials*, vol. 13, no. 12, pp. 4624–4628, 2001.

[15] S. Kohtani, J. Hiro, N. Yamamoto, A. Kudo, K. Tokumura, and R. Nakagaki, "Adsorptive and photocatalytic properties of Ag-loaded BiVO$_4$ on the degradation of 4-n-alkylphenols under visible light irradiation," *Catalysis Communications*, vol. 6, no. 3, pp. 185–189, 2005.

[16] S. Kohtani, M. Koshiko, A. Kudo et al., "Photodegradation of 4-alkylphenols using BiVO$_4$ photocatalyst under irradiation with visible light from a solar simulator," *Applied Catalysis B*, vol. 46, no. 3, pp. 573–586, 2003.

[17] J. D. Bierlein and A. W. Sleight, "Ferroelasticity in BiVO$_4$," *Solid State Communications*, vol. 16, no. 1, pp. 69–70, 1975.

[18] L. Hoffart, U. Heider, R. A. Huggins, W. Witschel, R. Jooss, and A. Lentz, "Crystal growth and conductivity investigations on BiVO$_4$ single crystals," *Ionics*, vol. 2, no. 1, pp. 34–38, 1996.

[19] L. Zhou, W. Wang, L. Zhang, H. Xu, and W. Zhu, "Single-crystalline BiVO$_4$ microtubes with square cross-sections: microstructure, growth mechanism, and photocatalytic property," *Journal of Physical Chemistry C*, vol. 111, no. 37, pp. 13659–13664, 2007.

[20] P. Madhusudan, J. Ran, J. Zhang, J. Yu, and G. Liu, "Novel urea assisted hydrothermal synthesis of hierarchical BiVO$_4$/Bi$_2$O$_2$CO$_3$ nanocomposites with enhanced visible-light photocatalytic activity," *Applied Catalysis B*, vol. 110, pp. 286–295, 2011.

[21] P. B. Avakyan, M. D. Nersesyan, and A. G. Merzhanov, "New materials for electronic engineering," *American Ceramic Society Bulletin*, vol. 75, no. 2, pp. 50–55, 1996.

[22] P. Shuk, H. D. Wiemhöfer, U. Guth, W. Göpel, and M. Greenblatt, "Oxide ion conducting solid electrolytes based on Bi$_2$O$_3$," *Solid State Ionics*, vol. 89, no. 3-4, pp. 179–196, 1996.

[23] K. Shantha and K. B. R. Varma, "Preparation and characterization of nanocrystalline powders of bismuth vanadate," *Materials Science and Engineering B*, vol. 60, no. 1, pp. 66–75, 1999.

[24] A. W. Sleight, H. Y. Chen, A. Ferretti, and D. E. Cox, "Crystal growth and structure of BiVO$_4$," *Materials Research Bulletin*, vol. 14, no. 12, pp. 1571–1581, 1979.

[25] A. R. Lim, S. H. Choh, and M. S. Jang, "Prominent ferroelastic domain walls in BiVO$_4$ crystal," *Journal of Physics: Condensed Matter*, vol. 7, no. 37, pp. 7309–7323, 1995.

[26] T. Yang, D. Xia, G. Chen, and Y. Chen, "Influence of the surfactant and temperature on the morphology and physico-chemical properties of hydrothermally synthesized composite oxide BiVO$_4$," *Materials Chemistry and Physics*, vol. 114, no. 1, pp. 69–72, 2009.

[27] D. Ke, T. Peng, L. Ma, P. Cai, and K. Dai, "Effects of hydro-thermal temperature on the microstructures of BiVO$_4$ and its photocatalytic O$_2$ evolution activity under visible light," *Inorganic Chemistry*, vol. 48, no. 11, pp. 4685–4691, 2009.

[28] B. Cheng, W. Wang, L. Shi, J. Zhang, J. Ran, and H. Yu, "One-pot template-free hydrothermal synthesis of monoclinic BiVO$_4$ hollow microspheres and their enhanced visible-light photocatalytic activity," *International Journal of Photoenergy*, vol. 2012, Article ID 797968, 10 pages, 2012.

[29] K. Sayama, A. Nomura, Z. Zou, R. Abe, Y. Abe, and H. Arakawa, "Photoelectrochemical decomposition of water on nanocrystalline BiVO$_4$ film electrodes under visible light," *Chemical Communications*, vol. 9, no. 23, pp. 2908–2909, 2003.

[30] D. Ke, T. Peng, L. Ma, P. Cai, and P. Jiang, "Photocatalytic water splitting for O$_2$ production under visible-light irradi-ation on BiVO$_4$ nanoparticles in different sacrificial reagent solutions," *Applied Catalysis A*, vol. 350, no. 1, pp. 111–117, 2008.

[31] S. M. Gao, Q. A. Qiao, P. P. Zhao et al., "Synthesis of different morphologies and structures of nano-sized BiVO$_4$ by precip-itation method," *Chinese Journal of Inorganic Chemistry*, vol. 23, no. 7, pp. 1153–1159, 2007.

[32] G. Li, D. Zhang, and J. C. Yu, "Ordered mesoporous BiVO$_4$ through nanocasting: a superior visible light-driven photocat-alyst," *Chemistry of Materials*, vol. 20, no. 12, pp. 3983–3992, 2008.

[33] B. Ohtani, Y. Okugawa, S. I. Nishimoto, and T. Kagiya, "Pho-tocatalytic activity of TiO$_2$ powders suspended in aqueous silver nitrate solution. Correlation with pH-dependent surface structures," *Journal of Physical Chemistry*, vol. 91, no. 13, pp. 3550–3555, 1987.

Research Article

Synthesis and Characterization of CeO$_2$-SiO$_2$ Nanoparticles by Microwave-Assisted Irradiation Method for Photocatalytic Oxidation of Methylene Blue Dye

R. M. Mohamed[1, 2] and E. S. Aazam[1]

[1] *Chemistry Department, Faculty of Science, King Abdulaziz University, P.O. Box 80203, Jeddah 21589, Saudi Arabia*
[2] *Advanced Materials Department, Central Metallurgical Resarch and Devolpment Institute CMRDI, P.O. Box 8742, Helwan 11421, Egypt*

Correspondence should be addressed to R. M. Mohamed, redama123@yahoo.com

CeO$_2$-SiO$_2$ nanoparticles were synthesized for the first time by a facile microwave-assisted irradiation process. The effect of irradiation time of microwave was studied. The materials were characterized by N_2 adsorption, XRD, UV-vis/DR, and TEM. All solids showed mesoporous textures with high surface areas, relatively small pore size diameters, and large pore volume. The X-ray diffraction results indicated that the as-synthesized nanoparticles exhibited cubic CeO$_2$ without impurities and amorphous silica. The transmission electron microscopy (TEM) images revealed that the particle size of CeO$_2$-SiO$_2$ nanoparticles, which were prepared by microwave method for 30 min irradiation times, was around 8 nm. The photocatalytic activities were evaluated by the decomposition of methylene blue dye under UV light irradiations. The results showed that the irradiation under the microwave produced CeO$_2$-SiO$_2$ nanoparticles, which have the best crystallinity under a shorter irradiation time. This indicates that the introduction of the microwave really can save energy and time with faster kinetics of crystallization. The sample prepared by 30 min microwave irradiation time exhibited the highest photocatalytic activity. The photocatalytic activity of CeO$_2$-SiO$_2$ nanoparticles, which were prepared by 30 min irradiation times was found to have better performance than commercial reference P25.

1. Introduction

Dye pollutants from textile papers and other industries are important sources of environmental contamination. Conventional treatment of such wastewater generally involves coagulation/flocculation [1, 2], electrocoagulation [3], coagulation/carbon adsorption process [4], and so on. These methods, however, merely transfer dyes from the liquid phase to the solid phase, requiring further treatment and causing secondary pollution [5]. Photocatalytic degradation of them continues to attract interest as a method to mitigate their impact on the environment. When photocatalyst is excited, it produces photogenerated holes in the valence band and the photogenerated electrons in the conduction band. Photogenerated holes have strong oxidation power, which are widely studied for environmental cleaning [6–10].

One important application of photocatalyst in environment cleaning is degradation of organic pollutants in waste water, especially those from the textile and the photographic industries. The photocatalysis technology has several advantages over other processes, such as cost-effectiveness, the use of ultraviolet (UV), near-UV or solar light as energy source, no addition of other chemicals, the operation at near room temperature, the capability of efficiently mineralizing most organic compounds, and the simple implementation with other conventional technologies to form a hybrid system [11]. Among these catalysts, TiO$_2$ has been proved to be a competent photocatalyst for environmental applications because of its strong oxidizing ability, nontoxicity, and long-term stability [6–10]. However, TiO$_2$ with a band gap of 3.0–3.2 eV can be photoexcited under irradiation of UV light ($\lambda < 395$ nm), which is only about 2–4% of sunlight [12].

TABLE 1: The calculated average crystallite sizes of CeO_2-SiO_2 samples.

Sample	Average crystallite sizes (nm)
M-30 min	8
M-60 min	10
M-90 min	11
M-120 min	12
M-180 min	14
H-24 h	15
P_{25}	25

Therefore, considerable effort has been made to increase the absorption of TiO_2 in the visible region to improve its visible light response through various surface modifications such as doping of various metal or metal oxides [13–17].

Dyes such as methylene blue (MB) are the main organic pollutants from dyeing and printing, textile industries, paper and ink manufacturing industries, cosmetics, pharmaceuticals, denim industries, food industries, and so on [18]. Methylene blue (MB), a common organic dye, was selected as a target compound because MB is ubiquitously used and the removal of the dye from wastewaters has been an acute problem [19]. Li et al. found that, during liquid-phase photocatalytic degradation of MB under visible light irradiation (>420 nm), the as-prepared S-doped TiO_2 exhibited much higher activity than pure TiO_2 [20].

We know that a rare-earth oxide such as CeO_2 has been applied widely in many fields. The applications of ceria are in solid oxide fuel cells, oxygen gas sensors, fluorescent materials, acting as the three-way catalysts in vehicle emission control systems, ultraviolet blocking materials, gates for metal-oxide semiconductor devices and phosphors, and so forth [21–24]. Furthermore, nanocrystalline CeO_2-based materials not only benefit from those applications, but also possess some unique properties, including lattice expansion [25], transition from boundary diffusion to lattice diffusion [26], and blue shift in ultraviolet absorption spectra [27]. Therefore, it is of critical importance to regulate the size and shape to explore its novel applications and properties. Up to now, big efforts have been devoted to the chemical synthesis of CeO_2 nanomaterials with various morphologies and sizes, such as porous structures, films, nanoparticles, and so forth [28–44]. The development of efficient methods to synthesize nanostructures with well-defined size and shape is one of the key trends in material chemistry because of their size/shape-dependent properties and potential applications. In the past few years, some effective methods have been developed to prepare monodispersed CeO_2 with different shapes. For example, nanocubes were prepared by a two-step precipitation method using oleic acid as a capping agent [45], nanopolyhedrals and nanocubes were synthesized via the decanoic acid-assisted supercritical hydrothermal process at 400°C [46], and nanopolyhedrons were obtained by the thermolysis reaction of cerium benzoylacetonate complex in oleic acid/oleylamine solvents under vacuum condition at 310–330°C [47]. However, the above methods required complicated procedure, special equipments, or organometallic

precursor. So it still remains a great challenge to fabricate ceria nanocrystals with uniform size and well-defined crystal shape by a simple and economical method. Here in this study, we report the synthesis of nanocrystalline CeO_2-SiO_2 by a microwave-assisted irradiation process for the first time. The synthesized nanocrystalline CeO_2-SiO_2 samples were characterized by X-ray diffraction (XRD) technique, Brunauer-Emmett-Teller (BET) surface measurements, transmission electron microscopy (TEM), and UV-vis diffuse reflectance spectra (UV-vis DRS). The photocatalytic activities of CeO_2-SiO_2 were investigated by the degradation of methylene blue dye under the irradiations of UV light.

2. Experimental

The dye under investigation, namely, methylene blue (MB), with a labeled purity of more than 90% was obtained from Sigma-Aldrich and used as received. Deionized water was used to make the dye solutions of desired concentration.

2.1. Catalyst Preparation and Characterization. All chemicals were of reagent grade without further purification. Ce-Si binary oxide was synthesized by a microwave method according to the following procedure: 1.4 g hexadecyltrimethylammonium bromide (CTAB) was added gradually to 10 g tetraethyl orthosilicate (TEOS, Aldrich) solution and the mixture was stirred at 60°C for 10 min till the CTAB was completely dissolved. 2.5 g of hexahydrated cerium nitrate ($Ce(NO_3)_3$-$6H_2O$, Alfa Aesar) dissolved in ethanol (18.0 g) was subsequently added to the mixture of CTAB and TEOS and continually stirred for further 10 min at 60°C. The solution was cooled to room temperature and 1 mL aqueous HCl (0.05 mol L^{-1}) was added and stirred for 2 h. The above mixtures were poured into the Teflon lined digestion vessel, where vessel cover acts as an overpressure release valve surrounded by a safety shield and then heated by a microwave synthesizer (ETHOS TC from Milestone Inc.) and maintained at 160°C for different times.

The resultant precipitates were collected by centrifugation, washed by the deionized water and then dried at 80°C for 24 h to gain precursors.

At last, the precursors were heat treated at 500°C for about 4 h at a ramping rate of 0.5°C min^{-1} to obtain CeO_2-SiO_2. The samples obtained under 30, 60, 90, 120, and 180 min microwave irradiation are denoted as M-30 min, M-60 min, M-90 min, M-120 min, and M-180 min, respectively. As a comparative study, a conventional hydrothermal process was used as a preparation method (H, reaction temperature: 160°C, reaction time: 24 h, calcination temperature: 500°C for 4 h at a ramping rate of 0.5°C min^{-1}). The obtained CeO_2-SiO_2 sample was denoted as H-24 h. TiO_2 P_{25} from Degussa was employed as a standard photocatalyst for comparison purpose. It consists of mainly anatase phase (ca. 80%), non-porous polyhedral particles of ca. 25 nm mean size, and a BET surface area of ca. 50 m^2 g^{-1}.

2.2. Characterization. To determine the crystallite sizes and identities of CeO_2-SiO_2, all the samples were characterized by

TABLE 2: Texture parameters of CeO_2-SiO_2 samples.

Sample	S_{BET} (m²/g)	S_t (m²/g)	S_{micro} (cm²/g)	S_{ext} (cm²/g)	V_p (cm³/g)	V_{micro} (cm³/g)	V_{meso} (cm³/g)	r (Å)
M-30 min	335	340	240	95	0.59	0.090	0.500	5.58
M-60 min	300	320	210	90	0.58	0.085	0.495	5.57
M-90 min	236	250	170	66	0.44	0.050	0.390	5.56
M-120 min	118	130	95	23	0.30	0.040	0.260	5.55
M-180 min	100	110	85	15	0.28	0.030	0.250	5.54
H-24 h	90	10	77	13	0.26	0.020	0.240	5.53
P_{25}	50	—	—	—	—	—	—	—

TABLE 3: The band gap energy of CeO_2-SiO_2 samples.

Sample	Band gap energy (eV)
M-30 min	3.25
M-60 min	3.32
M-90 min	3.42
M-120 min	3.55
M-180 min	4.02
H-24 h	4.10
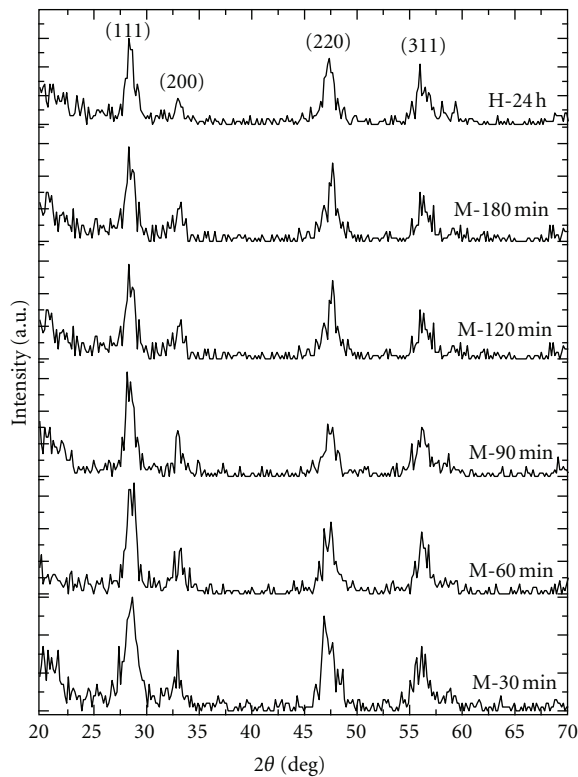
FIGURE 1: X-ray diffraction patterns of CeO_2-SiO_2 samples prepared by different irradiation times and hydrothermal method.

X-ray diffraction (XRD), transmission electron microscope (TEM), and UV-vis diffuse reflectance spectra (UV-vis DRS). The XRD measurements were performed on a Rigaku X-ray diffractometer system equipped with as RINT 2000 wide-angle goniometer using Cu Kα radiation and a power of $40 \, kV \times 30 \, mA$. The intensity data were collected at 25°C over a 2θ range of 10–80°. TEM images were obtained on Hitachi H-9500 operated at 300kv. UV-vis diffuse reflectance absorption spectra were recorded in air at room temperature in the wavelength range of 200–800 nm using a Shimadzu UV-2450 at 295 K. The Brunauer-Emmet-Teller (BET) surface areas were determined from N_2-adsorption measurements at 77 K using Nova 2000 series, Chromatech. Prior to analysis, the samples were outgased at 250°C for 4 h.

2.3. Photocatalytic Activity Measurements. A set of photocatalytic degradation experiments of methylene blue (100 ppm) was carried out by photoreactor under UV light irradiation. The light source for photocatalysis was a mercury lamp (150 W high pressure). The catalysts and solution were separated by filtration; the collected samples were analyzed by UV-Vis spectrophotometer (Shimadzu UV-2450). The photodegradation efficiency of methylene blue has been calculated by applying the following equation:

$$\%\text{photodegradation efficiency} = \frac{(C_o - C)}{C_o} \times 100, \quad (1)$$

where C_o is the original methylene blue content, C is the retained methylene blue in solution.

3. Results and Discussion

3.1. Evaluation and Characterization of Synthesized Materials

3.1.1. Phase Analysis. All the obtained peaks in the pattern of Figure 1 belong only to CeO_2. No other peaks related to impurities were detected, which confirm that the synthesized nanoparticles are pure CeO_2 with cubic phase [47]. It was observed from the XRD patterns that with the increase of the treatment time, intensity of XRD peaks increased and full width at half maximum decreased, indicating the enhancement of the crystallinity and crystallite size. Compared with the conventional hydrothermal route, the irradiation under the microwave produces a better crystallinity in a shorter treatment time (30 min), which is a good evidence that the introduction of the microwave really can save energy and time with faster kinetics of crystallization [48–50]. The particle sizes were calculated from (1 1 1) peak using Scherrer's formula $D = k\lambda/\beta \cos \theta$, where D is the average grain size, k a constant equal to 0.89, λ the wavelength of X-rays and β is the corrected half width. The calculated average crystallite sizes of the samples are tabulated in Table 1.
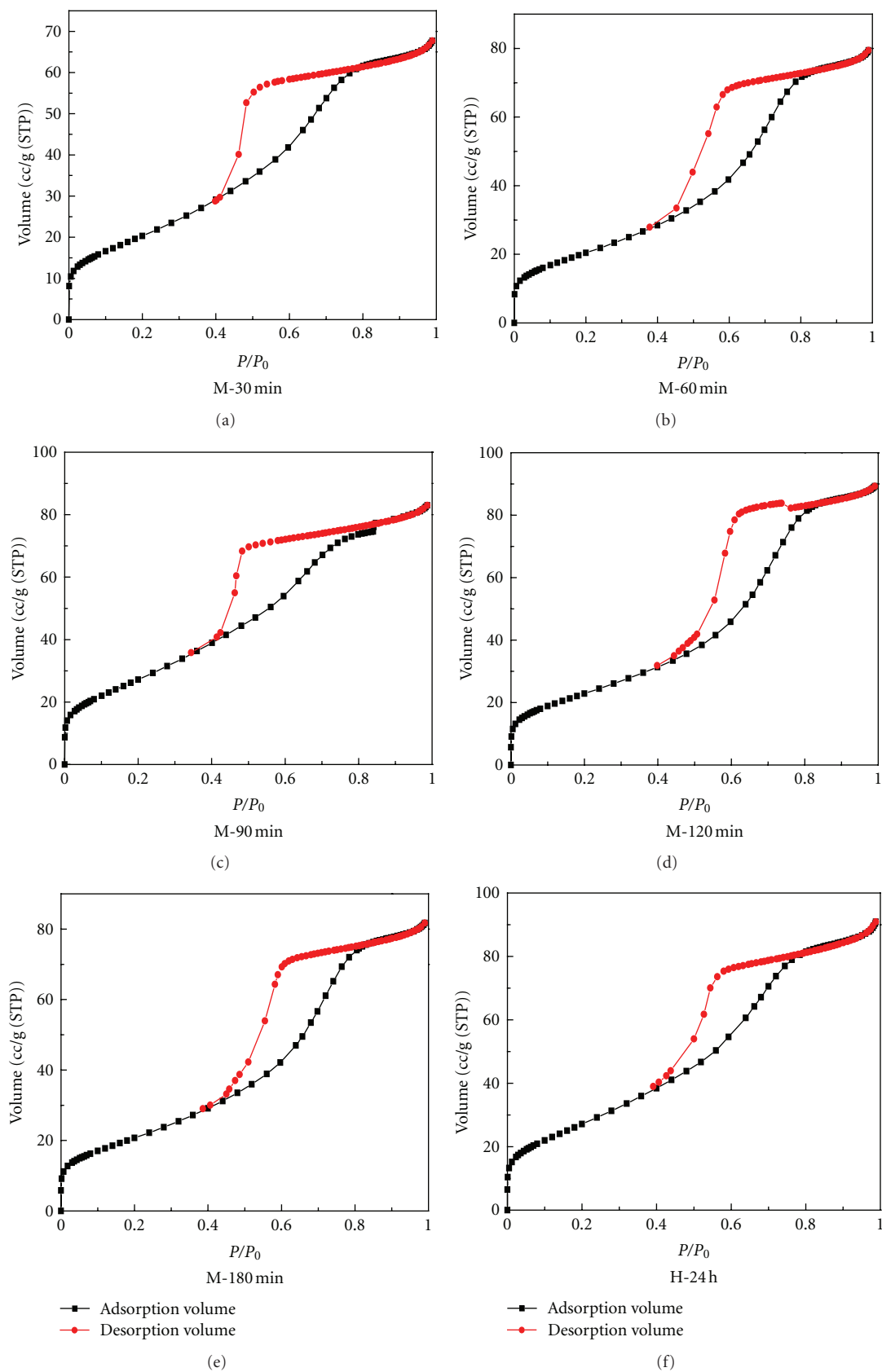
Figure 2: N_2 adsorption and desorption isotherm for CeO_2-SiO_2 samples prepared by different irradiation times and hydrothermal method.

TABLE 4: Effect of CeO$_2$-SiO$_2$ nanoparticles on the photoactivity.

Sample	S_{BET} (m^2/g)	Band gap eV	MB removal efficiency, %	V_p (cm^3/g)	Crystallite size, nm
M-30 min	335	3.25	93	0.59	8
M-60 min	300	3.32	90	0.58	10
M-90 min	236	3.42	89	0.44	11
M-120 min	118	3.55	88	0.30	12
M-180 min	100	4.02	87	0.28	14
H-24 h	90	4.10	85	0.26	15

TABLE 5: Effect of pH of MB solution on MB removal efficiency.

pH of MB	MB removal efficiency, %
3	93.0
4	95.0
7	96.0
9	96.2

TABLE 6: Effect of MB concentration on MB removal efficiency.

MB concentration, ppm	MB removal efficiency, %
100	96.0
150	96.0
200	96.0
300	90.0
400	95.0

3.1.2. Surface Area Analysis. The CeO$_2$-SiO$_2$ samples are characterized by specific surface area S_{BET} as shown in Table 2, which indicates that the increase of irradiation time decreases surface area and surface area of sample prepared by microwave method is higher than that prepared by the hydrothermal method. The parameters of surface area and the data calculated from the t-plot are collected in Table 2. The obtained results from the N_2-adsorption isotherms for CeO$_2$-SiO$_2$ samples indicate that both are typical of mesoporous solids type IV as shown in Figure 2. However, a decrease in the adsorption capacity of the CeO$_2$-SiO$_2$ samples was observed after increase irradiation time of the microwave. Furthermore, it was noticed that the total pore volume of M-30 min sample had the highest value. The values of S_{BET} and S_t are generally close in most samples indicating the presence of mesopores.

3.1.3. UV-Vis-DRS Analysis. The optical properties of synthesized CeO$_2$-SiO$_2$ samples were examined by UV-visible spectrophotometer, and the results are displayed in Figure 3. The results reveal an increase in absorbency in the visible light region parallel to the declining irradiation time of the examined systems. Therefore, the study of UV-vis radiation absorption is an important tool for the evaluation of the changes in the produced semiconductor materials by different treatments. Further, the band gap energy was
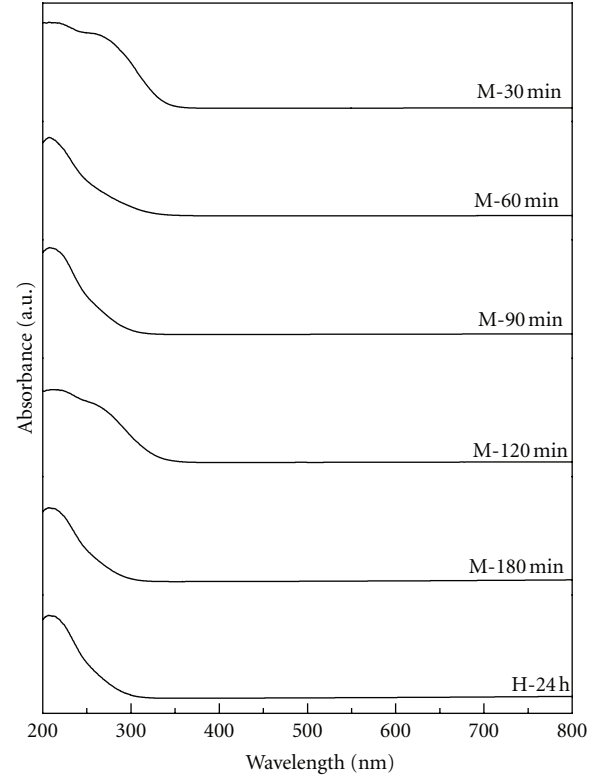
FIGURE 3: UV-vis spectra of CeO$_2$-SiO$_2$ samples prepared by different irradiation times and hydrothermal method.

calculated on the basis of the maximum absorption band of CeO$_2$-SiO$_2$ nanoparticles according to (2).

$$Eg = \frac{1240}{\lambda}, \quad (2)$$

where Eg is the band gap energy, and λ is the lower cutoff wavelength (nm) of the photocatalyst. The values of Eg, the band gap of the CeO$_2$-SiO$_2$ samples, are compiled in Table 3.

3.1.4. TEM Observation. With the aid of transmission electron microscope, size and morphology of as-synthesized samples were recorded. Based on the results of photocatalytic activity as given in Section 3.2.1, the highest catalytic activity was observed for the sample M-30, and the respective samples M-30 and H-24 were subjected to TEM analysis. The corresponding TEM analysis is shown in Figures 4(a) and 4(b). The results show that the shape of
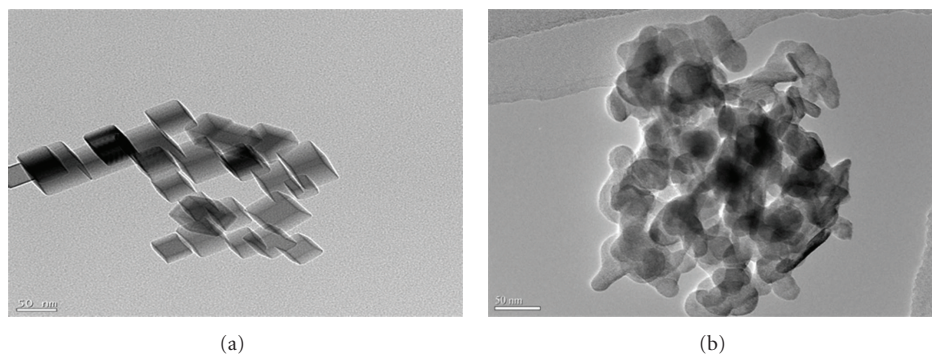
(a)

(b)

FIGURE 4: TEM images of CeO$_2$-SiO$_2$ samples prepared by (a) 30 min different irradiation times and (b) hydrothermal method.

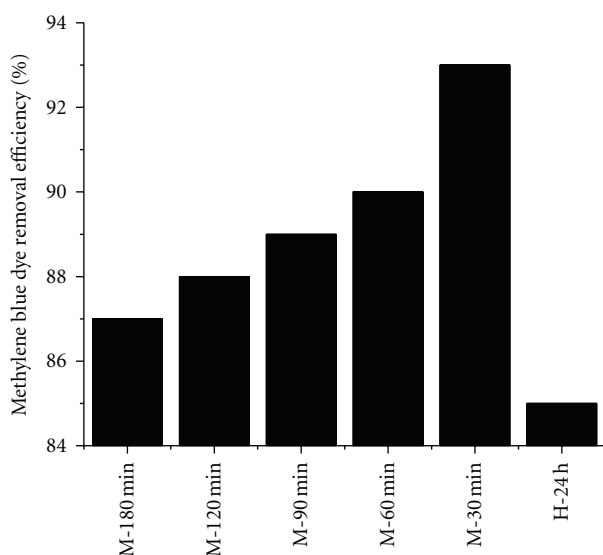FIGURE 5: Effect of irradiation time and preparation method on photocalytic efficiency percentage of methylene blue dye.

the CeO$_2$-SiO$_2$ sample prepared by hydrothermal method is spherical shape particles with size of about 15 nm. But the shape of CeO$_2$-SiO$_2$ sample prepared by microwave method for 30 min irradiation time is nanocubes with size of about 8 nm. These findings suggest that the shape and size of nanoparticles depend essentially on the preparation method.

3.2. Evaluation of Photocatalytic Activity

3.2.1. Effect of Preparation Method and Irradiation Time on Photocatalytic Degradation of Methylene Blue Dye. Within the frame of the present study, the photocatalytic degradation of methylene blue dye was taken as a probe reaction to test the catalytic activity of the system under consideration and Figure 5 shows the effect of irradiation time and preparation method on photocatalytic oxidation of methylene blue dye.

A keen insight into the obtained results, one could observe the following.

The highest value of degradation was M-30. The variation in activity should be due to the differences in physical properties such as band gap, particle size, and surface texture. The photocatalytic activities in relation to other obtained physical properties (S_{BET}, band gap, V_p, and crystallite sizes) are compiled in Table 4.

A maximum photocatalytic activity is found for M-30, where the surface area and pore volume own the maximum values counter to the band gap values. One could explain such increase due to a decrease in energy to exit electron from conduction band to valence band. Also, the M-30 min has the best photoactivity, since it has the lowest band gap and particle size and the highest surface area and pore volume.

3.2.2. Factors Affecting on Photocatalytic Activity

Effect of pH. A series of experiments has been carried out to study the effect of pH on MB removal efficiency under the following conditions: 0.3 g/L catalyst/MB solution ratio, 100 ppm Conc. of MB, and 1 h reaction time. The findings are summarized in Table 5. The results indicate that increasing the pH of MB solution from 3 to 7 leads to an increase in MB removal efficiency from 93 to 96.0%, but at pH more than 7, the MB removal efficiency almost remains unchanged. The possible reason for this behavior is that alkaline pH range favours the formation of more OH radical due to the presence of large quantity of OH$^-$ ions in the alkaline medium, which enhances the photocatalytic degradation of MB significantly [51]. The optimum condition for pH is 7 at which photodegradation percentage of MB reach to 96%.

Effect of MB Concentration. A series of experiments has been carried out to study the effect of the MB concentration on MB removal efficiency under the aforementioned conditions at pH 7. The results are summarized in Table 5. It can be seen that increasing MB concentration from 100 to 200 ppm has no significant effect on MB removal efficiency, but at a concentration higher than 200 ppm, the MB removal efficiency was decreased. The optimum condition for MB concentration is 200 ppm at MB removal efficiency of 96% (see Table 6).
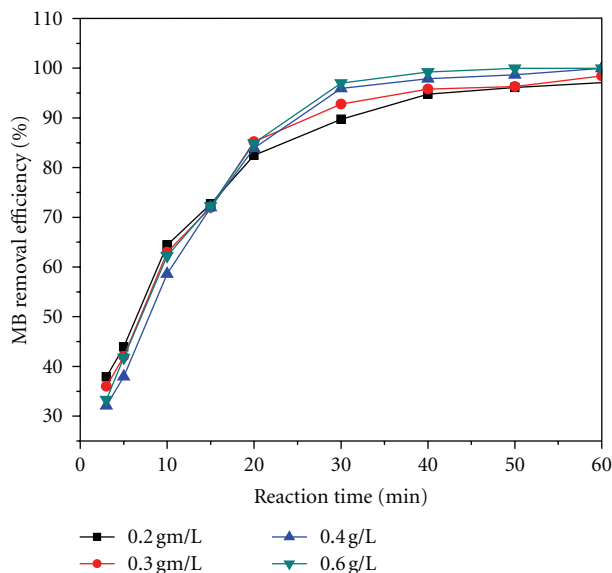
FIGURE 6: Effect of loading of optimum CeO$_2$-SiO$_2$ sample on MB removal efficiency percentage.

Effect of Catalyst/MB Solution Ratio. A series of experiments has been carried out to study the effect of catalyst/MB solution ratio g/L on MB removal efficiency under the aforementioned conditions at MB concentration of 200 ppm. The findings are shown in Figure 6. The results indicate that increasing the catalyst/MB solution ratio from 0.2 to 0.4 g/L leads to an increase in MB removal efficiency from 96.0 to 99.9%, respectively, but at a catalyst/MB solution ratio more than 0.4 g/L the MB removal efficiency almost remains unchanged. The optimum condition of catalyst/MB solution ratio g/L is 0.4 at 99.9% MB removal efficiency.

Comparison between Photocatalytic Activity of CeO$_2$-SiO$_2$ and TiO$_2$ Degussa. Finally, in the present study, a series of experiments has been carried out in order to compare the photocatalytic activity of optimum sample (M-30 min) and commercial reference P25 under the following conditions: 0.4 g/L catalyst/MB solution ratio, 200 ppm Conc. of MB, and 1 h reaction time. We found the photocatalytic activity of M-30 min and P25 are 99.9 and 94%, respectively. Therefore, the photocatalytic activity of CeO$_2$-SiO$_2$ nanoparticles which prepared by 30 min irradiation time was found to have a better performance than the commercial reference P25. Because the surface area of CeO$_2$-SiO$_2$ (335 m^2/gm) is higher than that of P25 (50 m^2/gm). It is concluded that the synthesized CeO$_2$-SiO$_2$ is one of the best candidate for environmental applications as a photocatalyst.

4. Conclusion

The microwave method is a useful for the preparation of CeO$_2$-SiO$_2$ nanoparticles with high photocatalytic activity, high surface area, and desirable pore structures. The irradiation time showed significant effect on the texture structure, band gap, and particle size. These physical changes affected

the efficiency of the photo degradation of methylene blue dye. The activity is well correlated with the band gap, surface area and pore volume. The CeO$_2$-SiO$_2$ nanoparticles, which were prepared for 30 min irradiation times exhibited the highest photoactivity due to its high surface area, large pore volume, small particle size, and small band gap. The photocatalytic activity of CeO$_2$-SiO$_2$ nanoparticles, which were prepared for 30 min irradiation time was found to have a better performance than commercial reference P25. It is concluded that the synthesized CeO$_2$-SiO$_2$ is one of the best candidate for environmental applications as a photocatalyst.

References

[1] C. Allegre, M. Maisseu, F. Charbit, and P. Moulin, "Coagulation-flocculation-decantation of dye house effluents: concentrated effluents," *Journal of Hazardous Materials*, vol. 116, no. 1-2, pp. 57–64, 2004.

[2] V. Golob, A. Vinder, and M. Simonič, "Efficiency of the coagulation/flocculation method for the treatment of dyebath effluents," *Dyes and Pigments*, vol. 67, no. 2, pp. 93–97, 2005.

[3] A. Alinsafi, M. Khemis, M. N. Pons et al., "Electro-coagulation of reactive textile dyes and textile wastewater," *Chemical Engineering and Processing: Process Intensification*, vol. 44, no. 4, pp. 461–470, 2005.

[4] S. Papic, N. Koprivanac, A. LoncaricBozic, and A. Metes, "Removal of some reactive dyes from synthetic wastewater by combined Al(III) coagulation/carbon adsorption process," *Dyes and Pigments*, vol. 62, no. 3, pp. 291–298, 2004.

[5] K. Tanaka, K. Padermpole, and T. Hisanaga, "Photocatalytic degradation of commercial azo dyes," *Water Research*, vol. 34, no. 1, pp. 327–333, 2000.

[6] M. R. Hoffmann, S. T. Martin, W. Choi, and D. W. Bahnemann, "Environmental applications of semiconductor photocatalysis," *Chemical Reviews*, vol. 95, no. 1, pp. 69–96, 1995.

[7] C. H. Li, Y. H. Hsieh, W. T. Chiu, C. C. Liu, and C. L. Kao, "Study on preparation and photocatalytic performance of Ag/TiO$_2$ and Pt/TiO$_2$ photocatalysts," *Separation and Purification Technology*, vol. 58, no. 1, pp. 148–151, 2007.

[8] D. F. Ollis and C. S. Turchi, "Heterogeneous photocatalysis for water purification: contaminant mineralization kinetics and elementary reactor analysis," *Environmental Progress*, vol. 9, no. 4, pp. 229–234, 1990.

[9] F. B. Li, X. Z. Li, and M. F. Hou, "Photocatalytic degradation of 2-mercaptobenzothiazole in aqueous La^{3+}-TiO$_2$ suspension for odor control," *Applied Catalysis B*, vol. 48, no. 3, pp. 185–194, 2004.

[10] F. B. Li and X. Z. Li, "Photocatalytic properties of gold/gold ion-modified titanium dioxide for wastewater treatment," *Applied Catalysis A*, vol. 228, no. 1-2, pp. 15–27, 2002.

[11] T. D. Nguyen-Phan and E. W. Shin, "Morphological effect of TiO$_2$ catalysts on photocatalytic degradation of methylene blue," *Journal of Industrial and Engineering Chemistry*, vol. 17, no. 3, pp. 397–400, 2011.

[12] C. B. Almquist and P. Biswas, "Role of synthesis method and particle size of nanostructured TiO$_2$ on its photoactivity," *Journal of Catalysis*, vol. 212, no. 2, pp. 145–156, 2002.

[13] K. Aoki, Y. Takeuchi, and Y. Amao, "Visible-light sensitisation of nanocrystalline TiO$_2$ film by Mg chlorophyll-a through the axial imidazole-4-acetic acid ligand," *Bulletin of the Chemical Society of Japan*, vol. 78, no. 1, pp. 132–134, 2005.

[14] S. Sakthivel, M. V. Shankar, M. Palanichamy, B. Arabindoo, D. W. Bahnemann, and V. Murugesan, "Enhancement of photocatalytic activity by metal deposition: characterisation and photonic efficiency of Pt, Au and Pd deposited on TiO$_2$ catalyst," *Water Research*, vol. 38, no. 13, pp. 3001–3008, 2004.

[15] C. G. Wu, C. C. Chao, and F. T. Kuo, "Enhancement of the photo catalytic performance of TiO$_2$ catalysts via transition metal modification," *Catalysis Today*, vol. 97, no. 2-3, pp. 103–112, 2004.

[16] Y. Q. Wu, G. X. Lu, and G. X. Li, "The long-term photocatalytic stability of Co^{2+}-modified P25-TiO$_2$ powders for the H$_2$ production from aqueous ethanol solution," *Journal of Photochemistry and Photobiology A*, vol. 181, no. 2-3, pp. 263–267, 2006.

[17] R. M. Mohamed and I. A. Mkhalid, "The effect of rare earth dopants on the structure, surface texture and photocatalytic properties of TiO$_2$-SiO$_2$ prepared by sol-gel method," *Journal of Alloys and Compounds*, vol. 501, no. 1, pp. 143–147, 2010.

[18] M. A. Brown and S. C. de Vito, "Predicting azo dye toxicity," *Critical Reviews in Environmental Science and Technology*, vol. 23, no. 3, pp. 249–324, 1993.

[19] H. Gnaser, M. R. Savina, W. F. Calaway, C. E. Tripa, I. V. Veryovkin, and M. J. Pellin, "Photocatalytic degradation of methylene blue on nanocrystalline TiO$_2$: surface mass spectrometry of reaction intermediates," *International Journal of Mass Spectrometry*, vol. 245, no. 1–3, pp. 61–67, 2005.

[20] H. X. Li, X. Y. Zhang, Y. N. Huo, and J. Zhu, "Supercritical preparation of a highly active S-doped TiO$_2$ photocatalyst for methylene blue mineralization," *Environmental Science & Technology*, vol. 41, no. 12, pp. 4410–4414, 2007.

[21] Q. Fu, H. Saltsburg, and M. Flytzani-Stephanopoulos, "Active nonmetallic Au and Pt species on ceria-based water-gas shift catalysts," *Science*, vol. 301, no. 5635, pp. 935–938, 2003.

[22] E. P. Murray, T. Tsai, and S. A. Barnett, "A direct-methane fuel cell with a ceria-based anode," *Nature*, vol. 400, no. 6745, pp. 649–651, 1999.

[23] A. Corma, P. Atienzar, H. García, and J. Y. Chane-Ching, "Hierarchically mesostructured doped CeO$_2$ with potential for solar-cell use," *Nature Materials*, vol. 3, no. 6, pp. 394–397, 2004.

[24] A. H. Morshed, M. E. Moussa, S. M. Bedair, R. Leonard, S. X. Liu, and N. El-Masry, "Violet/blue emission from epitaxial cerium oxide films on silicon substrates," *Applied Physics Letters*, vol. 70, no. 13, pp. 1647–1649, 1997.

[25] B. S. Liu, X. J. Zhao, N. Z. Zhang, Q. N. Zhao, X. He, and J. Y. Feng, "Photocatalytic mechanism of TiO$_2$-CeO$_2$ films prepared by magnetron sputtering under UV and visible light," *Surface Science*, vol. 595, no. 1–3, pp. 203–211, 2005.

[26] X. D. Zhou, W. Huebner, and H. U. Anderson, "Processing of nanometer-scale CeO$_2$ particles," *Chemistry of Materials*, vol. 15, no. 2, pp. 378–382, 2003.

[27] X. D. Zhou, W. Huebner, and H. U. Anderson, "Room-temperature homogeneous nucleation synthesis and thermal stability of nanometer single crystal CeO$_2$," *Applied Physics Letters*, vol. 80, no. 20, pp. 3814–3816, 2002.

[28] S. Tsunekawa, T. Fukuda, and A. Kasuya, "Blue shift in ultraviolet absorption spectra of monodisperse CeO$_{2-x}$ nanoparticles," *Journal of Applied Physics*, vol. 87, no. 3, pp. 1318–1321, 2000.

[29] A. Corma, P. Atienzar, H. García, and J. Y. Chane-Ching, "Hierarchically mesostructured doped CeO$_2$ with potential for solar-cell use," *Nature Materials*, vol. 3, no. 6, pp. 394–397, 2004.

[30] D. Terribile, A. Trovarelli, J. Llorca, C. de Leitenburg, and G. Dolcetti, "The synthesis and characterization of mesoporous high-surface area ceria prepared using a hybrid organic/inorganic route," *Journal of Catalysis*, vol. 178, no. 1, pp. 299–308, 1998.

[31] D. M. Lyons, K. M. Ryan, and M. A. Morris, "Preparation of ordered mesoporous ceria with enhanced thermal stability," *Journal of Materials Chemistry*, vol. 12, no. 4, pp. 1207–1212, 2002.

[32] C. Ho, J. C. Yu, T. Kwong, A. C. Mak, and S. Lai, "Morphology-controllable synthesis of mesoporous CeO$_2$ nano- and microstructures," *Chemistry of Materials*, vol. 17, no. 17, pp. 4514–4522, 2005.

[33] H. I. Chen and H. Y. Chang, "Synthesis of nanocrystalline cerium oxide particles by the precipitation method," *Ceramics International*, vol. 31, no. 6, pp. 795–802, 2005.

[34] A. Bumajdad, M. I. Zaki, J. Eastoe, and L. Pasupulety, "Microemulsion-based synthesis of CeO$_2$ powders with high surface area and high-temperature stabilities," *Langmuir*, vol. 20, no. 25, pp. 11223–11233, 2004.

[35] D. S. Bae, B. Lim, B. I. Kim, and K. S. Han, "Synthesis and characterization of ultrafine CeO$_2$ particles by glycothermal process," *Materials Letters*, vol. 56, no. 4, pp. 610–613, 2002.

[36] M. Lundberg, B. Skårman, F. Cesar, and L. R. Wallenberg, "Mesoporous thin films of high-surface-area crystalline cerium dioxide," *Microporous and Mesoporous Materials*, vol. 54, no. 1-2, pp. 97–103, 2002.

[37] J. P. Nair, E. Wachtel, I. Lubomirsky, J. Fleig, and J. Maier, "Anomalous expansion of CeO$_2$ nanocrystalline membranes," *Advanced Materials*, vol. 15, no. 24, pp. 2077–2081, 2003.

[38] B. Tang, L. H. Zhuo, J. C. Ge, G. L. Wang, Z. Q. Shi, and J. Y. Niu, "A surfactant-free route to single-crystalline CeO$_2$ nanowires," *Chemical Communications*, no. 28, pp. 3565–3567, 2005.

[39] D. S. Zhang, H. X. Fu, L. Y. Shi et al., "Synthesis of CeO$_2$ nanorods via ultrasonication assisted by polyethylene glycol," *Inorganic Chemistry*, vol. 46, no. 7, pp. 2446–2451, 2007.

[40] G. Z. Chen, C. X. Xu, X. Y. Song, W. Zhao, Y. Ding, and S. X. Sun, "Interface reaction route to two different kinds of CeO$_2$ nanotubes," *Inorganic Chemistry*, vol. 47, no. 2, pp. 723–728, 2008.

[41] D. Zhang, H. Fu, L. Shi, J. Fang, and Q. Li, "Carbon nanotube assisted synthesis of CeO$_2$ nanotubes," *Journal of Solid State Chemistry*, vol. 180, no. 2, pp. 654–660, 2007.

[42] K. L. Yu, G. L. Ruan, Y. H. Ben, and J. J. Zou, "Convenient synthesis of CeO$_2$ nanotubes," *Materials Science and Engineering B*, vol. 139, no. 2-3, pp. 197–200, 2007.

[43] K. B. Zhou, Z. Q. Yang, and S. Yang, "Highly reducible CeO$_2$ nanotubes," *Chemistry of Materials*, vol. 19, no. 6, pp. 1215–1217, 2007.

[44] K. Kaneko, K. Inoke, B. Freitag et al., "Structural and morphological characterization of cerium oxide nanocrystals prepared by hydrothermal synthesis," *Nano Letters*, vol. 7, no. 2, pp. 421–425, 2007.

[45] L. Qian, J. Zhu, W. Du, and X. Qian, "Solvothermal synthesis, electrochemical and photocatalytic properties of monodispersed CeO$_2$ nanocubes," *Materials Chemistry and Physics*, vol. 115, no. 2-3, pp. 835–840, 2009.

[46] S. W. Yang and L. Gao, "Controlled synthesis and self-assembly of CeO$_2$ nanocubes," *Journal of the American Chemical Society*, vol. 128, no. 29, pp. 9330–9331, 2006.

[47] J. Zhang, S. Ohara, M. Umetsu, T. Naka, Y. Hatakeyama, and T. Adschiri, "Colloidal ceria nanocrystals: a tailor-made crystal

morphology in supercritical water," *Advanced Materials*, vol. 19, no. 2, pp. 203–206, 2007.

[48] R. Si, Y. W. Zhang, L. P. You, and C. H. Yan, "Rare-earth oxide nanopolyhedra, nanoplates, and nanodisks," *Angewandte Chemie International Edition*, vol. 44, no. 21, pp. 3256–3260, 2005.

[49] F. Niu, D. Zhang, L. Shi, X. He, H. Li, and H. Mai, "Facile synthesis, characterization and low-temperature catalytic performance of Au/CeO_2 nanorods ," *Materials Letters*, vol. 63, no. 24-25, pp. 2132–2135, 2009.

[50] S. Komarneni, R. Roy, and Q. H. Li, "Microwave-hydrothermal synthesis of ceramic powders," *Materials Research Bulletin*, vol. 27, no. 12, pp. 1393–1405, 1992.

[51] S. F. Liu, I. R. Abothu, and S. Komarneni, "Barium titanate ceramics prepared from conventional and microwave hydrothermal powders," *Materials Letters*, vol. 38, no. 5, pp. 344–350, 1999.

Research Article

Comparison between Solar and Artificial Photocatalytic Decolorization of Textile Industrial Wastewater

Falah H. Hussein

Chemistry Department, College of Science, Babylon University, Iraq

Correspondence should be addressed to Falah H. Hussein, abohasan_hilla@yahoo.com

The photocatalytic decolorization of industrial wastewater was investigated by using TiO_2 and ZnO photocatalysts. Heterogeneous photocatalytic processes applied under natural weathering conditions, in the presence of solar radiation show a promising degradation capability. The complete removal of color could be achieved in a relatively short time of about 20 minutes, when ZnO was used and about 100 minutes when TiO_2 was used under solar irradiation. However, in the presence of artificial UV-light, complete decolorization of textile industrial wastewater was obtained after less than one hour of irradiation when ZnO was used and in less than two hours, when TiO_2 was used at the same temperature. The results indicate that the degree of photocatalytic decolorization of textile industrial wastewater was obviously affected by different parameters. These parameters include catalyst mass, type of catalyst, type of reactor, type of dye, dye concentration, and temperature. The procedure used in this research can be used as an efficient technology for solar photocatalytic decolorization of the colored wastewater discharged from the textile industry under the climatic conditions of most countries.

1. Introduction

Treatments of industrial wastewater, especially textile wastewater, will provide huge amount of water to face water scarcity around the world. Moreover the reliable treatments of wastewater will reduce contamination of soils, surface, and ground water, and as a result public health will be protected. Textile wastewaters are strongly colored and contain high amounts of organic matter depending on forms of dyes and auxiliary chemicals [1, 2].

Titanium dioxide and zinc oxide are widely and economically available. These semiconductors can be excited with light of a wavelength in the range of the solar spectrum ($\lambda > 310$ nm). Using of solar irradiation is very attractive technology from the economical point of view.

Titanium dioxide and zinc oxide are universally considered as the most important photocatalysts, due to their considerably low bandgap energy (~ 3.2 eV) and their lower cost. However, various methods have been developed to reduce the band gap and the electron-hole recombination. Jing et al. [3] reported that the photocatalytic activity of

the semiconductor is strongly dependent on its crystallite size, specific surface area, morphologies, and textures. The photocatalytic activity of ZnO hollow spheres with porous crystalline shells was increased significantly compared with untreated samples of ZnO at ambient temperature [4]. The hierarchical organization of nanosheets together with annealing-induced carbon doping within the ZnO lattice accounting for the improved visible light photocatalytic activity of porous carbon self-doped ZnO consequently gave better photocatalytic activity of ZnO products [5]. The photocatalytic properties of titanium dioxide are improved significantly in the presence of high energy facets, making this material attractive for various environmental applications [6]. The surface structure at the atomic level plays an important role in tuning the adsorption selectivity and, consequently, photocatalytic activity of semiconductor [7]. Graphene-based semiconductor photocatalysts also have important environmental and energy applications [8]. Titanium dioxide response toward visible light was increased after the addition of silver using the hydrothermal synthesis due to the formation of Ag aggregation on the TiO_2 surface
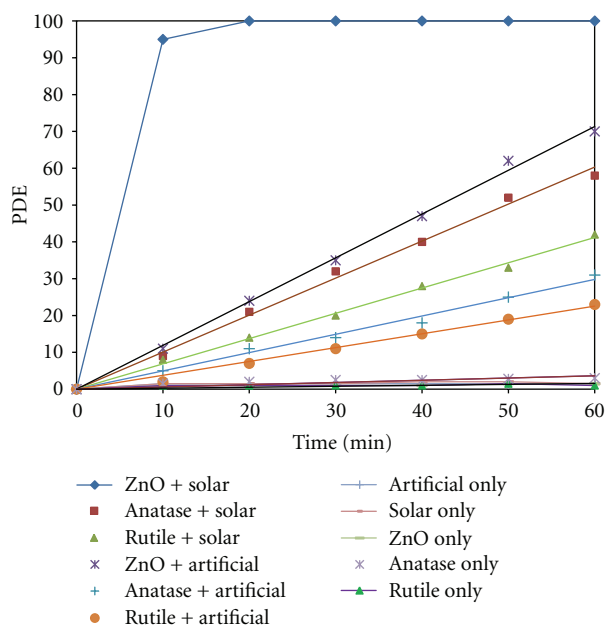
FIGURE 1: Effect of types of catalyst and irradiation on photocatalytic decolorization efficiency of real industrial wastewater.

FIGURE 2: Mass effect of TiO_2 (anatase) on photocatalytic decolorization efficiency of real textile industrial wastewater for different times of irradiation under solar and artificial radiation.

[9]. The photocatalytic activity of titanium dioxide is also significantly enhanced by those embedding gold nanoparticles in the Au-TiO_2 nanocomposites. The prepared Au-TiO_2 nanocomposites exhibit a highly visible light photocatalytic activity, and their photocatalytic activity is higher than that of the pristine TiO_2 nanoparticles due to the surface plasmon resonance [10]. Wang et al. [11] reported that photocatalytic activity of TiO_2 powders calcined at $500°C$ was two times higher than that of the uncalcined TiO_2. The authors explained that this was due to the enhancement of anatase crystallization and the optimal mass ratio (ca. $1:2$) of rutile to anatase.

The band gap of metalized titanium dioxide prepared by a simple impregnation method was reduced to 2.80 eV. Moreover, the solar decolorization and mineralization rates for Ta/TiO_2- and Nb/TiO_2-mixed oxide photocatalysts were improved by about 140% and 237%, respectively compared with untreated Degussa P25 TiO_2 [12].

The prepared carbon-modified TiO_2 powders by impregnation method using a commercial available titania powder, Hombikat UV100, as matrix material, showed better photoactivity of nitrogen oxides degradation than that of unmodified TiO_2 [13]. Comparing with the untreated TiO_2, anatase mesoporous titanium dioxide codoped with nitrogen and chlorine (N-Cl-TiO_2) greatly improves the photoresponse of TiO_2, thereby reducing the band gap [14]. The authors explained the enhancement of photocatalytic activity due to the small crystalline size, intense light absorption in visible region, and narrow band gap [14].

Wang et al. [15] in a recent review mentioned that doping of metal and nonmetal elements can improve the photocatalytic activity of titanium dioxide.
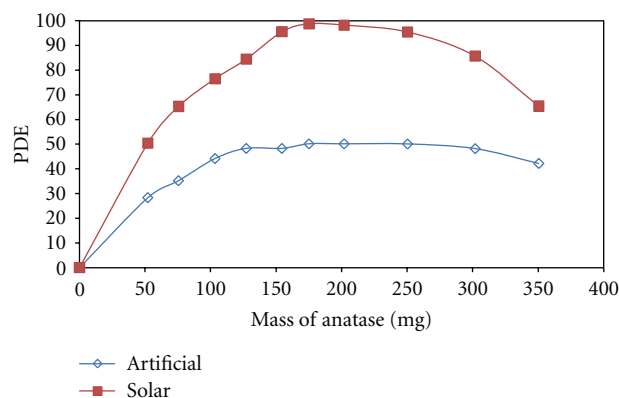
Solar disinfection (SODIS) is a simple and low-cost technique used to disinfect drinking water. It was found that this important technique was enhanced in the existence of photocatalysts by far more effective way than SODIS alone for the inactivation of both the total coliforms and the faecal coliforms [16].

Low pH and high concentration of Cl^- solutions were found beneficial to the photocatalytic activity of titanium dioxide [17].

By monitoring the surface chemistry of Pt-TiO_2 microspheres before and after photocatalytic reactions, it was found that the degradation of methyl orange molecules was more complete in the presence of platinum particles on the surface of titanium dioxide [18].

We have investigated previously, prolifically, the decolorization, photodegradation, and phytoremediation of many water-soluble toxic compounds in real and simulated industrial wastewater. The treated wastewaters could be recycled in the same industry or reused in another industry or for agricultural fields. The efficiency of these methods of treatments is between 70 and 95% [19–29].

The aim of the present paper is to investigate photocatalytic decolorization of real and simulated textile wastewater using TiO_2 and ZnO as photocatalysts with irradiation with solar and artificial radiation at different conditions.

2. Experimental Procedure

Real textile industrial wastewater sample was collected at the mid of December 2008 from textile factory in Hilla (Babylon Governorate, Iraq) at the discharging point. The sample was collected in hydrochloric acid-washed polyethylene container, 10 dm^{-3} in volume, which previously washed for several times with nitric acid (0.05 N) and rinsed for several times with redistilled water.

Experiments were carried out during December 2008 till July 2009. Solar irradiation experiments have been performed at the floor of the Chemistry Department building in the College of Science, Babylon University, in an open atmosphere between 11.00 a.m. and 1.00 p.m.
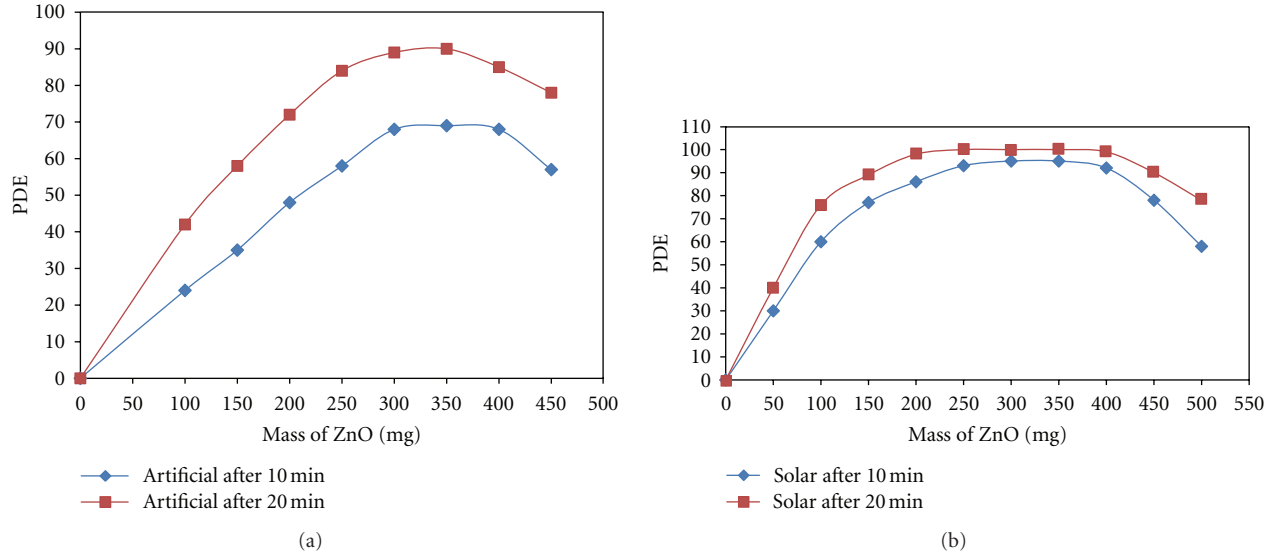
(a)

(b)

FIGURE 3: Mass effect of ZnO on photocatalytic decolorization efficiency of real textile industrial wastewater for different times of irradiation under artificial radiation (a) and solar irradiation (b).

Sunlight illuminations were accomplished in a 300 cm³ glass container containing 100 cm³ of the industrial wastewater solution. The sunlight radiation was collected using converging lens with a focal length of 14 cm. Artificial irradiation experiments are performed in a homemade reactor. The reactor consists of graduated 400 cm³ Pyrex glass beaker and a magnetic stirring setup. The radiation source was a Philips 125 w/542 high-pressure mercury lamp (Holland). The lamp was positioned perpendicularly above the beaker. The mercury lamp was allowed to warm up for 3 minutes to ensure a stable light intensity before commencing a reaction.

Titanium dioxide P-25 anatase (commercial TiO_2), of surface area 50 m² g⁻¹, was purchased from Degussa. Titanium dioxide rutile was obtained from Fluka (Assay 97%) and zinc oxide with 99.5% purity, supplied by Carlo ERBA.

In all experiments, the required amount of the catalyst, titanium dioxide (anatase or rutile) or zinc oxide, was suspended in 100 cm³ of industrial wastewater using a magnetic stirrer. At predetermined times, 1.5 cm³ of reaction mixture was collected and centrifuged (4,000 rpm, 15 minutes) in an 800B centrifuge. The supernatant was carefully removed by a syringe with a long pliable needle and centrifuged again at same speed and for the same period of time. This second centrifugation was found necessary to remove fine particles of ZnO or TiO_2. After the second centrifugation, the absorbance at certain wavelengths of the supernatants was determined using ultraviolet-visible spectrophotometer, type UV-1650 PC, Shimadzu and visible spectrophotometer type v-1000, T-Chromatech.

Photocatalytic decolorization efficiency (PDE) of the dye was followed, spectrophotometrically, by a comparison of the absorbance, at specified interval times, with a calibration curve accomplished by measuring the absorbance, at known wavelengths, with different concentrations of the dye solution. PDE is calculated from a mathematical equation
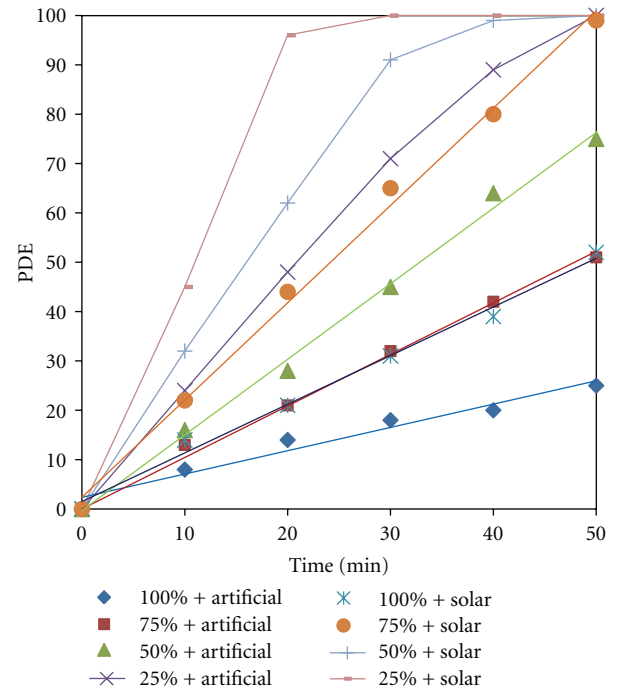
FIGURE 4: Effect of initial dye on photocatalytic decolorization of real textile industrial wastewater on TiO_2 (anatase) and solar radiation.

adapted from measurements of decolorization used before [30, 31].

$$\text{PDE} = \frac{(\text{absorbance})_0 - (\text{absorbance})_t}{(\text{absorbance})_0} \times 100, \quad (1)$$

where $(\text{absorbance})_0$ is the absorbance at 422 nm before irradiation and $(\text{absorbance})_t$ is the absorbance at time t. To

FIGURE 5: Effect of TiO$_2$ (anatase and rutile) and zinc oxide reuse on photocatalyic decolorization efficiency after 60 minutes of solar irradiation.

TABLE 1: Effect of temperature on photocatalytic decolorization efficiency of real textile industrial wastewater on TiO$_2$ and solar radiation.

Time/min.	Temperature/K			
	293.15	298.15	304.15	310.15
0	0	0	0	0
10	9.11	11.23	12.43	14.22
20	18.23	20.88	23.54	26.44
30	26.66	30.43	34.05	39.76
40	36.55	40.22	46.12	55.45
50	45.65	51.65	58.54	70.34
60	55.24	58.34	65.45	78.85

check the validity of the previous equation for used textile industrial wastewater, the photodegradation percentage of the dye was followed, spectrophotometrically, by a comparison of the absorbance, at specified interval times, with a calibration curve accomplished by measuring the absorbance, at known wavelengths, with different concentrations of the dye solution.

3. Results and Discussion

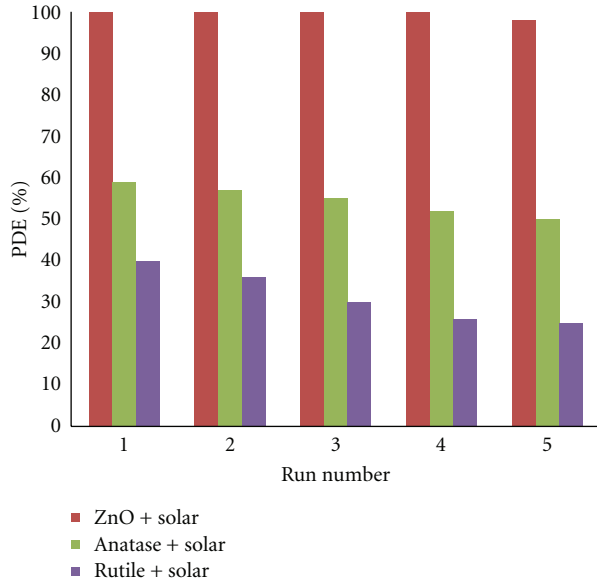### 3.1. Photocatalytic Decolorization of Real Textile Industrial Wastewater at Different Conditions. Figure 1 shows the change in photocatalytic decolorization efficiency (PDE) of real textile industrial wastewater in the present and absent of catalyst and in the present and absent of solar or artificial irradiation.

The results indicate that the activity of different catalysts fell in the sequence:

TABLE 2: Effect of temperature on photocatalytic decolorization efficiency of real textile industrial wastewater on ZnO and artificial radiation.

| Time/min	Temperature/K			
	290.15	298.15	313.15	319.15
0	0	0	0	0
10	10.22	12	17.25	18.22
20	21.4	14.12	35.25	38.04
30	32.8	36.22	52.33	56.22
40	42.44	48.35	68.88	77.25
50	52.3	62.55	85.25	100
60	63.55	72.85	97.88	100

ZnO (solar) > ZnO (artificial) > Anatase (solar) > Rutile (solar) > Anatase (artificial) > Rutile (artificial) ≫ No catalyst = No solar or artificial irradiation = 0.

These results also indicate that there was no dark reaction. Incubations of colored industrial wastewater without solar or artificial radiation and/or without catalyst was performed to demonstrate that decolorization of the dye was dependent on the presence of both; light and catalyst.

Results indicate that ZnO in the existence of solar irradiation is most active. Sakthivel et al. [32] explained the higher activity of ZnO due to absorption of large fraction of the solar spectrum and absorption of more light quanta by ZnO than TiO$_2$. However, the amount of zinc oxide required to reach the optimum activity is two times more than that for titanium dioxide (anatase or rutile) [25, 26]. In another study, Attia et al., [23], observed that ZnO is less active than anatase when the same weight of catalysts is used for photocatalytic degradation of textile wastewater. Akyol et al., [33] reported that ZnO is more active than TiO$_2$ for the decolorization efficiency of aqueous solution of a commercial textile dye due to the band gap energy, the charge carrier density, and the crystal structure.

All types of catalysts used in this research showed higher photocatalytic activity under sunlight irradiation. This may be due to high light intensity of solar radiation in IRAQ. Neppolian et al. [34] reported that solar energy may emerge as a viable method for textile wastewater treatment because of its eco-friendliness and cost effective where 96% of textile industrial wastewater was photodegradated during April–June; peak summer period of the year in Chennai, India. However, Akbal [35] concluded that the photocatalytic decolorization rate of methylene blue and methyl orange with UV light irradiation was higher than that with solar light irradiation.

3.2. Effect of Catalyst Mass. Figure 1 shows that 175 mg of anatase is sufficient for maximum rate of decolorization when mercury lamp was used for irradiation. Moreover the same mass was found also sufficient when the reaction vessel was illuminated with solar irradiation. These observations proved that the optimum mass to achieve maximum decolorization percentage is independent on type of irradiation
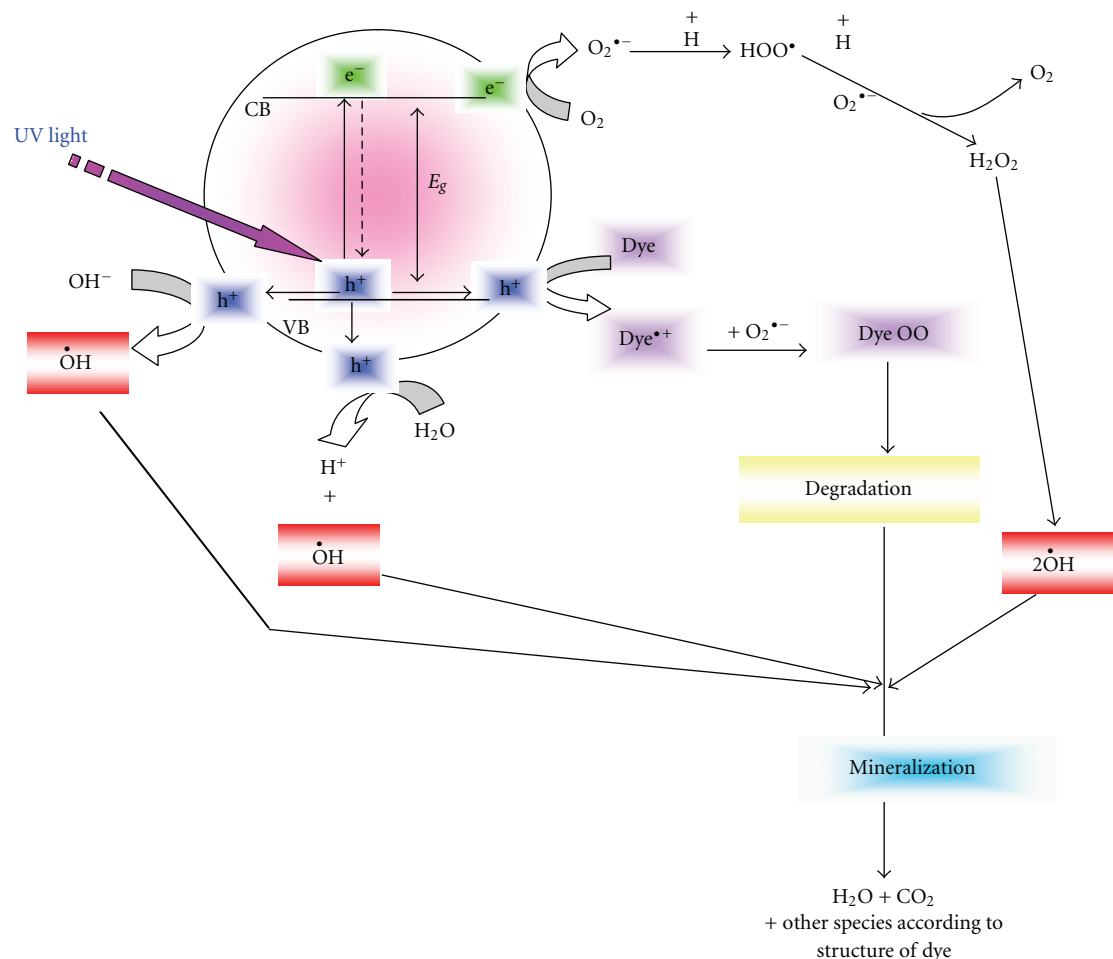
SCHEME 1: Dye/semiconductor/UV light system.

source and solar irradiation in this system is more efficient than 125 w/542 high pressure mercury lamp.

The same observations were noted when ZnO was used as photocatalyst. However the optimum mass to achieve maximum PDE is 350 mg. These results are shown in Figure 2.

Mass of catalyst is regarded as the major parameter affecting the photocatalytic degradation efficiency [36]. The results plotted in Figures 2 and 3 shows that the photocatalytic degradation efficiency of real industrial wastewater increases linearly with the increasing in catalysts mass at the first stages. This behavior may be due to an increase in the amount of active site on surface of photocatalyst particles and as a result, the number of dye molecule that adsorbed on the surface of photocatalyst will be increased and that will lead to an increase in the density of particles in the area of illumination [37]. However, after reaching maximum photocatalytic degradation rate, addition of excess amount of catalysts has no effect on photocatalytic rate, so a plateau region was observed. After the plateau region is achieved, the activity of photocatalytic decolorization decrease with increase of catalyst concentration for titanium dioxide and zinc oxide. This behavior is more likely due to Light

scattering by catalyst particles at higher concentration which leads to decrease in the passage of irradiation through the sample leading to poor light utilization [38, 39]. Deactivation of activated photocatalyst molecules colliding ground state molecules with increasing the load of photocatalyst may be also cause reduction in photocatalyst activity [37]. High concentration of loading catalyst also decreases the number of surface active sites [40].

3.3. Effect of Temperature.

Reaction was followed at four different temperatures in the range 293.15–315.15 K using 175 mg of anatase under solar radiation. The results in Table 1 indicate that the PDE of real textile industrial wastewater increases with increasing of temperature.

Reaction was also followed at four different temperatures in the range 290.15–319.15 K using mercury lamp and 350 mg of zinc oxide. The results are listed in Table 2. The results indicate that PDE of real textile industrial wastewater increases with increasing of temperature. However it is clear that temperature is the least active parameter in the photocatalytic decolorization of real textile industrial wastewater.
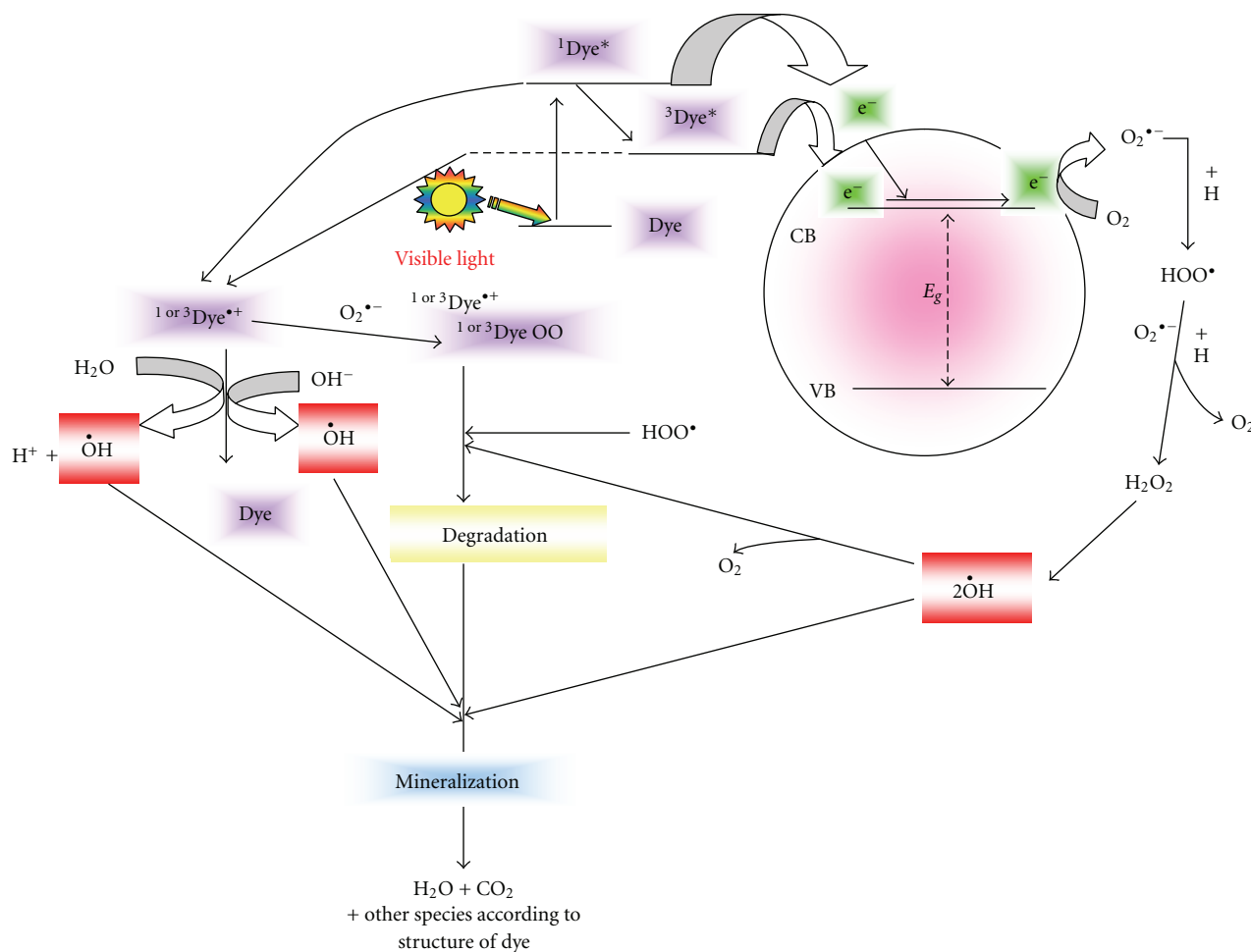
Scheme 2: Nonregenerative dye/semiconductor/visible light system.

It is well known that the most desirable system for complete mineralization of a wide range of organic substrates is that which operates under natural weathering conditions without producing of harmful byproducts [41]. Photocatalytic treatments and especially with solar irradiation offer that because they are mostly proceeding under natural weathering conditions. Adsorption of reactants on the surface of catalysts is a spontaneous exothermic phenomenon so it is enhanced by reduction of temperature [42].

3.4. Effect of Initial Dye Concentration. The results in Figure 4 show the changing of rate of decolorization of real textile industrial wastewater on 175 mg of anatase by using solar and artificial irradiation at 298.15 K with the initial direct dye concentrations (25%–100%) at different times. The results indicate that decreasing of dye concentration decreases the time of decolorization.

This behavior related to decreasing of the path length of photons entering the solution as the initial concentration of dye increases, and as a result the number of photon absorbed by the catalyst decreases.

This behavior related to decreasing of the path length of photons entering the solution as the initial concentration of

dye increases, and as a result the number of photon reached the catalyst surface decreases [43–45].

3.5. The Reusability of Catalyst. The reusability of the titanium dioxide (anatase or rutile) and zinc oxide was examined. The recovered catalysts were reused for five consecutive runs. Figure 5 shows only a slight decrease in the activity of these photocatalysts after five consecutive uses. However, rutile showed more decrease than anatase and zinc oxide.

4. Kinetics of Decolorization

In photosensitization process, which is defined as the conversion of light energy to chemical reactivity [46], a colored organic or inorganic material is added to a semiconductor. The added sensitizer (Sens) absorbs light in to the visible range to yield an excited state of the sensitizer (Sens)*. The excited sensitizing molecule injects an electron from excited singlet (S1) or triplet (T1) states into the conduction band of the semiconductor [47].

The illumination of suspended semiconductor in an aqueous solution of dye with unfiltered light (polychromatic light) leads to the possibility of the existence of two pathways [21, 48].
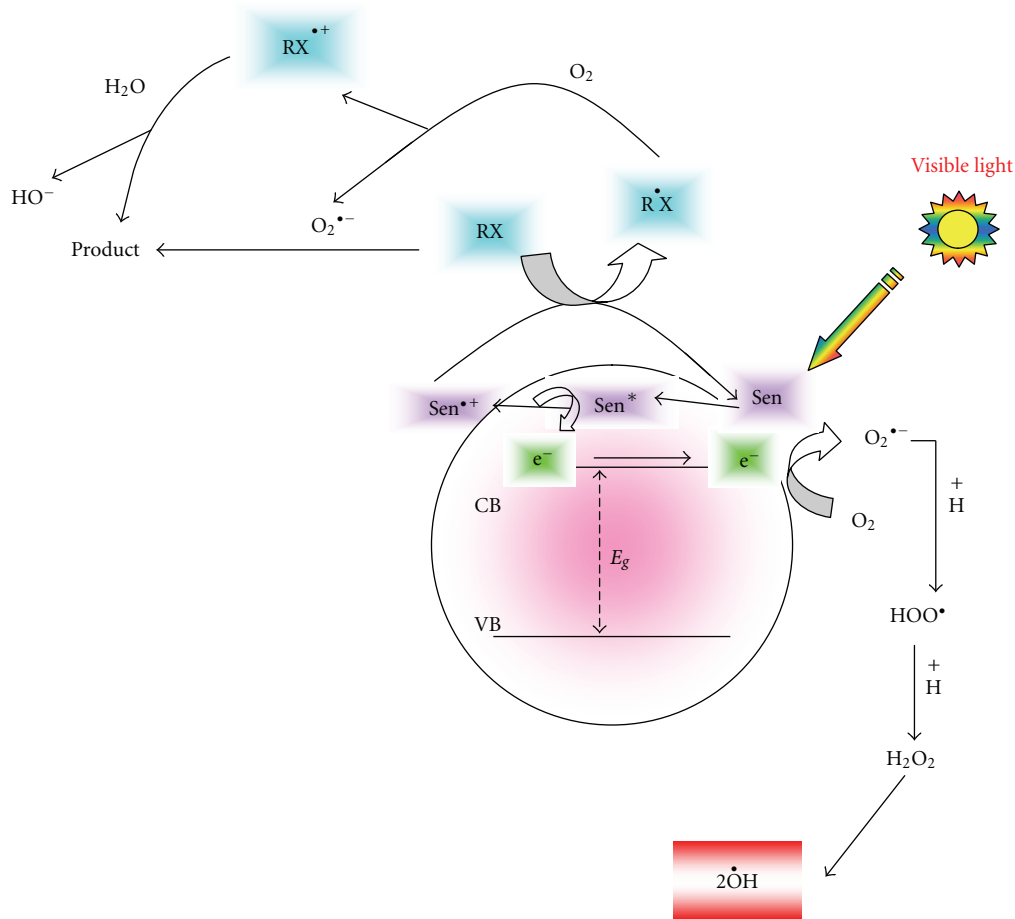
Scheme 3: Regenerative dye/semiconductor/visible light system.

(1) In the first pathway, the part of light with energy equal to or more than the band gap of the illuminated semiconductor will cause a promotion of an electron to conduction band of the semiconductor, a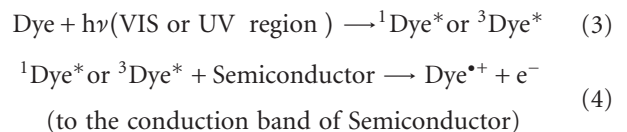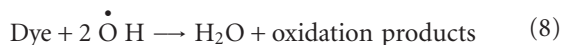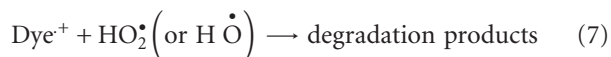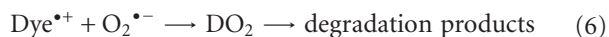nd as a result, a positive hole will be created in the valence band. The formed photoholes and photoelectrons can move to the surface of the semiconductor in the presence of light energy. The positive hole will react with adsorbed water molecules on the surface of semiconductor producing $^\bullet$OH radicals, and the electron will react with adsorbed oxygen on the surface. Moreover, they can react with deliquescent oxygen and water in suspended liquid and produce perhydroxyl radicals ($HO_2^\bullet$) with high chemical activity [49]. The processes in this pathway, as shown in Scheme 1, can be summarized by the following equations:

$$h^+ + OH^- \longrightarrow \overset{\bullet}{O}H$$

$$h^+ + H_2O \longrightarrow H^+ + \overset{\bullet}{O}H$$

$$e^- + O_2 \longrightarrow O_2^{\bullet-}$$

$$O_2^{\bullet-} + H^+ \longrightarrow HO_2^\bullet$$

$$HO_2^\bullet + O_2^{\bullet-} \overset{H^+}{\longrightarrow} H_2O_2 + O_2$$

$$H_2O_2 \longrightarrow 2\,\overset{\bullet}{O}H$$

$$Dye + Semiconductor(h^+_{VB}) \longrightarrow Dye^{\bullet+} + Semiconductor$$

$$Dye^{\bullet+} + O_2^{\bullet-} \longrightarrow DO_2 \longrightarrow degradation\ products$$

$$(2)$$
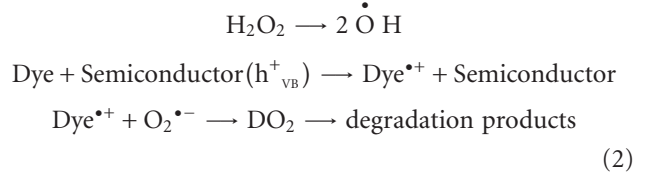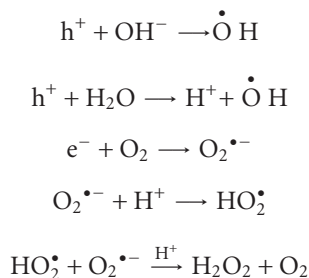
(2) In the second pathway, the other part of light with energy which is less than the band gap of the illuminated semiconductor will be absorbed by the adsorbed dye molecules. Dye molecules will be decolorized by a photosensitization process. The photocatalytic decolorization of dyes, which is described as photosensitization processes, is also characterized by a free radical mechanism. In this process, the adsorbed dyes molecules on the surface of the semiconductor can absorb a radiation in the visible range in addition to the radiation with short wavelengths [19, 50, 51]. The excited colored dye (dye*) (in the singlet or triplet state) will inject an electron to the conduction band of the semiconductor [24]. The processes in this pathway, as shown in Scheme 2, can be summarized by the following equations:

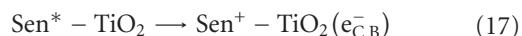$$Dye + h\nu(VIS\ or\ UV\ region\ ) \longrightarrow {}^1Dye^* or\ {}^3Dye^* \quad (3)$$

$$^1Dye^* or\ {}^3Dye^* + Semiconductor \longrightarrow Dye^{\bullet+} + e^-$$

$$(4)$$

$$(to\ the\ conduction\ band\ of\ Semiconductor)$$

$$e^- + O_2 \longrightarrow O_2^{\bullet -} + \text{Semiconductor} \tag{5}$$

$$\text{Dye}^{\bullet +} + O_2^{\bullet -} \longrightarrow DO_2 \longrightarrow \text{degradation products} \tag{6}$$

$$\text{Dye}^{\bullet +} + HO_2^{\bullet} \left(\text{or } H\overset{\bullet}{O} \right) \longrightarrow \text{degradation products} \tag{7}$$

$$\text{Dye} + 2\overset{\bullet}{O}H \longrightarrow H_2O + \text{oxidation products} \tag{8}$$

$$\text{Dye}^{\bullet +} + {}^- OH \longrightarrow \text{Dye} + \overset{\bullet}{O}H \tag{9}$$

$$\text{Dye}^{\bullet +} + H_2O \longrightarrow \text{Dye} + \overset{\bullet}{O}H + H^+ \tag{10}$$

The mechanism above is favoured by nonregenerative organic dye where dye/semiconductor/visible light system and the sensitizer itself degrade. However, in regenerative semiconductor system, (Scheme 3), the following mechanism may be followed:

$$\text{Sen} + TiO_2 \longleftrightarrow \text{Sen} - TiO_2 \tag{11}$$

$$\text{Sen} - TiO_2 + RX \longleftrightarrow \text{Sen} - TiO_2 \cdots RX_{(ads)} \tag{12}$$

$$\text{Sen} - TiO_2 + O_2 \longleftrightarrow \text{Sen} - TiO_2 \cdots O_{2(ads)} \tag{13}$$

$$\text{Sen} - TiO_2 \underset{h\nu}{\overset{h\nu \text{ visible light}}{\rightleftharpoons}} \text{Sen}^* - TiO_2 \tag{14}$$

$$\text{Sen}^* - TiO_2 \cdots O_{2(ads)} \longrightarrow \text{Sen}^+ - TiO_2 + O_2^- \tag{15}$$

$$\text{Sen}^+ - TiO_2 + O_2^- \longrightarrow \text{Sen} - TiO_2 + O_2 \tag{16}$$

$$\text{Sen}^* - TiO_2 \longrightarrow \text{Sen}^+ - TiO_2(e_{C.B}^-) \tag{17}$$

$$\text{Sen}^+ - TiO_2(e_{C.B}^-) \longrightarrow \text{Sen} - TiO_2 \tag{18}$$

$$\text{Sen}^+ - TiO_2(e_{C.B}^-) \cdots RX \longrightarrow \text{Sen}^+ - TiO_2 + \overset{\bullet}{R}X + X^- \tag{19}$$

$$\text{Sen}^+ - TiO_2(e_{C.B}^-) \cdots O_{2(ads)} \longrightarrow \text{Sen}^+ - TiO_2 + O_2^- \tag{20}$$
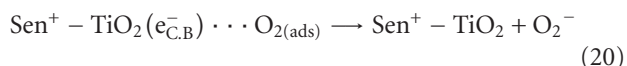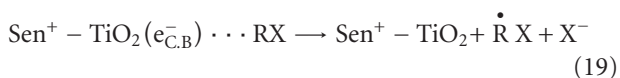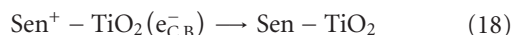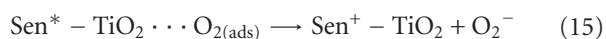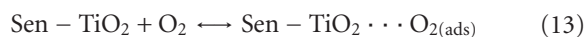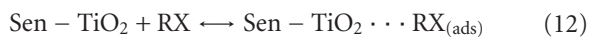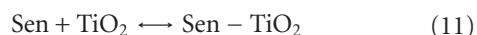
Cho et al. [52] conclude that there is no direct electron transfer between an excited sensitizer and CCl_4 molecules, in homogeneous solution, and the existence of semiconductor is essential for sensitized photocatalysis. Platinum supported on titanium dioxide acts as an excellent sensitizer and could have practical advantages as a mild and convenient photocatalyst for selective oxidation processes [53]. The addition of rhodamine B, as sensitizer to TiO_2 dispersion system, increases the rate of photooxidation properties [54]. The authors explained that due to the fact that more light absorbed by rhodamine B between 460 and 580 nm, then the energy transfer from sensitizer to TiO_2 or to any other active species hence promotes the photocatalytic activity of titanium dioxide.

5. Conclusions

(1) The existence of catalyst and lights is essential for photocatalytic degradation of colored dyes.

(2) Solar photocatalytic treatment is an efficient technique for decolorization of industrial wastewater through a photocatalytic process, and the transformation is practically complete in a reasonable irradiation time.

(3) Visible light/ZnO and visible light/TiO_2 systems could be efficiently used for photodegradation of textile industrial wastewater. The results indicate that the degree of photodegradation of textile industrial wastewater was obviously affected by different parameters. The complete removal of color could be achieved in a relatively short time of about 20 minutes, when ZnO was used under solar irradiation.

(4) The procedure used in this research can be used as an efficient technology for solar photocatalytic degradation of the colored wastewater discharged from the textile industry under natural weathering conditions.

References

[1] S. Meriç, D. Kaptan, and T. Ölmez, "Color and COD removal from wastewater containing Reactive Black 5 using Fenton's oxidation process," *Chemosphere*, vol. 54, no. 3, pp. 435–441, 2004.

[2] M. Muruganandham and M. Swaminathan, "Decolourisation of reactive orange 4 by fenton and photo-Fenton oxidation technology," *Dyes and Pigments*, vol. 63, no. 3, pp. 315–321, 2004.

[3] L. Jing, Y. Qu, B. Wang et al., "Review of photoluminescence performance of nano-sized semiconductor materials and its relationships with photocatalytic activity," *Solar Energy Materials and Solar Cells*, vol. 90, no. 12, pp. 1773–1787, 2006.

[4] J. Yu and X. Yu, "Hydrothermal synthesis and photocatalytic activity of zinc oxide hollow spheres," *Environmental Science and Technology*, vol. 42, no. 13, pp. 4902–4907, 2008.

[5] S. Liu, C. Li, J. Yu, and Q. Xiang, "Improved visible-light photocatalytic activity of porous carbon self-doped ZnO nanosheet-assembled flowers," *CrystEngComm*, vol. 13, no. 7, pp. 2533–2541, 2011.

[6] S. Liu, J. Yu, and M. Jaroniec, "Anatase TiO_2 with dominant high-energy 001 facets: synthesis, properties, and applications," *Chemistry of Materials*, vol. 23, no. 18, pp. 4085–4093, 2011.

[7] S. Liu, J. Yu, and M. Jaroniec, "Tunable photocatalytic selectivity of hollow TiO_2 microspheres composed of anatase polyhedra with exposed 001 facets," *Journal of the American Chemical Society*, vol. 132, no. 34, pp. 11914–11916, 2010.

[8] Q. Xiang, J. Yu, and M. Jaroniec, "Graphene-based semiconductor photocatalysts," *Chemical Society Reviews*, vol. 41, no. 2, pp. 782–796, 2012.

[9] C. A. Castro, A. Jurado, D. Sissa, and S. A. Giraldo, "Performance of Ag-TiO₂ photocatalysts towards the photocatalytic disinfection of water under interior-lighting and solar-simulated light irradiations," *International Journal of Photoenergy*, vol. 2012, Article ID 261045, 10 pages, 2012.

[10] M. Zhou, J. Zhang, B. Cheng, and H. Yu, "Enhancement of visible-light photocatalytic activity of mesoporous Au-TiO₂ nanocomposites by surface plasmon resonance," *International Journal of Photoenergy*, vol. 2012, Article ID 532843, 10 pages, 2012.

[11] G. Wang, L. Xu, J. Zhang, T. Yin, and D. Han, "Enhanced photocatalytic activity of TiO₂ powders (P25) via calcination treatment," *International Journal of Photoenergy*, vol. 2012, Article ID 265760, 9 pages, 2012.

[12] H. Znad, M. H. Ang, and M. O. Tade, "Ta/TiO₂ -and Nb/TiO₂-mixed oxides as efficient solar photocatalysts: Preparation, characterization, and photocatalytic activity," *International Journal of Photoenergy*, vol. 2012, Article ID 548158, 9 pages, 2012.

[13] C. Huang, Y. Lin, I. Wang, and C. Lu, "Photocatalytic activity and characterization of carbon-modified titania for visible-light-active photodegradation of nitrogen oxides," *International Journal of Photoenergy*, vol. 2012, Article ID 548647, 13 pages, 2012.

[14] X. Cheng, X. Yu, Z. Xing, and L. Yang, "Enhanced visible light photocatalytic activity of mesoporous anatase TiO₂ codoped with nitrogen and chlorine," *International Journal of Photoenergy*, vol. 2012, Article ID 593245, 6 pages, 2012.

[15] J. Wang, Q. Cai, H. Li, Y. Cui, and H. Wang, "A review on TiO₂ nanotube film photocatalysts prepared by liquid-phase deposition," *International Journal of Photoenergy*, vol. 2012, Article ID 702940, 11 pages, 2012.

[16] J. A. Byrne, P. A. Fernandez-Ibañez, P. S. M. Dunlop, D. M. A. Alrousan, and J. W. J. Hamilton, "Photocatalytic enhancement for solar disinfection of water: a review," *International Journal of Photoenergy*, vol. 2011, Article ID 798051, 12 pages, 2011.

[17] X. Wu, Z. Huang, Y. Liu, and M. Fang, "Investigation on the photoelectrocatalytic activity of well-aligned TiO₂ nanotube arrays," *International Journal of Photoenergy*, vol. 2012, Article ID 832516, 7 pages, 2012.

[18] J. Zhang, L. Li, and G. Li, "Enhancing photocatalytic performance through tuning the interfacial process between TiO₂-assembled and Pt-loaded microspheres," *International Journal of Photoenergy*, vol. 2012, Article ID 913630, 7 pages, 2012.

[19] A. N. Alkhateeb, F. H. Hussein, and K. A. Asker, "Photocatalytic decolonization of industrial wastewater under natural weathering conditions," *Asian Journal of Chemistry*, vol. 17, no. 2, pp. 1155–1159, 2005.

[20] A. Alkhateeb, J. Ismail, and F. Hussein, "Solar photolysis and photocatalytic degradation of murexide using titanium dioxide and zinc oxide," *JAAUBAS*, vol. 4, pp. 70–76, 2007.

[21] F. H. Hussein, A. N. Alkhateeb, and J. K. Ismail, "Solar photolysis and photocatalytic decolorization of thymol blue," *E-Journal of Chemistry*, vol. 5, no. 2, pp. 243–250, 2008.

[22] F. Al-Zahra, A. N. Alkhateeb, and F. H. Hussein, "Photocatalytic oxidation of benzyl alcohol using pure and sensitized anatase," *Desalination*, vol. 209, no. 1–3, pp. 342–349, 2007.

[23] A. J. Attia, S. H. Kadhim, and F. H. Hussein, "Photocatalytic degradation of textile dyeing wastewater using titanium dioxide and zinc oxide," *E-Journal of Chemistry*, vol. 5, no. 2, pp. 219–223, 2008.

[24] F. H. Hussein and A. N. Alkhateeb, "Photo-oxidation of benzyl alcohol under natural weathering conditions," *Desalination*, vol. 209, no. 1–3, pp. 350–355, 2007.

[25] F. Hussein and T. Abbas, "Photocatalytic treatment of textile industrial wastewater," *International Journal of Chemical Sciences*, vol. 8, no. 3, pp. 1353–1364, 2010.

[26] F. H. Hussein and T. Abbas, "Solar photolysis and photocatalytic treatment of textile industrial wastewater," *International Journal of Chemical Sciences*, vol. 8, no. 3, pp. 1409–1420, 2010.

[27] F. H. Hussein, A. F. Halbus, H. A. K. Hassan, and W. A. K. Hussein, "Photocatalytic degradation of bismarck brown G using irradiated ZnO in aqueous solutions," *E-Journal of Chemistry*, vol. 7, no. 2, pp. 540–544, 2010.

[28] F. H. Hussein, M. Obies, and A. Drea, "Photocatalytic decolorization of bismarck brown R by suspension of titanium dioxide," *International Journal of Chemical Sciences*, vol. 8, no. 4, pp. 2736–2746, 2010.

[29] F. H. Hussein, M. Obies, and A. Drea, "Photocatalytic decolorization of bismarck brown R by suspension of titanium dioxide," *International Journal of Chemical Sciences*, vol. 8, no. 4, pp. 2763–2774, 2010.

[30] P. F. F. Amaral, D. L. A. Fernandes, A. P. M. Tavares et al., "Decolorization of dyes from textile wastewater by Trametes versicolor," *Environmental Technology*, vol. 25, no. 11, pp. 1313–1320, 2004.

[31] D. Hongve and G. Åkesson, "Spectrophotometric determination of water colour in hazen units," *Water Research*, vol. 30, no. 11, pp. 2771–2775, 1996.

[32] S. Sakthivel, B. Neppolian, M. V. Shankar, B. Arabindoo, M. Palanichamy, and V. Murugesan, "Solar photocatalytic degradation of azo dye: comparison of photocatalytic efficiency of ZnO and TiO₂," *Solar Energy Materials and Solar Cells*, vol. 77, no. 1, pp. 65–82, 2003.

[33] A. Akyol, H. C. Yatmaz, and M. Bayramoglu, "Photocatalytic decolorization of remazol red RR in aqueous ZnO suspensions," *Applied Catalysis B*, vol. 54, no. 1, pp. 19–24, 2004.

[34] B. Neppolian, H. C. Choi, S. Sakthivel, B. Arabindoo, and V. Murugesan, "Solar light induced and TiO₂ assisted degradation of textile dye reactive blue 4," *Chemosphere*, vol. 46, no. 8, pp. 1173–1181, 2002.

[35] F. Akbal, "Photocatalytic degradation of organic dyes in the presence of titanium dioxide under UV and solar light: effect of operational parameters," *Environmental Progress*, vol. 24, no. 3, pp. 317–322, 2005.

[36] D. Dong, P. Li, X. Li et al., "Investigation on the photocatalytic degradation of pyrene on soil surfaces using nanometer anatase TiO₂ under UV irradiation," *Journal of Hazardous Materials*, vol. 174, no. 1–3, pp. 859–863, 2010.

[37] T. Kim and M. Lee, "Effect of pH and temperature for photocatalytic degradation of organic compound on carbon-coated TiO₂," *International Journal of Advances in Engineering and Technology*, vol. 3, no. 2, pp. 193–198, 2010.

[38] U. Gaya, A. Abdullah, Z. Zainal, and M. Hussein, "Photocatalytic degradation of 2,4-dichlorophenol in irradiated aqueous ZnO suspension," *International Journal of Chemistry*, vol. 2, no. 1, pp. 180–193, 2010.

[39] S. K. Kavitha and P. N. Palanisamy, "Photocatalytic and sonophotocatalytic degradation of reactive red 120 using dye sensitized Tio₂ under visible light," *International Journal of Civil and Environmental Engineering*, vol. 3, pp. 1–6, 2011.

[40] R. S. Thakur, R. Chaudhary, and C. Singh, "Fundamentals and applications of the photocatalytic treatment for the removal of industrial organic pollutants and effects of operational

parameters: a review," *Journal of Renewable and Sustainable Energy*, vol. 2, no. 4, Article ID 042701, pp. 42–70, 2010.

[41] S. K. Kansal, M. Singh, and D. Sud, "Comparative evaluation of UV/solar light induced photodegradation of phenol in aqueous solutions," *Indian Chemical Engineering*, vol. 49, no. 1, pp. 11–20, 2007.

[42] S. Malato, J. Blanco, A. Vidal et al., "Applied studies in solar photocatalytic detoxification: an overview," *Solar Energy*, vol. 75, no. 4, pp. 329–336, 2003.

[43] R. J. Davis, J. L. Gainer, G. O'Neal, and I. W. Wu, "Photocatalytic decolorization of wastewater dyes," *Water Environment Research*, vol. 66, no. 1, pp. 50–53, 1994.

[44] L. Rideh, A. Wehrer, D. Ronze, and A. Zoulalian, "Photocatalytic degradation of 2-chlorophenol in TiO_2 aqueous suspension: modeling of reaction rate," *Industrial and Engineering Chemistry Research*, vol. 36, no. 11, pp. 4712–4718, 1997.

[45] V. Murugesan and S. Sakthivel, "Photocatalytic degradation of leather dyes in aqueous solution using solar/UV illuminatedTiO_2/ZnO," in *Proceedings of the International Symposium on Environmental Pollution Control and Waste Management (EPCOWM '02)*, pp. 654–659, Tunis, January 2002.

[46] T. Dahl, "Examining the role of singlet oxygen in photosensitized cytotoxity," in *Aquatic and Surface Photochemistry*, G. Heiz, R. Zepp, and D. Crosby, Eds., pp. 241–260, Lewis, Chelsea, Mich, USA, 1994.

[47] P. Kamat, "Photochemical solar cells; a successful marriage between semiconductor nanoclusters and excited dyes," *APS Newsletter*, pp. 1–11, 1996.

[48] F. H. Hussein, "Photochemical treatments of textile industries wastewater," in *Advances in Treating Textile Effluent*, P. J. Hauser, Ed., pp. 117–144, InTech Open Access Publishing, Vienna, Austria, 2011.

[49] M. Zhao and J. Zhang, "Wastewater treatment by photocatalytic oxidation of nano-ZnO," *Global Environmental Policy in Japan*, no. 12, pp. 1–9, 2008.

[50] P. Fernández-Ibáñez, J. Blanco, S. Malato, and F. J. de Las Nieves, "Application of the colloidal stability of TiO_2 particles for recovery and reuse in solar photocatalysis," *Water Research*, vol. 37, no. 13, pp. 3180–3188, 2003.

[51] T. Ohno, "Preparation of visible light active S-doped TiO_2 photocatalysts and their photocatalytic activities," *Water Science and Technology*, vol. 49, no. 4, pp. 159–163, 2004.

[52] Y. Cho, W. Choi, C. H. Lee, T. Hyeon, and H. I. Lee, "Visible light-induced degradation of carbon tetrachloride on dye-sensitized TiO_2," *Environmental Science and Technology*, vol. 35, no. 5, pp. 966–970, 2001.

[53] F. H. Hussein, G. Pattenden, R. Rudham, and J. J. Russell, "Photo-oxidation of alcohols catalysed by platinised titanium dioxide," *Tetrahedron Letters*, vol. 25, no. 31, pp. 3363–3364, 1984.

[54] F. Hussein, S. Radi, and S. Naman, "The effect of sensitizer on the photocatalytical oxidation of propan-2-ol by Pt-TiO_2 and other catalysts," in *Solar Energy Applications, Bioconversion and Sun Fules*, vol. B of *Energy and Environmental Progress 1*, pp. 337–353, Nova Science, 1991.

Research Article

Mesoporous TiO$_2$ Micro-Nanometer Composite Structure: Synthesis, Optoelectric Properties, and Photocatalytic Selectivity

Kun Liu,[1] Lianjie Zhu,[1] Tengfei Jiang,[2] Youguang Sun,[1] Hongbin Li,[1] and Dejun Wang[2]

[1] *School of Chemistry & Chemical Engineering, Tianjin University of Technology, Tianjin 300384, China*
[2] *College of Chemistry, Jilin University, Changchun 130023, China*

Correspondence should be addressed to Lianjie Zhu, zhulj@tjut.edu.cn

Mesoporous anatase TiO$_2$ micro-nanometer composite structure was synthesized by solvothermal method at 180°C, followed by calcination at 400°C for 2 h. The as-prepared TiO$_2$ was characterized by X-ray diffraction (XRD), scanning electron microscope (SEM), transmission electron microscope (TEM), and Fourier transform infrared spectrum (FT-IR). The specific surface area and pore size distribution were obtained from N$_2$ adsorption-desorption isotherm, and the optoelectric property of the mesoporous TiO$_2$ was studied by UV-Vis absorption spectrum and surface photovoltage spectra (SPS). The photocatalytic activity was evaluated by photodegradation of sole rhodamine B (RhB) and sole phenol aqueous solutions under simulated sunlight irradiation and compared with that of Degussa P-25 (P25) under the same conditions. The photodegradation preference of this mesoporous TiO$_2$ was also investigated for an RhB-phenol mixed solution. The results show that the TiO$_2$ composite structure consists of microspheres (~0.5–2 μm in diameter) and irregular aggregates (several hundred nanometers) with rough surfaces and the average primary particle size is 10.2 nm. The photodegradation activities of this mesoporous TiO$_2$ on both RhB and phenol solutions are higher than those of P25. Moreover, this as-prepared TiO$_2$ exhibits photodegradation preference on RhB in the RhB-phenol mixture solution.

1. Introduction

In recent decades, TiO$_2$ has received considerable attention due to its wide applications in fields such as solar cell, photocatalysis and lithium-ion batteries [1–9]. As a potential excellent catalyst, TiO$_2$ has a great prospect in waste water treatment [10–12]. However, in order to commercialize this technique, a few problems need to be solved at the first time: (1) preparation of catalyst with high specific surface area; (2) extending the light absorption capability of the catalyst to visible region; (3) easy separation of the catalyst from the suspension after photodegradation. It was known that monodispersed nanocrystalline TiO$_2$ generally has high specific surface area and high photocatalytic activity. But normally it suffers from severe aggregation during photocatalytic reactions, which would reduce its active sites and light harvesting capability. As a result, its photocatalytic activity would be decreased. Moreover, it is too small to be separated from the

suspension by conventional method. Hence, in recent years, mesoporous TiO$_2$ microspheres have received much attention because the porous structures would offer a high specific surface area, and the large particle size causes them to be separated and reclaimed easily since they can settle down in aqueous suspensions by gravity [13]. However, increasing the particle size of a catalyst is often accompanied by a decrease in its photocatalytic activity, while a large-sized mesoporous micro-nanometer TiO$_2$ composite structure with high specific surface area may solve this problem. A facile route for large-scale synthesis of such TiO$_2$ photocatalyst may benefit practical applications of this photocatalysis technique in industrial waste water treatment.

Among the synthesis methods, hydrothermal or solvothermal method was often applied extensively [13–15] because of its simple, mild, and uniform crystallization. In the present paper, mesoporous micro-nanometer TiO$_2$ composite structures were synthesized by solvothermal
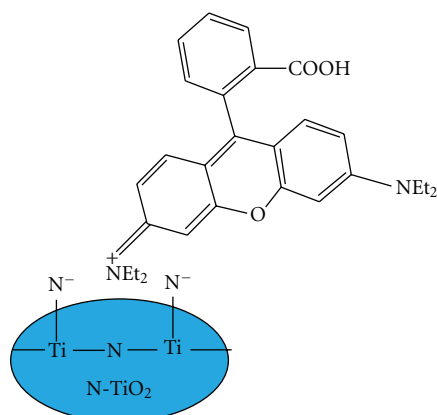
Scheme 1: Adsorption mode of RhB on the surface of N-doping TiO$_2$.

method. Since dye sensitization can easily extend the light absorption capability of the TiO$_2$ catalyst to visible region [16, 17], RhB was used to evaluate the photocatalytic activity of the as-prepared TiO$_2$ under simulated sunlight irradiation because the RhB itself can act as a sensitizer. Furthermore, photodegradation of phenol aqueous solution over this TiO$_2$ composite structure was also investigated because phenol is one of the common organic pollutants that can hardly adsorb the visible light.

Since it is usual that several organic pollutants are present simultaneously in the real effluents from industries and photocatalytic oxidation process based on TiO$_2$ was found a highly effective method for degradation of organic pollutants, studying the preferential degradation of organic pollutants in their mixture solutions over TiO$_2$ catalysts is important for the practical application. Some researchers have been devoted to this problem [18–23]. For example, Comparelli et al. [18] have explored the effect of two different substituents on photodegradation of two organic dyes, methyl red and methyl orange. Sahel et al. [20] have studied the photocatalytic degradation of a mixture of two anionic dyes, remazol black and red procion MX-5B. Yu et al. [21–23] have investigated photocatalytic selectivity towards decomposition of azo dyes, methyl orange, methyl blue, or methyl violet. But so far the preferential photodegradation by a mesoporous TiO$_2$ in an RhB-phenol mixture solution has been hardly seen. Therefore, we choose an RhB-phenol mixed aqueous solution as a model system to investigate the photodegradation preference of the TiO$_2$ catalyst.

2. Experimental

2.1. Preparation of TiO$_2$.
In a typical procedure, 0.1 mL of triethanolamine was added to 40 mL of absolute ethanol (99%) and kept stirring for a few minutes. Then, 1.5 mL of tetrabutyl titanate was dropped into the solution under vigorous stirring and a white suspension was obtained. After 4 h stirring, the suspension was transferred to a 50 mL Teflon-lined stainless steel autoclave and kept in an electric oven at 180°C for 24 h. The autoclave was taken out and left to cool naturally to the room temperature. A white precipitate was obtained via centrifugation, washed with ethanol for two times, and dried at 60°C for 6 h. Finally, the product was calcined at 400°C for 2 h with a heating rate of 1°C min^{-1} to obtain the mesoporous TiO$_2$.

2.2. Characterization.
X-ray powder diffraction (XRD) measurements were performed on a Rigaku D/max-2500 diffractometer with Cu Kα radiation ($\lambda = 0.154056$ nm) at 40 kV and 100 mA. Scanning electron microscope (SEM) images were taken with a JSM 6700F field-emission scanning electron microscope. Transmission electron microscope (TEM) and high-resolution TEM (HRTEM) images were obtained with a JEOL JEM-2100F transmission electron microscope operating at 200 kV. UV-Vis diffuse reflectance absorption spectra were recorded on a Hitachi/U-3900 UV-visible spectrophotometer. N$_2$ adsorption-desorption isotherm was obtained with a V-Sorb 2800P surface area and pore size analyzer. FT-IR spectrum was carried out on a Nicolet Avatar 370 Fourier transform infrared spectrometer. The XPS measurement was performed on a PHI-5300 ESCA system. Surface photovoltage spectrum (SPS) was measured by a homemade sandwich-type solid junction cell ITO/Sample/ITO with light monochromator-lock-in detection technique, and filed induced surface photovoltage spectra (FISPS) were obtained with aid of a DC electric field applied to two sides of the sample cell. The SPS data have been normalized to make the light intensity of the lamp the same at each wavelength. Details on the setup have been described elsewhere [24]. The absorbance of the RhB or phenol aqueous solutions during the photocatalytic reactions was examined by a UV-2100 UV-visible spectrophotometer. The relative concentration of RhB and phenol in their mixed solution at certain photodegradation time was measured by a COMETRO LC6000 high-performance liquid chromatography (HPLC).

2.3. Photocatalytic Activity Measurement.
Photocatalytic activity of the mesoporous TiO$_2$ was investigated by photodegradations of RhB (10 mg L^{-1}) and phenol (10 mg L^{-1}) aqueous solutions under simulated sunlight illumination, where a 400 W halogen light (from Beijing Lighting Research Institute) was used as the light source to simulate the sunlight (with ~5% UV light). The photocatalysis system and reaction conditions were described in our previous work [25]. The concentration of RhB at certain reaction time was determined by measuring its absorbance at 552 nm on a UV-visible spectrophotometer, from which the photodegradation percentage was calculated by using the formula $\Phi = (A_0 - A)/A_0 \times 100\%$, where Φ is the degradation percentage, A_0 the initial absorbance of the RhB solution, and A the absorbance at certain reaction time. The photodegradation of phenol aqueous solution over the mesoporous TiO$_2$ was studied by following the same procedure as above, but the absorbance at 270 nm was measured for the phenol solution.

3. Results and Discussion

3.1. Crystal Phase and Morphology of the Mesoporous TiO$_2$.
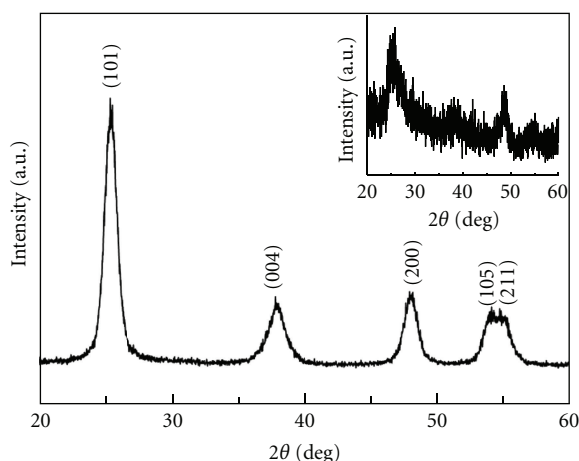The high crystallinity and phase purity of the calcined sample

FIGURE 1: XRD patterns of the as-prepared TiO_2 after calcination at 400°C and before calcination (the inset).

TiO_2 were characterized by XRD, as shown in Figure 1. All of the diffraction peaks can be indexed to anatase TiO_2 (JCPDS card no. 04-0477, space group $I4_1/amd$ (141), and cell $a = 3.785$ Å, $c = 9.514$ Å). The average primary particle size of the as-prepared TiO_2 was calculated by using the Debye-Scherrer formula based on the 101 diffraction peak, which is 10.2 nm. The weak and broad peaks in the inset of Figure 1 indicate a bad crystallinity of the uncalcined TiO_2 sample. Therefore, the calcination of the pristine product at 400°C for 2 h with a heating rate of 1°C min^{-1} led to a great increase in its crystallinity, but the anatase crystal phase was kept unchanged.

The morphology and microstructure of the as-obtained TiO_2 are clearly demonstrated by SEM, TEM, and HRTEM images, as shown in Figures 2 and 3. It is apparent (Figures 2(a) and 2(b)) that only part of the products possess microspherical structure with diameters of 0.5–2 μm. The most part is irregular aggregate with sizes of several hundred nanometers. Whatever the shape of the product is,0020 it is constructed by numerous interconnected primary nanocrystals and the surface is rather rough. The TEM images (Figures 3(a) and 3(b)) confirm the porous nature of the product with the main pore size of around 10 nm and the primary nanocrystal size of around 10 nm as well, which is consistent with the XRD result. These nanocrystals are connected with each other and the pores are the interparticle voids. The HRTEM image shows that many anatase primary nanocrystals are random in orientations. The lattice spacings for all the chosen adjacent three nanocrystals are measured to be 0.351 nm, as marked in Figure 3(c), corresponding to the (101) facet of the anatase phase. The fast Fourier transform (FFT) pattern (inset) displays somewhat dispersed spots with circles, which implies it is a multicrystalline.

3.2. N_2 Adsorption-Desorption Isotherm. Figure 4 shows the nitrogen adsorption-desorption isotherm of the as-synthesized TiO_2, which is characteristic of a type IV isotherm with a type H3 hysteresis loop, indicating the presence of mesopores in the size range of 2–50 nm. As

depicted in the Barrett-Joyner-Halenda (BJH) pore size distribution (the inset of Figure 4), the main pore sizes are in the range of 2–20 nm and the pore volume is 0.490 $cm^3 g^{-1}$. The Brunauer-Emmett-Teller-(BET-) specific surface area is as high as 179 $m^2 g^{-1}$, which may be benefit to its high photocatalytic activity.

3.3. FT-IR Spectrum. Figure 5(a) shows the FT-IR spectrum of the mesoporous TiO_2. The peaks at 464 cm^{-1} and 530 cm^{-1} are characteristic stretching vibrations of Ti–O–Ti network in TiO_2, and the bands around 3420 cm^{-1} and 1650 cm^{-1} could be assigned to the stretching and bending vibrations of the O–H group and adsorbed water, respectively [26]. The bands between 900 and 1300 cm^{-1} could be attributed to the stretching vibration of C–O or C–N bond [27], which might be from the residual of the triethanolamine. This could be further clarified by the following results.

As shown in Figures 5(b)–5(d), the XPS results confirmed that the products contain some residual nitrogen on the surface of TiO_2. The nitrogen percentage in the whole N-doping TiO_2 sample is small, ca. 1.4% (atomic ratio), but the N/Ti atomic ratio is as high as 0.1 : 1, which is far beyond the environmental contamination level (ca. 0.01 : 1 in the P25 sample [28]). This clearly indicates the N-doping in this mesoporous TiO_2. The peak of N 1s around 400.16 eV can be assigned to the N atom in the environment of O–Ti–N [29] or Ti–O–N [30]. The peak around 397 eV is attributable to N mainly interacting with Ti centers [31, 32]. The nitrogen element comes from the only source triethanolamine. According to the XPS result in C 1s region, three peaks were observed (after the Gaussian fitting) with binding energies of 284.8 eV, 286.4 eV, and 288.9 eV. They can be assigned to C–C, C–O, and C=O groups, respectively, by referring to [33], where these three peaks were attributed to adventitious carbon species from XPS measurement. No obvious signal at ~282 eV, corresponding to O–Ti–C bond, was observed in our case, which implies that no carbon doping occurred.

3.4. Optoelectric Properties. The light-harvesting capabilities of the as-prepared mesoporous TiO_2 and the P25 are slightly different, as shown in Figure 6(a). Besides the strong intrinsic absorption below 400 nm, the TiO_2 sample can also weakly absorb the visible light (400–700 nm), which was not observed for the P25. This, on the one hand, indicates a stronger light scattering ability of the as-prepared TiO_2 due to its larger particle sizes [1] of the microspherical and irregular aggregate structures. On the other hand, it could be attributed to the impurity states deriving from nitrogen insertion in the bulk of the oxide or intrinsic defects, including those defects associated with oxygen vacancies [34, 35]. The calculated band gap energy of the mesoporous TiO_2, 3.15 eV, by using the method in [36] is much higher than that of the P25, 2.95 eV, which is attributed to the quantum size effect because the average primary particle size of the sample TiO_2, 10.2 nm, is much smaller than that of P25, ~25 nm.
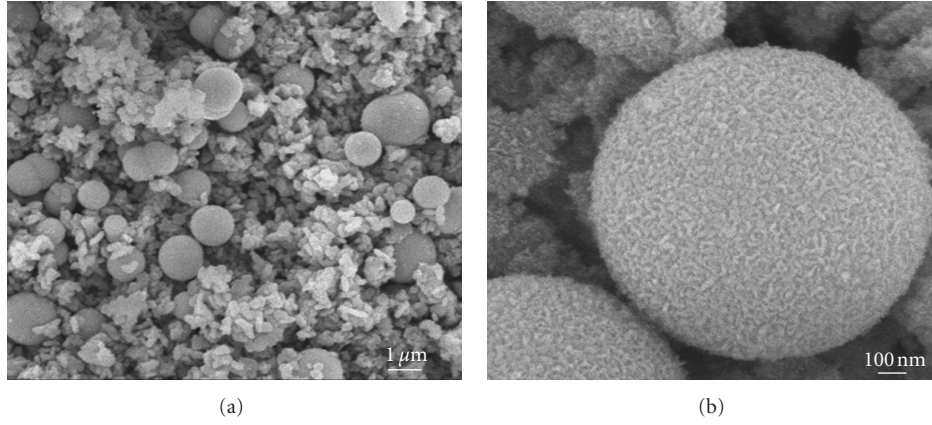
(a)

(b)

FIGURE 2: SEM images of the as-prepared TiO$_2$: (a) low magnification, (b) high magnification.
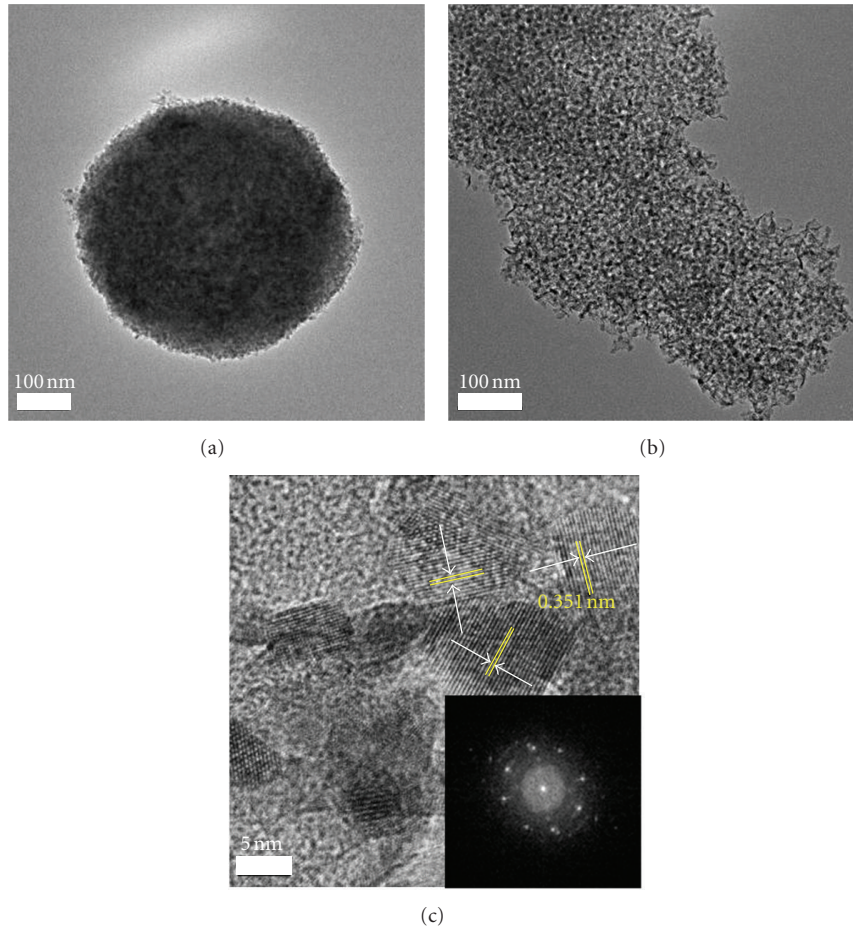

(a)

(b)

(c)

FIGURE 3: ((a) and (b)) TEM images. (c) HRTEM image and fast Fourier transform (FFT) pattern (inset) of the as-prepared mesoporous TiO$_2$.

Surface photovoltage spectrum (SPS) is a well-established contactless and nondestructive technique for semiconductor characterization, which can reflect the separation and recombination of photo-induced electron-hole pairs on the catalyst surface under illumination [37]. When the incident light energy is higher than the band gap energy of TiO$_2$, the electrons are excited from the valence band to the conduction band, which generates the electron-hole pairs. The electrons move to the surface and the holes to the bulk of the TiO$_2$ by the built-in electric field, which generates photovoltage signal. As shown in Figure 6(b), a pronounced surface photovoltage signal is observed in the
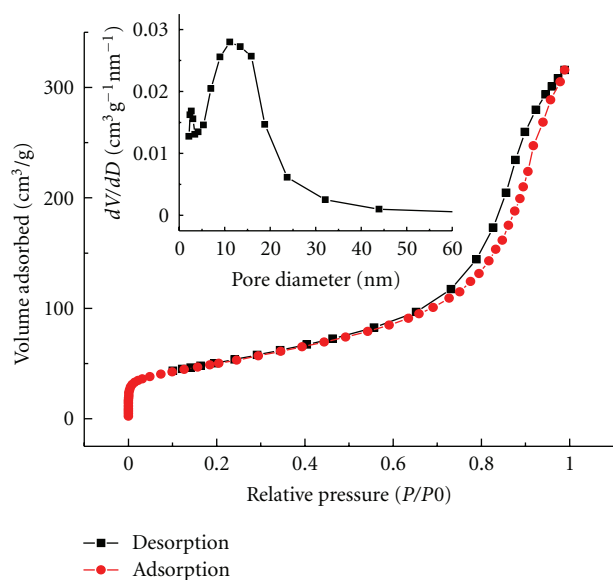
Figure 4: N_2 adsorption-desorption isotherm of the as-prepared mesoporous TiO_2, and the inset is the BJH pore-size distribution curve.

range of 300–425 nm, which includes two transition bands according to the Gaussian fitting (the inset of Figure 6(b)). Besides an intrinsic band-band transition from 300 nm to 375 nm ($O_{2p} - Ti_{3d}$ at 335 nm [38]), there is a sub-band-gap transition with the peak value of around 365 nm, which is attributed to the electron transition from valence band to surface state, deriving from the surface impurity. This impurity state in the mesoporous TiO_2 locates at 0.3 eV below the conduction band according to the calculation using the formula $x = 1240/y$. Here, x is the energy level and y is the wavelength at the responding peak. According to the fitting result, as shown in the inset of Figure 6(b), 335.6 nm and 365 nm are used for calculations of energy levels of the conduction band and surface state, respectively. Referring to the method in [39], by making a tangent line across the band edge of the SPS (see Figure 6(b)), the Eg of the mesoporous TiO_2 is calculated again, which is 3.23 eV, higher than the value obtained based on the absorption spectrum. This Eg value is more consistent with its quantum size of 10 nm. Therefore, SPS is a good method for accurately determining band gap energy of a semiconductor because SPS exactly reflects the electron transition behavior under illumination.

When a 0.5 V positive external electric field was applied to the sample, the surface photovoltage signal increases, which indicates that the direction of the external electric field is the same with that of the built-in electric field. On the contrary, it decreases in a 0.5 V negative electric field. These imply that this mesoporous TiO_2 exhibits a p-type semiconductor according to the field effect principle [40]. This p-type semiconductor character may be due to the surface impurity, a little nitrogen, which is consistent with the results of FT-IR, XPS, and UV-Vis absorption spectra.

3.5. Photocatalysis. The photocatalytic activity of the as prepared TiO_2 was first estimated on the basis of the

decomposition of RhB under simulated sunlight illumination. Degussa P25 was used as the reference material for comparison purpose. In the controlled experiment in which RhB was in the mesoporous TiO_2 suspensions in dark for 2 h, no obvious photocatalytic activity (<5%) was observed. However, the photolysis rate of RhB was serious, about 45%, in the absence of TiO_2 catalyst. Figures 7(a) and 7(b) present the photodegradation curves of RhB aqueous solutions under simulated sunlight irradiation, which demonstrate that both the sample TiO_2 and P25 exhibit high photocatalytic activities. This may be due to self-sensitization of the RhB dye on the TiO_2 catalyst, which extends the wavelength range for light absorption of the TiO_2 catalyst to the visible light region. Although the photodegradation activities of the sample TiO_2 and P25 on RhB solutions are similar, the sample TiO_2 would benefit from its larger particle sizes because it can be easily reclaimed under gravity from the suspension after reactions. The results show that the suspension of the sample TiO_2 settled down mostly after 5 min and completely after 18 min, whereas for P25 suspension no obvious change was observed after 30 min sedimentation. On the other hand, the larger particle sizes may reduce aggregate of the catalyst to a certain extent. It was well known that aggregation of nanosized TiO_2 was very difficult to avoid, and these aggregates can actually affect the number of the active sites, light scattering property of the TiO_2, and the photon penetration [41]. In the end it will reduce the photocatalytic activity of the catalyst. In general the smaller crystals are poorer light scatterer than the larger crystals as the scattering efficiency is proportional to r^4 in Rayleigh scattering [42]. With the reaction going on, the P25 gradually forms aggregates, which would reduce its active sites and scatter more incident photons because these aggregates are constructed by larger size of primary crystals (~25 nm) than the sample TiO_2 (10.2 nm). The decrease in active sites and light absorption capability would result in a decrease in its photocatalytic activity. As for the TiO_2, there would be no such serious aggregation in the case of its large particle size. Moreover, the high specific surface area offers the as-prepared catalyst a big number of active sites and the porous micro-nanometer composite structure allows a great number of scattered photons to penetrate into the mesopores so that the interior of the microspheres and irregular aggregates could be utilized for photodegradation reactions as well to a certain extent. These may explain the higher photocatalytic activity of the as-prepared TiO_2 at the latter stage of the photodegradation reaction.

No obvious degradations of the phenol aqueous solutions ($10 \, mg \, L^{-1}$) were observed (<5%) over the sample TiO_2 in the dark and photolysis in the absence of TiO_2 catalyst. Under simulated sunlight irradiation, the photodegradation percentage of phenol aqueous solution over the as-prepared TiO_2 is always higher than that of P25, see Figures 7(c) and 7(d). It reaches 49.3% after 2 h reactions, which is higher than that of P25 (38%). This high photocatalytic activity may be related with its high specific surface area. Moreover, the existence of the surface state, as shown in Figure 6(b), can reduce the recombination of the photogenerated electron-holes since the photogenerated electrons can transfer to the
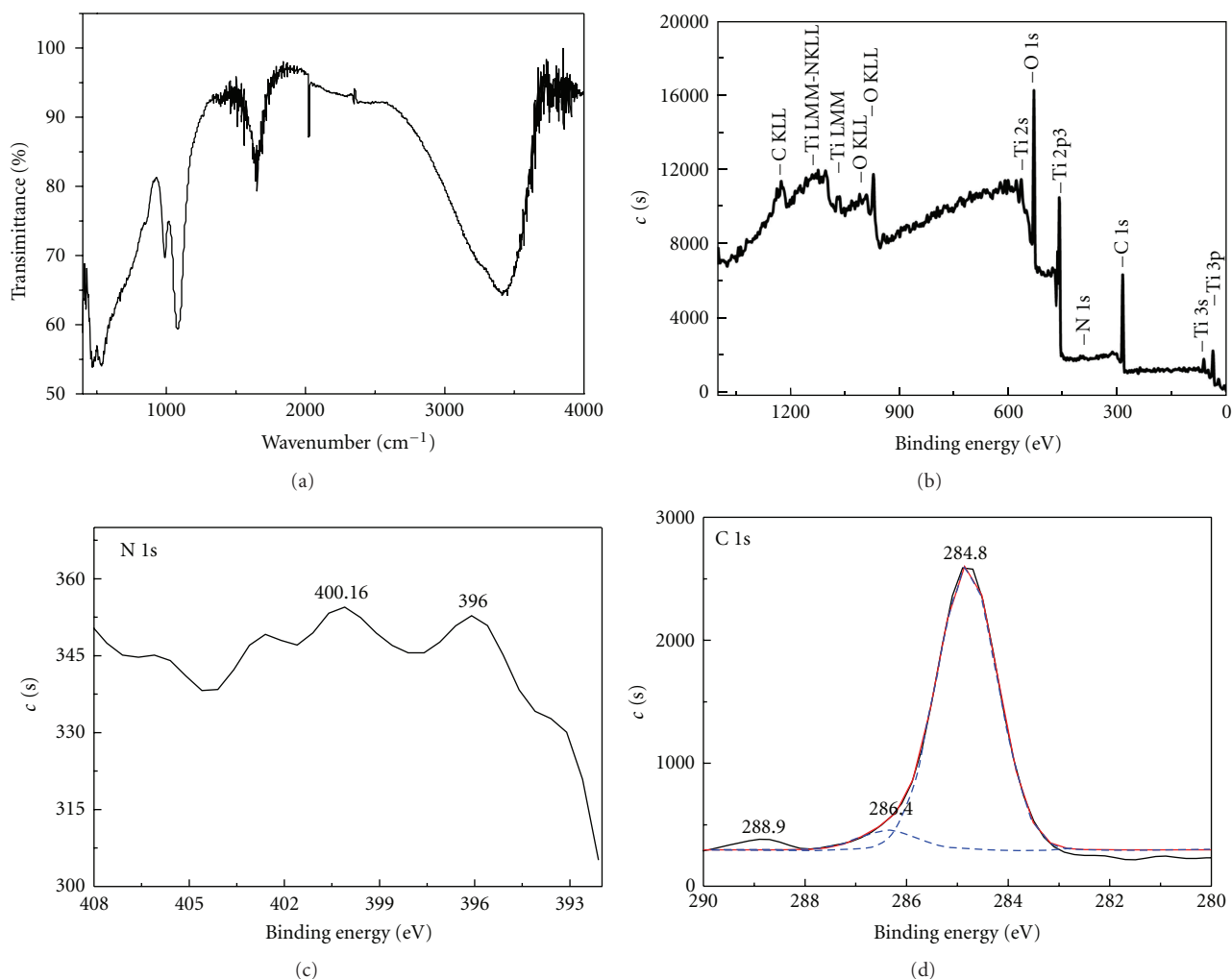
(a)

(b)

(c)

(d)

FIGURE 5: (a) FT-IR of the mesoporous TiO_2. ((b)–(d)) XPS of the mesoporous TiO_2: survey (b) and deconvoluted spectra for N 1s (c) and C 1s (d).
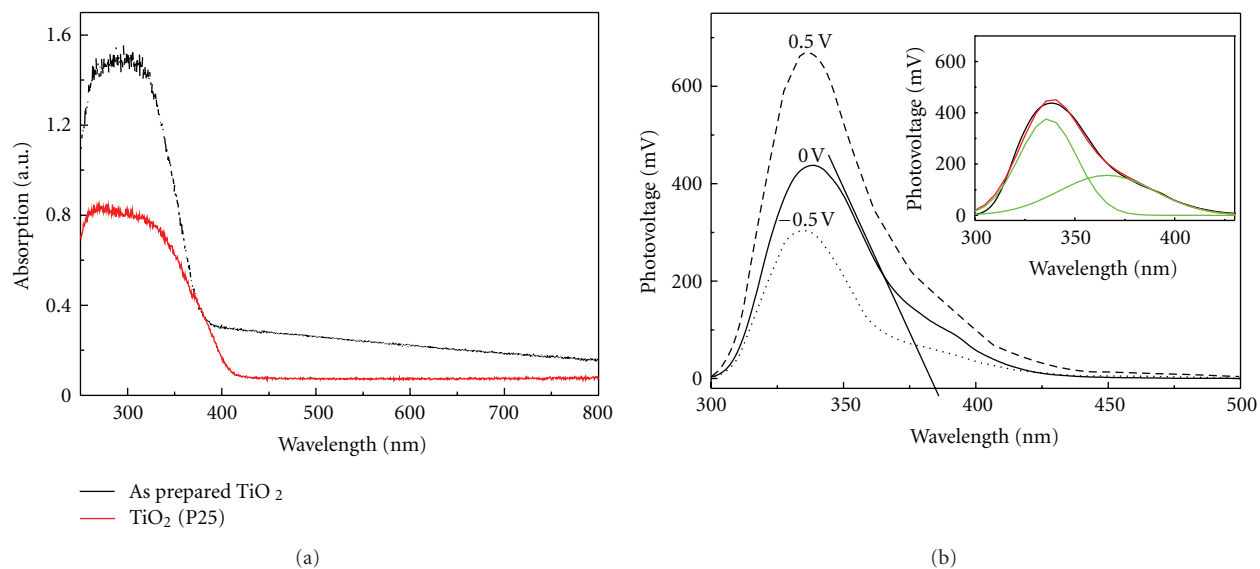

(a)

(b)

FIGURE 6: (a) UV-Vis diffuse reflection absorption spectra of the as-prepared mesoporous TiO_2 and P25. (b) Surface photovoltage spectrum (SPS) and field-induced surface photovoltage spectra (FISPS) of the mesoporous TiO_2, and the inset is the Gaussian fitting of the SPS.
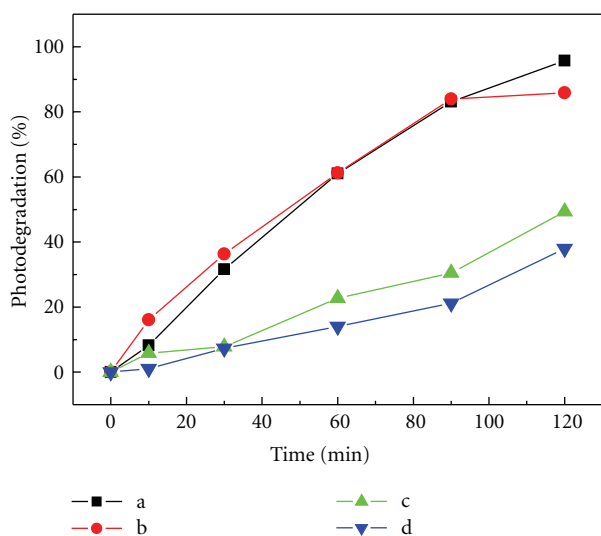
FIGURE 7: Photocatalytic performance of the as-prepared mesoporous TiO$_2$ and P25 under simulated sunlight irradiation: photodegradations of (a) the mesoporous TiO$_2$ on RhB, (b) P25 on RhB, (c) the mesoporous TiO$_2$ on phenol, and (d) P25 on phenol.
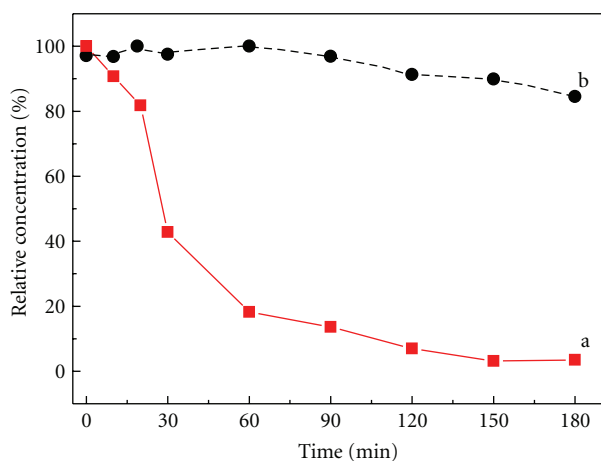

FIGURE 8: Photodegradation preference of the as-prepared TiO$_2$ on RhB and phenol in their mixture solution under simulated sunlight: (a) RhB, (b) phenol.

surface state. As a result, the photocatalytic activity will be increased. From the microstructure point of view, the porous structure of the sample TiO$_2$ also benefits the photon penetration and separation of photogenerated carriers. Thus, the photocatalytic activity will be increased.

Since the presence of organic pollutant mixtures in real effluents from industries is frequent, we studied the preferential photodegradation of a RhB-phenol mixed solution over the as-prepared mesoporous TiO$_2$ under simulated sunlight irradiation, as shown in Figure 8 where HPLC was used to monitor the relative concentration of the two organics in their mixture solution at any reaction time and the maximum absorption wavelengths (552 nm for RhB and 270 nm for phenol) were chosen, respectively, for the measurement. The concentration of RhB and phenol in the

mixture solution is the same, $10 \, mg \, L^{-1}$. It is obvious that the as-prepared TiO$_2$ exhibits much higher photocatalytic activity on RhB than phenol. The relative concentration of RhB drops to 18.2% after 1 h photodegradation reaction. At the same time, however, the relative concentration of phenol hardly changes (<5%). In the next reaction stage, from 1 h to 3 h, the residual RhB was decomposed completely and phenol was simultaneously degraded slightly. The photodegradation percentage of phenol in three hours is only 15.5%, which is much lower than that for the sole phenol aqueous solution (49.3%, as shown in Figure 7(c)). These results suggest that the simultaneous presence of RhB in the solution disturbs and postpones the photodegradation of phenol. It also implies that the RhB could not function as a sensitizer for the TiO$_2$ catalyst to increase the visible light utilization and photodegradation efficiency of phenol in the RhB-phenol mixture solution system.

The photodegradation preference on RhB in the mixed solution may be caused by the preferential adsorption of RhB molecules. It was reported [43–45] that RhB preferentially anchors on an F-doping TiO$_2$ through the cationic moiety (–NEt$_2$ group). Similarly, it could also adsorb on the N-doping TiO$_2$ surface through the NEt$_2$ group, as shown in Scheme 1. Here, the cationic –NEt$_2$ group has strong static electron interaction with the anionic N atom on the TiO$_2$ surface. Moreover, the RhB molecule can absorb UV-visible light in the range of 200–600 nm, whereas the phenol only absorbs the light below 280 nm. This could also be responsible partially for the higher photodegradation activity of RhB in the mixed solution.

4. Conclusions

Mesoporous anatase TiO$_2$ micro-nanometer composite with high specific surface area was synthesized by a facile solvothermal method. The high crystallinity of the product was obtained by heating it at 400°C for 2 h. The morphology of the as-prepared TiO$_2$ comprises microspheres and irregular aggregates with rather rough surfaces, which are composed of numerous nanocrystals. The primary particle size of this mesoporous TiO$_2$ is 10.2 nm. Its BET surface area is as high as $179 \, m^2 \, g^{-1}$ and the main pore sizes are in the range of 2–20 nm. The weak absorption on visible light, the sub-band-gap transition band in SPS, and the p-type semiconductor character (according to FISPS) of the mesoporous TiO$_2$ indicate there is surface impurity, which may derive from the raw material triethanolamine. The FT-IR spectrum shows there may be C–O or C–N groups on the TiO$_2$ surface, and XPS results confirm it is an N-doped TiO$_2$, where the N element is from triethanolamine. Under simulated sunlight irradiation, the photocatalytic activities of this mesoporous TiO$_2$ on both RhB and phenol aqueous solutions are higher than those of commercial TiO$_2$ (P25), which may be related with its high specific surface area, the light harvesting ability in visible region, mesoporous structure, and the existence of surface state. The as-prepared TiO$_2$ shows obvious photodegradation preference on RhB in the RhB-phenol mixture solution. Hence, RhB could not be

used as a sensitizer to increase the photocatalytic activity of phenol in visible light. Moreover, the sample TiO_2 can be easily reclaimed in 18 minutes by sedimentation from the suspension under gravity after photodegradation reactions. Thus, this TiO_2 catalyst is in favor of practical application in waste water treatment.

Acknowledgments

References

[1] W. G. Yang, F. R. Wan, Q. W. Chen, J. J. Li, and D. S. Xu, "Controlling synthesis of well-crystallized mesoporous TiO_2 microspheres with ultrahigh surface area for high-performance dye-sensitized solar cells," *Journal of Materials Chemistry*, vol. 20, no. 14, pp. 2870–2876, 2010.

[2] G. H. Wang, B. Cheng, J. Zhang, L. Xu, and T. T. Yin, "Facile synthesis and photocatalytic property of titania/carbon composite hollow microspheres with bimodal mesoporous shells," *International Journal of Photoenergy*, vol. 2012, Article ID 976389, 9 pages, 2012.

[3] J. S. Chen, Y. L. Tan, C. M. Li et al., "Constructing hierarchical spheres from large ultrathin anatase TiO_2 nanosheets with nearly 100% exposed (001) facets for fast reversible lithium storage," *Journal of the American Chemical Society*, vol. 132, no. 17, pp. 6124–6130, 2010.

[4] S. W. Liu, J. G. Yu, and M. Jaroniec, "Anatase TiO_2 with dominant high-energy 001 facets: synthesis, properties, and applications," *Chemistry of Materials*, vol. 23, no. 18, pp. 4085–4093, 2011.

[5] N. H. Lee, H. J. Oh, S. C. Jung, W. J. Lee, D. H. Kim, and S. J. Kim, "Photocatalytic properties of nanotubular-shaped TiO_2 powders with anatase phase obtained from titanate nanotube powder through various thermal treatments," *International Journal of Photoenergy*, vol. 2011, Article ID 327821, 7 pages, 2011.

[6] W. Zheng, X. Liu, Z. Yan, and L. Zhu, "Ionic liquid-assisted synthesis of large-scale TiO_2 nanoparticles with controllable phase by hydrolysis of $TiCl_4$," *ACS Nano*, vol. 3, no. 1, pp. 115–122, 2009.

[7] X. Zhang, J. H. Pan, A. J. Du, J. Ng, D. D. Sun, and J. O. Leckie, "Fabrication and photocatalytic activity of porous TiO_2 nanowire microspheres by surfactant-mediated spray drying process," *Materials Research Bulletin*, vol. 44, no. 5, pp. 1070–1076, 2009.

[8] J. A. Byrne, P. A. Fernandez-Ibañez, P. S. M. Dunlop, D. M. A. Alrousan, and J. W. J. Hamilton, "Photocatalytic enhancement for solar disinfection of water: a review," *International Journal of Photoenergy*, vol. 2011, Article ID 798051, 12 pages, 2011.

[9] M. H. Zhou, J. Zhang, B. Cheng, and H. G. Yu, "Enhancement of visible-light photocatalytic activity of mesoporous Au-TiO_2 nanocomposites by surface plasmon resonance," *International Journal of Photoenergy*, vol. 2012, Article ID 532843, 10 pages, 2012.

[10] S. Kumar, A. G. Fedorov, and J. L. Gole, "Photodegradation of ethylene using visible light responsive surfaces prepared from titania nanoparticle slurries," *Applied Catalysis B*, vol. 57, no. 2, pp. 93–107, 2005.

[11] F. Wei, H. Zeng, P. Cui, S. Peng, and T. Cheng, "Various TiO_2 microcrystals: controlled synthesis and enhanced photocatalytic activities," *Chemical Engineering Journal*, vol. 144, no. 1, pp. 119–123, 2008.

[12] L. Zhang, Y. Zhu, Y. He, W. Li, and H. Sun, "Preparation and performances of mesoporous TiO_2 film photocatalyst supported on stainless steel," *Applied Catalysis B*, vol. 40, no. 4, pp. 287–292, 2003.

[13] J. H. Xu, W. L. Dai, J. Li, Y. Cao, H. Li, and K. Fan, "Novel core-shell structured mesoporous titania microspheres: preparation, characterization and excellent photocatalytic activity in phenol abatement," *Journal of Photochemistry and Photobiology A*, vol. 195, no. 2-3, pp. 284–294, 2008.

[14] J. Luo and L. Gao, "Large-scale production of monodispersed titania microspheres by surfactant-guided self-assembly," *Journal of Alloys and Compounds*, vol. 487, no. 1-2, pp. 763–767, 2009.

[15] H. Zhang, Y. Han, X. Liu et al., "Anatase TiO_2 microspheres with exposed mirror-like plane 001 facets for high performance dye-sensitized solar cells (DSSCs)," *Chemical Communications*, vol. 46, no. 44, pp. 8395–8397, 2010.

[16] H. S. Hilal, L. Z. Majjad, N. Zaatar, and A. El-Hamouz, "Dye-effect in TiO_2 catalyzed contaminant photo-degradation: sensitization vs. charge-transfer formalism," *Solid State Sciences*, vol. 9, no. 1, pp. 9–15, 2007.

[17] Y. Cho and W. Choi, "Visible light-induced reactions of humic acids on TiO_2," *Journal of Photochemistry and Photobiology A*, vol. 148, no. 1–3, pp. 129–135, 2002.

[18] R. Comparelli, E. Fanizza, M. L. Curri et al., "Photocatalytic degradation of azo dyes by organic-capped anatase TiO_2 nanocrystals immobilized onto substrates," *Applied Catalysis B*, vol. 55, no. 2, pp. 81–91, 2005.

[19] E. M. Saggioro, A. S. Oliveira, T. Pavesi, C. G. Maia, L. F. V. Ferreira, and J. C. Moreira, "Use of titanium dioxide photocatalysis on the remediation of model textile wastewaters containing azo dyes," *Molecules*, vol. 16, no. 12, pp. 10370–10386, 2011.

[20] K. Sahel, N. Perol, F. Dappozze, M. Bouhent, Z. Derriche, and C. Guillard, "Photocatalytic degradation of a mixture of two anionic dyes: procion Red MX-5B and Remazol Black 5 (RB5)," *Journal of Photochemistry and Photobiology A*, vol. 212, no. 2-3, pp. 107–112, 2010.

[21] S. Liu, J. Yu, and M. Jaroniec, "Tunable photocatalytic selectivity of hollow TiO_2 microspheres composed of anatase polyhedra with exposed 001 facets," *Journal of the American Chemical Society*, vol. 132, no. 34, pp. 11914–11916, 2010.

[22] Q. Xiang, J. Yu, and M. Jaroniec, "Tunable photocatalytic selectivity of TiO_2 films consisted of flower-like microspheres with exposed 001 facets," *Chemical Communications*, vol. 47, no. 15, pp. 4532–4534, 2011.

[23] S. W. Liu, C. Liu, W. G. Wang, B. Cheng, and J. G. Yu, "Unique photocatalytic oxidation reactivity and selectivity of TiO_2-graphene nanocomposites," *Nanoscale*, vol. 4, pp. 3193–3200, 2012.

[24] L. Yanhong, W. Dejun, Z. Qidong, Y. Min, and Z. Qinglin, "A study of quantum confinement properties of photogenerated charges in ZnO nanoparticles by surface photovoltage spectroscopy," *Journal of Physical Chemistry B*, vol. 108, no. 10, pp. 3202–3206, 2004.

[25] L. Zhu, H. Miao, K. Liu, Y. Sun, M. Qiu, and X. Zhu, "Microwave and conventional hydrothermal synthesis of TiO_2 nanoparticles and their photocatalytic activities," *Advanced Materials Research*, vol. 391-392, pp. 988–992, 2012.

[26] Z. Li, M. Kawashita, and M. Doi, "Sol-gel synthesis and characterization of magnetic TiO_2 microspheres," *Journal of the Ceramic Society of Japan*, vol. 118, no. 1378, pp. 467–473, 2010.

[27] Wuhan University, *Instrument Analysis*, Higher Education Press, Beijing, China, 1st edition, 2001.

[28] X. Chen and C. Burda, "Photoelectron spectroscopic investigation of nitrogen-doped titania nanoparticles," *Journal of Physical Chemistry B*, vol. 108, no. 40, pp. 15446–15449, 2004.

[29] Y. Cong, J. Zhang, F. Chen, and M. Anpo, "Synthesis and characterization of nitrogen-doped TiO_2 nanophotocatalyst with high visible light activity," *Journal of Physical Chemistry C*, vol. 111, no. 19, pp. 6976–6982, 2007.

[30] F. Dong, H. Wang, and Z. Wu, "One-step "Green" synthetic approach for mesoporous C-doped titanium dioxide with efficient visible light photocatalytic activity," *Journal of Physical Chemistry C*, vol. 113, no. 38, pp. 16717–16723, 2009.

[31] T. C. Jagadale, S. P. Takale, R. S. Sonawane et al., "N-doped TiO_2 nanoparticle based visible light photocatalyst by modified peroxide sol-gel method," *Journal of Physical Chemistry C*, vol. 112, no. 37, pp. 14595–14602, 2008.

[32] C. Feng, Y. Wang, Z. Jin et al., "Photoactive centers responsible for visible-light photoactivity of N-doped TiO_2," *New Journal of Chemistry*, vol. 32, no. 6, pp. 1038–1047, 2008.

[33] Y. Wu, M. Xing, B. Tian, J. Zhang, and F. Chen, "Preparation of nitrogen and fluorine co-doped mesoporous TiO_2 microsphere and photodegradation of acid orange 7 under visible light," *Chemical Engineering Journal*, vol. 162, no. 2, pp. 710–717, 2010.

[34] Z. Lin, A. Orlov, R. M. Lambert, and M. C. Payne, "New insights into the origin of visible light photocatalytic activity of nitrogen-doped and oxygen-deficient anatase TiO_2," *Journal of Physical Chemistry B*, vol. 109, no. 44, pp. 20948–20952, 2005.

[35] I. N. Martyanov, S. Uma, S. Rodrigues, and K. J. Klabunde, "Structural defects cause TiO_2-based photocatalysts to be active in visible light," *Chemical Communications*, vol. 10, no. 21, pp. 2476–2477, 2004.

[36] L. Zhu, Y. Zheng, T. Hao, X. Shi, Y. Chen, and J. Ou-Yang, "Synthesis of hierarchical ZnO nanobelts via Zn(OH)F intermediate using ionic liquid-assistant microwave irradiation method," *Materials Letters*, vol. 63, no. 28, pp. 2405–2408, 2009.

[37] T. F. Xie, D. J. Wang, L. J. Zhu, T. J. Li, and Y. J. Xu, "Application of surface photovoltage technique in photocatalysis studies on modified TiO_2 photo-catalysts for photo-reduction of CO_2," *Materials Chemistry and Physics*, vol. 70, no. 1, pp. 103–106, 2001.

[38] X. Qian, D. Qin, Q. Song et al., "Surface photovoltage spectra and photoelectrochemical properties of semiconductor-sensitized nanostructured TiO_2 electrodes," *Thin Solid Films*, vol. 385, no. 1-2, pp. 152–161, 2001.

[39] L. Zhu, Y. Chen, Y. Sun et al., "Phase-manipulable synthesis of Cu-based nanomaterials using ionic liquid 1-butyl-3-methyl-imidazole tetrafluoroborate," *Crystal Research and Technology*, vol. 45, no. 4, pp. 398–404, 2010.

[40] Q. Zhao, D. Wang, L. Peng, Y. Lin, M. Yang, and T. Xie, "Surface photovoltage study of photogenerated charges in ZnO nanorods array grown on ITO," *Chemical Physics Letters*, vol. 434, no. 1–3, pp. 96–100, 2007.

[41] P. F. Lee, X. Zhang, D. D. Sun, J. Du, and J. O. Leckie, "Synthesis of bimodal porous structured TiO_2 microsphere with high photocatalytic activity for water treatment," *Colloids and Surfaces A*, vol. 324, no. 1–3, pp. 202–207, 2008.

[42] A. J. Maira, K. L. Yeung, C. Y. Lee, P. L. Yue, and C. K. Chan, "Size effects in gas-phase photo-oxidation of trichloroethylene using nanometer-sized TiO_2 catalysts," *Journal of Catalysis*, vol. 192, no. 1, pp. 185–196, 2000.

[43] K. L. Lv, B. Cheng, J. G. Yu, and G. Liu, "Fluorine ions-mediated morphology control of anatase TiO_2 with enhanced photocatalytic activity," *Physical Chemistry Chemical Physics*, vol. 14, no. 16, pp. 5349–5362, 2012.

[44] S. W. Liu, J. G. Yu, B. Cheng, and M. Jaroniec, "Fluorinated semiconductor photocatalysts: tunable synthesis and unique properties," *Advances in Colloid and Interface Science*, vol. 173, pp. 35–53, 2012.

[45] Q. Wang, C. Chen, D. Zhao, M. Wanhong, and J. Zhao, "Change of adsorption modes of dyes on fluorinated TiO_2 and its effect on photocatalytic degradation of dyes under visible irradiation," *Langmuir*, vol. 24, no. 14, pp. 7338–7345, 2008.